



HAL
open science

Impact of flow rotation on flame dynamics and hydrodynamic stability

Thomas Kaiser

► **To cite this version:**

Thomas Kaiser. Impact of flow rotation on flame dynamics and hydrodynamic stability. Fluid mechanics [physics.class-ph]. Institut National Polytechnique de Toulouse - INPT, 2019. English. NNT : 2019INPT0011 . tel-04160561

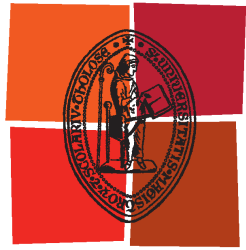
HAL Id: tel-04160561

<https://theses.hal.science/tel-04160561>

Submitted on 12 Jul 2023

HAL is a multi-disciplinary open access archive for the deposit and dissemination of scientific research documents, whether they are published or not. The documents may come from teaching and research institutions in France or abroad, or from public or private research centers.

L'archive ouverte pluridisciplinaire **HAL**, est destinée au dépôt et à la diffusion de documents scientifiques de niveau recherche, publiés ou non, émanant des établissements d'enseignement et de recherche français ou étrangers, des laboratoires publics ou privés.



Université
de Toulouse

THÈSE

En vue de l'obtention du

DOCTORAT DE L'UNIVERSITÉ DE TOULOUSE

Délivré par :

Institut National Polytechnique de Toulouse (Toulouse INP)

Discipline ou spécialité :

Dynamique des fluides

Présentée et soutenue par :

M. THOMAS KAISER

le jeudi 31 janvier 2019

Titre :

Impact of Flow Rotation on Flame Dynamics and Hydrodynamic Stability

Ecole doctorale :

Mécanique, Energétique, Génie civil, Procédés (MEGeP)

Unité de recherche :

Institut de Mécanique des Fluides de Toulouse (I.M.F.T.)

Directeur(s) de Thèse :

M. THIERRY POINSOT

M. LAURENT SELLE

Rapporteurs :

M. PASCAL BRUEL, CNRS

M. RONAN VICQUELIN, CENTRALESUPELEC GIF SUR YVETTE

Membre(s) du jury :

M. JEAN-MARC CHOMAZ, CNRS PARIS, Président

M. KILIAN OBERLEITHNER, TECHNISCHE UNIVERSITAT BERLIN, Membre

M. MATTHEW JUNIPER, UNIVERSITE DE CAMBRIDGE, Membre

M. THIERRY POINSOT, CNRS TOULOUSE, Membre

To my parents Ludwig and Maria-Theresia

Wohltätig ist des Feuers Macht,
Wenn sie der Mensch bezähmt, bewacht,
Und was er bildet, was er schafft,
Das dankt er dieser Himmelskraft.

Auszug aus *Das Lied von der Glocke*
- Friedrich Schiller

Most wholesome is the force of fire,
When man can tame and guard its ire,
And from this heavenly force man takes
Good help for what he moulds and makes.

Excerpt from *The song of the bell*
- Friedrich Schiller

English translation based on Margarete Münsterberg

Acknowledgements

In his poem *The song of the bell* (see excerpt on the preceding page) the German poet Friedrich Schiller describes the 18th century manufacturing process of a church bell from creating the casting mold until its first stroke. The main focus of the poem is on the human creative urge and his will to “mould” and “make”. And of course especially on the feelings and sentiments that are inherent to the creative process: Joy in creating, passion and diligence, but also despair, fear, loss of control. And finally the feeling of uncertainty, just before the casting mold is broken and the bell arises from the dust. To the authors knowledge, it is unknown if Friedrich Schiller, himself a doctor of medicine and law, was inspired to his poetic masterpiece by his own dissertation and he changed the story line to a manufacturing process in order to make it appealing to a broader audience.

The song of the bell however barely describes one aspect, which probably invokes the most positive sentiments during a creative process: The companions of the creative, be they directly or indirectly involved in the project. Without them it would not only be less joyful, it would be impossible. Similarly, in theses, as they are naturally focused on the results of the work, the appreciation for colleagues, supervisors, family and other supporters cannot be sufficiently expressed. This short text cannot compensate all the help that I received from my companions along this journey during the last three years and before. In fact nothing can. This nevertheless is the attempt to at least give them the stage and laurels they deserve.

One person however is mentioned in *The song of the bell*: It is the master (today called supervisor), who after the dangerous casting process counts the heads of his team and finds in relief that everyone was spared. In my case this role fell onto two persons. Firstly, I would like to thank my first supervisor Thierry Poinot. Thank you for having trust in me and creating a research environment in which I could follow my research freely. It is impressive how accurately you know, at what moments you have to increase or decrease the pressure on a doctoral student to help him being optimally motivated. Furthermore, I would like to thank Laurent Selle, my co-supervisor. Your active support has helped me to meet the one or other deadline. Also the fact that you are an inexhaustible source of ideas is well known beyond the borders of Toulouse. This trait of yours often helped me to find new perspectives on organizational and scientific problems. By working with the two of you I had

the possibility to learn countless lessons, which are not only restricted to my professional life. Thank you!

Beyond, I would like to thank Kilian Oberleithner, who helped me taking first steps in hydrodynamic stability analysis. Working with you was not only an immense professional benefit, due to your uncomplicated, down to earth character it was also always a pleasure. Also the collegiality of the whole research team at TU Berlin during my two months stay is gratefully acknowledged. I am glad, that I will have the opportunity to continue my work together with you in Berlin.

I am also grateful towards the reviewers of my doctoral thesis, Pascal Bruel and Ronan Vicquelin and jury members in my defense: Kilian Oberleithner, Jean-Marc Chomaz and Matthew Juniper. I am glad that you are taking the time to read my dissertation and come to my defense in Toulouse.

Thousand thanks also go to my great office mates, Quentin and Christian, and later Dominik and Jimmy. Thank you for all the valuable discussions about work and beyond. Of course my gratitude goes beyond my office doors to all my friends in the (former) Particle Spray and Combustion team at IMFT. When I came to Toulouse, I always felt welcomed in the group, both during and after work. Namely, I would like to mention in this context Maxence, Guillaume, Corentin and Emilien who altogether kicked me off into the numerical combustion world of Toulouse. Furthermore, I would like to thank our combustion experiment team, Daniel, Pradip and Görkem, for providing the valuable experimental data. I thank Abdulla, for his professional support but - in fact especially - for giving me an unforgettable first impression of CERFACS, Aynur for uplifting words not only but also after bicycle accidents and Francois for giving shelter to the homeless.

Without the support of the CFD group at CERFACS, our numerical work at IMFT would have been much harder. In the context of my own work I received valuable help from Gabriel Staffelbach. Thank you for answering all my naive and not naive questions about AVBP. How you manage to keep up with your work load remains a mystery to outsiders.

A special place in these acknowledgements is reserved for my family. Without the unconditional support of my parents, Ludwig and Maria-Theresia, not only this dissertation but much more than that would have been inconceivable. You never let any stone unturned to provide me with all possibilities for my education and clear my way. I am aware what a privilege it is to be born by coincidence in the situation to have parents like you. My gratitude towards you goes beyond what I can express with words. Therefore, this thesis is dedicated to you. Furthermore, I am grateful for the priceless help of my brother Marcus. You were not only a big brother but also a role model to me in the academic world. And that is even though I never really understood what you are doing. Yet, I am relieved that it is the same the other way around. Finally, I would like to thank my girlfriend Anna, who did her studies in Munich while I was in Toulouse for my dissertation. I know, it is not easy

to have a boyfriend who constantly thinks about strange equations and at the same time is often far away for several months. Therefore, I thank you for your patience and I cannot express how happy I am that we mastered this difficult challenge.

Abstract

This thesis investigates large scale flow rotation in two configurations. In the first, the focus is on the effect of flow rotation on a laminar flame. The flame is anchored in the wake of a cylindrical bluff body. The flow rotation is introduced by turning the cylinder along its axis. It is shown by Direct Numerical Simulation (DNS), that the cylinder rotation breaks the symmetry of both flame branches. Flame Transfer Function (FTF) measurements performed by the Wiener-Hopf Inversion suggest, that low rotation rates lead to deep gaps in the gain and the flame becomes almost insensitive to acoustic perturbation at a specific frequency. It furthermore is demonstrated that this decrease in gain of the FTF is due to destructive interference of the heat release signals caused by the two flame branches. The frequency at which the gain becomes almost zero can be adjusted by tuning the cylinder rotation rate. The study suggests that controlling the symmetry of the flame could be a tool of open-loop control of thermoacoustic instabilities.

In the second configuration the cause of flow rotation is a hydrodynamic instability, namely the Precessing Vortex Core (PVC) in an industrial fuel injection system. Experimental measurements and Large Eddy Simulation (LES) show that the non-reacting flow within the primary injector is superimposed by a PVC. The hydrodynamic instability furthermore is investigated by a Linear Stability Analysis (LSA). Both local and BiGlobal approaches are applied and compared regarding their respective results. Experimental, LES and LSA results demonstrate that mounting a central rod in the interior of the primary injector stabilizes the PVC. In addition, the same industrial injector is investigated for a reacting flow via LES. The results demonstrate, that the flame stabilizes the flow concerning the PVC. It is shown by a BiGlobal stability analysis, that the density gradient in the mean flame front has a significant dampening effect on the instability. Finally, the impact of the central rod is investigated also for reacting flows. It is shown, that the central rod only marginally effects the global flame shape, but has a beneficial effect on flame anchoring in the lean regime. Both cases, the one with rod and the one without rod are compared also by a LSA concerning the stability of the PVC. Results suggest, that the rod significantly increases the dampening of the PVC. This could lead to decreased turbulence levels in the flow, prevent flame quenching and therefore explain the beneficial influence of the rod regarding flame anchoring.

Résumé

Cette thèse a pour but l'étude de la rotation de l'écoulement des grandes échelles dans deux configurations. La première configuration se concentre sur l'effet de la rotation de l'écoulement sur une flamme laminaire. Elle est stabilisée dans le sillage d'un cylindre. La rotation de l'écoulement est introduite en faisant tourner le cylindre autour de son axe. La simulation numérique directe (Direct Numerical Simulation (DNS)) montre que la rotation du cylindre rompt la symétrie des deux branches de la flamme. La fonction de transfert de flamme (Flame Transfer Function (FTF)), obtenue grâce à l'inversion de Wiener-Hopf, indique qu'un faible taux de rotation réduit le gain de la FTF et donc la flamme devient presque insensible aux perturbations acoustiques à une fréquence donnée. De plus, il est démontré que cette diminution du gain est due à une interférence destructive des fluctuations de chaleur produites par les deux branches de la flamme. La fréquence à laquelle le gain de la FTF devient presque nul est ajustable par la vitesse de rotation du cylindre. Cette étude suggère que le contrôle de la symétrie de la flamme pourrait être un outil de contrôle en boucle ouverte des instabilités thermoacoustiques.

Dans le cas de la deuxième configuration, la rotation de l'écoulement est induite par une instabilité hydrodynamique, aussi nommée Precessing Vortex Core (PVC) dans un système d'injection de carburant industriel. Des expériences et des simulations aux grandes échelles (Large Eddy Simulation (LES)) montrent que l'écoulement non-réactif dans l'injecteur primaire peut être décomposé en une contribution moyenne et un PVC. Cette instabilité hydrodynamique est étudiée par l'analyse de stabilité linéaire (Linear Stability Analysis (LSA)) en utilisant deux approches différentes (locale et BiGlobale). Les résultats de l'expérience, de la LES et de la LSA démontrent que le montage d'une tige centrale à l'intérieur de l'injecteur stabilise le PVC. De plus, le même injecteur industriel est étudié dans le cas d'un écoulement réactif par LES. Les résultats démontrent que la flamme stabilise le PVC. L'analyse de stabilité BiGlobal montre que le gradient de densité dans le front moyen de la flamme a un effet important sur l'amortissement du PVC. Enfin, l'impact de la tige centrale est également étudié pour le cas réactif. La tige centrale impacte marginalement la forme globale de la flamme, mais a un effet positif sur l'accrochage de la flamme dans la zone de combustion pauvre. En comparant deux cas par LSA, celui avec la tige et celui sans la tige, les résultats suggèrent que la tige augmente considérablement l'amortissement du PVC. Cela pourrait

causer une diminution de la turbulence dans l'écoulement et empêcher l'extinction de la flamme et donc expliquer l'influence bénéfique de la tige sur la stabilisation de la flamme.

Contents

List of Symbols	xxv
Abbreviations	xxix
1 Introduction	1
1.1 Combustion - A Future Technology?	1
1.2 Fundamentals of Thermoacoustics	6
1.2.1 On the Cause and Nature of Thermoacoustic Instabilities	6
1.2.2 Analysis Tools for Thermoacoustic Instabilities in Combustion Systems	9
1.2.2.1 Brute-Force Time Integration of the Full Set of Reactive Navier-Stokes Equations	9
1.2.2.2 Isolation of Physical Phenomena by Low(er) Order Approaches	10
1.3 Impact of Flow Rotation on Flame Dynamics	11
1.4 Objectives	13
I Symmetry Breaking by Flow Rotation: Impact on the Thermoacoustic Behaviour of Laminar Flames	17
2 DNS Tools	19
2.1 Governing Equations	20
2.1.1 Perfect Gas Law	20
2.1.2 Continuity Equation	21
2.1.3 Momentum Equations	22
2.1.4 Energy Equation	22
2.2 Numerical Discretization	23
2.2.1 The Cell Vertex Method	23
2.2.2 Convection scheme	24
2.3 Chemistry Model	25
3 The INTRIG Configuration	27
	xv

3.1	Experimental Set-Up	29
3.2	Simulation Setup and Meshing	30
3.3	Results of Laminar DNS	33
3.3.1	Steady State Response to Bluff Body Rotation	33
3.3.2	Flame Response to Acoustic Forcing	36
3.3.2.1	System Identification: The Wiener-Hopf Inversion	36
3.3.2.2	Flame Response without Rotation	40
3.3.2.3	Flame Response with Rotation	48
3.3.2.4	Influence of Bluff Body Rotation on Flame Front Dynamics	53
3.4	Conclusion	55
 II Hydrodynamic Instabilities in Fuel Injection Systems		57
4	LES	59
4.1	LES Governing Equations	60
4.2	Turbulence Modelling	62
4.3	LES Chemistry Model	63
4.3.1	BFER	63
4.3.2	Thickened Flame Model	64
5	Linear Stability Analysis of Hydrodynamic Instabilities	65
5.1	Governing Equations of Hydrodynamic Stability	66
5.1.1	Coherent Structures in Uniform Density Flows	67
5.1.2	Coherent Structures in Non-Uniform Density Flows	69
5.2	Solution Approaches in Hydrodynamic Stability Analysis	71
5.2.1	BiGlobal Stability Analysis for Swirling Jets	72
5.2.1.1	BiGlobal Modal Approach	72
5.2.1.2	Solving BiGlobal Analysis with the Finite Element Method	75
5.2.1.3	Adjoint Modes and Structural Sensitivity	77
5.2.1.4	Validation of the BiGlobal stability code	78
5.2.2	Local Stability Analysis	80
5.2.2.1	Local Modal approach	80
5.2.2.2	Temporal Analysis, Spatial Analysis and Spatio-Temporal Analysis	81
5.2.3	Global Instability in Spatially Developing Flows	85
5.2.4	A Step-by-Step Strategy to Identify the Wave Maker Position and Reconstruct the Global Mode	87
5.2.5	Numerical Approach: The Chebychev Collocation	88
5.3	Conclusion	89

6	The PreINTRIG Experiment and Cold Flow Simulations	91
6.1	The Set-Up of the PreINTRIG Experiment	92
6.2	Coldflow LES	95
6.2.1	Numerical Set-Up for Non-Reactive LES of the PreINTRIG Configuration	95
6.2.2	Validation of LES Results	97
6.2.3	Results of Non-Reactive LES of the PreINTRIG Configuration	99
6.3	Hydrodynamic Stability Analysis of the PreINTRIG Swirler Flow	104
6.3.1	Results of Local Stability Analysis	105
6.3.2	Results of BiGlobal Stability Analysis	112
6.3.2.1	No-Rod Configuration	113
6.3.2.2	Rod Configuration	117
6.4	Conclusion and Interpretation	118
7	Reactive Simulations of the PreINTRIG Configuration	123
7.1	Reactive LES	123
7.1.1	Numerical Set-Up for Reactive LES of the PreINTRIG Configuration	124
7.1.2	Results	125
7.1.2.1	Influence of the Rod on the Temporal Means	125
7.1.2.2	Blow-off in Lean Flames	126
7.2	Stability Analysis of Passive Flames	126
7.2.1	Influence of Non-uniform Density on the Stability of the PVC	128
7.2.1.1	Stability Analysis of a Reacting Flow Ignoring the Density Gradient	130
7.2.1.2	Stability Analysis of a Reacting Flow Taking into Account the Density Gradient	130
7.2.2	Influence of the Central Rod on the Stability of the PVC in Reacting Flows	134
7.3	Conclusion	134
	Concluding Remarks	137
	Appendices	141
A	Hydrodynamic Linear Stability Analysis in Rotation Symmetric Flows of Uniform Density	143
A.1	Derivative Operators in Cylindrical Coordinates	143
A.2	Governing Equations	144
A.3	Linearization	145
A.4	BiGlobal Stability	146
A.5	Local Stability	149

B Hydrodynamic Linear Stability Analysis in Rotation Symmetric Flows of Non-uniform Density	153
B.1 Derivative Operators in Cylindrical Coordinates	153
B.2 Governing Equations	154
B.3 Linearization	156
B.4 BiGlobal Stability	157
B.5 Local Stability	161
B.6 Stochastic-Coherent Interaction in Non-uniform Density Flows	165

List of Figures

1.1	Share of energy sources in gross power generation in Germany in 2017; Data based on [268]	3
1.2	Share of primary energy consumption in Germany in 2017; Data based on [267]	3
1.3	Output of renewable energies in Germany in 2017/2018	4
1.4	Development of global primary energy consumption since 1992; Data based on [20]	5
1.5	Destructive impact of CIs; Burner nozzle before (left) and after (right) a CI event	6
1.6	Feedback loop leading to a thermoacoustic instability in a combustion engine; based on [133]	7
1.7	Typical pressure trace of the transient to a thermoacoustic oscillation to its limit cycle; based on [133]	8
1.8	PVC in a swirling jet; taken from [183]	12
1.9	Flame shape of a laminar flame anchored in the wake of a cylindrical bluff body for various rotation rates of the cylinder based on experiments and DNS; non-rotating cylinder at the left top; rotation rate increases from frame 1 to 4; taken from [152]	13
3.1	Spherical flames in air-propane-hydrogen mixtures; α corresponds to the mass ratio of hydrogen in the fuel. Taken from [119]	28
3.2	The INTRIG experiment; (a): Schematic; (b): Photograph of methane-air flame	29
3.3	2D-computational domain and mesh for the INTRIG configuration at a cylinder rotation rate of $\alpha = 0$ (a) and inlay showing the refinement at the cylinder (b)	31
3.4	Inlet velocity profile in simulation (line) versus experimental hot wire measurements (red circles)	31
3.5	Graphical representation of energy balance of the bluff body	32

LIST OF FIGURES

3.6	Steady state based on DNS; The field shows the flow speed in x -direction, the thin lines correspond to stream lines and the thick black line is the iso-surface of heat release. (a): $\alpha = 0$; (b): $\alpha = 0.625$; (c): $\alpha = 1.25$; (d): $\alpha = 2.5$; (e): $\alpha = 3.75$; (f): Definitions of the flame root positions, x_{root,y^\pm} , tip positions, x_{root,y^\pm} and the bulk velocities in the respective upper and lower half planes, v_{y^\pm} specified in Tab. 3.2	35
3.7	Sketch of a LTI system	37
3.8	SI process in temporal domain via WHI and in frequency domain via harmonic forcing	39
3.9	Convertibility of IR and TF by the (inverse) z -transform	39
3.10	Example of excitation signals for the acoustic forcing in the LDNS	40
3.11	Comparison of flame topologies of the steady flame (black line) and instantaneous snapshots of a pulsed flame (white iso surface of heat release) at various phase angles of harmonic velocity perturbation ($ u' = 5\%u_b$, $f = 100$ Hz, $\alpha = 0$)	41
3.12	(a) Flame normal displacements (see Fig. 3.12(b)) as a function of the flame position for a non rotating bluff body and various phase angles, ϕ , of harmonic velocity perturbation of frequency $f = 80$ Hz and amplitude $ u' = 5\%u_b$; (b) Schematics of laminar flame displacements; Thick solid line: unperturbed flame, thick dashed line: displaced flame; Definition of the flame angle, φ , flame displacement in flow direction, η , and flame normal displacement, ξ ; u indicates the fresh gas velocity and direction.	42
3.13	FTF based on WHI and harmonic forcing for a non rotating bluff body; $K = 500$ and 10000 curves correspond to the outlet relaxation coefficient in NSCBC and lead to the same results.	43
3.14	IR based on WHI for a non rotating bluff body	44
3.15	Flame root displacement, ξ_0 , caused by a Dirac like acoustic excitation (see Eqn. (3.3.8)) in dependence of time	45
3.16	Response of the flame topology to a short pulse of inlet velocity (see Eqn. (3.3.8)); Black line: Steady flame, white line: iso-surface of instantaneous heat release of the pulsed case; The times given are with respect to the end of the short pulse.	46
3.17	Response to an acoustic pulse: Velocity fluctuations at the reference point for the determination of the FTF (upper axis) and heat release fluctuations (lower axis) due to a dirac like acoustic pulse	47
3.18	Global FTFs for various rotation rates based on WHI of DNS results	48
3.19	FTFs of the upper flame branch (y^+) for various rotation rates based on WHI	49
3.20	FTFs of the lower flame branch (y^-) for various rotation rates based on WHI	50
3.21	Comparisons of gains of global FTFs and of the single flame branches FTFs; Frequencies of ideal destructive and ideal constructive interference are marked on the global gains	52

3.22	Response of flame topology to acoustic forcing; flame normal displacement, ξ , as a function of the flame front position, l for the upper and lower branch at various cylinder rotation rates and various phase angles of the harmonic acoustic forcing of frequency 80 Hz and amplitude $5\% u_b$	54
3.23	Relative flame tip position with respect to the respective branches flame tip position of the steady flame, $\Delta x = x_{\text{tip}} - x_{\text{tip,st}}$, versus the phase angle of the velocity perturbation, ϕ ; Cylinder rotation rate $\alpha = 0.625$; pulsation amplitude $ u' = 2\% u_b$; pulsation frequency $f_{d,1} = 132$ Hz	54
4.1	Comparison of the concepts of DNS, LES and RANS	60
4.2	Instantaneous snapshots of CFD simulations of a turbulent jet for DNS, LES and RANS [145]	61
4.3	DNS of a flame without artificial flame thickening (left) and with an artificial thickening of $\mathcal{F} = 5$ (right); taken from [190]	64
5.1	Validation of the BiGlobal code: Radial and axial velocity component of the laminar base flow around a sphere at $\text{Re} = 280.7$; Azimuthal velocity component is set to 0.	78
5.2	Validation of the BiGlobal code: Comparisons of eigenfunctions with results previously published in literature	79
5.3	Schematic representation of a wave packet caused by a pulse introduced in the flow at $x = t = 0$ for base flows with different stability properties	82
5.4	Example for temporal analysis: ω_i and ω_r as a function of the real axial wave number for various azimuthal wave numbers in a non-swirling jet; taken from Gallaire et Chomaz [74]	83
5.5	Local stability analysis of an obstacle-free wake flow at a globally constant Reynolds number $\text{Re} = 100$, taken from Juniper et al. [105]; Streamlines, and absolute frequency, $\omega_{0,i}$, α_i^+ (\circ) and α_i^- (\times) in dependence of streamwise location; The spatial analysis leading to the α^\pm branches in this case is based on the frequency of a global LSA.	85
6.1	Azimuthal combustion chamber of a helicopter gas turbine; The chamber (see(a)) is fed by 15 two staged counter-rotative injectors, similar in geometry to the one under investigation in this chapter (see (b) and (c))	92
6.2	Sketch of the cross section of the swirler	93
6.3	Schematic set up of the preintrig experiment	93
6.4	Experimental SPLs measured at $x = 0$ and $r = 300$ mm for the no-rod and rod case	94
6.5	Numerical domain and grid for the non-reactive simulations	95
6.6	Successive mesh refinement for the no-rod case; taken from Daviller et al. [48]	96

LIST OF FIGURES

6.7	Development of LES-pressure drop across the swirler with time during the successive mesh h-refinement (red thin line) in the no-rod case; Experimental pressure drop (black thick line): $\Delta p_{\text{exp}} = 3768 \text{ Pa}$; based on Daviller et al. [48]	97
6.8	Validation of LES mean flows in the Cartesian $z = 0$ -plane in the free stream field versus the average of experimental PIV snapshots; LES fields are both temporally and azimuthally averaged.	98
6.9	Fourier transform of numerical pressure measurements within the primary injector for the no-rod and the rod case	98
6.10	Mean fields of radial, azimuthal and axial velocity in the interior of the injector for the no-rod case (left) and the rod case (right); The LIC at the bottom are based on the mean radial and axial velocity component.	100
6.11	DMD spectra for the no-rod case and the rod case based on LES snapshots .	101
6.12	DMD-mode shapes in the y - z -plane at $x = -3 \text{ mm}$ (within the primary injector) based on three-dimensional LES snapshots for the no-rod PreINGTRIG case; single helix PVC in (a)-(d) corresponding to the dominant peak in Fig.6.11; double helix PVC in (e)-(h) corresponding to its first higher harmonic	102
6.13	Phase averaged light intensity fluctuation of a flame perturbed by a PVC; taken from [160]	102
6.14	DMD mode shapes in the z -plane based on three-dimensional LES snapshots of the two PreINTRIG configurations, the no-rod case (left) and the rod case (right); for corresponding DMD spectra, see 6.11; The illustrated mode shapes correspond to the maximum amplitude in the respective spectra.	103
6.15	Fields of molecular, LES subgrid, eddy and total viscosity for the PreINTRIG configuration, averaged in time and azimuthal direction	105
6.16	Base flow as used as input for the Linear Stability Analysis (LSA) obtained by azimuthally averaging the velocity fields illustrated in Fig. 6.10	106
6.17	Example of local stability for two different axial positions in the swirler; Velocity profile slightly upstream (a) and slightly downstream (c) of the exit plane of the primary injector and their respective temporal stability maps (b) and (d)	107
6.18	Estimation of the absolute frequency by localizing the saddle point of ω in the complex α -plane	108
6.19	Absolute frequency as a function of the streamwise position; the streamwise coordinate is dedimensionalized by the distance between the dump plane and the center body;	109
6.20	Estimation of the global frequency by localizing the saddle point of ω in the complex α -plane	110
6.21	α^+ and α^- branches as a function of the axial position; the swirler drafts in the background relate the curves to the corresponding axial position in the flow.	110

6.22	Mode shapes based on local stability analysis in a plane in the primary injector ($z = -3$ mm)	111
6.23	Reconstructed mode shapes based on local stability analysis in the r - z -plane	111
6.24	Numerical domain and grid for the BiGlobal LSA, exemplary for the no-rod configuration	112
6.25	BiGlobal spectrum of the no-rod case	113
6.26	BiGlobal mode shapes of the no-rod configuration in the r - z -plane	114
6.27	Adjoint BiGlobal mode shapes of the no-rod configuration in the r - z -plane	114
6.28	Structural sensitivity of the no-rod configuration	115
6.29	BiGlobal spectrum of the rod configuration	116
6.30	BiGlobal Mode shapes of Branches 1, 2 and 3 (see Fig.6.29) in the r - z -plane	116
6.31	BiGlobal mode shapes of the rod configuration in the r - z -plane	117
6.32	Pointcaré plots for the normalized pressure signal for both the no-rod (a) and the rod case (b) for several time shifts, $\Delta t = t + n\tau$	119
7.1	Numerical domain and grid for the reactive simulations	124
7.2	Temporal mean of heat release rates indicating the flame shapes for the rod and no-rod case for equivalence ratios of $\Phi = 0.75$ and $\Phi = 1.0$; $\dot{V} = 3.4 \text{ ls}^{-1}$	125
7.3	Temporal mean of heat release rates indicating the mean flame shapes for various flow rates in the rod and no-rod configuration; equivalence ratio $\Phi = 0.725$	127
7.4	BiGlobal mean fields based on reactive Large Eddy Simulation (LES); $\Phi = 1.0$; $\dot{V} = 1.7 \text{ ls}^{-1}$	129
7.5	BiGlobal spectrum of the no-rod case for a reacting flow when the non-uniform mean density field is neglected; $\Phi = 1.0$; $\dot{V} = 1.7 \text{ ls}^{-1}$	130
7.6	BiGlobal mode shapes of the no-rod case in the r - z -plane for a reacting flow when the non-uniform mean density field is neglected; $\Phi = 1.0$; $\dot{V} = 1.7 \text{ ls}^{-1}$	131
7.7	BiGlobal spectrum of the no-rod case for a reacting flow when the non-uniform mean density field is taken into account; $\Phi = 1.0$; $\dot{V} = 1.7 \text{ ls}^{-1}$	132
7.8	BiGlobal mode shapes of the no-rod configuration in the r - z -plane for a reacting flow when the non-uniform mean density field is taken into account; $\Phi = 1.0$; $\dot{V} = 1.7 \text{ ls}^{-1}$	133
7.9	BiGlobal spectrum for the rod and the no-rod case for a reacting flow taking into account the non-uniform base flow density; $\Phi = 0.725$; $\dot{V} = 3.83 \text{ ls}^{-1}$	134

LIST OF FIGURES

List of Tables

3.1	Key parameters of the flow, including adiabatic flame temperature, T_a and laminar flame speed s_1	32
3.2	Properties taken from the DNS solution for different rotation rates, α ; Definitions of the listed quantities are provided in Fig. 3.6(f)	34
3.3	Time delays of the two flame branches (τ_{y+} and τ_{y-} for the upper and lower branch, respectively) and values of the first two frequencies for destructive interference (cf. Eq. (3.3.13)).	51
5.1	BCs for LSA in case of $m = 1$; \mathbf{n} is the normal vector of the boundary. . . .	77
6.1	Comparison of nondimensional PVC frequencies and growth rates in the no-rod configuration based on the experiment, the LES and BiGlobal and local stability analysis; LES errors are with respect to the experiment, while LSA errors are based on the LES frequencies. Errors of growth rates are based on the frequency of the oscillation.	119
8.1	Comparison of computational time LES vs methods of LSA	138

LIST OF TABLES

List of Symbols

Latin

- c* Crosscorrelation vector
- c* Group velocity
- c* Speed of sound
- C* Heat capacity
- d* Number of dimensions
- D* Diameter
- D* Diffusion coefficient
- D* Dissipation
- e* Mass specific total energy
- E* Total energy
- f* Body forces
- f* Frequency
- F* Flux tensor
- \mathcal{F} Flame thickening factor
- h* Enthalpy
- h* Height
- H* Transfer function
- I** Unity matrix
- k* Species
- n* Gain of FTFs
- N* Number of chemical species
- p* Pressure
- P* Stem function for pressure perturbation
- q** Heat flux vector
- q* Heat release
- r* Residual
- R* Gas constant
- s* Source term vector
- t* Time

LIST OF SYMBOLS

T Period
 T Temperature
 u Velocity
 \mathbf{U} Stem function for velocity perturbation
 v Noise signal in time domain
 V Diffusion velocity
 V Noise signal in frequency domain
 V Volume
 w Width
 W Molecular mass
 x First Cartesian coordinate
 x Input signal in time domain
 X Mole fraction
 X Input signal in frequency domain
 y Output signal in time domain
 Y Mass fraction
 y Second Cartesian coordinate
 Y Output signal in frequency domain
 Z Number of Gauss-Lobatto points
 Z Complex stream wise coordinate
 z Third Cartesian coordinate

Greek

α Rotation rate
 α (Complex) wave number
 ϵ Emissiency coefficient
 Γ Autocorrelation matrix
 κ Adiabatic exponent
 λ Eigenvalue
 μ Dynamic viscosity
 ν Kinematic viscosity
 ω Chemical source term
 ω (Complex) angular frequency
 Φ Vector of conserved variables
 Φ Equivalence ratio
 Ψ Stem function for density perturbation
 ρ Density
 σ Structural Sensitivity
 $\boldsymbol{\tau}$ Stress tensor
 τ Time delay

Dimensionless Quantities

Cr Crest factor	$Cr = \sqrt{\frac{\max_n(x_n^2)}{\frac{1}{N} \sum_{n=1}^N x_n^2}}$
Ma Mach number	$Ma = \frac{u}{c}$
Pr Prandtl number	$Pr = \frac{\nu}{\beta}$
Re Reynolds number	$Re = \frac{uD}{\nu}$
Sc Schmidt number	$Sc = \frac{\nu}{D}$

Subscripts

- 0 Absolute (frequency/wave number)
- b** Bulk speed
- c** Constructive interference
- c** Critical
- c** Cut-off
- C** Cell centered
- cond** Conductive
- cyl** Cylinder
- d** Destructive interference
- e** Eddy
- eff** Effective
- in** Inlet
- LES** LES sub-grid-scale
- m** molecular
- out** Outlet
- p* Constant pressure
- rad** Radiative
- reac** Reactive
- ref** Reference
- s** Specific
- s** Saddle Point
- s** Sensible
- st** Steady
- tip** Flame tip
- v* Constant volume

LIST OF SYMBOLS

Abbreviations

A

AVBP A Very Big Project

B

BC Boundary Condition

C

CFD Computational Fluid Dynamics

CFL Courant-Friedrichs-Lewy

CI Combustion Instability

CPU Central Processing Unit

CRZ Central Recirculation Zone

CV Cell Vertex

D

DMD Dynamic Mode Decomposition

DNS Direct Numerical Simulation

F

FEM Finite Element Method

FFT Fast Fourier Transform

FTF Flame Transfer Function

G

GEVP Generalized Eigenvalue Problem

I

IMFT Institut de Mécanique des Fluides de Toulouse

ABBREVIATIONS

IR Impulse Response

L

LDNS Laminar Direct Numerical Simulation

LES Large Eddy Simulation

LHS Left Hand Side

LIC Line Integral Convolution

LSA Linear Stability Analysis

LTI Linear Time Invariant

LW Lax-Wendroff

N

NSCBC Navier-Stokes Characteristic Boundary Condition

O

ORZ Outer Recirculation Zone

P

P2G Power To Gas

P2L Power To Liquid

P2X Power To X

PIV Particle Image Velocimetry

POD Proper Orthogonal Decomposition

PRBS Pseudo Random Binary Signal

PVC Precessing Vortex Core

R

RANS Reynolds Averaged Navier-Stokes

RHS Right Hand Side

S

SGS Sub-Grid-Scale

SI System Identification

SPL Sound Pressure Level

T

TF Transfer Function

TFM Thickened Flame Model

TTGC Two-Step Taylor-Galerkin C

U

UAV Unmanned Aerial Vehicle

W

WHI Wiener-Hopf Inversion

ABBREVIATIONS

Chapter 1

Introduction

1.1 Combustion - A Future Technology?

“*Most wholesome is the force of fire*” wrote Friedrich Schiller, one of the most significant German classical writers, in his epochal poem *The song of the bell* in 1799. The excerpt (see Page iv of this manuscript) underlines the significance of combustion in this time. Its use, however, was restricted mainly to hand craft, like in the description in *The song of the bell*. Because then, when the industrial revolution was in full swing in Great Britain, the economy on the European continent and especially in Germany was still characterized by the agricultural sector [91]. The industrial revolution reached Germany late in the 1830s, around three decades after Schiller’s death. During the course of the industrial revolution, the exploitation of fossil fuels in combination with the flourishing art of engineering initiated a global technological, economical and social transition, the intensity and rapidity of which has never been witnessed before in human history. Without this boost and the use of carbon fuels down to the present day, today’s globalized world with its technologies, medicine and new industries would be inconceivable. Friedrich Schiller at his time and location, although referring to fire as a “heavenly force”, could not even grasp the actual potential of the use of combustion and its detrimental role in history that became apparent in retrospect only.

Nevertheless, the limitations and downsides of fossil fuels are well known today. The first of which is the amount of fossil fuels available to exploit. Recent studies predict the depletion times of today’s known reserves of oil and gas to be in 2040 and 2042, respectively, while the coal reserves will last at least until the 22nd century [222]¹. Of course depletion dates like this were frequently delayed into the future due to exploration of new reserves and more

¹The source was published before the method of hydraulic fracturing was applied on the large scale. The depletion times of gas may have been delayed significantly.

efficient mining technologies. Nevertheless, the depletion of fossil fuels in general remains without doubt.

The second downside is with respect to the reaction products emerging from combustion processes. Probably the largest concern in this context is the impact of fossil fuel combustion on the global climate, a hypothesis which was firstly proclaimed by the end of the 19th century, amongst others by Arrhenius [7]. Today, the vast majority of scientists agree that the CO₂ emissions caused by the combustion of hydro carbons are the driving factor for an increase in global temperatures, which have been observed during the last decades [174]. The result of further increasing global temperatures and therefore fossil fuel combustion could be increasing sea levels, harsher winters and more frequent floodings and droughts [108]. A recent study furthermore examines the possibility of self-reinforcing feedback mechanisms, e.g. the melting of permafrost in Siberia, which could cause additional significant increases in global temperatures [231].

Considering these downsides of fossil fuel combustion, the question arises whether the golden age of combustion is over, or if it will continue to shape the future in energy production. In order to address this question, it is helpful to analyze both the current energy markets and the alternatives to fossil fuels. Today's available alternatives for electricity production is the use of renewable energies, mainly hydro, solar and wind power, and nuclear energy. The advantages of nuclear energy are the low energy costs and its marginal impact on climate change, since it is almost CO₂ neutral. Nevertheless, due to the unsolved question of the disposal of burnt out fuel rods and several severe accidents in nuclear power plants, with catastrophic consequences, this technology is highly controversial. While some nations (or states), such as France, Turkey and Japan continue their efforts or start applying this technology, others, like Germany, California and Austria decided to either not develop or end their nuclear power programs. If they wish not to increase their share of fossil fuel consumption, renewable energies are their only option left. These countries which take on the challenge of transition to renewable energies face major problems. In the following, some of these problems will be discussed and also how combustion could help to solve them. To do so, the German energy market will serve as an example for a market in energy transition.

Fig. 1.1 illustrates the share of energy sources in gross power generation in Germany, i.e. the total amount of produced electricity. Huge efforts have been taken on the political level in Germany in order to elevate the share of renewable energies during the last twenty years. Therefore, the German electricity is produced to one third by renewable energies, today, of which over three quarters are solar, wind and hydro electric energy. Together with nuclear energy, almost half of the electricity production is CO₂ neutral. While this seems like a huge progress, a glance at Germany's primary energy consumption (see Fig. 1.2) has a sobering effect. In contrast to the gross power generation the primary energy consumption includes traffic, which is mainly driven by fossil fuels, heating and combustion of primary energy carriers in industry. Here, the share of renewable energies is only at 13.1%, and within this

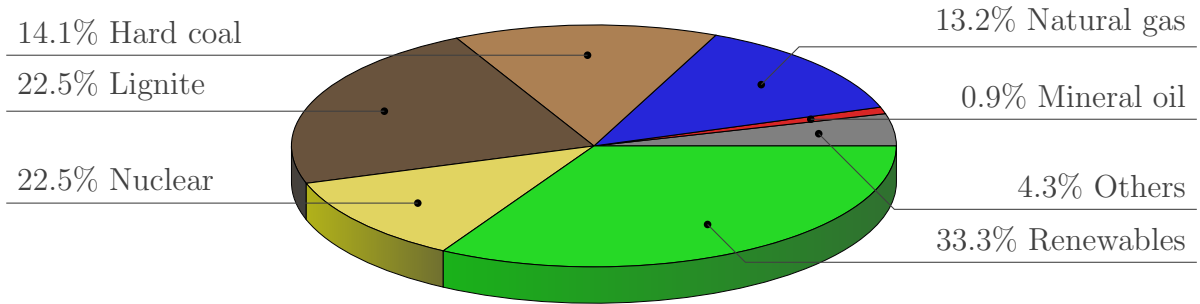


Figure 1.1: Share of energy sources in gross power generation in Germany in 2017; Data based on [268]

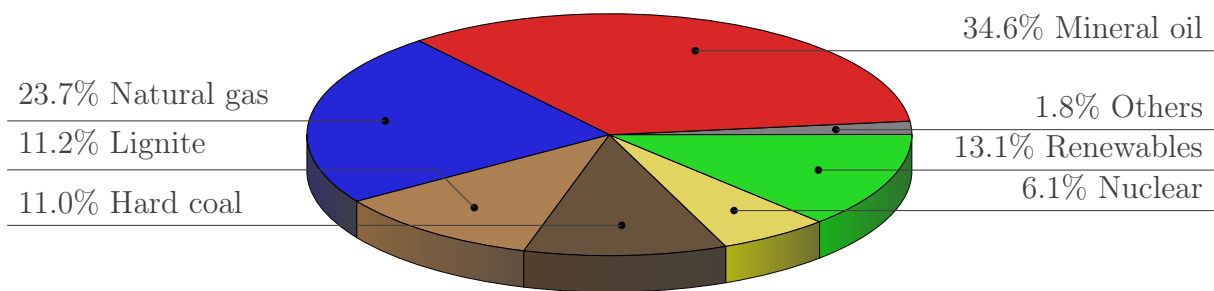


Figure 1.2: Share of primary energy consumption in Germany in 2017; Data based on [267]

share almost two thirds are produced via combustion of biomass or waste. Elevating the renewable energies' share over this threshold is difficult. This is due to the volatility of wind and solar energy. Fig. 1.3 illustrates the cumulative output powers over time of German wind and solar power plants. The volatility of both energy sources is evident. Besides fluctuations of a characteristic time of hours, seasonal fluctuations are visible in the plots. While more solar power is produced in the summer months than in the winter months, it is opposite for wind power. Sinn [226], a renowned, yet controversial German economist, recently analyzed the available and potential buffering capabilities. He took into account the possibility of constructing new storage power plants and demand management, i.e. the artificial manipulation of demand in order to balance the momentary electric energy output with its consumption. He showed that high frequency fluctuations are comparably easy to buffer. The seasonal fluctuations in storage demand however, which are of much higher amplitude, pose the real challenge. He concludes that in case Germany wants to rely to 100% on solar and wind energy, approximately 40,000 new hydroelectric storage power plants of average German size would have to be constructed, a number by far exceeding the Germany's geographic potential for these kind of power plants. Furthermore, demand management, e.g. by smart power grids and consumption, has almost no effect on the seasonal fluctuations since it can only be applied to buffer high frequency fluctuations. But how can combustion help to

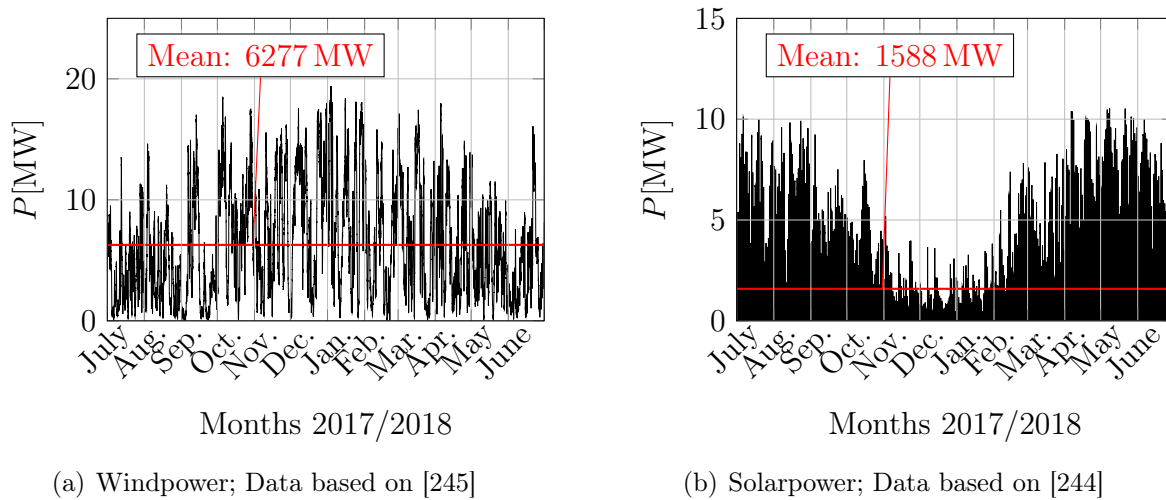


Figure 1.3: Output of renewable energies in Germany in 2017/2018

solve this problem? The answer is called Power To X (P2X). The idea of these technologies is to store the excess energy which is provided by volatile renewable power plants in chemical form. In Power To Gas (P2G), electrical energy is used to produce combustible gases like hydrogen and methane, while in Power To Liquid (P2L), liquid fuels are produced. These technologies have increasingly been in the focus of research since the beginning of the 21st century, due to the demand of storing electrical energy [204]. The CO_2 needed in the P2G production of methane and in the P2L production of liquid fuels can be captured in the exhaust of combustion power plants or directly from the air [263]. Once the electrical energy is transformed in chemical energy it can be stored even over large time spans [148]. This makes this technology attractive in order to buffer the seasonal fluctuations in the electricity balance. Especially the subsequent combustion in gas turbines has significant advantages: Firstly, gas turbines are highly flexible. Typical start-up times reach from 7 to 20 minutes. And secondly they can be used in a combined cycle with a steam turbine, where the excess heat can still be applied as district heat. This way, the energy in chemical form can not only be transformed in electrical energy, but it can also be used for heating, which today is still mainly covered by fossil fuels. This way P2X provides the potential to increase the share of renewable energies in electricity consumption, but also in heating.

Finally, the P2L technology can be used to tackle the last big sector in primary energy consumption: traffic. Producers of electric cars today struggle with the expensive, heavy and environmentally questionable batteries, which are needed in order to store the electric energy. Especially commercial aviation is highly dependent on fossil fuels today. While the market for Unmanned Aerial Vehicles (UAVs), the so called drones, is booming [31], alternatives to liquid fuels are not in sight in the frame work of large scale passenger and

cargo transport. At the same time predictions for both cargo and passenger flights are expected to explode during the next decades [101, 69, 2], which will lead to a higher demand in combustible fuels in this sector, which partially could be provided by P2L.

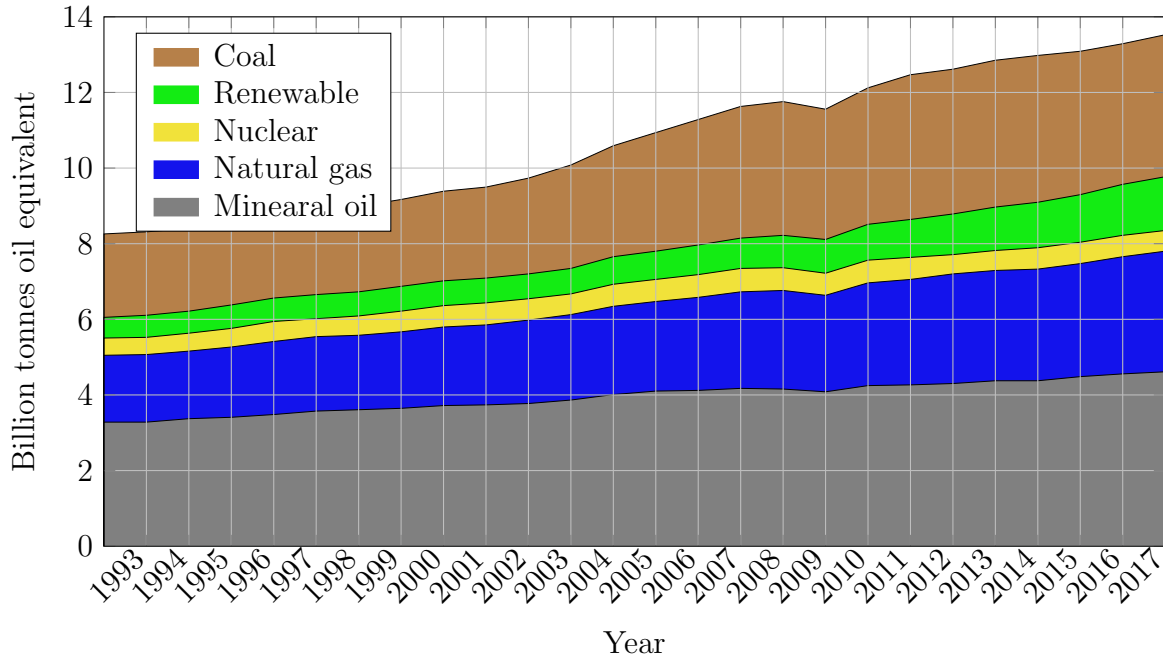


Figure 1.4: Development of global primary energy consumption since 1992; Data based on [20]

The P2X technologies may at some point be an important tool in the framework of renewable energy transition. Nevertheless, on the global level we still are far from this point. In general, the significance of combustion in the present and also the near future's forecast of energy production is extraordinary. Figure 1.4 shows the development of global primary energy sources during the last 25 years. Without doubt, the share of renewable energy sources has increased. Nevertheless, the recent increase in fossil fuel consumption exceeds the increase in renewable energy many times over, so that today the share of combustion in global energy transition is close to 90% [213, 156]. In line with sustainability and climate protection it is therefore mandatory that fossil fuels are burnt with highest possible efficiency, since they are the predominant energy carrier of the present and will remain so for many years to come [117].

To conclude, combustion did not only allow for the industrial revolution by the consumption of fossil fuels during the preceding centuries, it also is by far the dominant energy source of the present. Furthermore, the use of power to gas it is a promising tool to shape the future of energy production in the framework of transition to renewable energies. It therefore is the task of both research and industry to continue their effort in developing combustion



Figure 1.5: Destructive impact of CIs; Burner nozzle before (left) and after (right) a CI event

engines of increasingly high efficiency in order to both limit the impact of combustion on our environment and to support energy transition to renewable resources.

1.2 Fundamentals of Thermoacoustics

As laid out in the previous chapter one strength of gas turbines is their high flexibility and short start-up time. One factor that can limit this flexibility and prevent stationary gas turbines (but also aeronautical gas turbines and rocket engines) from running at their optimal operating point can be the onset of Combustion Instabilities (CIs). If not taken care of, these instabilities can cause serious damage to the structural integrity of the combustion chamber. Fig. 1.5 shows the destructive capabilities of CIs. Unfortunately, lean combustion regimes, which are favored due to lower flame temperatures and therefore lower NO_x emissions [24], are especially vulnerable to these kind of instabilities [52, 28]. Being able to control CIs therefore may reduce nitric oxide emissions and enhance the efficiency of gas turbines.

1.2.1 On the Cause and Nature of Thermoacoustic Instabilities

One source of a fluctuation in heat release in a flame is turbulence. As turbulence typically consists of broad band frequencies, the flame's response to turbulence is typically broad band and incoherent [26]. These heat release fluctuations in the flame in turn emit sound waves, which are known as combustion noise [58]. While this is typically not a problem concerning safety or efficiency, several recent studies focus on this phenomenon in order to understand combustion noise and thereby reduce unwanted structural vibrations and noise emission of aerospace engines [155, 230, 235, 27].

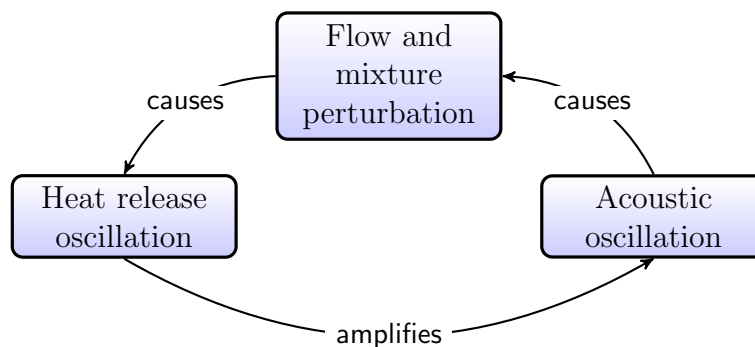


Figure 1.6: Feedback loop leading to a thermoacoustic instability in a combustion engine; based on [133]

In certain cases however, the heat release fluctuation locks in an acoustic mode of the combustion chamber. This phenomenon is based on the thermoacoustic effect, i.e. a feedback loop between an acoustic mode of the chamber and the heat release fluctuation in the flame. A schematic representation of an thermoacoustic instability is illustrated in Fig. 1.6. The thermoacoustic effect was described first by Lord Rayleigh at the end of the 20th century [200]. He stated that in order for a thermoacoustic instability to arise, a pressure fluctuation based on an acoustic mode of a vessel, p' , must be in phase with the heat release fluctuation caused by the same acoustic mode, q' . This is known as the famous Rayleigh criterion:

$$\int_0^T \int_0^V p'(x, t) q'(x, t) dv dt > \int_0^T \int_0^V D(x, t) dv dt, \quad (1.2.1)$$

where t and T stand for the time and the period of an oscillation, respectively, and V and v for the volume. x is the spatial coordinate, while D stands for the wave energy dissipation. The equation above states, that if the pressure acoustic energy source term on the Left Hand Side (LHS) is greater than the dampening (e.g. by acoustic dampening at walls or partially acoustically open inlets and outlets) then a thermoacoustic instability arises. A typical pressure fluctuation trace of the onset of a thermoacoustic instability is illustrated in Fig. 1.7. A small fluctuation, e.g. caused by turbulence, is sufficient to trigger an acoustic mode. In the linear regime, i.e. where non-linear effects are negligible, the amplitude of pressure fluctuation increases exponentially ($t < 50$ in Fig 1.7). When non-linear effects become large, the growth in amplitude decreases until a steady limit cycle is reached. In many cases an overshoot between the linear growth and the steady limit cycle is observed as can be seen in Fig. 1.7.

The mechanisms that cause flame fluctuations due to acoustic waves are manifold. They depend both on the combustor type and fuel. Firstly, and most evidently, acoustic waves cause a fluctuation of fresh gas flow rate into the combustion chamber. This leads to a variation of flame surface, which is directly linked to the heat release rate. This mechanism

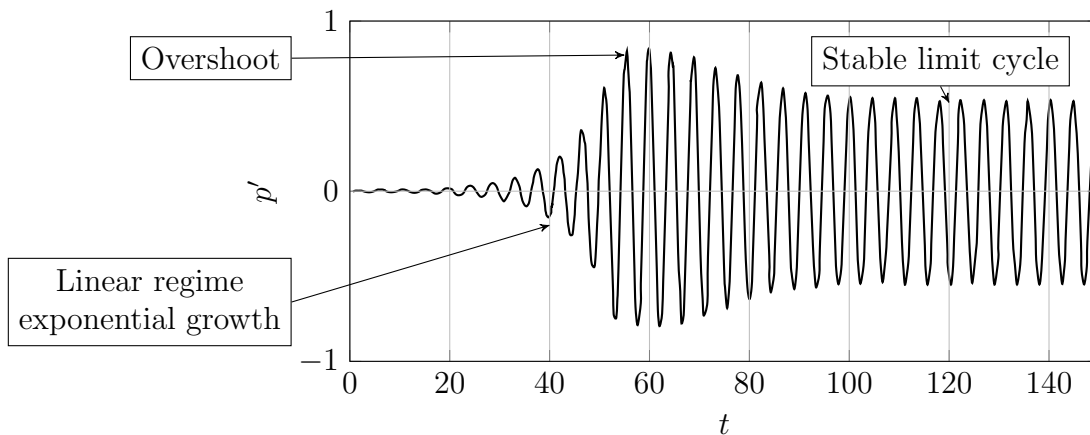


Figure 1.7: Typical pressure trace of the transient to a thermoacoustic oscillation to its limit cycle; based on [133]

was studied in various studies, involving premixed swirled [121, 252] and bunsen flames [217], as well as bluff body stabilized flames [144, 201].

A quite related mechanism is the creation of equivalence ratio fluctuations, based on a different receptivity to acoustics of the fuel and the oxidizer line in partially premixed or non-premixed flames. This mechanism was for example studied for swirled flames [236, 122] and theoretically for Bunsen burners [132].

Another mechanism is the cause of vortex shedding based on the Kelvin-Helmholtz instability [32]. As the vortex reaches the flame, this in turn can lead to an increase in flame surface and therefore to heat release fluctuations. This effect was observed amongst others in studies involving bluff body stabilized flames [201, 203, 191] for flames in the wake of a backward facing step [269] and in ramjet experimental engines [25]. A review over flame vortex interactions is given by Candel [29]. More recently, Oberleithner et al. [172] showed a direct connection between the shear layer receptivity and the flames response to acoustic forcing.

In the case of liquid fuels the interaction between the liquid phase and the gaseous phase can lead to several mechanisms leading to CIs [44]. Davvur et al. [63] describe the impact of acoustic waves on the droplet evaporation process and show that this interaction can lead to CIs. The slip velocity, i.e. the velocity difference between the fluid phase and the gaseous phase due to their different inertia, was proven to cause thermoacoustic oscillations in some cases [51].

The examples above, that only pose an overview over the various different mechanisms leading to CIs, demonstrate how diverse the causes for thermoacoustic oscillations are. Keeping in mind the complexity of the phenomena leading to these instabilities, it is not surprising,

that their prediction is difficult and they most often become apparent in the last stages of the development process of a gas turbine or rocket engine [188]. Finding out that the newly developed engine is prone to high amplitude CIs is the worst case scenario for a development team and can make comprehensive changes to the engine design necessary. This in turn can be costly. A well known example for this is the development of the F-1 engine, the first-stage rocket engine that landed men on the moon during the Apollo mission [173]. In order to get the thermoacoustic instabilities under control, 108 different injector plates were tested in 1332 full scale experiments until a sufficiently stable configuration was found[6]. It is supposed to be the most expensive project solely focusing on thermoacoustics in history [45].

1.2.2 Analysis Tools for Thermoacoustic Instabilities in Combustion Systems

In the last decades the prediction tools have developed significantly in comparison with the development of the F-1 engine. Nevertheless, the prediction of combustion instabilities remains a difficult topic. Besides an exhaustive number of experimental investigations on the topic, several new analytic and numeric tools enhanced the knowledge of combustion systems in general and their stability behavior. In the following two categories of the latter will be described.

1.2.2.1 Brute-Force Time Integration of the Full Set of Reactive Navier-Stokes Equations

Of course, knowing the behavior of a flame in a combustion chamber already at early stages of the development process by the aid of Computational Fluid Dynamics (CFD) is the dream of every gas turbine engineer. Direct Numerical Simulation (DNS), i.e. CFD simulations resolving the Kolmogorov scale and therefore the whole turbulence spectrum, would make this possible. Due to the large difference in orders of magnitude between the length scales of the combustor and the Kolmogorov scale this however is not affordable for the moment [190]. However it might become possible in the not too distant future [147, 163]. Reynolds Averaged Navier-Stokes (RANS), i. e. solving the Navier-Stokes equations for the temporal mean values by modelling the fluctuating quantities on the other hand is known not to account for unstable behavior of the flow. A widely applied trade off between precision and affordability are LES [87, 253]. In this approach, small scale turbulence is modeled while large scale turbulence is resolved by the simulation. Besides the smallest turbulence length scale, which limits this approach, there are several aspects that still make this approach a challenge. It is a multiphysics problem, as it includes among others chemistry [76], turbulence flame interaction [254, 194], particle flows [219], evaporation processes [94, 1], solid structure interaction [115], correct modeling of acoustic boundary conditions [189, 55] and

the list goes on and on. Nevertheless, due to advancement in the last decades in the topic and a reduction of Central Processing Unit (CPU)-hour costs, today this approach is not only widely applied in research, but also increasingly for industrial purposes.

1.2.2.2 Isolation of Physical Phenomena by Low(er) Order Approaches

In many cases it can be advantageous to isolate certain physical phenomena in a combustion system instead of following the brute-force approach described in the preceding section. This can provide additional information about this phenomenon, which may be difficult to extract from the brute-force approach. Another reason is, that these approaches are typically cheaper and only take a fractional amount of CPU-hours in comparison with the brute-force approach. A common approach in the framework of thermoacoustics is the analysis of the Helmholtz equation, which is based on a small perturbation approach and describes the acoustics in a vessel assuming that the flow velocity is equal to 0. It reads:

$$\gamma p_0 \nabla \cdot \left(\frac{1}{\rho_0} \nabla \widehat{p} \right) + \omega^2 \widehat{p} = i\omega (\gamma - 1) \widehat{q}(\mathbf{x}). \quad (1.2.2)$$

Here, the variables γ , p_0 , \widehat{p} , ρ_0 , ω and \widehat{q} are the isentropic exponent, the mean pressure, the pressure fluctuation, the mean density, the circular frequency of the acoustic mode and the fluctuation of heat release, respectively. For non-reacting flows the Right Hand Side (RHS) is equal to zero and the equation poses a linear eigenvalue problem for ω^2 . Solving the equation over the volume of a vessel with suitable boundary conditions applied yields the eigenvectors describing the pressure mode shapes and the corresponding eigenvalues describe the respective frequencies. In order to evaluate the stability behavior of a combustion system, the interaction of the pressure fluctuations of the mode and the heat release in the flame must be taken in to account, which is described by the term on the RHS of the Helmholtz equation. In this case the Helmholtz equation becomes a non-linear eigenvalue problem for the circular frequency, ω . Yet, the equation remains to be closed by describing the flame's response in terms of heat release to the pressure fluctuation. This link is provided by the Flame Transfer Function (FTF), which relates the heat release signal to the acoustic velocity at a reference point, \mathbf{x}_{ref} . In Crocco's n - τ -model [41, 42] it is described by

$$\widehat{q}(\mathbf{x}) = n(\mathbf{x}) \widetilde{u}(\mathbf{x}_{\text{ref}}) \exp(i\omega\tau). \quad (1.2.3)$$

A FTF can be based on analytical descriptions [57, 60, 131, 218] and experimental [114, 60, 177, 214] or numerical measurements [109, 78, 35]. Once the FTF is known to sufficient accuracy, the influence of geometry adaptations or boundary conditions on the stability properties of the combustion system can be examined by solving Eqn. (1.2.3).

Further, the application of network models is a promising way to perform parameter studies on thermoacoustics (see e.g. Bellucci et al. [16] and Schuermans et al. [216]). In this

approach, a combustion system is divided in sub-systems, each of which is described by a scattering function for the one dimensional upstream and downstream traveling acoustic waves. The dynamics of the system are described by combining the sub-systems scattering functions. This approach is an exceptionally CPU-time saving way to investigate CIs.

Another phenomenon that occurs in various fields of fluid dynamics and does so as well in combustion systems is the evolution of coherent hydrodynamic structures in free or boundary shear layers. The examples reach from a flame anchoring in the wake of a backward facing step [5, 186] to a bluff body stabilized flame [79, 223]. As mentioned above, they were in many cases shown to interfere with or lead to combustion instabilities [32, 201, 203, 191, 269, 25, 29]. A way to isolate this phenomenon is the LSA. Like the Helmholtz equation, the LSA is based on a small perturbation approach, where the velocities and the pressure are linearized in the Navier-Stokes equations. This method was applied in various fields of fluid dynamics. Amongst those are canonical flows, like the Poiseuille flow and the Couette flow [169], and plasma physics [159]. In recent years, this approach was also applied to study the Precessing Vortex Core (PVC) in the flow field of fuel injection systems. In the following section, this effect will be examined in greater detail.

1.3 Impact of Flow Rotation on Flame Dynamics

The interference of flow rotation, i.e. vortices, and flames is a frequently studied topic. Especially in the context of sub grid scale models in LES and RANS the turbulence flame interaction is of interest. Turbulence in cold flows is already a highly complicated phenomenon, which up to today is not well understood. The coupling of turbulence and flame is two-ways, meaning that vortices can have an impact on the chemistry, while flame can also impact turbulence [190]. In some cases a flame can increase the turbulence level [164], while in others it may laminarize the flow [127]. The strongest effect of turbulence on flames is the wrinkling of the flame, first described by Damköhler [47]. Due to this effect the consumption rate increases, which leads on the large scale to an increase in flame speed, which then is called turbulent flame speed.

The origin of turbulence are large scale instabilities, which often manifest as vortices in shear layers. Then the kinetic energy of these large scale instabilities is dissipated down the turbulent energy cascade. But not only the small scale turbulence impacts the flame dynamics, also the large scale hydrodynamic instabilities may have a significant impact on the consumption rate, if they interact with a flame [32, 201, 203, 191].

In fuel injection systems of gas turbines, large scale flow rotation may even occur manifold. Most modern injection systems are swirled, which means the fresh gas is injected in a jet with a strong azimuthal velocity component, and therefore rotation. For sufficiently large

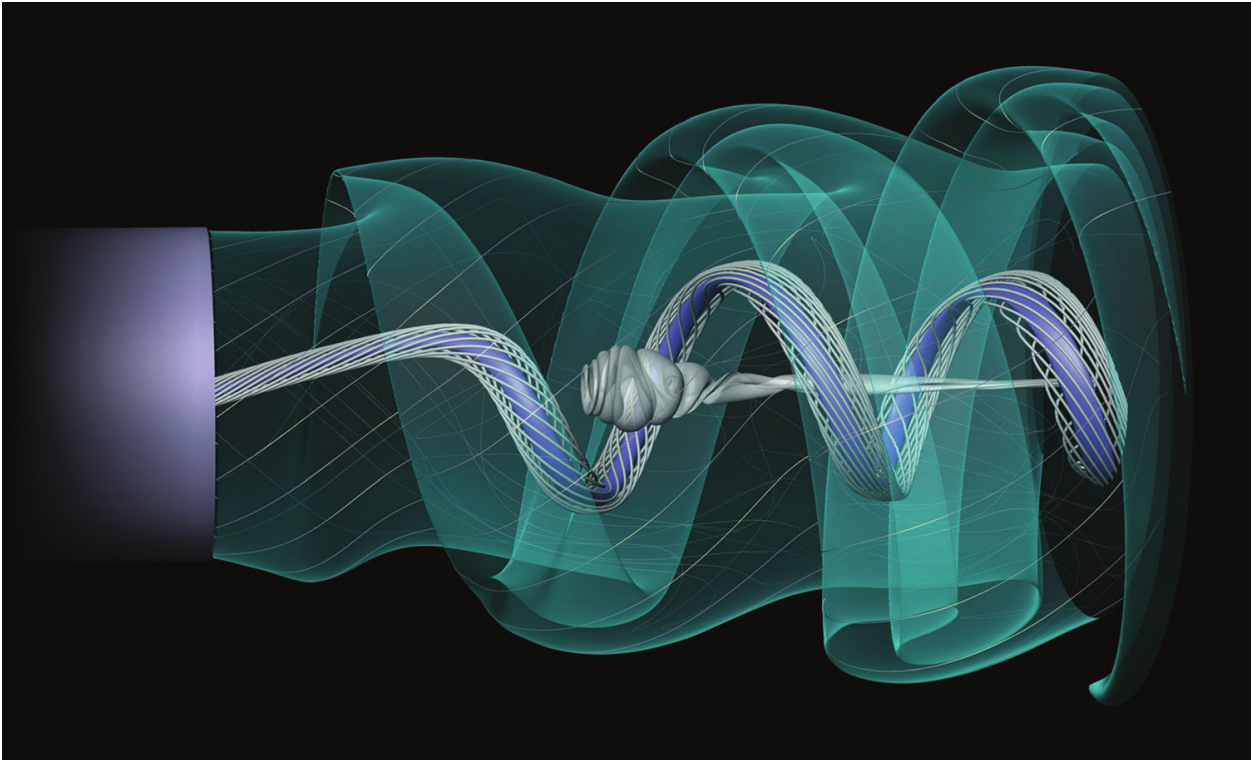


Figure 1.8: PVC in a swirling jet; taken from [183]

swirl, a phenomenon called vortex breakdown, i.e. the evolution of a Central Recirculation Zone (CRZ) at the jet axis, occurs. This provides flame anchoring in the CRZ. Furthermore, swirl is thought of increasing turbulence levels and therefore the turbulent flame speed. Another flow rotation, which enhances this effect is the evolution of a coherent structure in the shear layer between the CRZ and the surrounding jet: The PVC (see Fig. 1.8). This phenomenon is furthermore thought of enhancing fuel atomization and mixing [233]. In recent years, this phenomenon has been more and more in the focus of research due to its beneficial contribution to combustion, but also due to its coherent nature, which might lock in a thermoacoustic instability [160, 80].

Another case where large scale flow rotation has an impact on combustion is the case of a laminar flame stabilized in the wake of a cylindrical flame holder. In case the cylinder is not moving, two symmetric flame branches occur, one at each side of the cylinder [158]. However, turning the cylinder around its axis it creates flow rotation. This flow rotation in turn causes a symmetry break between both steady flame branches [262, 152] (see Fig. 1.9). While the impact of the flow rotation on the steady flame branches was examined in previous studies by Mejia et al. [152] and Xavier et al. [262], its impact on the flame dynamics remains unknown.

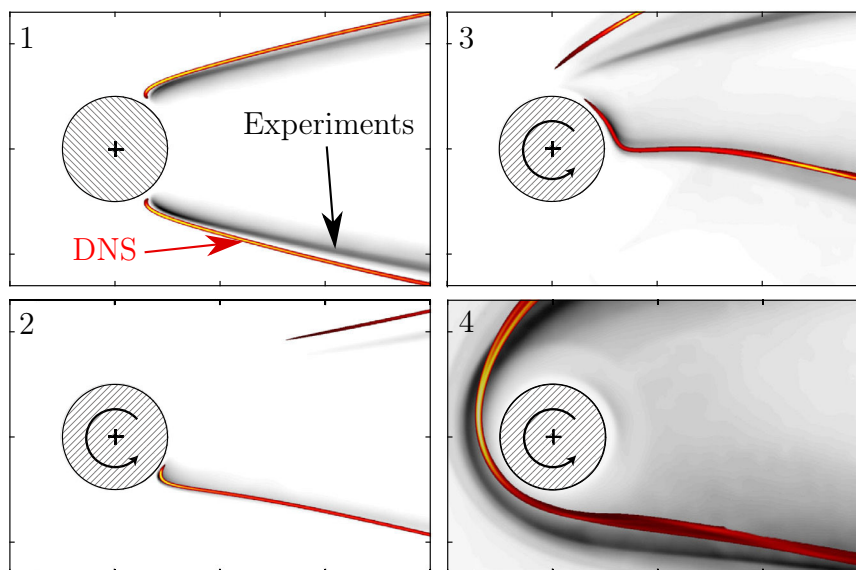


Figure 1.9: Flame shape of a laminar flame anchored in the wake of a cylindrical bluff body for various rotation rates of the cylinder based on experiments and DNS; non-rotating cylinder at the left top; rotation rate increases from frame 1 to 4; taken from [152]

1.4 Objectives

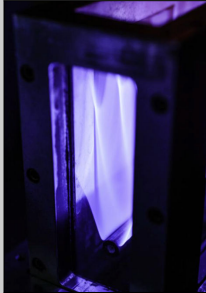
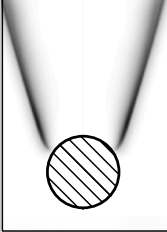
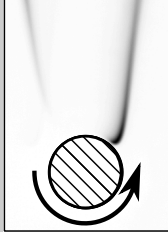
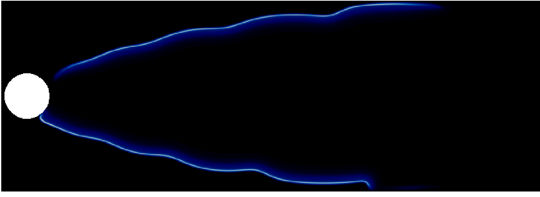
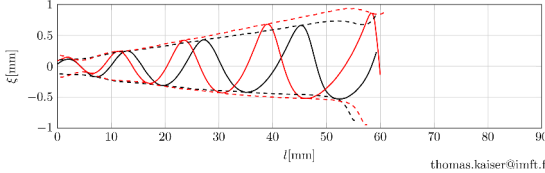
The goal of this thesis is to investigate the origin and the effect of large scale flow rotation on flames. In this context two configurations are considered.

Part I studies the first case. Here, the flow rotation introduced by a rotating cylindrical flame holder in laminar cross flow (see Fig. 1.9) is investigated. Introducing flow rotation by turning the flame holder in this context is an elegant way to change the flame shape, without changing the geometry of the combustion chamber or the operating point. Based on the different shape of both flame branches, it can be assumed that their dynamics may be different as well. The goal of the first part of the thesis is to test this hypothesis. To do so, DNS are applied and the response of the flames to acoustic forcing is investigated.

The second part of the thesis focuses on the other large scale flow rotation phenomenon introduced in the last section. Namely, the evolution of hydrodynamic instabilities in shear layers, or more specifically the PVC. This phenomenon has been increasingly investigated in the last years. Several studies identified the phenomenon as a global mode [75, 130, 209], that appears after a supercritical Hopf bifurcation. The parameter the change of which leads to the bifurcation can be the Reynolds number [209] or the swirl number [130]. The PVC was investigated by experimental and numerical means (e.g. [206, 165]). In various studies LSA was applied to understand the origin of the PVC. Mostly simple academic swirlers

were analyzed by local stability analysis, which is restricted to parallel or weakly-nonparallel jets. Global stability analyses, which are not restricted by a parallel flow assumption, were applied, however most solvers use structured meshes. Most real, modern combustion systems however are of highly complex geometry. Therefore, neither the parallel flow assumption is well met, nor structured meshes can be applied.

So far, LSA was applied mainly to understand the PVC in the context of academical configurations. The goal of the second part of this thesis is to take the first step towards industrial applications, by extending the applicability to complex geometries and develop analysis tools for the control of the PVC. First, local stability analysis is reviewed and a global LSA strategy based on an unstructured mesh is presented. The applicability of both approaches on an industrial swirled fuel injection system is investigated, and their results will be applied to find information where the PVC is most receptive to external forcing, and therefore control. Furthermore, geometry changes in the injector and their impact on the PVC remain an open question, which could be answered by LSA. In this context, the influence of a central plug in the primary injector on the PVC will be analyzed in both non-reactive and reactive flows by LES and LSA. Finally, the impact of the density change across the flame front remains not addressed by the global LSA approach and will be investigated in this thesis.

	Part I: Symmetry breaking by flow rotation	Part II: Flow rotation in fuel injection systems															
Objectives	<p>Analyze flame dynamics of a laminar flame stabilized on a rotating cylinder with respect to</p> <ul style="list-style-type: none"> • Flame topology • Flame Transfer Function 	<p>Analyze</p> <ul style="list-style-type: none"> • the origin of hydrodynamic instabilities in complex (industrial) geometries • the influence of a central plug in a fuel injection system on the hydrodynamic stability in both non-reacting and reacting configurations • the effect of a flame on hydrodynamic stability 															
Experimental Setup	<p>The INTRIG experiment of the INTECOCIS project at IMFT (Conducted by Daniel Mejia and Pradip Xavier)</p>   	<p>PreINTRIG setup at IMFT, cold flow through a two-staged industrial swirled injection system (Conducted by Pradip Xavier): PIV and microphone measurements; no experiments performed for reacting flows</p>  															
Numerical Setup	<p>2-D Laminar Direct Numerical Simulations (the experiment is quasi 2-D) performed with AVBP with detailed chemistry (19 transported species)</p>   <p style="text-align: right; font-size: small;">thomas.kaiser@imft.fr</p>	<ul style="list-style-type: none"> • Large Eddy Simulation performed with AVBP; Thickened Flame model and two-step chemistry (BFER) • Hydrodynamic Linear Stability Analysis: Local approach: Chebychev collocation; Global Approach: Finite-Element method <table border="1"> <thead> <tr> <th></th> <th>\hat{u}_r</th> <th>\hat{u}_θ</th> <th>\hat{u}_z</th> <th>\hat{p}</th> </tr> </thead> <tbody> <tr> <th>LES/DMD</th> <td></td> <td></td> <td></td> <td></td> </tr> <tr> <th>loc. LSA</th> <td></td> <td></td> <td></td> <td></td> </tr> </tbody> </table>		\hat{u}_r	\hat{u}_θ	\hat{u}_z	\hat{p}	LES/DMD					loc. LSA				
	\hat{u}_r	\hat{u}_θ	\hat{u}_z	\hat{p}													
LES/DMD																	
loc. LSA																	

Part I

Symmetry Breaking by Flow Rotation: Impact on the Thermoacoustic Behaviour of Laminar Flames

Chapter 2

DNS Tools

In every CFD project a trade off has to be made between required accuracy and the availability of computational resources. One of the determining questions in this context is which method for the solution of the Navier-Stokes equations is applied. These methods can be categorized into three groups. In the first two groups - RANS and LES - the computational grid is not sufficiently refined in order to resolve the smallest turbulent length scales, which are attributed to the Kolmogorov scale. In fact, in the case of RANS the equations are solved for the mean flow, meaning no temporal fluctuations of the resolved conservative variables occur. For these two groups of methods, the Reynolds stresses caused by the sub grid velocity fluctuations therefore are *a priori* unknown and must be provided by an appropriate model, which in general yield a turbulent contribution to diffusion and viscosity. RANS heretofore has been both applied in industry and research due to its unbeatable numerical costs. Its drawbacks on the other hand are that temporal flow fluctuations are not considered and that the approach is often imprecise. In LES on the other hand large eddies are resolved while small eddies are to be modeled. While in the past LES used to be mainly restricted to academical studies, today this approach is increasingly applied for industrial purposes. A more detailed description of the approach will be given in Chapter 4. In contrast to the latter methods, in the third group, the DNS, the numerical mesh is sufficiently refined to account for the smallest fluctuation length scales. The Reynolds stresses which act on the mean field quantities are directly solved for and no models for additional viscosity or diffusion have to be considered. If conducted properly, DNS is a highly reliant tool. Nevertheless, due to its high computational costs applications remain mainly restricted to academic applications today.

In the framework of numerical simulation of laminar flames DNS is a widely used method. It nevertheless is more appropriate to use the phrase Laminar Direct Numerical Simulation (LDNS) in this context, since the Kolmogorov length scale is not resolved due to the absence of turbulence. The maximum length scale for the computational grid therefore is most

often not given by the viscous forces but by the thickness of the flame, i.e. by chemical processes. In the following, our numerical strategy for the investigation of laminar flames will be presented.

2.1 Governing Equations

The governing equations describing a flow in CFD are based on the perfect gas law and the conservation laws for mass, species, momentum and energy. This section provides a compact overview of the corresponding transport equations of the conservative variables, which will be the basis for the following section, where the numerical tools for their spatial and time integration is given. It is not the goal of this section to provide a complete description of the topic. For this, the interested reader is referred to [190] for a more theoretical or [187] for a more technical approach.

2.1.1 Perfect Gas Law

For a wide range of CFD-applications, it is sufficient to rely on the perfect gas law for the coupling between density, ρ , pressure, p , and temperature, T . It reads:

$$p = \rho R_s T, \quad (2.1.1)$$

The proportionality factor, R_s , is the specific gas constant, given by the ratio of the universal gas constant and the molecular weight of the gas, $R_s = \frac{R}{W}$. Furthermore, in a perfect gas the following relations for the heat capacities, C , and the adiabatic exponent hold:

$$\kappa = \frac{C_p}{C_v}, \quad (2.1.2a)$$

$$C_p - C_v = R_s, \quad (2.1.2b)$$

$$\frac{R_s}{C_v} = \kappa - 1, \quad (2.1.2c)$$

where κ is the adiabatic exponent, and the subscripts p and v mark heat capacities in a constant pressure or respectively in a constant volume process. In case of multispecies calculations, the heat capacities depend on the local composition of gases. The composition's heat capacity is the sum of the heat capacities of the single species, k , weighted by their local mass fractions, Y_k . The speed of sound is described by

$$c = \sqrt{\kappa R_s T} \quad (2.1.3)$$

2.1.2 Continuity Equation

The continuity equation describes the conservation of mass and reads for compressible fluids:

$$\frac{\partial \rho}{\partial t} + \nabla \cdot (\rho \mathbf{u}) = 0, \quad (2.1.4)$$

where t and \mathbf{u} stand for time and the velocity vector respectively, while ∇ is the nabla operator. In reactive CFD the transport of some quantity or quantities representing the reaction progress must be taken into account. One way to do this, is solving the transport equations for the mass of the relevant chemical species, k , which read:

$$\frac{\partial \rho_k}{\partial t} + \nabla \cdot (\rho_k \mathbf{u}) = -\nabla \cdot (\rho_k \mathbf{V}_k) + \dot{\omega}_k. \quad (2.1.5)$$

The LHS is equivalent with the Eqn. (2.1.4). On the RHS however, a source term due to chemical reactions, ω , and an expression accounting for the species diffusion, the diffusion velocity, V , is added. Williams [259] provides a differential equation for the estimation of the diffusion velocity based on the interspecial exchange of momentum on molecular level. The Hirschfelder and Curtis approximarion [93] is its best first order approximation (Ern and Giovangigli [66]), given by

$$\mathbf{V}_k = D_k \frac{W_k}{W} \nabla X_k. \quad (2.1.6)$$

Here, D is the diffusion coefficient, W the molecular mass and X corresponds to the mole fraction. With the mass fraction, Y , the species density can be written as $\rho_k = Y_k \rho$ and per definition, the sum of all species mass fractions add up to 1:

$$\sum_{i=1}^N Y_k = 1. \quad (2.1.7)$$

Eqns. (2.1.4–2.1.7) are over determined. This can pose a problem, especially in reactive flows, when due to species diffusion processes Eqn. (2.1.7) in general is not fulfilled. In current codes, two ways to deal with this difficulty are frequently applied. Firstly, instead of solving the transport equation for all the species N , only $N - 1$ transport equations are solved leaving out a - if possible - chemically passive species, for example nitrogen in air-fuel mixtures, and solve Eqn. (2.1.7) for Y_{N_2} . The disadvantage of this method is, that it is non conservative for the species masses. A more advanced method adjusts the diffusion velocity by a correction velocity. Including this correction quantity the diffusion velocity becomes [190]:

$$\mathbf{V}_{k,\text{corr}} = D_k \frac{W_k}{W} \nabla X_k - \sum_{l=1}^N D_l \frac{W_l}{W} \nabla X_l. \quad (2.1.8)$$

2.1.3 Momentum Equations

In cold flow simulations where the maximum velocity does not exceed a certain threshold value (approximately $Ma < 0.3$), the equations governing the conservation of momentum can be simplified significantly when assuming incompressible fluids. In reacting flows on the other hand, energy is transformed into heat within the flame, causing a significant increase in temperature and decrease in density. In the present work the fully compressible set of Navier-Stokes equations are solved.

The Navier-Stokes equation states the conservation of momentum within a control volume in a compressible gas. It reads

$$\rho \left(\frac{\partial \mathbf{u}}{\partial t} + \mathbf{u} \cdot \nabla \mathbf{u} \right) = -\nabla p + \nabla \cdot \boldsymbol{\tau} + f, \quad (2.1.9)$$

where f is the sum of the volume forces and $\boldsymbol{\tau}$ the viscous stress tensor, which for a newtonian fluid is equal to

$$\boldsymbol{\tau} = \mu \left(\nabla \mathbf{u} + (\nabla \mathbf{u})^T - \frac{2}{3} (\nabla \cdot \mathbf{u}) \mathbf{I} \right), \quad (2.1.10)$$

where μ is the dynamic viscosity and \mathbf{I} is the unity matrix.

2.1.4 Energy Equation

There are various ways to state the conservation of energy. One of which is to solve a transport equation for the total energy, $E = \rho e$, which can be stated as

$$\frac{\partial \rho e}{\partial t} + \nabla \cdot (\rho e \mathbf{u}) = -\nabla \cdot (\mathbf{u} p - \mathbf{u} \cdot \boldsymbol{\tau} + \mathbf{q}) + \dot{\omega}_{\text{reac}} + \dot{\omega}_{\text{rad}} \quad (2.1.11)$$

The source terms, $\dot{\omega}_{\text{reac}}$ and $\dot{\omega}_{\text{rad}}$, on the RHS of the transport equation stand for the increase of the control volume's energy due to reaction and radiation respectively. The heat flux vector, \mathbf{q} , is the sum of the heat conductivity in the gas and an additional term taking into account the heat flux due to species diffusion:

$$\mathbf{q} = -\lambda \nabla T - \rho \sum_{k=1}^N \left(D_k \frac{W_k}{W} \nabla X_k - Y_k \sum_{l=1}^N D_l \frac{W_l}{W} \nabla X_l \right) h_{s,k} \quad (2.1.12)$$

Here, the sensible mass specific enthalpy, h , is defined as

$$h_{s,k} = \int_{T=0}^{T=T_1} C_{p,k} dT \quad (2.1.13)$$

2.2 Numerical Discretization

In order to find a solution to the governing equations laid out in Section 2.1, they have to be integrated in the domain of interest and in time. Only very few configurations are known for which analytical solutions to these equations exist (e.g. viscous flow on an infinitely large rotating disc [256], Hagen-Poiseuille flow [192, 90]). Especially on complex geometries however, analytic solutions are not feasible. Therefore, it is the goal in CFD to find approximate solutions to the governing equations via numerical methods.

In the context of this thesis, the software AVBP [187] was used for time integration of the governing equations in both DNS and LES. It offers various numerical schemes, models and gas compositions. In the following sections, the schemes applied for the DNS will be laid out. For simplicity the governing equations are written in the compact form

$$\frac{\partial \Phi}{\partial t} + \nabla \cdot \mathbf{F} = \mathbf{s}, \quad (2.2.1)$$

where $\Phi = (\rho, \rho \mathbf{u}, \rho E)$ is the vector containing the conserved variables, F is the corresponding flux tensor and s is the source term.

2.2.1 The Cell Vertex Method

Real combustion systems pose a difficult challenge for CFD codes. In contrast to academical burners, industrial combustion systems often are of highly complex geometry. Hexagonal or even structured spatial discretization is therefore unsuitable. At the same time the codes must be highly parallelizable. A method which grants these assets and at the same time a rather high order of spatial discretization is the Cell Vertex (CV) method, which was developed by the OUCL [43, 208] team and first applied by Ni [166]. In order to enable massive parallel computing, the strategy is completely explicit in time. The method of time integration can be divided into three steps [187]:

1. The cell residuals are computed based on the node values of the current time step by

$$r_C = -\frac{1}{d|C|} \sum_{k \in C} \mathbf{F}_k \cdot \mathbf{n}_k. \quad (2.2.2)$$

Here, r_C is the cell centered residual and d is 2 for two dimensional and 3 for three dimensional computations. C is respectively the surface or volume of the cell.

2. The cell residuals are distributed to the surrounding nodes indexed by j :

$$r_j = \frac{1}{|C_j|} \sum_{C \in \mathcal{D}} \mathbf{D}_{j,C} |C|, \quad (2.2.3)$$

where C_j is the control volume of the node j . The distribution matrix $\mathbf{D}_{j,C}$ is defined by the schemes chosen. To ensure conservation, the distribution matrix has to fulfill [237]:

$$\sum_{k \in C} \mathbf{D}_{k,C} = \mathbf{I} \quad (2.2.4)$$

3. Estimation of the time derivative by evaluating Eqn. (2.2.1):

$$\frac{d\Phi_j}{dt} = -\mathbf{r}_j \quad (2.2.5)$$

Eqn. (2.2.5) is then integrated in time. For the evaluation of the maximal possible time step three criteria must be considered:

1. The Courant-Friedrichs-Lewy (CFL) number limits the time step due to convection.

$$\text{CFL} = \max \left(\frac{(u+c)\Delta t}{\Delta x} \right) \leq \text{CFL}_c \quad (2.2.6)$$

2. The Fourier number, d , limits the time steps with respect to diffusion.

$$d = \max \left(\frac{D\Delta t}{\Delta x^2} \right) \leq d_c \quad (2.2.7)$$

3. And - especially in case of combustion - the stiffness of the source terms can lead to negative values of mass fractions. Therefore, the value of the time step must be large enough with respect to the time scales of the chemical reaction.

2.2.2 Convection scheme

Two different convection schemes were used:

1. Lax-Wendroff (LW): The LW scheme [120] is originally based on the finite difference approach and is of second order accuracy in both space and time. Its adaptation to the cell-vertex method goes back to Ni [166]. Its advantage is its low numerical cost. Nevertheless, it is dissipative and dispersive. It therefore is used in order to get first estimates of a simulation before a less dissipative and dispersive scheme is used in order to get high quality simulation results.
2. Two-Step Taylor-Galerkin C (TTGC): The TTGC scheme[54] is based on a Galerkin finite element. It is third order accurate in both space and time on unstructured meshes and uses a prediction correction approach [53]. In comparison with the LW scheme, TTGC is around two and a half times more costly per time step. Nevertheless, it is only marginally dispersive and dissipative. In all calculations leading to results which are presented in this thesis this scheme was used.

2.3 Chemistry Model

In order to accurately reproduce the source terms in Eqns. (2.1.5) and (2.1.11) which are caused by a chemical reaction in the experiment, a chemical model is needed. While in LES an one or two-step model often is sufficient, in DNS the demand on accuracy is higher. Especially in terms of the interaction of the flame with cooled or heated walls, the wall quenching distance and correct chemical kinetics of preheated or subadiabatic flames must be reproduced. This cannot be done by simple two step mechanisms, which often are tuned in order to reproduce the correct adiabatic flame speeds of a laminar flame. Therefore, a more detailed chemistry model is necessary. A widely applied chemical model is *GRI-Mech 3.0* [88], which is acknowledged to correctly reproduce properties of natural gas combustion. In order to apply this model, transport equations for 53 species must be solved. Due to the related immense increase of computational costs, this is not a practical solution. Sung et al. [238] and Lu et al. [136] showed, that right flame speeds and adiabatic flame temperatures, as well as many other chemical properties (such as the effect of pressure and of stretch) could be maintained when selectively reducing the number of involved species. In the context of this study, their most precise model with 19 transported species (*Lu19*) is applied. Its implementation in AVBP was validated by experimental results and the *GRI-Mech 3.0* mechanism in the open source software package *Cantera* [86] in Xavier et al. [262] and Brebion et al. [158].

Chapter 3

The INTRIG Configuration

Even though thermoacoustic instabilities involve a strong contribution of the acoustic field, the second mechanism leading to instabilities in this resonance is the flame dynamics, a phenomenon which can be studied separately and controls the movement of the flame front to perturbation. A significant part of the present work was dedicated to studies of the response of stabilized laminar flames to ingoing perturbations.

A flame anchored in the wake of a bluff body is a frequently studied academical configuration for both turbulent [135, 81, 33, 65, 46] and laminar flows [262, 158, 153, 224, 157, 111]. The interest of the research community on turbulent flames, is driven by the fact that most industrial burners use turbulent flames due to their significantly higher flame speeds and global reaction rates. Nevertheless, laminar flames can be seen as the core of combustion research and their understanding is a required step to study turbulent flames. It is mandatory also in order to enhance comprehension of turbulent combustion, since many turbulent combustion models (e.g. the flamelet model which is based on the ideas of Damköhler [47]), are directly based on folding of a laminar flame. In order to further reduce complexity in comparison with their industrial counterparts, premixed fresh gases are preferably used in academic burners. These configurations often allow a comprehensive comparison between numerical simulations, theory and experiments for many different configurations. This way numerical models, e.g. chemistry models, or analytic assumptions can be tested.

One of these configurations is the spherical flame, which often is used also as an attempt to measure laminar flame speeds [56, 9, 89]. This has been proven to be troublesome. This is partially due to the fact that spherical flames are always curved and therefore stretched, which causes a modification of the burning velocity. Although several models have been proposed to account for the impact of stretch on the flame speed, this problem could not entirely be solved. Law et al. [119] investigated on the same configuration the impact of several parameters on another property of a laminar flame front: Its stability (see Fig. 3.1).

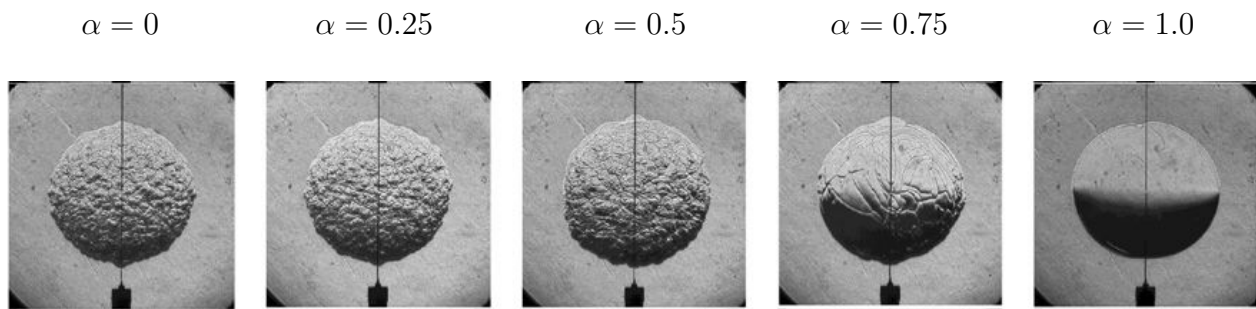


Figure 3.1: Spherical flames in air-propane-hydrogen mixtures; α corresponds to the mass ratio of hydrogen in the fuel. Taken from [119]

Laminar flames have shown to be susceptible to many different instability mechanisms [104, 229, 260, 36, 182, 146]. However, model combustors aiming to investigate laminar flames most often are designed to support laminar flames which at first hand are not prone to these kind of intrinsic instabilities. One classical example of these flames, are the so called stagnation point flames, which have been analyzed comprehensively by experimental, analytic and numeric means. They are used preferably in order to avoid flame curvature and isolate influence of flame stretch.

In order to study laminar flame dynamics, i.e. the response of laminar flames to acoustic fluctuations in terms of heat release, various laminar burners have been investigated. Among those are laminar bunsen burners, slot flames or, as mentioned above, the case of a laminar flame in the wake of a bluff body. The configuration of a conical flame has been extensively studied by experiments (e.g. [61]) and by numerical simulations (e.g. [221, 151]). The cause of temporal flame surface variations is generally a displacement of the flame root. The mechanisms leading to these front displacements are various, and often depend on the specific configuration. Experiments show that the displacements are convected along the flame front after their creation at the flame root.

The INTRIG set-up is an experiment which has been investigated at Institut de Mécanique des Fluides de Toulouse (IMFT) in the recent years. In this configuration, a laminar flame anchors in the wake of a cylindrical bluff body. Several recent studies were conducted for this configuration. Brebion et al. [158] investigated the influence of the cylinder temperature on the flame topology and flame root dynamics. The impact of the bluff body temperature on the FTF was examined by Mejia et al. [153]. They found that, while for a hot bluff body, the gain peaks at a comparably high value of ~ 2.8 , the gain for a cooled bluff body by far exceeds this value and peaks at a value > 9 . This is in contradiction of the analytical results found by Wang et al. [257].

An additional feature of the INTRIG experiment is that the bluff body, in this case a cylinder, can be rotated. This feature is an elegant way to break the symmetry of the flow without changing the geometry. The rotation also breaks the symmetry of both fronts of the V-flame.

It will be shown how the steady position of these two fronts are affected by rotation and that FTFs are also modified.

Results based on the LDNS strategy layed out in Chapter 2 were successfully compared to experimental results in several previous studies on the INTRIG configuration [153, 262, 158]. It therefore is used without modification.

3.1 Experimental Set-Up

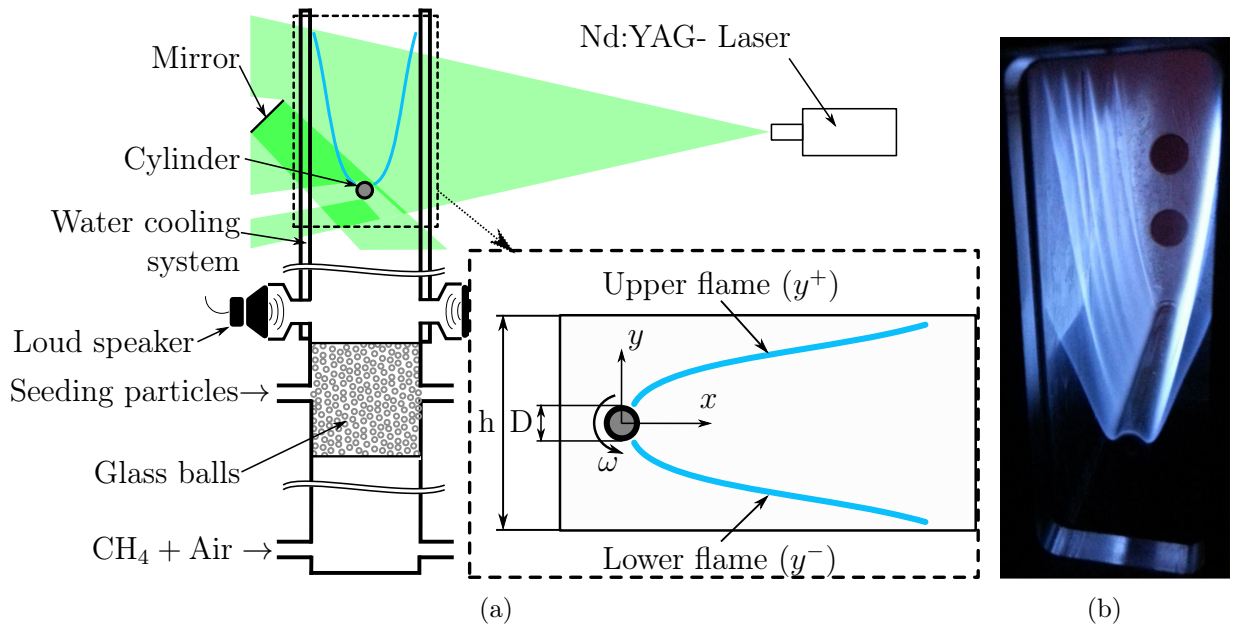


Figure 3.2: The INTRIG experiment; (a): Schematic; (b): Photograph of methane-air flame

In the INTRIG experiment a flame anchoring in the wake of a bluff body of circular cross section is investigated. Figure 3.2 shows a schematic of the experiment. Two Brooks Instruments mass flow meters measure the flow rates of air and the gaseous fuel on two independent lines. Both lines lead to a mixing arrangement, where a perfectly premixed gas is produced. Consequentially, the gas is injected into the upstream plenum at the bottom of the set-up via six pipes. To achieve a homogeneous, laminar flow, the gas streams through a layer of glass balls, which are vertically confined by two grids. In the combustion chamber a cylinder of diameter $D = 8$ mm acts as a flame holder for the laminar flame. It is held at one end by a sealed bearing cage and its rotation rate can be controlled using a brushless electric DC motor. Its operating range reaches from 600 to 20000 RPM. In the context of this study a

nondimensional rotation rate defined as

$$\alpha = \frac{\omega D}{u_b}. \quad (3.1.1)$$

is used. Here, ω is the circular rotation frequency of the cylinder and u_b the bulk speed. All dimensions in the x - y plane are measured with respect to the cylinder axis. The dimensions of the cross section are $h = 34$ mm perpendicular to the axis and $w = 94$ mm in its direction. Visual access for Particle Image Velocimetry (PIV) and CH* measurements is granted from the front (i.e. in the direction of the cylinder axis) by a quartz window spanning over the whole wall to wall distance and at the lateral sides through vertical slits. All windows reach in flow direction from $x = -25$ mm to $x = 75$ mm. To ensure a constant fresh gas temperature, the plenum is water cooled from the lateral walls.

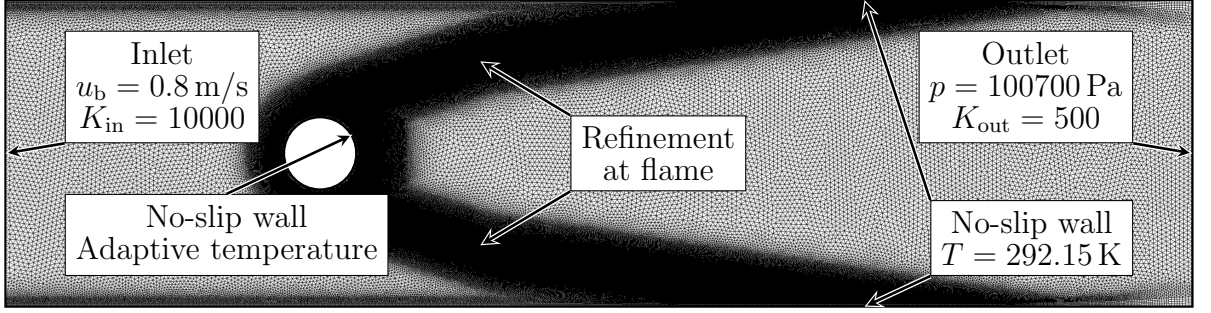
For PIV measurements, oil droplets are used as seeding particles, which are illuminated by a Nd:YAG LASER. PIV were compared in a previous study to numerical results [176]. CH* illumination is optically filtered and recorded depending on the purpose via a photo multiplier or by a high speed camera. For FTF measurements, the flow can be acoustically forced via two loudspeakers mounted downstream of the glass balls. In order to estimate FTFs, the reference velocity perturbation, u' , is measured by the hot wire technique, while the photo multiplier provides the signal of heat release fluctuation, q' . Furthermore, microphones measure the acoustic pressure fluctuation at various positions in the experiment.

Results of LDNS of the present configuration were validated versus experimentally measured FTFs [21, 153]. Results of LDNS were successfully validated against experimental results in previous studies in terms of flame topology in both steady and pulsed cases as well as in terms of the estimation of FTFs [153, 262, 21]. The studies within the framework of this thesis therefore rely on LDNS only.

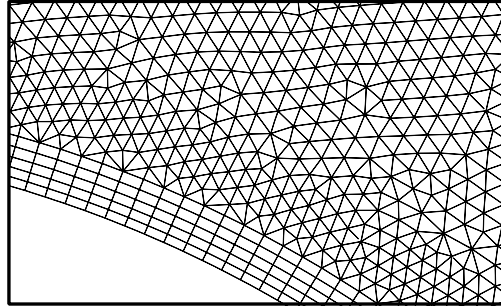
3.2 Simulation Setup and Meshing

Due to the laminar flow and the homogeneity of the configuration in direction of the cylinder axis it is sufficient to model the set up with a two dimensional computational grid. Figure 3.3 illustrates the numerical grid used for a cylinder rotation rate of $\alpha = 0$. Both at the inlet and at the outlet relaxed Navier-Stokes Characteristic Boundary Condition (NSCBC) boundary conditions were applied [189]. Using a relaxation coefficient, K , these Boundary Conditions (BCs) allow to blend between a fully non reflective condition ($K = 0$) and a fully reflective condition ($K = \infty$). It was shown by Selle et al. [220] that these BCs act as a low pass filter with cut-off frequency

$$f_{\text{cut}} = \frac{K}{4\pi}, \quad (3.2.1)$$



(a) Whole domain



(b) Mesh refinement at the cylinder wall

Figure 3.3: 2D-computational domain and mesh for the INTRIG configuration at a cylinder rotation rate of $\alpha = 0$ (a) and inlay showing the refinement at the cylinder (b)

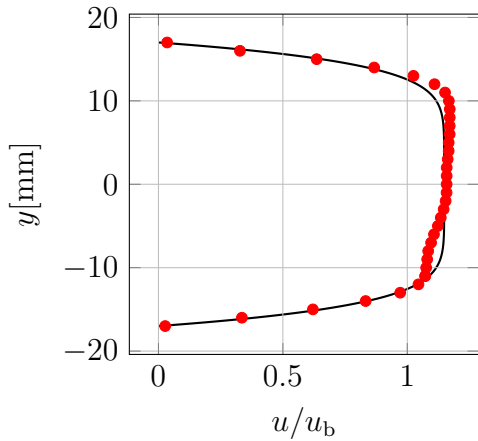


Figure 3.4: Inlet velocity profile in simulation (line) versus experimental hot wire measurements (red circles)

file to hot wire anemometry yielded an exponent of $a = 6.75$ (see Fig. 3.4). The domain is fed

where the outgoing wave is the input and the ingoing wave the output of the filter. If not mentioned otherwise, a hard inlet ($K_{in} = 10000$) and a soft outlet ($K_{out} = 500$) were applied for the INTRIG configuration. Note that while self excited modes depend on acoustic properties of inlet and outlet, the FTFs do not and can be measured for any flow state

As inlet velocity profile an analytic exponential profile of the form

$$u^* = 1 - (1 - d^*)^a \quad (3.2.2)$$

was applied, where u^* and d^* are the nondimensionalized velocity and wall distance respectively. The exponent a is a model parameter and for example is equal to 2 for a Poiseuille flow. A least mean squares error optimization algorithm comparing the inlet profile to hot wire anemometry yielded an exponent of $a = 6.75$ (see Fig. 3.4). The domain is fed

T_b [K]	p [Pa]	u_b [ms ⁻¹]	Re	Φ	K_{in}	K_{out}	T_a [K]	s_l [ms ⁻¹]
293.15	100700	0.8	410	0.75	10000	500	1923	0.23

Table 3.1: Key parameters of the flow, including adiabatic flame temperature, T_a and laminar flame speed s_l

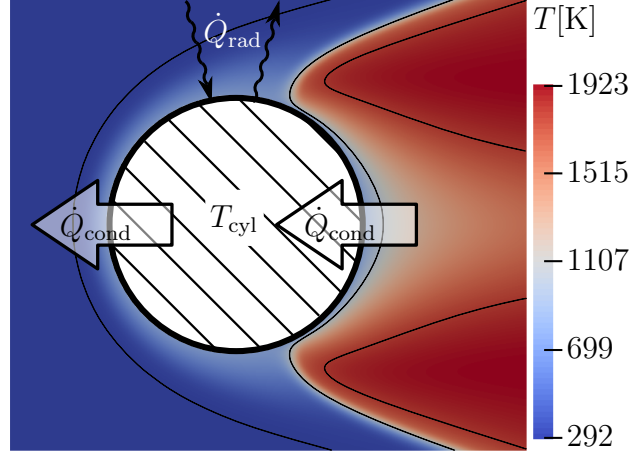


Figure 3.5: Graphical representation of energy balance of the bluff body

by a methane-air mixture of equivalence ratio $\Phi = 0.75$ and inlet temperature $T_b = 292.15$ K. The inlet bulk speed is set to $u_b = 0.8$ m/s. The pressure in the domain is regulated via the outlet, where the target value is set to $p = 100700$ Pa. Since the lateral walls are cooled in the experiment, no slip iso-thermal walls are used and their temperature is set to the temperature of the fresh gas, $T_b = 292.15$ K. The key parameters of the flow are illustrated together in Tab. 3.1.

Several studies showed that the temperature of the flame holder can have a non negligible or even large impact on the flame anchoring mechanism [158, 151]. Since the bluff body is exposed to both hot burnt gases as well as cold fresh gases (see Fig. 3.5) its temperature is *a priori* unknown. Additionally to these conductive heat fluxes, beyond a certain cylinder temperature, heat radiation has an additional significant cooling effect. Taking into account these effects and assuming that the heat conductivity of the flame holder is much higher than in the surrounding gases, the cylinder temperature, T_{cyl} , is determined by time integration of

$$\frac{dT_{cyl}}{dt} = \frac{\dot{Q}_{cond} - \dot{Q}_{rad}}{C_{cyl}\rho_{cyl}V_{cyl}}, \quad (3.2.3)$$

where C_{cyl} and ρ_{cyl} are the mass specific heat capacity and density of steel, respectively. V_{cyl} denotes the volume of the cylinder. The conductive power, \dot{Q}_{cond} , is obtained by integrating the heat fluxes at the cylinder surface. Assuming perfectly transparent gases, the heat exchange with the cold surroundings can be described by the Boltzmann-radiation law [19]:

$$\dot{Q}_{\text{rad}} = \epsilon \sigma (T_{\text{cyl}}^4 - T_{\text{b}}^4), \quad (3.2.4)$$

where σ is the Boltzmann constant and ϵ the emissivity coefficient, which is set to 0.9.

It was shown by Brebion[21] that given the numerical strategy laid out in Section 2.2, numerical stability is enhanced by inflating the domain with a few layers of quadrilateral cells on solid walls. Therefore, a hybrid mesh, a combination of triangular cells and five layers of quadrilateral cells around the cylinder and the lateral walls, is used (see Fig. 3.3(b)). The mesh exhibits two refined zones localized around the flame branches. The grid size of $\Delta x = 70 \mu\text{m}$ in this region was determined by a mesh convergence study of laminar flame speeds in a 1-D flame. Since the flame thickness for a methane-air flame at an equivalence ratio of $\Phi = 0.75$ is approximately 0.58 mm, the numerical grid size corresponds to at least 8 cells in the flame front. For laminar flames like investigated in this study, the mechanisms occurring at the flame root and at the flame tip are of major importance. At both positions the flame interacts with walls: While the flame anchors at the heated cylinder, it is laterally confined at its tip by cold walls. Therefore, special attention is paid to flame wall interaction. In order to well capture this effect, the mesh was additionally refined at the wall boundaries, i.e. at the lateral walls and around the cylinder (see Fig. 3.3(b)). The height of the quadrilateral layers at the solid wall boundaries was set to $25 \mu\text{m}$.

3.3 Results of Laminar DNS

While both the influence of bluff body rotation on the flame anchoring mechanisms (Xavier et al. [262]) was analyzed and the response of the INTRIG configuration to acoustic forcing was estimated by both experimental and numerical means (Mejia et al. [153]), the influence of bluff body rotation on the configuration's acoustic response remains unknown. This section therefore addresses this open question and analyses the FTF, i.e. the response of the flame to acoustic forcing in the linear regime.

3.3.1 Steady State Response to Bluff Body Rotation

For a cylinder in non-reacting cross flow, the Reynolds number at which a bifurcation to the famous Kármán vortex street occurs is $\text{Re}_c = 47$. That flames anchored in the bluff body wake nevertheless have a stabilizing effect on this mechanism was shown by numerous both experimental [72, 17, 111] and numerical [73, 212, 150, 81] studies. Amongst others it was also shown in previous studies that the flame branches in the INTRIG configuration stay symmetric if no external acoustic forcing is carried out [158, 152]. There are several possible explanations why this effect does not occur in the present configuration. Firstly,

the destabilizing effect of a large recirculation zone is missing in the flow. Secondly, in burnt gases the kinematic viscosity is due to the lower density strongly increased. Furthermore, it is known that density gradients have an effect on the hydrodynamic stability of flows [377, 142, 143].

Figure 3.6(a) shows streamlines, iso-contour of heat release and the field of flow velocity in x -direction. After converging to a steady state (i.e. the fluctuation of heat release is below 0.01% of its mean value), the flow field and the flame as expected are absolutely symmetric for a rotation rate of $\alpha = 0$.

For increasing rotation rates however (see Figs. 3.6(b)–3.6(e)), the symmetry of the flow profile in the unburnt gases is increasingly broken, leading to an increase of flow rate in the y^- -half plane and a corresponding decrease in the y^+ -half plane. Table 3.2 shows the flow speeds in the corresponding half planes depending on the cylinder rotation rate. Note, that here the bulk velocities are measured at $x = 0$ with respect to the corresponding cross section. The influence of the rotation rate on the lower branch is rather simple. With increasing α the flame root stays attached to the cylinder, but moves slightly downstream. Due to the increasing flow in the corresponding half plane, the flame angle decreases and therefore the flame tip shifts to higher positions of x .

α	T_{cyl}	x_{root,y^-}	x_{root,y^+}	x_{tip,y^-}	x_{tip,y^+}	v_{y^-}	v_{y^+}
0	758.6 K	1.9 mm	1.9 mm	60.1 mm	60.1 mm	1.05 m/s	1.05 m/s
0.625	697.6 K	2.4 mm	7.8 mm	63.4 mm	67.3 mm	1.08 m/s	1.02 m/s
1.25	757.7 K	2.4 mm	12.1 mm	65.2 mm	68.2 mm	1.12 m/s	0.97 m/s
2.5	804.7 K	3.4 mm	14.8 mm	74.8 mm	62.2 mm	1.26 m/s	0.83 m/s
3.75	791.2 K	4.3 mm	8.3 mm	90.1 mm	44.5 mm	1.46 m/s	0.64 m/s

Table 3.2: Properties taken from the DNS solution for different rotation rates, α ; Definitions of the listed quantities are provided in Fig. 3.6(f)

The steady state behaviour of the upper branch is slightly more complicated. Even for low rotation rates ($\alpha = 0.625$) the flame close to the cylinder extinguishes and the root of the flame detaches from the cylinder and moves slightly downstream, shifting the whole flame in downstream direction. This effect can be explained by the upstream transportation of burnt gases in the rotating bluff body's viscous boundary layer. The burnt gas temperature in this region is below adiabatic conditions due to the cooling effect of the cylinder. These cooled burnt gases dilute the fresh gases, leading to a subadiabatic mixture and consequentially to a delayed ignition. A thorough description of this mechanism is given by Xavier et al. [262]. For low and moderate rotation rates ($\alpha \leq 1.25$) this effect is dominant and the flame tip position is moving with the flame in downstream direction. For high rotation rates however ($\alpha \geq 2.5$), the effect of the reduction in flow velocity is dominant also in the upper half plane, leading firstly to an upstream movement of the flame root and secondly to a decrease

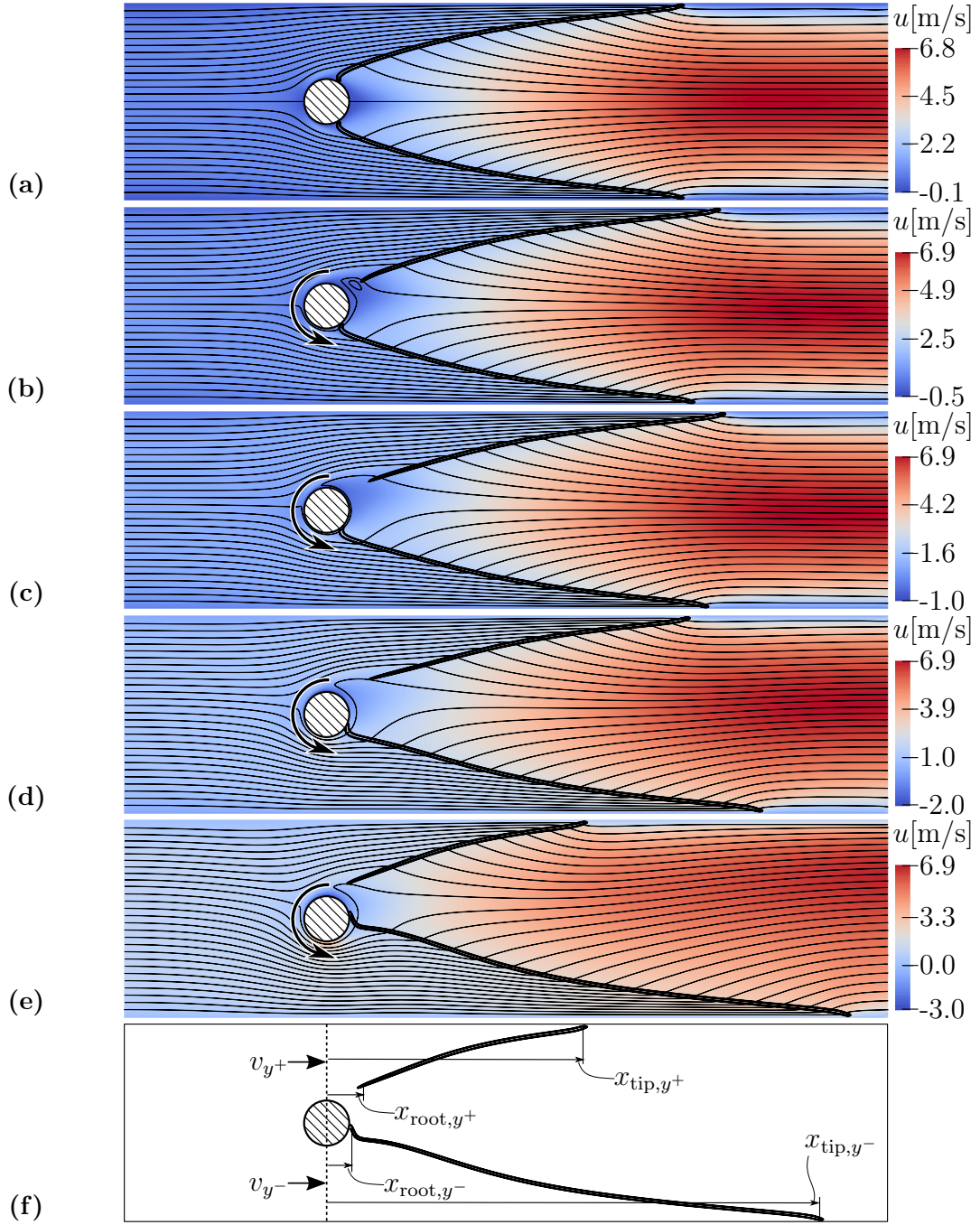


Figure 3.6: Steady state based on DNS; The field shows the flow speed in x -direction, the thin lines correspond to stream lines and the thick black line is the iso-surface of heat release. (a): $\alpha = 0$; (b): $\alpha = 0.625$; (c): $\alpha = 1.25$; (d): $\alpha = 2.5$; (e): $\alpha = 3.75$; (f): Definitions of the flame root positions, x_{root,y^\pm} , tip positions, x_{tip,y^\pm} and the bulk velocities in the respective upper and lower half planes, v_{y^\pm} specified in Tab. 3.2

in flame angle. As a consequence, the flame length and therefore the flame tip's position of x decreases. The rotation rate impacts the flow pattern around the cylinder. Therefore, the heat transfer between cylinder and both unburnt and burnt gases is affected, leading to a non-trivial variation of the cylinder surface temperature with the rotation rate. The resulting temperatures are listed in Tab. 3.2, besides the flame root and tip positions for both the y^+ and the y^- -branch, and the bulk speeds in the upper and lower half planes.

The LDNS results show that the flame topology strongly changes with the rotation rate and introduce asymmetry of both flame branches. One can therefore assume that the rotation rate also impacts the FTF, which will be analyzed in the following section

3.3.2 Flame Response to Acoustic Forcing

It is known that for laminar flames the anchoring mechanism, the bulk speed and the flame length have an impact on the flame's FTF. Studies show that the flame anchoring mechanism drives mainly the gain [153, 151], while flame length and bulk speed on the other hand impact mainly the phase delay [18, 218]. It was shown by the LDNS steady state results that all these parameters are impacted strongly by the rotation rate. We therefore can anticipate, that the flames response to acoustic forcing varies with the bluff body rotation rate. Furthermore, it can be assumed that the flame response of both flame branches will differ, for rotation rates $\alpha \neq 0$ due to their asymmetry.

This section focuses on the impact of bluff body rotation rate on flame dynamics and the FTF. First, a description of the System Identification (SI) method used for estimating the FTF will be given. Then the influence of bluff body rotation on the flame properties will be investigated, starting with the case of $\alpha = 0$.

3.3.2.1 System Identification: The Wiener-Hopf Inversion

As described in Section 1.2.2.2, the FTF describes the response of a flame in terms of heat release fluctuations to acoustic perturbations to which the flame is exposed to [41]. It serves as a measure for comparison between different flame types in thermoacoustics (see e.g. Kedia et al. [110], Durox et al. [62]) as well as a closure of the Helmholtz equation in a combustion system (e.g. in Silva et al. [225]). In experiments, the state of the art procedure is the use of loud speakers to excite the bulk flow and measure the resulting flame response by for example photomultipliers or high speed cameras. Most of the time, effort and money goes to the set up of the experiment. Once it is ready to measure, the measurements themselves are comparably cheap and quickly made. Therefore, most often the simplest method for the estimation of the FTF is used: Excitation with a harmonic acoustic signal at a single frequency and subsequent repetition for all frequencies of interest.

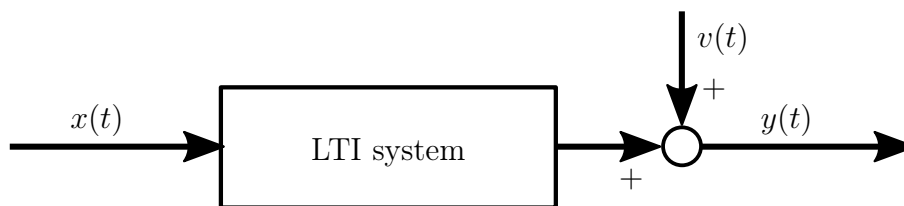


Figure 3.7: Sketch of a LTI system

In CFD studies on the other hand one limiting factor when performing simulations are the computational costs of the measurements themselves. Repeating a simulation for every frequency of interest is often too expensive and therefore not the best choice. A cheaper method is a broad band excitation of the flame and a subsequent post processing of the velocity and heat release signals in order to extract the FTF. A method which has been proven reliable in the context of SI is the Wiener-Hopf approach (see the comprehensive book of Ljung for this and other related methods [134]). This method was first applied to problems of thermoacoustics by Polifke et al. [193, 95, 96]. In this section, a description of the Wiener-Hopf technique is given.

When estimating a FTF the flame is supposed to act as a Linear Time Invariant (LTI)-system. This means that it fulfills the following criteria:

- **Linearity:** If the response to a systems input $x = f(t)$ is $y = g(t)$ then the response of this system to $x = af(t)$ is $y = ag(t)$, where a is a constant factor.
- **Time Invariant:** The systems response to an input signal is independent of time, i.e. the system's properties do not change.

A sketch of a LTI system is shown in Fig. 3.7. The input into the system is called $x(t)$ and its output $y(t)$ in the temporal framework or $X(f)$ and $Y(f)$ in the frequency domain. In the framework of a FTF this corresponds to fluctuation of velocity at the reference point and fluctuation of heat release fluctuations, respectively. Before the output signal can be measured it always is disturbed by some kind of noise signal, $v(t)$. In the frequency domain, the output signal of a LTI system is related to its input signal by multiplication with the Transfer Function (TF) of the system, H

$$Y(f) = H(f)X(f) + V(f). \quad (3.3.1)$$

Or in contrast in the time frame, the output of a LTI system is given by the convolution of the input signal with the Impulse Response (IR) of the system.

$$y(t) = h(t) * x(t) + v(t), \quad (3.3.2)$$

where the $*$ operator stands for a convolution, which is defined by

$$(f * g)(t) = \int_{-\infty}^{\infty} f(\tau) g(t - \tau) d\tau. \quad (3.3.3)$$

A LTI system therefore is entirely described by either the IR or the TF, which are connected via the z-transform, or respectively the inverse z-transform. The goal of a SI process therefore is to estimate either the IR or the TF. In a white box approach, the systems properties are examined and a TF or a IR is analytically derived. Since this is often impossible or at least very difficult (as it is for flames), a black box method can be applied. Here the system is deliberately excited by an *a priori* designed signal, input and output signals are measured and in a post processing procedure the IR and/or the TF is estimated. As mentioned above one straightforward way to do so is the excitation of a system with a harmonic signal. In the post processing the measured input and output signal are transformed into the frequency frame by an Fast Fourier Transform (FFT) and subsequently the transfer function is estimated for this frequency by Eqn. (3.3.1), while a large time series leads to a vanishing FFT of the noise. The strategy is displayed graphically in the lower part of Fig. 3.8 Figure 3.9 provides the relations to use to go from the TF to the IR and *vice versa*.

An alternative method is the broad band excitation of the signal. Assuming an arbitrary signal as input for the system, it can be shown under the assumption that the noise is equally white, that the error in least mean squares sense of

$$\mathbf{h}\Gamma = \mathbf{c}_{x,y} \quad (3.3.4)$$

tends to zero for sufficiently large time series. This equation is known as the Wiener-Hopf equation, with the auto correlation matrix defined as

$$\Gamma_{i,j} = \frac{1}{N - L + 1} \sum_{m=L}^N x_{m-i}x_{m-j} \quad (3.3.5)$$

and the cross correlation vector

$$\mathbf{c}_i = \frac{1}{N - L + 1} \sum_{m=L}^N y_m x_{m-i}. \quad (3.3.6)$$

The Wiener-Hopf Inversion (WHI) method takes advantage of this equation. First the system is excited by a broad band signal and the cross correlation vector and the auto correlation matrix are calculated. Then, Eqn. (3.3.4) is solved for the IR, h , and subsequently the TF is found by a z-transform of h . The strategy is schematically illustrated in the upper half of Fig. 3.8.

The excitation signal has proven to have a large impact on the quality of the SI process. In order to achieve a good signal to noise ratio, the power at the frequencies of interest has to be sufficiently high. On the other hand the response to the excitation must stay in the linear regime of the corresponding system and therefore, the amplitude of the signal is bounded by a certain value. A measure for the energy content in a signal bounded by a certain threshold

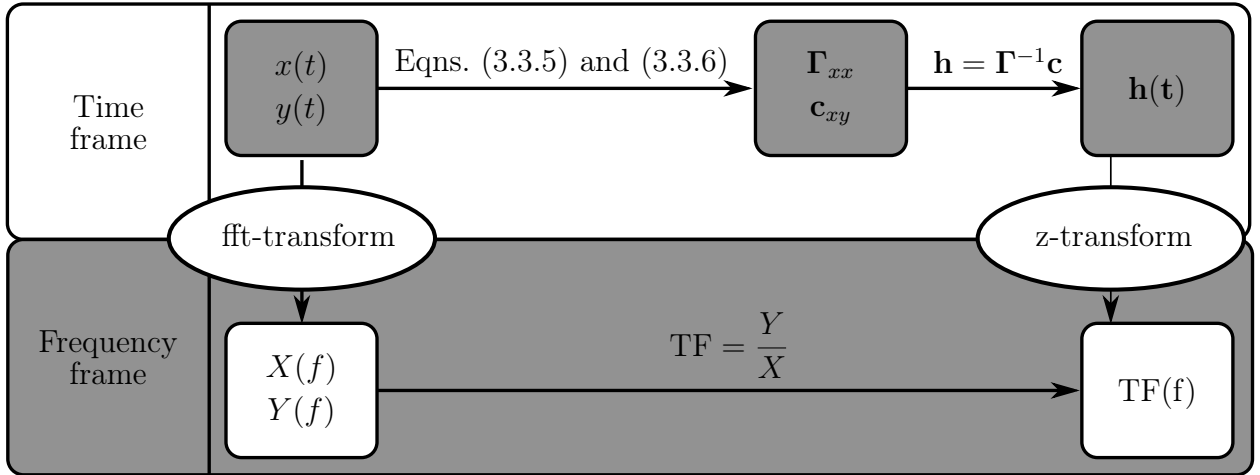


Figure 3.8: SI process in temporal domain via WHI and in frequency domain via harmonic forcing

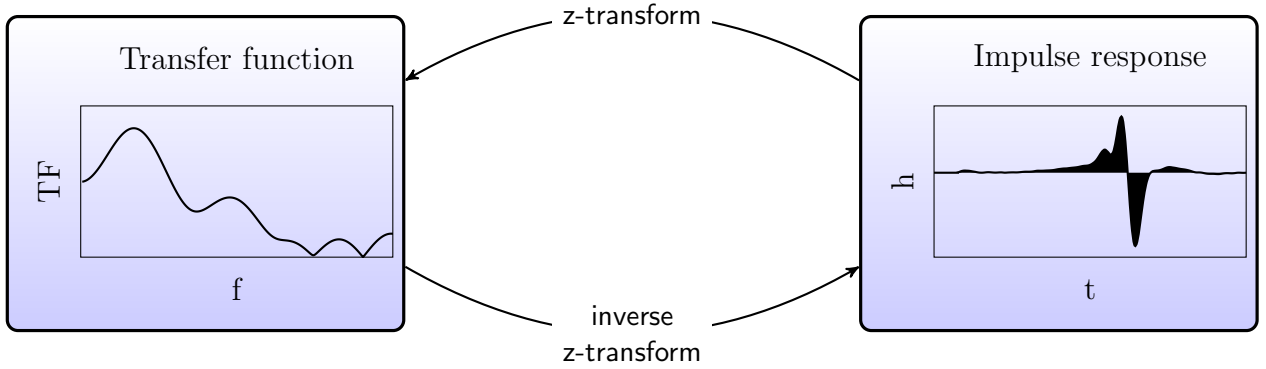


Figure 3.9: Convertibility of IR and TF by the (inverse) z-transform

value is the so called crest factor or peak to average ratio [134]:

$$\text{Cr} = \sqrt{\frac{\max_n (x_n^2)}{\frac{1}{N} \sum_{n=1}^N x_n^2}} \quad (3.3.7)$$

A low value of Cr corresponds to a well suited signal, while $\text{Cr} = 1$ corresponds to the optimum. A signal type which is ideal in the sense of the crest factor is the Pseudo Random Binary Signal (PRBS) (see Fig. 3.10(a)), where the signal only takes random values of $\pm A$, where A is the amplitude of the perturbation [95]. In the framework of this thesis, as not to excite acoustic chamber modes, the excitation signal was low pass filtered by a finite impulse response filter with a cut off frequency far beyond the frequencies of interest of the given flame. A corresponding excitation signal is shown in Fig. 3.10(b).

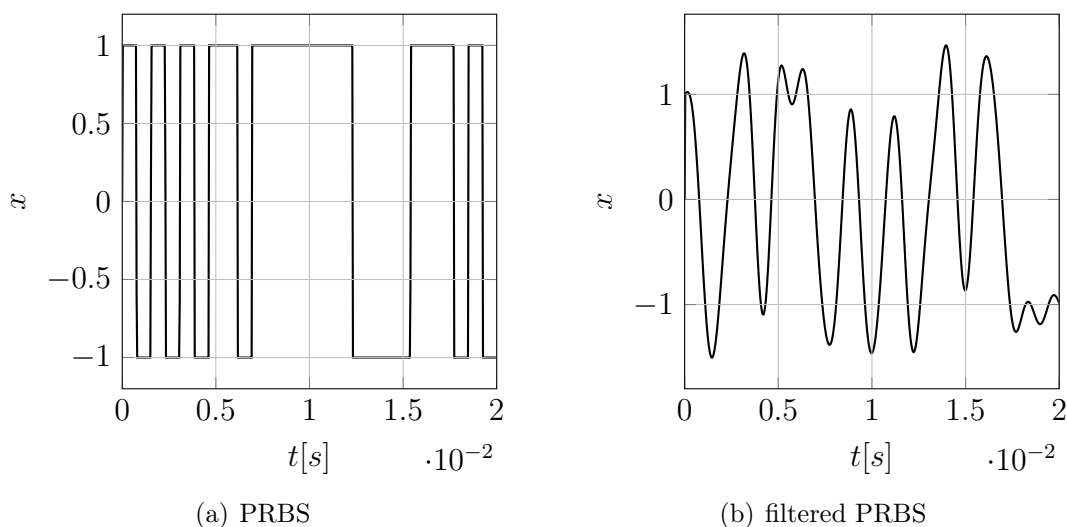


Figure 3.10: Example of excitation signals for the acoustic forcing in the LDNS

An important part of every SI process is its validation. In this context, various methods can be applied [134]. In some of them a new random signal is fed into the system and the output is measured. Subsequently, the estimated IR is convolved with the same new excitation signal, which yields a prediction of the systems response to this signal. This way the system's actual response to the signal can be compared to the predicted signal via a quality measuring number. Examples for these measuring numbers can be found in [95]. These methods represent a very efficient way of validation. In the context of this work a more illustrative and straightforward way of validation is applied, by checking the accuracy of the FTFs by its evaluation at distinct frequencies with harmonic excitation.

3.3.2.2 Flame Response without Rotation

First, the flame behind a non rotating bluff body is acoustically forced using harmonic excitation at a velocity perturbation of $|u'| = 5\%u_b$ and $f = 100$ Hz. The resulting flame topology (white iso-surface of heat release) is illustrated in Fig. 3.11 for various phase angles of the velocity perturbation and compared to the steady state flame (black line). The figure confirms, that the acoustic wave causes a periodic displacement of the flame root, ξ_0 , which is subsequently convected away from its source. Unlike in many previous studies, where the flame displacement did not change while being convected along the flame front, it appears that it grows in the present configuration. It can be seen that at the flame tip, the periodic displacements cause a significant variation in flame length and therefore heat release. The arrows drawn in Fig. 3.11 connect locations with equal phase angle of ξ and this way give an approximate measure of the wave length of the harmonic displacement and of its speed. It

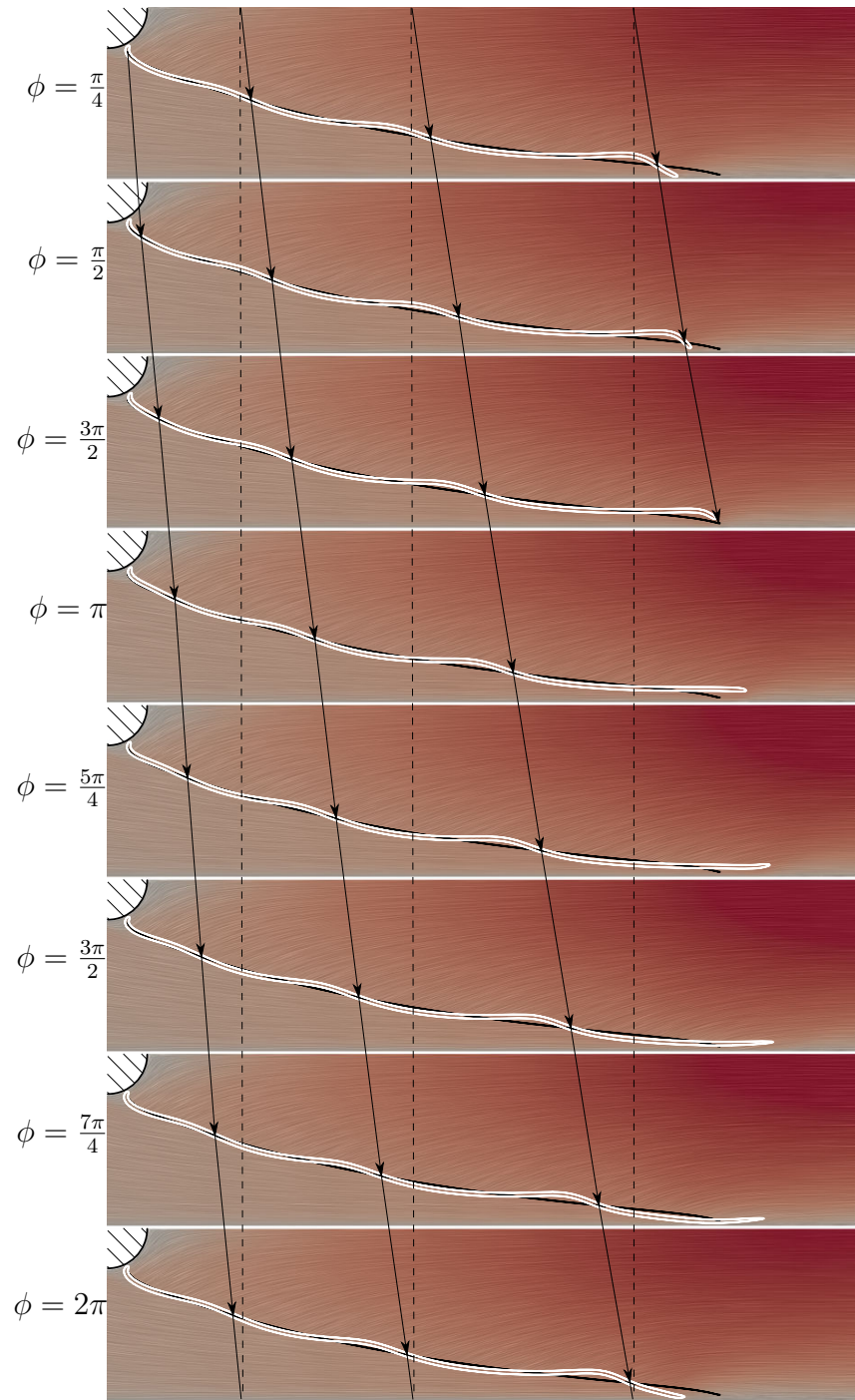


Figure 3.11: Comparison of flame topologies of the steady flame (black line) and instantaneous snapshots of a pulsed flame (white iso surface of heat release) at various phase angles of harmonic velocity perturbation ($|u'| = 5\%u_b$, $f = 100$ Hz, $\alpha = 0$)

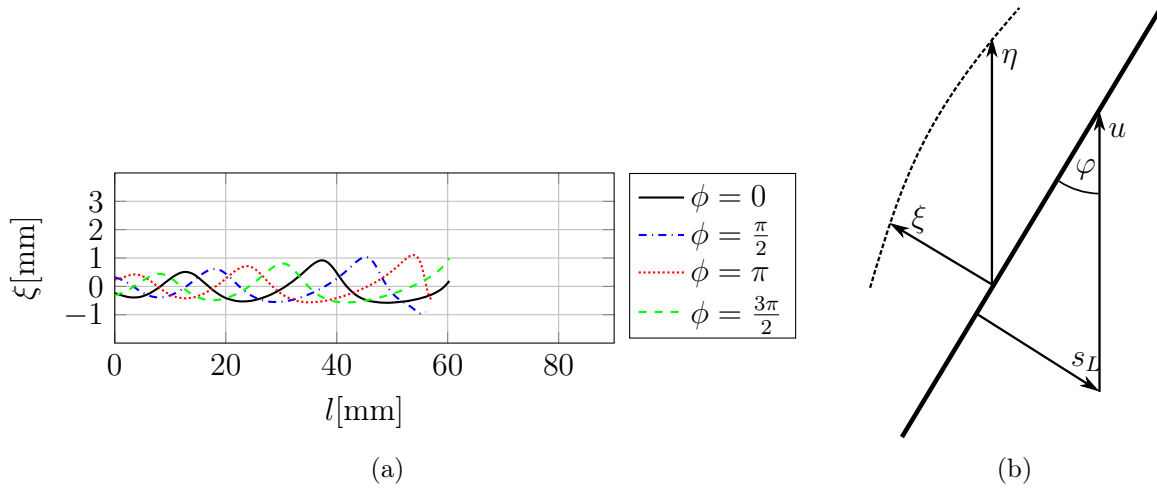


Figure 3.12: (a) Flame normal displacements (see Fig. 3.12(b)) as a function of the flame position for a non rotating bluff body and various phase angles, ϕ , of harmonic velocity perturbation of frequency $f = 80$ Hz and amplitude $|u'| = 5\%u_b$; (b) Schematics of laminar flame displacements; Thick solid line: unperturbed flame, thick dashed line: displaced flame; Definition of the flame angle, φ , flame displacement in flow direction, η , and flame normal displacement, ξ ; u indicates the fresh gas velocity and direction.

is evident, that the wave length distinctively increases in x -direction. Schuller et al. [218] as well as Blumenthal et al. [18] note that the convective velocity of the perturbation is in the order of magnitude of the bulk speed in the cold flow. Unlike in the configurations they were investigating, the flow speed of the unburnt gas is not remotely constant along the flame in the INTRIG configuration. The acceleration of the unburnt gases along the flame with increasing coordinate of x is visualized by a simultaneous decrease of flame angle, explaining the change of convection velocity of the flame perturbation. This convective speed varies from approximately 1.1 m/s at the flame root, which corresponds approximately to the flow speed in the lower half plane (see Tab. 3.2), to approximately 2.3 m/s close to the flame tip.

To improve illustration of the effect of acoustic forcing on the flame topology, and to simplify comparison with cases of non-zero rotation rate (see Section 3.3.2.4), the flame normal displacement of a harmonically forced flame is extracted and plotted in Fig. 3.12(a) for four phase angles of the velocity perturbation. The acoustic forcing is of amplitude $|u'| = 5\%u_b$ and frequency $f = 80$ Hz (instead of 100 Hz). The plot confirms that the amplitude of the flame normal displacement grows while being convected along the flame front also for a forcing at 80 Hz. Furthermore, the flame normal displacement shows non-linear deformation close to the flame tip. The increase in amplitude of the normal disturbance along the flame front and the associated movement at its tip suggest that a major part of the flame surface variation and therefore heat release fluctuation stems from the interaction of the flame with

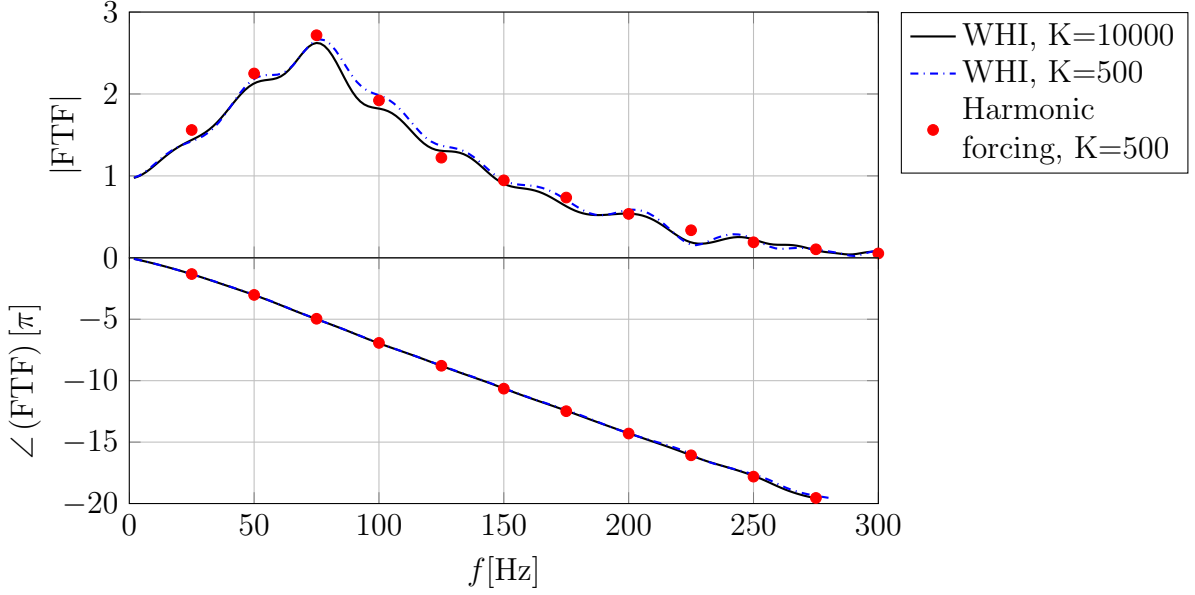


Figure 3.13: FTF based on WHI and harmonic forcing for a non rotating bluff body; $K = 500$ and 10000 curves correspond to the outlet relaxation coefficient in NSCBC and lead to the same results.

the lateral walls.

In order to quantify the heat release fluctuation, the FTF of the laminar flame is estimated via the WHI method. As mentioned above, the WHI methodology is based on assuming that the flame acts as a LTI-system. It is known from prior studies [152] that the configuration shows non-linear behavior for comparably low excitation amplitudes. In order to ensure that the flame response is linear, the excitation amplitude hence was kept at 1% of the bulk velocity for all measurements of FTF. The reference point chosen for the measurements of velocity fluctuations is at $x = -10$ mm and $y = 0$.

The resulting FTF for the symmetric reference flame, i.e. the case without rotation, is shown in Fig. 3.13. As seen in previous studies on different operating points, the flame responds only at comparably low frequencies, in this case below 250 Hz. Furthermore, its gain peaks at a high value of ~ 2.7 at a frequency around 80 Hz. The phase delay increases approximately linear with the frequency, which indicates a constant time delay, which is estimated by the slope of the phase as, $\tau = 35.5$ ms. The accuracy of the WHI was crosschecked by FTF evaluations at discrete frequencies via harmonic acoustic excitation. Their results are shown by the red dots in Fig. 3.13 and show an almost perfect agreement between harmonic forcing and WHI. Note also that small dips and valleys occur in the gain of the FTF. The estimation of the FTF was additionally carried out for an acoustically closed outlet, where the relaxation coefficient was set to $K_{\text{out}} = 10000$. Figure 3.13 demonstrates that the FTFs

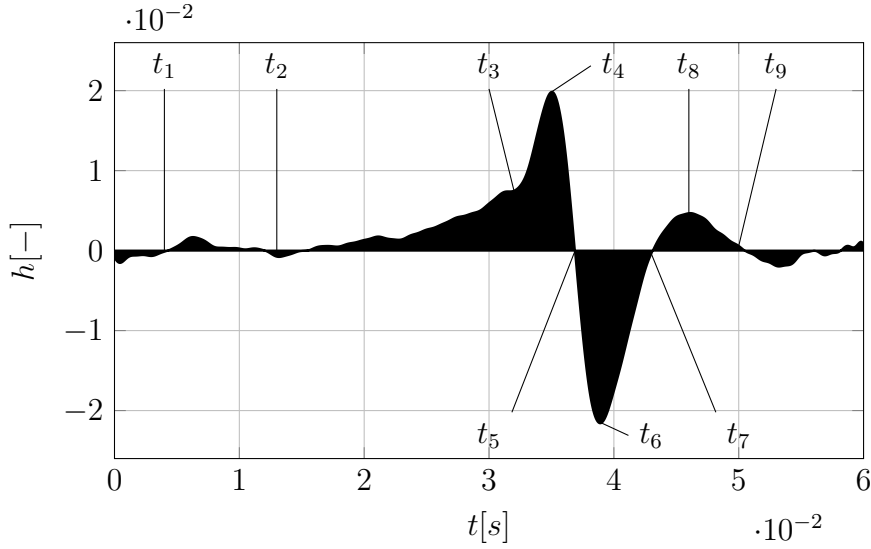


Figure 3.14: IR based on WHI for a non rotating bluff body

for the acoustically open and closed outlet are congruent, except for a visible but marginal deviation around $f = 100$ Hz. Closing the outlet comes along with a significant modulation of the pressure signal at the reference point. The fact that this seems not to have any influence on the FTF demonstrates that the flame is sensitive to velocity fluctuations only.

The IR (see Fig. 3.14) is the counterpart of a TF in the time domain. Assuming that the flame speed is constant, the normalized flame surface variation caused by an acoustic pulse is directly linked with the IR of the flame. The first striking features of the IR are its largest spikes at $t_4 \approx 35$ ms and $t_6 \approx 39$ ms. While analytic flame models based on a convective perturbation model showed that positive spikes in the flame's IR occur when the perturbation reaches the flame tip [18], the negative spike and the consequent two smaller peaks at $t_8 \approx 46$ ms and $t \approx 53$ ms can not be explained by these methods. The impulse response furthermore is slightly negative at $t = 0$ and peaks at a low value at $t_1 \approx 7$ ms.

In order to understand this non trivial behavior of the IR the converged flame is exposed to an acoustic pulse, i.e. a with respect to the acoustic time scales of interest very short but strong increase in flow rate. The pulse satisfies

$$\int_0^\tau u_p dt = 0.25\text{mm}, \quad (3.3.8)$$

where u_p corresponds to the increase in flow velocity (target value in the NSCBC) and $\tau = 0.64$ ms is the length of the pulse. The resulting temporal evolution of the flame root displacement, X_0 , which is depicted in Fig. 3.15 is analyzed in the following. The plot shows that the pulse has caused an initial displacement of the flame, which immediately decreases. It appears that the flame root fulfills a damped oscillation around its unperturbed

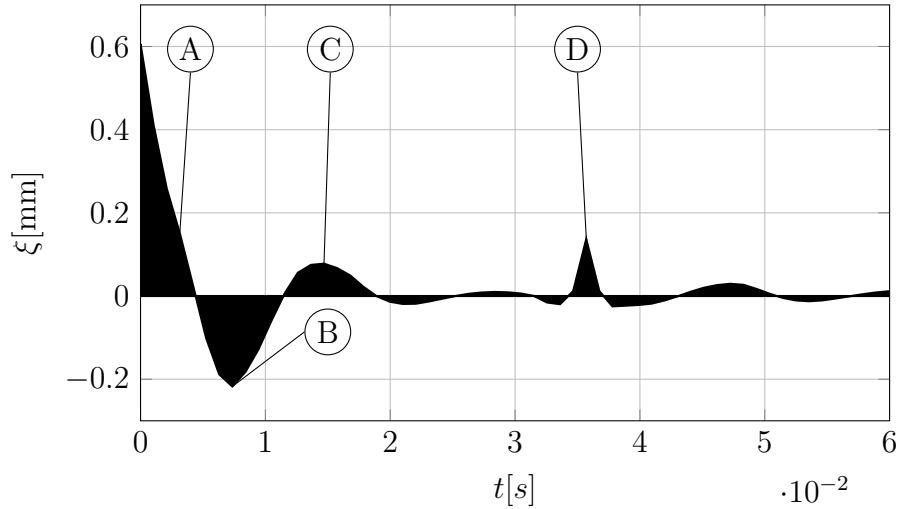


Figure 3.15: Flame root displacement, ξ_0 , caused by a Dirac like acoustic excitation (see Eqn. (3.3.8)) in dependence of time

position. Note, that it was verified that this oscillation is not correlating with any acoustic fluctuations in the domain, e.g. based on an acoustic eigenmode of the chamber, which are of much higher frequency. A second smaller peak is visible at around $t = 36$ ms. Since this value corresponds almost exactly to the time delay estimated for this flame, which is driven mainly by the convection of the perturbation along the flame, at this point it can already be assumed that this peak is caused by an interaction of the flame perturbation with the wall.

Now the gap between the flame root movement in Fig. 3.15 and the IR illustrated in Fig. 3.14 is closed by examining the convection of the flame displacements along the flame front. The instantaneous flame position of various temporal snapshots are compared to the unperturbed flame in Fig. 3.16. Note that the corresponding points in time t_i are additionally marked in Fig. 3.14. Fig. 3.16 shows that directly after the pulse at t_0 the displacement of the flame causes a decrease in global flame length and therefore heat release, explaining the negative value of the IR at $t = 0$. *Vice versa* a negative flame root displacement causes an increase in global flame length. Figs. 3.15 and 3.14 indicate a good temporal agreement between the flame root displacement and the evolution of the heat release seen in the IR for $t < 15$ ms. After this point of time the heat release rate grows slowly but steadily until t_3 , while the flame root stays unperturbed. This growth in heat release seems to be related to the displacements growth along the flame front. The flame displacements which were caused at the flame root and have been convected along the flame can be depicted easily in the temporal snapshot of t_3 (marked by A, B and C in Figs. 3.16 and 3.15). At this point in time, the flame displacement is about to reach the lateral wall. As seen in the snapshot of t_4 , the flame reaches its maximum length at this instant, which causes the peak in the IR. At t_6 on the contrary, the negative flame displacement has reached the wall and the flame

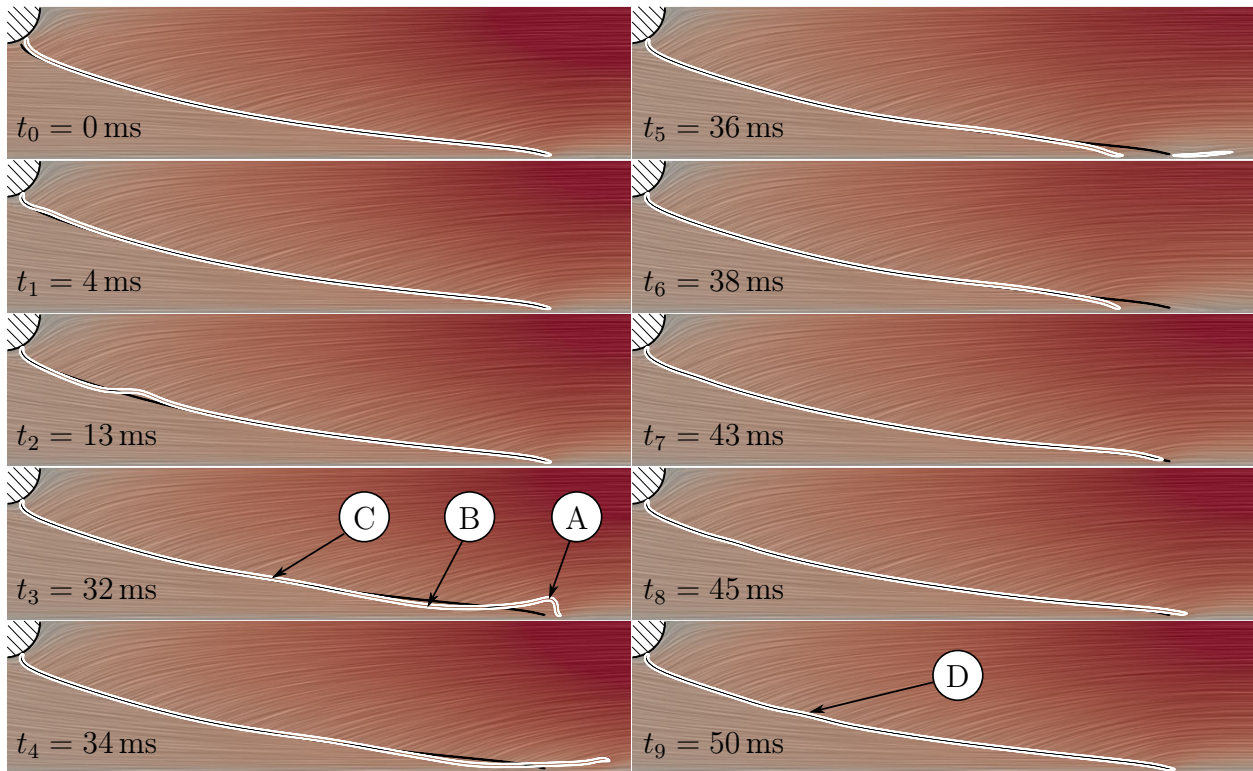


Figure 3.16: Response of the flame topology to a short pulse of inlet velocity (see Eqn. (3.3.8)); Black line: Steady flame, white line: iso-surface of instantaneous heat release of the pulsed case; The times given are with respect to the end of the short pulse.

reaches its minimum total length, leading to the negative spike in the impulse response. The snapshots at t_5 , t_7 and t_9 are taken at instants where the IR is equal to zero according to the WHI. At t_7 and t_9 the instantaneous flame corresponds approximately to the unperturbed flame, which is in line with the value of the IR of 0 at these instants. Evaluating the total heat release based on the snapshot is difficult since the flame exhibits a strongly non-linear shape. Note here however that the displacement amplitudes in the simulations that were used to estimate the IR were much lower. Here on the other hand, for illustrative purposes a comparably strong pulse was applied. Finally, in the snapshot t_9 a small flame displacement of low amplitude originating from the spike in the flame root movement at $t = 36$ ms is discernible (marked by D in Figs. 3.16 and 3.15).

Finally, the response to the acoustic pulse introduced in the computational domain is analyzed in terms of heat release fluctuations in Fig. 3.17. For the heat release fluctuation (lower axis of Fig. 3.17) a similar temporal evolution as seen in the IR based on the WHI in Fig. 3.14 is expected. The overall agreement of both plots is very well. Nevertheless, some discrepancies occur, which can be explained by the temporal evolution of the velocity

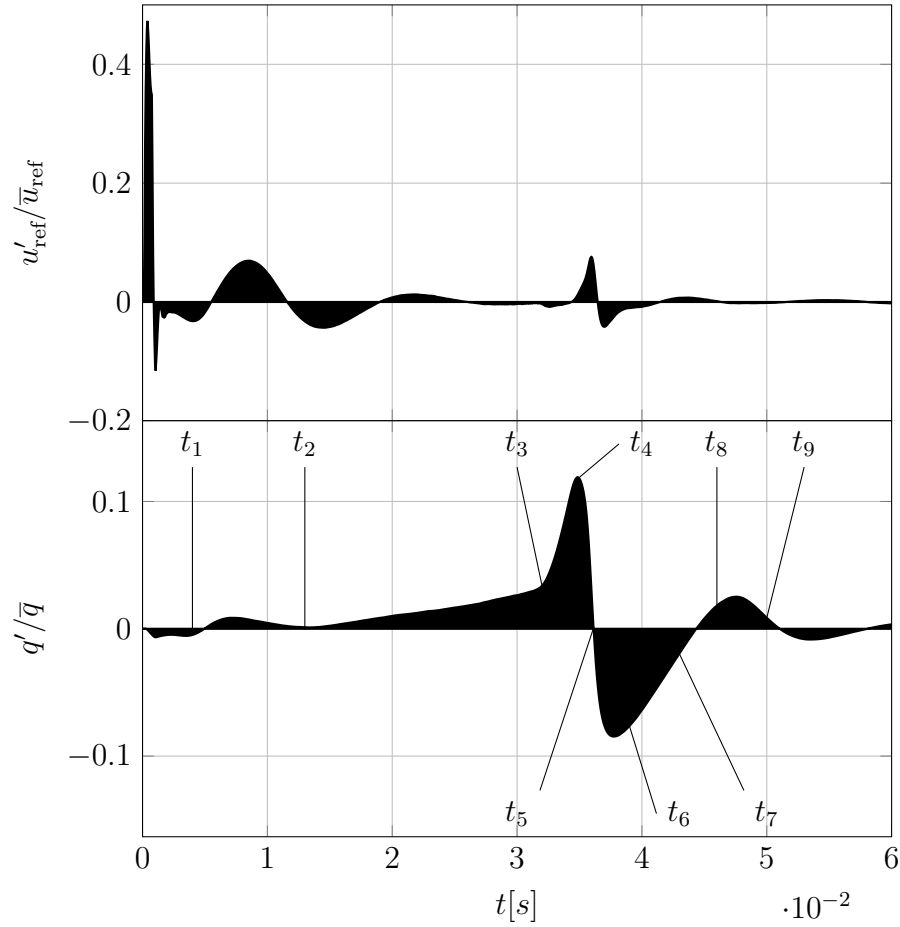


Figure 3.17: Response to an acoustic pulse: Velocity fluctuations at the reference point for the determination of the FTF (upper axis) and heat release fluctuations (lower axis) due to a dirac like acoustic pulse

at the reference point (upper axis of Fig. 3.17). While in the framework of the WHI the IR is the response to a dirac pulse, in the time resolved simulations this dirac excitation of the flame can hardly be obtained. In fact, the plot of the velocity fluctuation at the reference point shows that after the comparably short pulse the velocity fluctuation does not remain at zero, but apparently performs a damped harmonic oscillation. This damped oscillation correlates well with the movement of the flame root illustrated in Fig. 3.15. The heat release oscillation illustrated in Fig. 3.17 therefore is not the response to a single acoustic pulse but to the velocity signal illustrated in the very same figure. This results in certain discrepancies between the responses in Figs. 3.14 and 3.17, which can be seen by the markers inserted in both figures relating the snapshots in Fig. 3.16 to the time after the pulse. Nevertheless, the well overall agreement provides an additional validation of the IR obtained by the WHI process.

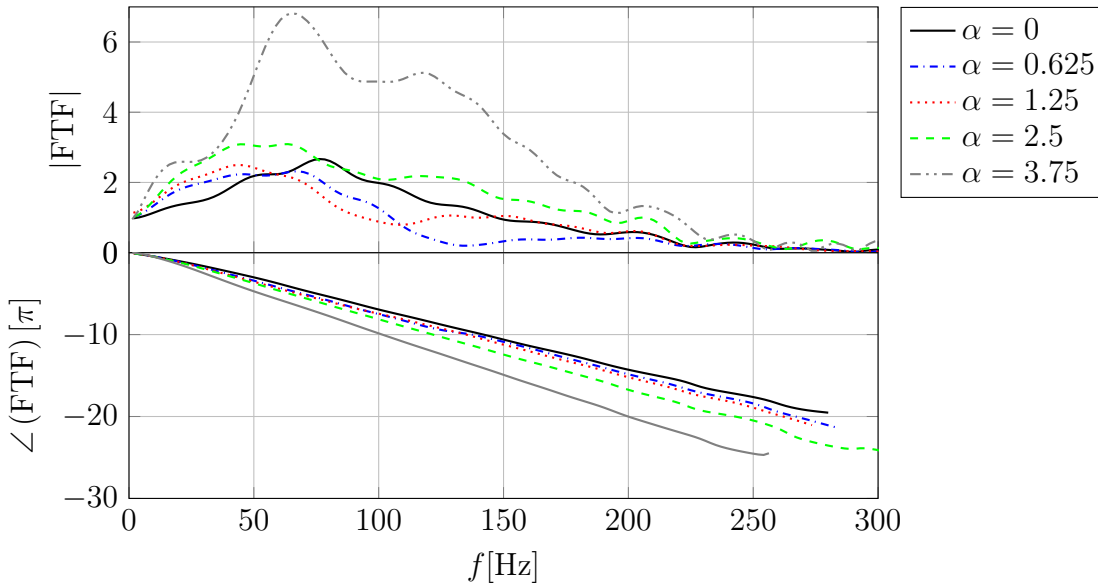


Figure 3.18: Global FTFs for various rotation rates based on WHI of DNS results

3.3.2.3 Flame Response with Rotation

After studying the FTF of a flame stabilized in the wake of a fixed cylinder, now rotating cylinders are considered. Here, the same analysis is repeated and the FTFs are determined by performing WHI only.

The FTFs for various rotation rates are shown in Fig. 3.18. The range of rotation rates depicted in the figure is from the reference case of $\alpha = 0$ up to a rotation rate of $\alpha = 3.75$. With low and moderate rotation rates ($\alpha \leq 2.5$) the maximum gain only changes marginally. For $\alpha = 3.75$ on the other hand, the gain reaches very high values for a broad band of frequencies and peaks at a value of approximately 6.8. The location of the maximum gain remains in the low frequency range between 50 and 80 Hz, while no clear trend is visible. The slope of the phase lag is approximately constant for all rotation rates and the corresponding FTF's time delay increases monotonically with the cylinder rotation rate.

At further examination, the FTFs at all rotation rates except $\alpha = 2.5$ exhibit strong dips, i.e. local minima, in their gain. In order to investigate these dips the FTFs of the upper and lower branches are analyzed separately under the assumption, that their dynamics are not or sufficiently weakly coupled. The FTF of the upper ($y > 0$, labeled y^+) and the lower branch ($y < 0$, labeled y^-) are estimated by integrating the instantaneous spatially averaged heat release in the upper or respectively lower half plane. In order to ease comparability between both branches, the resulting instantaneous heat release signals are normalized with the temporal mean of the global heat release signal. Note that the FTFs of the single branches

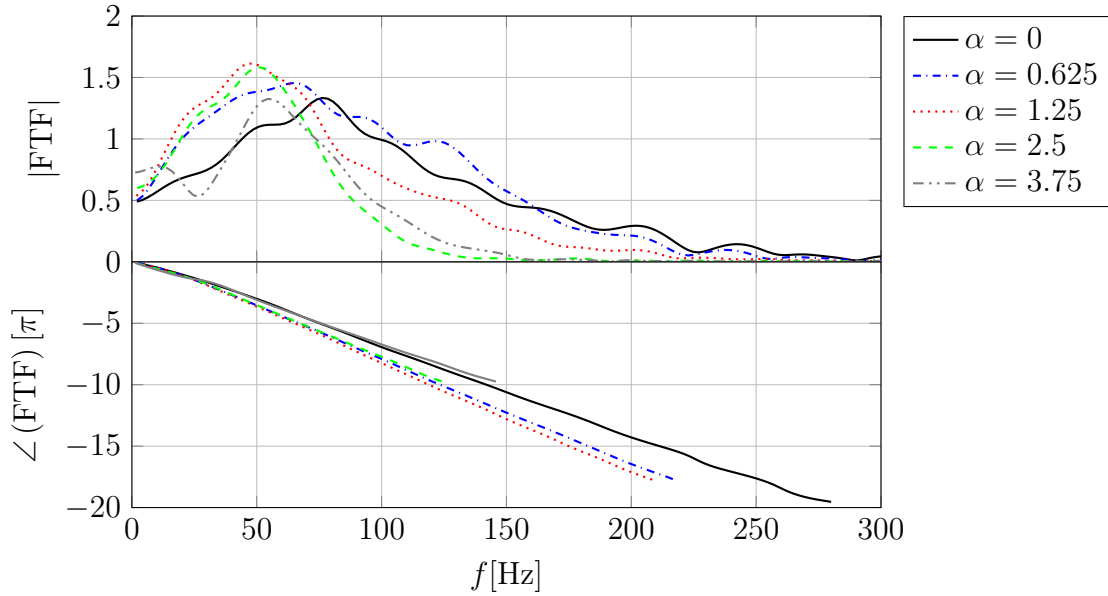


Figure 3.19: FTFs of the upper flame branch (y^+) for various rotation rates based on WHI

hence is not equal to 1 at $f = 0$ Hz. The resulting FTF of the upper branch versus bluff body rotation rate is shown in Fig. 3.19. While with increasing rotation rate the maximum of the gain shifts to lower frequencies its magnitude only changes marginally and without clear trend. The cut off frequency clearly decreases with increasing rotation rate. It appears that for low rotation rates (until $\alpha = 1.25$) the time delay increases, then however decreases again for moderate and high rotation rates (see Table 3.3). This is in line with the downstream shift of the flame tip of the upper branch at low rotation rates and its upstream shift for high rotation rates, seen in Fig. 3.6.

The FTF of the lower branch reacts very differently to the rotation of the flame holder (see Fig 3.20). Concerning the gain, the cut off frequency stays approximately constant, as does the frequency of the maximal gain. The outstanding feature however is that over a broad frequency range the gain drastically increases past a rotation rate of $\alpha = 2.5$. The time delay monotonically increases, which again is in line with the flame lengths shown in Fig. 3.6.

It was demonstrated that the rotation rate modifies the FTFs of the upper and lower branch independently including the respective time delays. In the following, the assumption that destructive interference between the heat release signals of both flame branches based on their different time delays causes the dips in the FTFs will be verified. A simple model will be used to predict the location of the dips and elevations in the respective gains, based on the time delays extracted from the FTFs. The total heat release fluctuation is equal to the

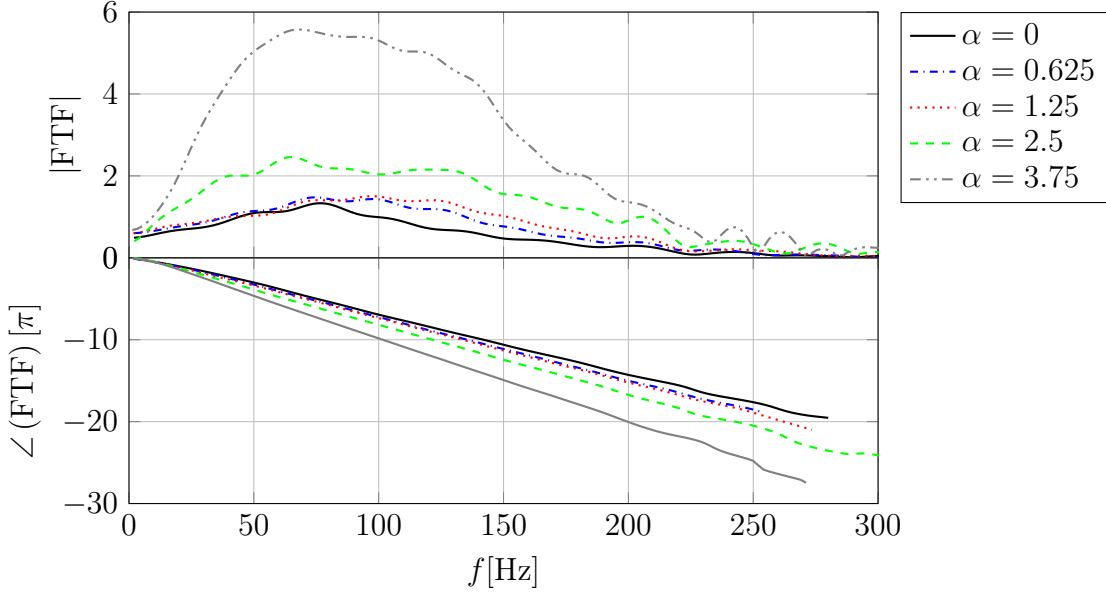


Figure 3.20: FTFs of the lower flame branch (y^-) for various rotation rates based on WHI

sum of both branches' heat releases fluctuations:

$$q'_{\text{tot}} = q'_{y^+} + q'_{y^-}. \quad (3.3.9)$$

Using the FTFs the latter can be expressed by velocity fluctuations. With the notation of Crocco [42], where n denotes the gain and τ the time delay of the respective branches, the total heat release fluctuation can be written as

$$\frac{q'_{\text{tot}}}{\bar{q}} = \frac{u'}{\bar{u}} (n_{y^+} + n_{y^-} \exp(i\omega\Delta\tau)) \exp(i\omega\tau_{y^+}), \quad (3.3.10)$$

where the difference in time delays is defined by $\Delta\tau = \tau_{y^-} - \tau_{y^+}$. Equation 3.3.10 shows that the gain of the global FTF depends on the difference in phase angles of both branches which can be expressed as

$$\Delta\phi = \omega\Delta\tau. \quad (3.3.11)$$

For the phenomenon of interference, two extreme cases exist: Ideal constructive and ideal destructive interference. Which case occurs is only depending on the phase angles of both superimposed signals. For the former case, the phase angle has to be zero or equal to an even multiple of π . Is this the case, then Eqn. (3.3.10) simplifies to $n_{\text{tot}} = n_{y^+} + n_{y^-}$. Inserting $\omega = 2\pi f$ into Eqn. (3.3.11) therefore yields the frequency at which constructive interference occurs:

$$f_{c,j} = \frac{\Delta\phi}{2\pi\Delta\tau}, \quad \Delta\phi = 2j\pi, \quad j \in \mathbb{Z}. \quad (3.3.12)$$

α	τ_{y^+}	τ_{y^-}	$\Delta\tau$	$f_{d,1}$	$f_{d,2}$
0.0	35.5 ms	35.5 ms	0 ms	—	—
0.625	40.9 ms	37.1 ms	-3.8 ms	132 Hz	395 Hz
1.25	42.5 ms	37.9 ms	-4.6 ms	109 Hz	326 Hz
2.5	38.6 ms	41.6 ms	3.0 ms	167 Hz	500 Hz
3.75	33.6 ms	49.7 ms	16.1 ms	31 Hz	93 Hz

Table 3.3: Time delays of the two flame branches (τ_{y^+} and τ_{y^-} for the upper and lower branch, respectively) and values of the first two frequencies for destructive interference (cf. Eq. (3.3.13)).

In the case of destructive interference on the other hand the difference in phase has to be equal to an odd multiple of π . The global gain then is equal to $n_{\text{tot}} = |n_{y^+} - n_{y^-}|$. Analogously, the frequencies at which constructive interference occurs are:

$$f_{d,j} = \frac{\Delta\phi}{2\pi\Delta\tau}, \quad \Delta\phi = (2j - 1)\pi, \quad j \in \mathbb{Z}. \quad (3.3.13)$$

This way, the frequencies of ideal destructive and ideal constructive interference can be estimated, based on the time delays extracted from the FTFs. Table 3.3 shows the time delays of both branches, the respective difference in time delays of both branches and the first and second frequencies of ideal constructive and destructive interference based on Eqns. (3.3.12) and (3.3.13). Note that $\Delta\tau$ is negative for low rotation rates, becomes however positive for moderate and high rotation rates. The frequencies listed in Table 3.3 are also shown by markers in Fig. 3.21. They show that the dips are in very good agreement with the frequencies of constructive and destructive interference predicted by the simple model that resulted in Eqns. (3.3.12) and (3.3.13) for the FTF of all rotation rates except for $\alpha = 2.5$. For this rotation rate the gain of the upper branch is already zero at $f_{d,1}$ and therefore no destructive interference occurs. Except for the rotation rate of $\alpha = 3.75$, all second frequencies of ideal destructive interference, $f_{d,2}$, are beyond the cut off frequencies of both the upper and lower branch and therefore are of no further interest. In contrast, the high difference in time delays for a bluff body rotation rate of $\alpha = 3.75$ lead to a comparably low value of the second frequency of destructive interference, which is below the cut off frequency of both flame branches. Therefore, only for the highest rotation rate a second dip in the gain is visible. In comparison to the reference case of $\alpha = 0$, low bluff body rotation rates ($\alpha \leq 1.25$) lead to a drastic decrease of gain in the frequency range around the frequency of ideal destructive interference. For increasing rotation rates however, the increase in gain in the lower branch is so strong, that even if destructive interference occurs, the corresponding gain is much higher than in the reference case.

It appears that the simple model of Eqns. (3.3.12) and (3.3.13) provides a correct estimation of the locations of the dips and elevations in the FTF. Therefore, it *a posteriori* confirms the assumption that destructive interference leads to the dips in the gains of the FTFs.

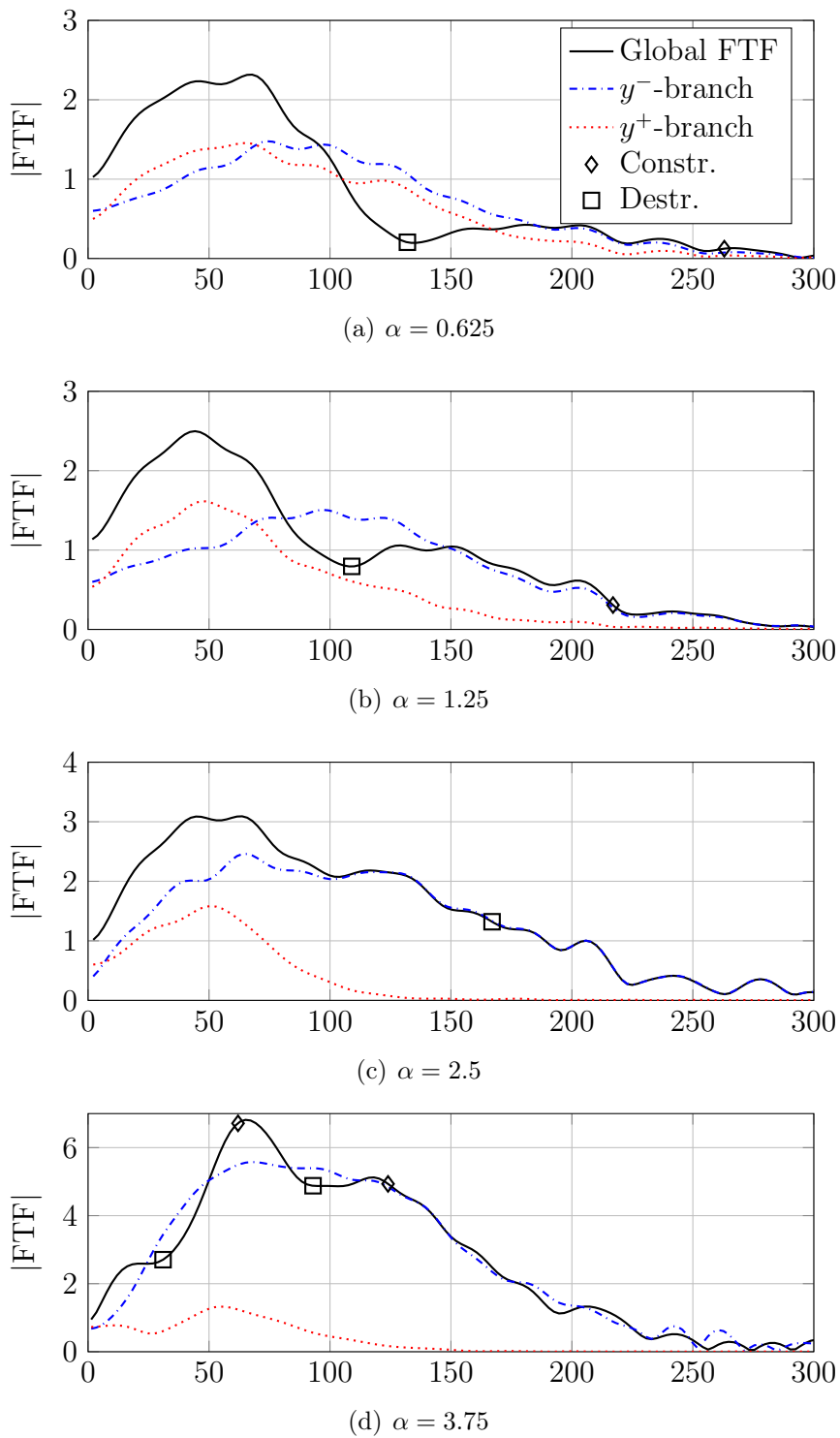


Figure 3.21: Comparisons of gains of global FTFs and of the single flame branches FTFs; Frequencies of ideal destructive and ideal constructive interference are marked on the global gains

3.3.2.4 Influence of Bluff Body Rotation on Flame Front Dynamics

In the previous section, the changes in FTFs of the upper and lower flame branch were analyzed by changing the bluff body rotation rate. In order to examine the thermoacoustic interaction further, the dynamics of flame topology is analyzed now for harmonic acoustic excitation. The excitation which Fig. 3.12(a) is based upon is repeated for the rotating bluff body configurations. The corresponding plot, illustrating the flame's response to harmonic acoustic forcing in terms of flame topology, is depicted in Fig. 3.22 for the upper and lower flame branch at various bluff body rotation rates. The flame normal displacement, ξ , along the flame front, l is shown for four different phase angles of the velocity perturbation of $f = 80$ Hz, which is close to the maximum gain for all cylinder rotation rates.

First the upper branch is analyzed. The amplitude of the flame normal displacement increases along the flame front for all rotation rates. The amplitude of ξ at the flame tip decreases with increasing rotation rate until $\alpha = 2.5$, while beyond this value it slightly increases again. This behavior is in line with the change in gain of the upper branch with α at the same frequency. It appears that a non linear deformation of the flame normal displacement occurs close to the flame tip. The degree of non-linearity follows the same trend as the magnitude, i.e. it decreases until to a value of $\alpha = 2.5$ and increases again beyond this rotation rate.

At the lower flame branch, the flame root displacement at $l = 0$ decreases with increasing rotation rate. In contrast, the growth of the perturbations along the flame front increases significantly with the bluff body rotation. This effect is especially strong for rotation rates $\alpha \geq 2.5$. As can be seen on the right side of Fig. 3.22, this goes along with a significant increase in non-linearity. Note, that the flame displacement grows along the flame front monotonically for both the upper and lower branch at all rotation rates except for the lower branch at $\alpha = 3.75$. Here ξ grows until $l \approx 40$ mm. After that, saturation occurs and the flame displacement stays approximately constant until it reaches the flame tip. Figure 3.22 suggests that some kind of instability mechanism seems to lead to the growth of the flame normal displacements along the flame front. At the frequency under investigation this effect decreases with the bluff body rotation rate for the upper branch and increases for the lower branch, which leads to the strong increase in the gain of the FTF of the flame in y^- -half plane.

The results suggest, that the difference in convective time of the flame perturbations along the flame front causes destructive interference between both flame branches. To further confirm this hypothesis, Fig. 3.23 illustrates the impact of acoustic perturbation on the flame tip position of both branches for a rotation rate of $\alpha = 0.625$. It shows the relative shift of either flame branch tip with respect to its unperturbed position (see also Tab. 3.2) with respect to the phase angle of a harmonic acoustic perturbation. It pulses at the first frequency of perfect destructive interference, $f_{d,1} = 132$ Hz, based on Eqn. (3.3.13). It is obvious, that

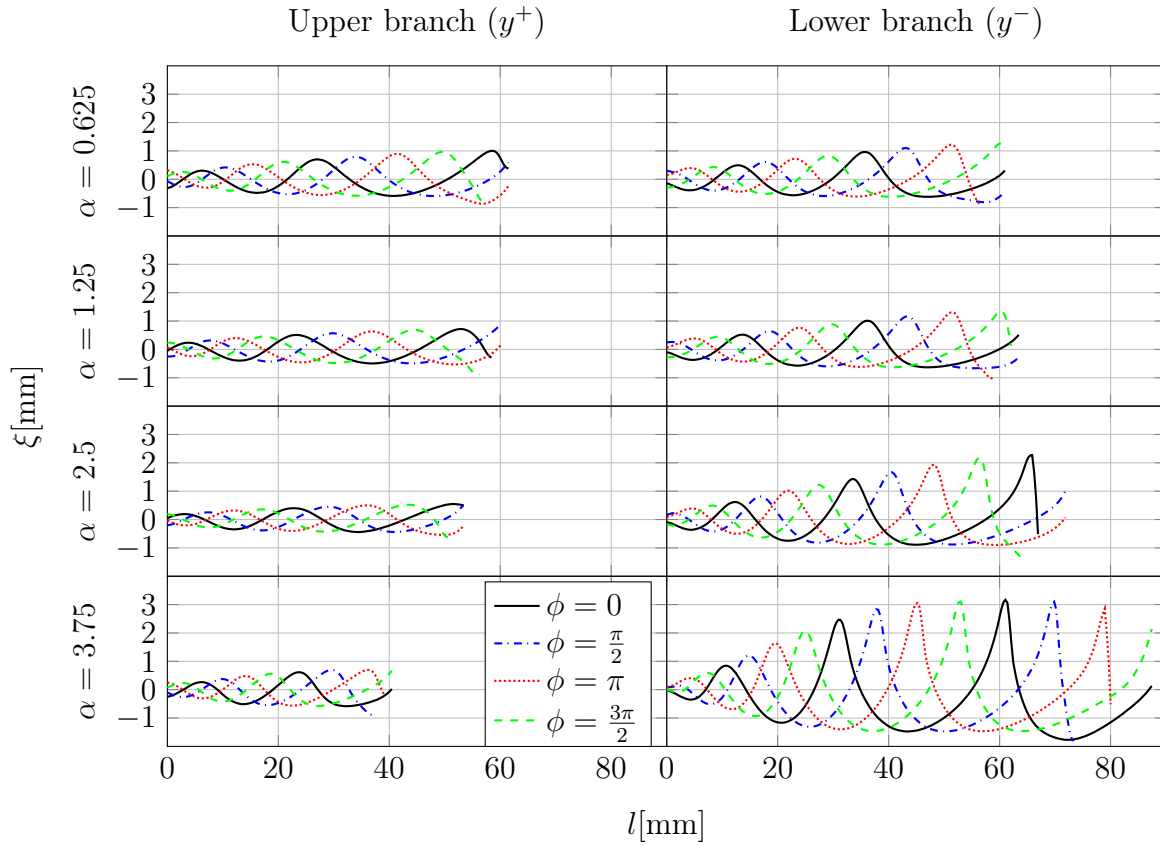


Figure 3.22: Response of flame topology to acoustic forcing; flame normal displacement, ξ , as a function of the flame front position, l for the upper and lower branch at various cylinder rotation rates and various phase angles of the harmonic acoustic forcing of frequency 80 Hz and amplitude $5\% u_b$

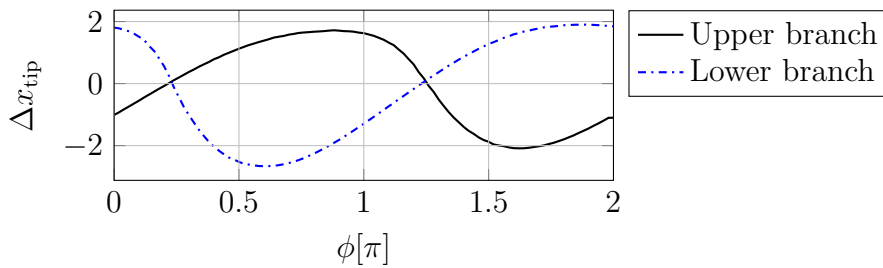


Figure 3.23: Relative flame tip position with respect to the respective branches flame tip position of the steady flame, $\Delta x = x_{\text{tip}} - x_{\text{tip,st}}$, versus the phase angle of the velocity perturbation, ϕ ; Cylinder rotation rate $\alpha = 0.625$; pulsation amplitude $|u'| = 2\% u_b$; pulsation frequency $f_{d,1} = 132$ Hz

the flame tips move perfectly out of phase, which again confirms the accuracy of the simple model given by Eqns. (3.3.12) and (3.3.13). Figs. 3.18 and 3.23 suggest that controlling the rotation rate of the bluff body allows to build a flame which is almost insensitive to acoustic perturbations, suggesting that it could be applied in the framework of combustion instability control. Note however, that this method of control would be limited to a certain frequency range.

3.4 Conclusion

In this chapter, a laminar flame anchored in the wake of a rotating bluff body was under investigation by the means of LDNS. The flame is absolutely symmetric for a non rotating bluff body. The symmetry however is broken by a bluff body rotation rate $\alpha \neq 0$. The lower flame branch stays attached to the cylinder and increases in length due to an increase of bulk flow in the lower half plane. For low rotation rates the flame root of the upper branch detaches from the cylinder and therefore causes a downstream shift of the whole flame. For increasing rotation rates the decrease of flow rate in the upper plane shifts the flame upstream again and causes an increase of flame angle and a decrease in flame length.

Furthermore, the flame's response to acoustic fluctuations was investigated. Acoustic fluctuations cause a displacement of the flame root, which is transported along the flame front until it vanishes at the flame tip. This process causes a strong fluctuation of flame surface and therefore heat release. This effect is reinforced by a growth of the perturbations along the flame front, for all rotation rates and flame branches. It is demonstrated that the growth however is the strongest for the lower branch at high rotation rates, leading to a drastic increase in gain of the respective flame branch.

It was shown that the changes in flame topology cause a difference in time delays between the flame branches which is adjustable by the cylinder rotation rate. This causes interference between the heat release signals of both branches leading for some frequencies to destructive interference for others to constructive interference. The frequency of destructive interference can be adjusted by tuning the cylinder rotation rate, leading to a drastic decrease in gains of the global flame around this frequency. Very low frequencies of destructive interference can be achieved for high rotation rates (e.g. $\alpha = 3.75$). Nevertheless, a reduction in gain for the global flame can not be produced for these cases due to the strong growth of perturbations on the lower flame branch. An efficient reduction of the gain by tuning the bluff body rotation can be achieved approximately for the upper half of the frequency spectrum.

The results demonstrate that the rotation rate might be a suitable tool to control combustion instabilities for these laminar burners. The very most industrial combustors however involve highly turbulent flames. Therefore, it remains to be shown if bluff body rotation leads to

similar effects for a corresponding turbulent flow. Nevertheless, symmetry and symmetry breaking has been investigated for real combustion systems in the past. The idea of breaking the symmetry in order to increase dampening rates of combustion instabilities is at least as old as the F-1 engine, used in the Apollo missions by NASA [173]. The effect of symmetry breaking on the stability of an annular combustion chamber by changing the flames along the azimuthal direction was addressed by several authors. Bauerheim et al. [14] nevertheless showed analytically that at first order this procedure could not enhance stability properties of an annular combustor. In contrast, the results of this work however emphasize the asset of being able to control the degree of asymmetry of a flame in order to directly impact the gain of the FTF.

Besides the applicability in real engines the effect of the perturbations growth along the flame front remains an open topic. A similar effect which can occur in lean laminar flames is the Darrieus-Landau instability. While the Darrieus-Landau instability is intrinsic, i.e. it leads to a growth of perturbation without external excitation, in the INTRIG configuration the instability is merely convective. Nevertheless, it is conceivable that their origin is the same. Growth and decay of these kind of perturbations was already investigated by Markstein [146] and Petersen [182] experimentally. The former in 1951 furthermore analytically solved the two-dimensional Euler equations including a simple combustion model to find with a small perturbation approach a stability criterion for laminar flames. The small perturbation approach today better known as the linear stability analysis of hydrodynamics has progressed immensely during the last 65 years. The community is no longer depending on analytic solutions of the Euler equations, but the full coupled set of linearized Navier-Stokes, continuity and energy equations can be solved numerically. Nevertheless, the question of the convectively amplified perturbations in a flame front remains not addressed by these more modern approaches.

Part II

Hydrodynamic Instabilities in Fuel Injection Systems

Chapter 4

LES

The problem of solving the Navier-Stokes equations for turbulent flows has been addressed since almost a century. Figure 4.1(a) illustrates the turbulent energy cascade. Turbulent kinetic energy is produced at large scales (and therefore small wave numbers α). This energy is transferred to eddies of higher and higher wave numbers. This process is stopped at the Kolmogorov scale, where viscous forces become dominant over the inertial forces and the turbulent kinetic energy is dissipated to heat. In order to correctly simulate the flow, the turbulent energy cascade has to be either resolved, or modeled. In the case of DNS (see Section 2) the full energy spectrum is spatially resolved. Nevertheless, this approach is not affordable in most practical cases. One way to circumvent the resolution of the Kolmogorov scale is to solve the temporally averaged Navier-Stokes equations or RANS equations. Yet, the turbulent fluctuations, which act as Reynolds stresses on the temporal means, remain unknown. Therefore, the influence of the turbulent spectrum on the means must be modeled. As a consequence, RANS simulations only provide the mean fields, and do not yield insight in the dynamics of a system.

A trade off between DNS and RANS is LES. While DNSs resolve the full turbulent energy spectrum and RANSs model the full energy spectrum, in LESs the turbulent spectrum is spatially filtered (e.g. by the numerical grid size). Eddies attributed to a wave number below the cut-off wave number, α_c , are spatially resolved, while eddies of smaller size are modeled (see Fig. 4.1(a)). Figure 4.2 illustrates the different results of DNS, LES and RANS for the same configuration of a turbulent jet.

This chapter addresses the numerical LES methods, which will be applied in Chapters 6 and 7 on the problem of swirling flows. The software used is like in the DNSs AVBP. Section 4.1 deals with the governing equations of LES. The turbulence closure and modeling is addressed in Section 4.2 and the chemistry models applied for the reactive simulations are discussed in Section 4.3.

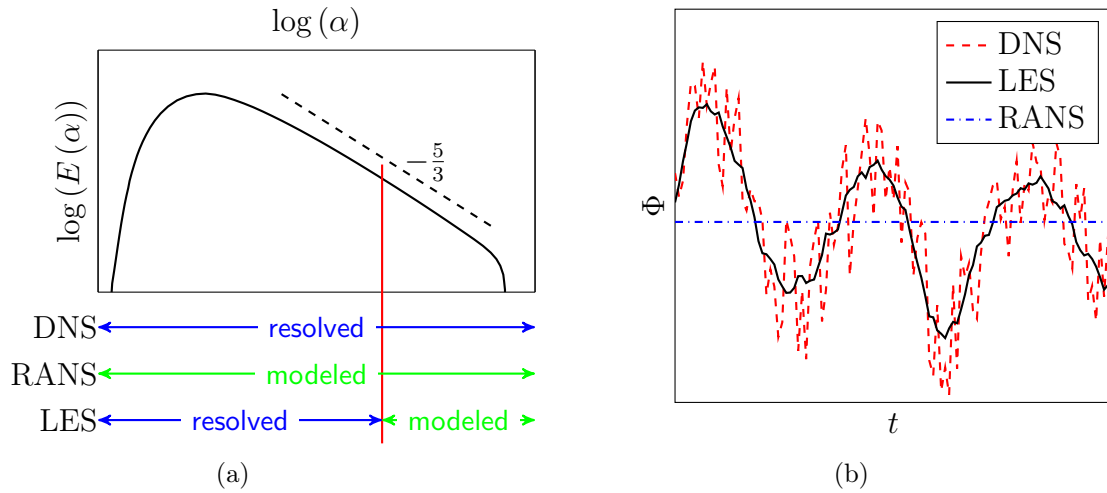


Figure 4.1: Comparison of the concepts of DNS, LES and RANS

4.1 LES Governing Equations

The governing equations of LES are based on the continuity equation (Eqn. (2.1.4)), the Navier-Stokes equation (Eqn. (2.1.9)) and the energy equation (Eqn. (2.1.11)). In case of multi species simulations a transport equation for the species mass fraction, Y_k (see Eqn. (2.1.5)) is added. The state variables are split into a part, which is resolved by the computational grid (indicated by an overbar) and a Sub-Grid-Scale (SGS) contribution (indicated by a prime superscript), which remains to be modeled. For the pressure and the density, these filtered variables read [124]

$$\bar{\Phi} = \int_{-\infty}^{\infty} G(r)\Phi(x-r) dr, \quad (4.1.1)$$

and the decomposition of the variable then becomes:

$$\Phi = \bar{\Phi} + \Phi'. \quad (4.1.2)$$

Here, $G(r)$ is a suitable spatial filter function. For examples for the spatial filter function see [195]. In A Very Big Project (AVBP) the spatial filtering is performed directly by the spatial grid, so that no additional filter $G(r)$ is applied.

In case of compressible flows, or in general flows of non-uniform density, applying the same averaging technique for the velocity components and the energy yields additional terms (products of the respective quantity with the SGS density variation, ρ') in the Navier-Stokes and energy equation and in transport equation of mass fractions, which do not vanish when

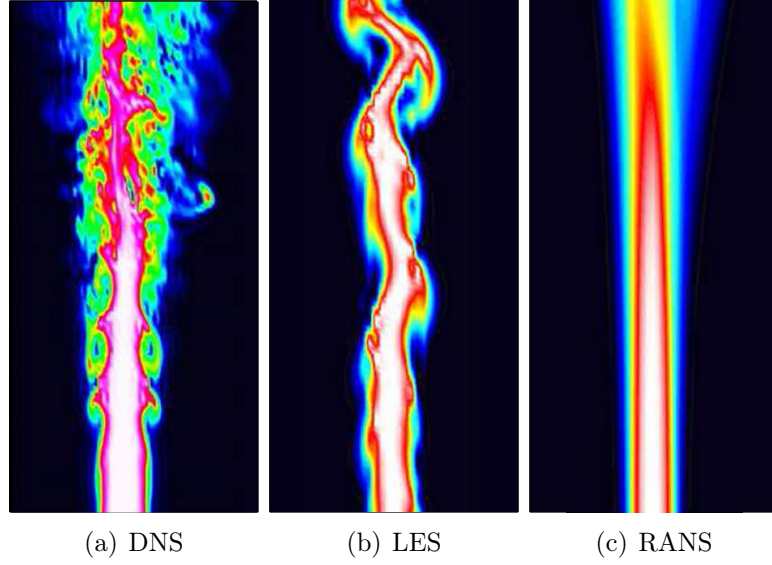


Figure 4.2: Instantaneous snapshots of CFD simulations of a turbulent jet for DNS, LES and RANS [145]

temporally averaged. This problem can be avoided when applying a Favre-average instead of a temporal average for these quantities, which is defined as

$$\tilde{\Phi} = \frac{1}{\bar{\rho}} \int_{-\infty}^{\infty} G(r) \rho(x-r) \Phi(x-r) dr. \quad (4.1.3)$$

The decomposition for quantities, which appear in nonlinear terms then becomes

$$\Phi = \tilde{\Phi} + \Phi''. \quad (4.1.4)$$

In order to arrive at the governing equations of LES, the state variables in the form of Eqns. (4.1.2) and (4.1.4) are inserted in the equations of continuity (Eqn. (2.1.4)), conservation of momentum (Eqn. (2.1.9)), energy (Eqn. (2.1.11)) and transport equation for the species mass fraction (Eqn. (2.1.5)). Subsequently, the equations are filtered with the same filter operation, $G(r)$, which yields:

$$\frac{\partial \bar{\rho}}{\partial t} + \nabla \cdot (\bar{\rho} \tilde{\mathbf{u}}) = 0, \quad (4.1.5)$$

$$\frac{\partial \bar{\rho} \tilde{\mathbf{u}}}{\partial t} + \nabla \cdot (\bar{\rho} \tilde{\mathbf{u}} \otimes \tilde{\mathbf{u}}) = -\nabla \cdot (\bar{\rho} \mathbf{I} + \tilde{\boldsymbol{\tau}} + \tilde{\boldsymbol{\tau}}^t) \quad (4.1.6)$$

$$\frac{\partial \bar{\rho} \tilde{e}}{\partial t} + \nabla \cdot (\bar{\rho} \tilde{e} \tilde{\mathbf{u}}) = -\nabla \cdot (\overline{\mathbf{u} p} - \mathbf{u} \cdot \tilde{\boldsymbol{\tau}} + \tilde{\mathbf{q}} + \tilde{\mathbf{q}}^t) + \dot{\omega}_{\text{reac}} + \dot{\omega}_{\text{rad}}, \quad (4.1.7)$$

$$\frac{\partial \bar{\rho} \tilde{Y}_k}{\partial t} + \nabla \cdot (\bar{\rho} \tilde{Y}_k \tilde{\mathbf{u}}) = -\nabla \cdot (\bar{\rho} \tilde{Y}_k (\tilde{\mathbf{V}}_k + \tilde{\mathbf{V}}_k^t)) + \dot{\omega}_k. \quad (4.1.8)$$

Here, the resolved viscous stress tensor, the heat flux, and the corrected diffusion velocity are

$$\tilde{\boldsymbol{\tau}} = \mu \left(\nabla \tilde{\mathbf{u}} + (\nabla \tilde{\mathbf{u}})^T - \frac{2}{3} (\nabla \cdot \tilde{\mathbf{u}}) \mathbf{I} \right), \quad (4.1.9)$$

$$\tilde{\mathbf{q}} = -\lambda \nabla \tilde{T} - \bar{\rho} \sum_{k=1}^N \left(D_k \frac{W_k}{W} \nabla \tilde{X}_k - Y_k \sum_{l=1}^N D_l \frac{W_l}{W} \nabla \tilde{X}_l \right) \tilde{h}_{s,k}, \quad (4.1.10)$$

$$\tilde{\mathbf{V}}_{k,\text{corr}} = D_k \frac{W_k}{W} \nabla \tilde{X}_k - \sum_{l=1}^N D_l \frac{W_l}{W} \nabla \tilde{X}_l, \quad (4.1.11)$$

respectively.

4.2 Turbulence Modelling

The non-linear terms in the Navier-Stokes, energy and species equation lead to product terms of fluctuating quantities, which do not vanish in the LES equations (Eqns. (4.1.6–4.1.8)). In the momentum equation for example, this yields 6 independent terms in the SGS Reynolds stress tensor which are *a priori* unknown and therefore remain to be modeled. Most often the Boussinesq approximation, which in Einstein notation reads

$$-\widetilde{u'_i u'_j} = -\frac{2}{3} K \delta_{ij} + \nu_{\text{LES}} \left(\frac{\partial \tilde{u}_i}{\partial x_j} + \frac{\partial \tilde{u}_j}{\partial x_i} \right), \quad (4.2.1)$$

where K is the turbulent kinetic SGS energy, is applied in order to relate the terms in the Reynolds stress tensor to the resolved shear strain rates by a SGS viscosity. The amount of terms which remain to be modeled are thus reduced to one, the SGS viscosity, ν_{LES} . In doing so, the Reynolds stress tensor becomes:

$$\tilde{\boldsymbol{\tau}}^t = \bar{\rho} \nu_{\text{LES}} \left(\nabla \tilde{\mathbf{u}} + (\nabla \tilde{\mathbf{u}})^T - \frac{2}{3} (\nabla \cdot \tilde{\mathbf{u}}) \mathbf{I} \right), \quad (4.2.2)$$

Various models have been proposed in literature to address the problem of modeling the SGS viscosity. In the framework of this thesis the σ -model is applied [168, 248]:

$$\nu_{\text{LES}} = (C_\sigma \Delta)^2 \frac{\sigma_3 (\sigma_1 - \sigma_2) (\sigma_2 - \sigma_3)}{\sigma_1^2}. \quad (4.2.3)$$

Here, C_σ is the modeling constant and is typically set to 1.5. σ_1 , σ_2 and σ_3 are estimated by computing the singular values of the local resolved velocity gradient tensor and are ordered $\sigma_1 \geq \sigma_2 \geq \sigma_3$.

The SGS viscosity based on the σ -model vanishes for various configurations for which no sub grid scale contribution is expected, e.g. pure rotation, pure shear [187]. This includes, that it vanishes with appropriate asymptotic behavior at solid boundary walls.

The SGS fluctuations also lead to unknown terms in the transport equations of energy and species mass fraction. These are modeled analogously to the terms in the momentum equation by additional contributions to diffusion for both energy and species transport (see $\tilde{\mathbf{q}}^t$ and $\tilde{\mathbf{V}}^t$ in Eqn. (4.1.7) and Eqn. (4.1.8), respectively). In most CFD codes this effect is not explicitly modeled but coupled to the turbulent viscosity by a proportionality factor. For the energy equation this proportionality factor is the turbulent Prandtl number defined as

$$\text{Pr}^t = \frac{\nu_{\text{LES}}}{a_{\text{LES}}} = \frac{\nu_{\text{LES}} \rho c_p}{\lambda_{\text{LES}}}, \quad (4.2.4)$$

while for the species diffusion the proportionality factor is the turbulent Schmidt number given by

$$\text{Sc}^t = \frac{\nu_{\text{LES}}}{D_{\text{LES}}}. \quad (4.2.5)$$

Literature suggests different values for the turbulent Prandtl and Schmidt number, which typically range from 0.6 to 0.9. Here the standard values used in AVBP are applied, which are

$$\text{Sc}^t = \text{Pr}^t = 0.6. \quad (4.2.6)$$

4.3 LES Chemistry Model

In the DNS simulations that lead to the results presented in Chapter 3, a rather detailed chemistry model with 19 transported species was applied. In LES simulations the demand on the accuracy of the chemistry model is typically lower. In the framework of the LES calculations the BFER model is applied in combination with the Thickened Flame Model (TFM), both of which will be discussed in the subsequent sections.

4.3.1 BFER

The BFER mechanism was first developed for kerosene-air flames [70] and then adapted to methane-air flames [71]. It accounts for two reactions and six species. Two correction functions in the pre-exponential factor of the Arrhenius terms, allow for correct laminar flame

speeds in the rich regime and correct post-flame zone thickness. This way, laminar flame speeds and adiabatic flame temperatures are well reproduced for a wide range of pressures, fresh gas temperatures and equivalence ratios [71].

4.3.2 Thickened Flame Model

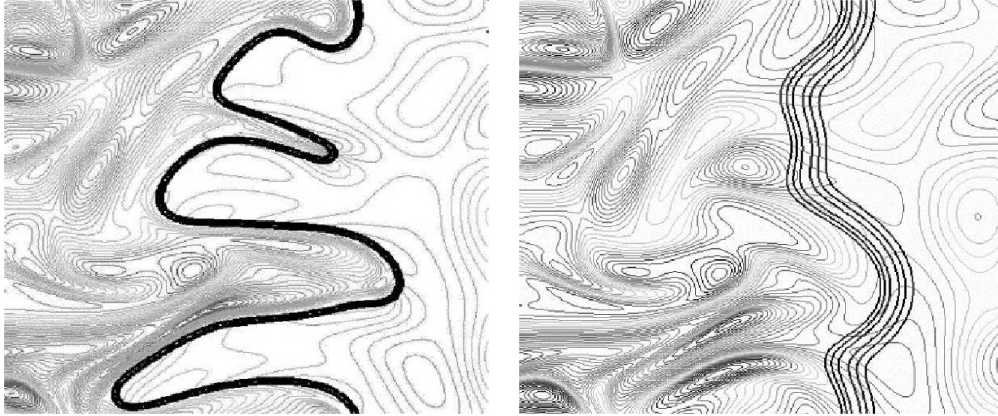


Figure 4.3: DNS of a flame without artificial flame thickening (left) and with an artificial thickening of $\mathcal{F} = 5$ (right); taken from [190]

Unlike in DNS, where the flame thickness is resolved by the numerical grid, in LES the laminar flame thickness is typically smaller than the numerical grid size. Without adaptation, this would lead to stiff chemical source terms and therefore not satisfactory results. A frequently applied method is the application of the TFM. Here, the flame thickness is artificially increased by a certain factor, \mathcal{F} , so that the flame is well resolved by the computational grid. In turbulent flows, where the interaction between the turbulence and the flame has a significant influence on the global reaction rate, the interaction between vortices and the flame front is altered by this approach. Some of the vortices that lead to a wrinkling in the unthickened flame front are now smaller than the flame thickness when the TFM is applied (see Fig. 4.3). Therefore, the ability of turbulence to wrinkle the flame is reduced leading to a incorrect decrease in reaction rate and therefore turbulent flame speed. This effect is corrected by applying a efficiency function \mathfrak{C} developed by Colin et al. [38, 39], which models the gap in turbulence flame interaction caused by the TFM.

Chapter 5

Linear Stability Analysis of Hydrodynamic Instabilities

The brute-force method of LES, presented in the last section, is an extremely valuable tool, not only in the framework of combustion research and engineering. Although it may be applied to solve multi-physics problems (e.g. in combustion: fluid-dynamics, chemistry, two-phase flow...), understanding the dynamics of the incompressible Navier-Stokes equations alone remains a challenge in many cases. The dynamics and most importantly the vortex street in the cylinder wake flow for example, a configuration which can barely be outreached in simplicity, were first and most famously analyzed by von Kármán [256]. Today, nearly a century later, studies in contemporary research focus on the topic still [11, 116]. Although LES and DNS reproduce experimental results well in this configuration, they might not be the ideal tools to analyze the origin of its dynamics. The method of LSA for example provides insight in the origin by analyzing the feedback mechanism of hydrodynamic instabilities like the von Kármán vortex street. These insights might be for example appealing if one wishes to control their occurrence.

Hydrodynamic instabilities also often occur in the combustion chambers [5, 186, 79, 223, 32, 201, 203, 191, 269, 25, 29]. Especially in swirled jet flows, a configuration which is often used to inject the fresh gases in the combustion chamber, a helical instability frequently occurs, the PVC. This chapter focuses on the method of LSA in swirling jet flows with focus on this helical instability. The governing equations of the LSA for base flows in uniform density flows are discussed in Section 5.1.1. Since in flames the reaction heat causes an expansion and therefore decrease in density of the fluid, the base-flows of reacting flows are in general of non-uniform density. Section 5.1.2 deals with the corresponding LSA equations, which take the non-uniformity of the base flow density into account. Section 5.2 introduces the modal approach and introduces BiGlobal and local LSA and the numerical approach.

5.1 Governing Equations of Hydrodynamic Stability

The dynamics of coherent structures evolving on a given base flow are governed by the Navier-Stokes equations (Eqn. (2.1.9)), the continuity equation (Eqn. (2.1.4)) and the conservation equation of internal energy (Eqn. (2.1.11)). In the context of LSA, it is convenient to express the equations in dimensionless form. Therefore, all dimensional quantities are written as:

$$\mathbf{u} = U_{\text{ref}} \mathbf{u}^*, \quad (5.1.1a)$$

$$x = D_{\text{ref}} x^*, \quad (5.1.1b)$$

$$t = \frac{D_{\text{ref}}}{U_{\text{ref}}} t^*, \quad (5.1.1c)$$

$$\rho = \rho_{\text{ref}} \rho^*, \quad (5.1.1d)$$

$$p = \rho_{\text{ref}} U_{\text{ref}}^2 p^*, \quad (5.1.1e)$$

where U_{ref} , D_{ref} , ρ_{ref} are arbitrary quantities for a characteristic convective velocity, a length scale and a reference density. Furthermore, the following assumptions are made:

1. The fluid follows the perfect gas law (see Eqn. (2.1.1)).
2. The base flow is superimposed by not more than one dominant coherent fluctuation. The influence of all other coherent structures can be neglected.
3. Gas properties, namely the specific gas constant, R_s , the heat capacities, c_v and c_p , the isotropic exponent γ , the heat conductivity, k , and the dynamic viscosity, μ , are constant.
4. The Reynolds average of the pressure is spatially constant (constant pressure combustion)
5. Low Mach number

Assumptions 3,4 and 5 are important in non-uniform density flows due to the presence of a flame and are not needed if the inhomogeneity of the density can be neglected. The assumptions listed above yield non-dimensional variations of the momentum, continuity and energy equations (for a rigorous derivation see Chapter B in the Appendix):

$$\rho^* \left(\frac{\partial \mathbf{u}^*}{\partial t^*} + (\mathbf{u}^* \cdot \nabla^*) \mathbf{u}^* \right) = -\nabla^* p^* + \frac{1}{\text{Re}} \left(\Delta \mathbf{u}^* + \frac{1}{3} \nabla^* (\nabla^* \cdot \mathbf{u}^*) \right) \quad (5.1.2)$$

$$\frac{\partial \rho^*}{\partial t^*} + \nabla^* \cdot (\rho^* \mathbf{u}^*) = 0 \quad (5.1.3)$$

$$\rho^{*3} \nabla^* \cdot \mathbf{u}^* = \frac{1}{\text{Re Pr}} (2 \nabla^* \rho^* \cdot \nabla^* \rho^* - \rho^* \Delta^* \rho^*) + \Phi^*. \quad (5.1.4)$$

Here, the dimensionless quantities are the Reynolds number with respect to the reference values chosen in Eqns. (5.1),

$$\text{Re} = \frac{U_{\text{ref}} D_{\text{ref}}}{\nu_{\text{ref}}} = \frac{U_{\text{ref}} D_{\text{ref}} \rho_{\text{ref}}}{\mu}, \quad (5.1.5)$$

and the corresponding Prandtl number,

$$\text{Pr} = \frac{c_p \mu}{k}. \quad (5.1.6)$$

Note that in the energy equation the time derivatives have vanished. This is due to assumptions 4 and 5. For details see the comprehensive derivation in Appendix B. In LSA or the approach of small perturbations, velocity, pressure and density are written as a temporal average and a fluctuating part. This study follows the triple decomposition suggested by Hussain et al. [100, 99] and Reynolds et al. [202]. They divide the fluctuating part in a coherent component and in a stochastic part:

$$\mathbf{u}^* = \overline{\mathbf{u}^*} + \widehat{\epsilon \mathbf{u}^*} + \mathbf{u}'', \quad (5.1.7a)$$

$$p^* = \overline{p^*} + \widehat{\epsilon p^*} + p'', \quad (5.1.7b)$$

$$\rho^* = \overline{\rho^*} + \widehat{\epsilon \rho^*} + \rho''. \quad (5.1.7c)$$

The temporal average marked by the superscript overbar is the Reynolds average given by

$$\overline{\Phi} = \frac{1}{T} \int_0^T \Phi dt. \quad (5.1.8)$$

The arch superscript and apostrophe stand for the coherent and stochastic contributions, respectively. While the stochastic fluctuations are supposed to be significant even at zero order, the coherent fluctuations are supposed to be small. This is taken into account by the factor ϵ , which represents a very small number. The temporal means of velocity and density can be either based on a flow at the limit cycle (see e.g. Barkley [11]) or at a transient state (e.g. Stöhr et al. [234]). Depending on the purpose of the analysis, these base flows can be provided by either analytic profiles (e.g. the Batchelor vortex [13, 125, 59]) or by experimental measurements or numerical simulations. The goal is to estimate the temporal and/or spatial behavior of the coherent perturbations superimposing the base flow. Note that the amount of unknown eigenfunctions corresponds to the number of equations which are provided.

5.1.1 Coherent Structures in Uniform Density Flows

In many flows density is nearly constant so that changes in ρ can be neglected. In this case, the density is equal to its Reynolds average:

$$\rho^* = \overline{\rho^*} = \rho_{\text{ref}}. \quad (5.1.9)$$

Since the coherent fluctuation of density, $\widehat{\rho}$, is 0 (in the low Mach number limit), the amount of unknowns is reduced by one. Here, the equation of energy therefore is omitted, and the coherent fluctuations of velocity and pressure are found by solving the continuity and momentum equations alone. These then simplify to:

$$\left(\frac{\partial \mathbf{u}^*}{\partial t^*} + (\mathbf{u}^* \cdot \nabla^*) \mathbf{u}^* \right) = -\nabla^* p^* + \frac{1}{\text{Re}} \Delta^* \mathbf{u}^*, \quad (5.1.10)$$

$$\nabla^* \cdot \mathbf{u}^* = 0. \quad (5.1.11)$$

Inserting Eqns. (5.1.7a) and (5.1.7b), neglecting terms of second and higher order and subtracting the temporal average of the resulting equation from its phase average yields

$$\frac{\partial \widehat{\mathbf{u}}^*}{\partial t^*} + (\overline{\mathbf{u}^*} \cdot \nabla^*) \widehat{\mathbf{u}}^* + (\widehat{\mathbf{u}^*} \cdot \nabla^*) \overline{\mathbf{u}^*} + \langle (\mathbf{u}^{*'} \cdot \nabla^*) \mathbf{u}^{*'} \rangle - \overline{(\mathbf{u}^{*'} \cdot \nabla^*) \mathbf{u}^{*'}} = -\nabla^* \widehat{p}^* + \frac{1}{\text{Re}} \Delta^* \widehat{\mathbf{u}}^*. \quad (5.1.12)$$

$$\nabla^* \cdot \widehat{\mathbf{u}}^* = 0. \quad (5.1.13)$$

The angle brackets denote a phase average with respect to the period, T , of a perturbation, defined as:

$$\langle \Phi \rangle (\tau) = \frac{1}{n} \sum_{i=0}^{n-1} \Phi(\tau + iT), \tau \in [0; T[. \quad (5.1.14)$$

While the temporal average of the product of both the mean properties and the coherent properties with the stochastic fluctuations is equal to zero, it can be shown that the temporal mean of a product of two stochastic fluctuations is not equal to zero. This leads to the 5th term in Eqn. (5.1.12), which arises from the non linear term in Eqn. (5.1.10). The term represents the Reynolds stresses known from the RANS equations. The fourth term is the equivalent arising from the phase average of the equations. As Reynolds and Hussein [202] comment, the fourth and fifth term together can be understood as the change in Reynolds stresses during a period of the coherent fluctuation. Like the governing equations of RANS and LES, the set of Eqns. (5.1.12) and (5.1.13) pose an unclosed system of equations. In many studies these terms are simply ignored. However, solving the equations directly, i.e. assuming that the only viscous dampening is due to the laminar viscosity, gives rise to both nonphysical oscillations and - judging from their mode shapes - apparently physical oscillations, which however do not occur in the time resolved flow. This problem is often solved by adding a random value to the viscosity, resulting in a significant artificial decrease of the Reynolds number (e.g. [126, 37]). This way, spurious modes and typically also potentially physical modes are filtered out. For a perturbation at a constant limit cycle for example, this procedure can be applied by decreasing the Reynolds number until the growth rate of the perturbation under investigation is equal to zero.

Other authors make use of the Boussinesq approximation to model terms 4 and 5 in Eqn. (5.1.12) and therefore the influence of stochastic coherent interaction, which in Einstein notation is given by

$$-\overline{u'_i u'_j} = -\frac{2}{3}K\delta_{ij} + \nu_t \left(\frac{\partial \overline{u}_i}{\partial x_j} + \frac{\partial \overline{u}_j}{\partial x_i} \right), \quad (5.1.15)$$

with the turbulent kinetic energy, K , and the Kronecker delta, $\delta_{i,j}$. Unlike in RANS, here both the temporal mean flow (at the limit cycle) and the fluctuations thereon are known. Hence the product terms of the velocity fluctuations can be calculated and Eqn. (5.1.15) is solved for the eddy viscosity. Since this yields 6 independent eddy viscosities, one for each independent entry in the Reynolds stress tensor, a least mean square approach of all Reynolds stresses is applied which yields [102]:

$$\nu_e = \frac{\left(-\overline{u'_i u'_j} + \frac{2}{3}K\delta_{ij} \right) \cdot \left(\frac{\partial \overline{u}_j}{\partial x_i} + \frac{\partial \overline{u}_i}{\partial x_j} \right)}{\left(\frac{\partial \overline{u}_k}{\partial x_l} + \frac{\partial \overline{u}_l}{\partial x_k} \right) \cdot \left(\frac{\partial \overline{u}_k}{\partial x_l} + \frac{\partial \overline{u}_l}{\partial x_k} \right)}, \quad (5.1.16)$$

All hydrodynamic LSA conducted in the framework of this thesis is performed on base flows provided by LES. Additionally to the molecular viscosity, which is a material property, and the eddy viscosity based on the stochastic fluctuations which are resolved by the simulation, there is also an LES-subgrid viscosity, which models the interaction of the subgrid scale turbulence on the resolved flow. It is assumed here, that these three components add up to the effective viscosity yielding an effective Reynolds number of

$$\text{Re}_{\text{eff}} = \frac{U_{\text{ref}} D_{\text{ref}}}{\nu_e + \nu_{\text{LES}} + \nu_{\text{m}}}. \quad (5.1.17)$$

If not mentioned otherwise, all calculations in the framework of this thesis are based on this Reynolds number.

5.1.2 Coherent Structures in Non-Uniform Density Flows

In some laminar flows, coherent structures occur in the absence of stochastic fluctuations. One example for flows behaving in this way is once more the cylinder wake flow. At the critical Reynolds number of approximately $\text{Re}_c \approx 46$ a supercritical Hopf bifurcation to the von Kármán vortex street occurs [103, 196]. Despite the unsteady behavior, the flow remains laminar until another three dimensional mode (often described as *Mode A*) becomes unstable and stochastic fluctuations therefore occur. The Reynolds number at which this occurs differs both for experiments (see the Reviews of Roshko [205], $\text{Re} \approx 180$ and Williamson [261] $\text{Re} = 140 - 194$) and DNS ($\text{Re} \approx 200$ [247]). In several other studies of hydrodynamic stability, it is simply assumed that stochastic-coherent interaction is weak and the effect is neglected. In relation to flames these assumptions are valid for laminar flames, where turbulence levels are

low. In these cases it is sufficient to decompose the properties of state into a temporal mean and a coherent fluctuation instead of performing the a triple decomposition. Most practical flames however are highly turbulent and the impact of stochastic fluctuations on both the mean flow and also the coherent structures cannot be neglected.

However, it is well known from the RANS framework, that temporal averaging of the compressible Navier-Stokes equations leads to a large number of additional product terms including the fluctuation of density, ρ' , which remain in the averaged equations. Splitting the equations in a Reynolds average, a coherent part and a stochastic fluctuation as in Section 5.1.1 leads to the same problem when deriving the governing equations of hydrodynamic stability analysis of non uniform density flows. For the governing equations of the mean flow quantities this problem is most often solved by introducing a Favre average for velocity and temperature fluctuations:

$$\mathbf{u} = \tilde{\mathbf{u}} + \mathbf{u}'' \quad (5.1.18)$$

When deriving the governing equations of hydrodynamic stability applying the corresponding technique for the fluctuating quantities yields non zero terms in the phase averages of first order and therefore this technique is not applicable.

At this point, the effect of the additional not vanishing non-linear terms including the fluctuation of density, ρ' , in the first order equations remains an open question. In this thesis, it will be assumed that they are negligible in comparison with the stochastic fluctuations, which are modeled by Eqn. (5.1.16). Therefore, an effective Reynolds number is further on applied, based on the model discussed in Section 5.1.1, and the LSA is performed on a temporally averaged base flow. In the following the resulting equations of LSA of base flows with non-homogeneous density will be briefly discussed. A thorough derivation can be found in Appendix B

If stochastic fluctuations cannot be neglected, the triple decomposition must be applied (see Eqn. (5.1)). Inserting these equations into the Navier-Stokes, continuity and energy equations (Eqns. (5.1.2)–(5.1.4)), neglecting terms of second and higher order, performing both a temporal and a phase average on the equations and assuming that the flow velocity is low in comparison with the speed of sound, yields

$$\begin{aligned} & \overline{\rho^*} \left(\frac{\partial \widehat{\mathbf{u}}^*}{\partial t^*} + (\widehat{\mathbf{u}}^* \cdot \nabla^*) \overline{\mathbf{u}}^* + (\overline{\mathbf{u}}^* \cdot \nabla^*) \widehat{\mathbf{u}}^* \right) + \widehat{\rho^*} (\overline{\mathbf{u}}^* \cdot \nabla^*) \overline{\mathbf{u}}^* \\ & + \langle (\rho^* \mathbf{u}^{*'} \cdot \nabla^*) \mathbf{u}^{*'} \rangle - \overline{(\rho^* \mathbf{u}^{*'} \cdot \nabla^*) \mathbf{u}^{*'}} = -\gamma \nabla^* \widehat{p^*} + \frac{1}{\text{Re}} \left(\Delta^* \widehat{\mathbf{u}}^* + \frac{1}{3} \nabla^* (\nabla^* \cdot \widehat{\mathbf{u}}^*) \right), \end{aligned} \quad (5.1.19)$$

$$\frac{\partial \widehat{\rho^*}}{\partial t^*} + \nabla^* \widehat{\rho^*} \cdot \overline{\mathbf{u}}^* + \nabla^* \overline{\rho^*} \cdot \widehat{\mathbf{u}}^* + \overline{\rho^*} (\nabla^* \cdot \widehat{\mathbf{u}}^*) + \widehat{\rho^*} (\nabla^* \cdot \overline{\mathbf{u}}^*) = 0, \quad (5.1.20)$$

$$\begin{aligned} \overline{\rho^*}^3 \nabla^* \cdot \widehat{\mathbf{u}^*} + 3\overline{\rho^*}^2 \widehat{\rho^*} \nabla^* \cdot \overline{\mathbf{u}^*} + \frac{1}{\text{RePr}} \left(\overline{\rho^*} \Delta^* \widehat{\rho^*} + \widehat{\rho^*} \Delta^* \overline{\rho^*} - 4\nabla^* \widehat{\rho^*} \nabla^* \overline{\rho^*} \right) \\ + \langle \nabla^* \cdot (\rho^* T^{*'} \mathbf{u}^{*'}) \rangle - \overline{\nabla^* \cdot (\rho^* T^{*'} \mathbf{u}^{*'})} = 0. \end{aligned} \quad (5.1.21)$$

The last two terms on the LHS in Eqns. (5.1.19) and (5.1.21) arise from the non linear terms in the momentum and the energy equations. In the momentum equation they are modeled analogously to Section 5.1.1 by a contribution to the viscosity, leading to a decrease of the effective Reynolds number (see Eqn. (5.1.1)). The corresponding terms in the energy equation remain still to be modeled. In RANS and LES the respective terms are modeled by a turbulent Prandtl number (see Section 4.2). This approach is followed here, and the effective Prandtl number is set to

$$\text{Pr}_{\text{eff}} = 0.9, \quad (5.1.22)$$

which corresponds to a value often used in literature. The equations above describe the linear hydrodynamics, while taking into account a non-uniform mean density field, caused by an inhomogeneous temperature. Note however that in the case of reactive flows the reaction of the flame to flow perturbations (and *vice versa*) is not considered here, which is analogous to the passive flame approach in thermoacoustics (see e.g. Silva et al. [225] and Nicoud et al. [167]).

5.2 Solution Approaches in Hydrodynamic Stability Analysis

In modal analysis, perturbations of a dynamic system are supposed to be harmonic fluctuations, related to a certain mode shape and a growth or dampening rate. This method is applied in many fields of physics, including structural vibrations in solid mechanics[84], radiation of electromagnetics in conducting objects, or acoustics in compressible gases [185]. Assuming that the fluctuations are harmonic, the underlying equations are transformed into an eigenvalue problem. In the examples mentioned above, solving the eigenvalue problem, yields eigenvectors, which represent the mode shapes and eigenvalues which yield information about the perturbations frequency and growth or dampening rates.

This method is also applied in linear stability analysis of hydrodynamics. For brevity, all the in the following presented equations are based on the equations for hydrodynamic instabilities in non-uniform density flows (Eqns. (5.1.19–5.1.21)). For a thorough derivation of all the equations, see Section B in the Appendix. Inserting the modal approach

$$[\widehat{\mathbf{u}^*}(x, y, z), \widehat{p^*}(x, y, z), \widehat{\rho^*}(x, y, z)] = [\widehat{\mathbf{U}^*}(x, y, z), \widehat{P^*}(x, y, z), \widehat{\Psi^*}(x, y, z)] \exp(i\omega t) \quad (5.2.1)$$

into the set of Eqns. (5.1.19–5.1.21) yields the equations for three dimensional harmonic perturbations $\widehat{\mathbf{U}}^*(x, y, z)$, $\widehat{P}^*(x, y, z)$ and $\widehat{\Psi}^*(x, y, z)$ on a base flow given by $\overline{\mathbf{u}}^*(x, y, z)$, $\overline{p}^*(x, y, z)$ and $\overline{\rho}^*(x, y, z)$:

$$\begin{aligned} & \overline{\rho}^* \left(i\omega \widehat{\mathbf{U}}^* + (\widehat{\mathbf{U}}^* \cdot \nabla^*) \overline{\mathbf{u}}^* + (\overline{\mathbf{u}}^* \cdot \nabla^*) \widehat{\mathbf{U}}^* \right) + \widehat{\Psi}^* (\overline{\mathbf{u}}^* \cdot \nabla^*) \overline{\mathbf{u}}^* \\ & = -\gamma \nabla^* \widehat{P}^* + \frac{1}{\text{Re}_{\text{eff}}} \left(\Delta^* \widehat{\mathbf{U}}^* + \frac{1}{3} \nabla^* (\nabla^* \cdot \widehat{\mathbf{U}}^*) \right), \end{aligned} \quad (5.2.2)$$

$$i\omega \widehat{\Psi}^* + \nabla^* \widehat{\Psi}^* \cdot \overline{\mathbf{u}}^* + \nabla^* \overline{\rho}^* \cdot \widehat{\mathbf{U}}^* + \overline{\rho}^* (\nabla^* \cdot \widehat{\mathbf{U}}^*) + \widehat{\Psi}^* (\nabla^* \cdot \overline{\mathbf{u}}^*) = 0, \quad (5.2.3)$$

$$\overline{\rho}^{*3} \nabla^* \cdot \widehat{\mathbf{U}}^* + 3\overline{\rho}^{*2} \widehat{\Psi}^* \nabla^* \cdot \overline{\mathbf{u}}^* + \frac{1}{\text{Re}_{\text{eff}} \text{Pr}_{\text{eff}}} \left(\overline{\rho}^* \Delta^* \widehat{\Psi}^* + \widehat{\Psi}^* \Delta^* \overline{\rho}^* - 4\nabla^* \widehat{\Psi}^* \nabla^* \overline{\rho}^* \right) = 0. \quad (5.2.4)$$

The equations pose a complex Generalized Eigenvalue Problem (GEVP) of form

$$\mathbf{A}\Phi = \lambda\mathbf{B}\Phi, \quad (5.2.5)$$

where the eigenvalue λ is the temporal frequency ω and the eigenvector is $\Phi = [\widehat{\mathbf{U}}^*(x, y, z), \widehat{P}^*(x, y, z), \widehat{\Psi}^*(x, y, z)]$. Note that in general the eigenfrequency ω is complex. Its real part is the harmonic frequency of the perturbation in time, while its imaginary part corresponds to the temporal growth rate.

5.2.1 BiGlobal Stability Analysis for Swirling Jets

The set of Eqns. (5.2.2–5.2.4) governing the temporal evolution of three dimensional perturbations on a base flow pose a very large eigenvalue problem. Many hydrodynamic instabilities nevertheless are two dimensional, for example the Kelvin-Helmholtz instability in shear layers [255, 228] or the von Kármán vortex street [256]. For these cases the set of equations can be reduced to two dimensions resulting in a considerable diminution in computational effort to solve the problem. In other flows the base flow is two-dimensional, but the perturbations are three dimensional. One example for these kind of flows is the PVC in an axisymmetric swirling jet undergoing vortex breakdown. In the following two different methods of reducing the number of spacial dimensions, which were used in the past for the investigations of PVCs in uniform density fields will be introduced.

5.2.1.1 BiGlobal Modal Approach

Introducing Eqn. (5.2.1) into the governing equations of hydrodynamic instabilities yielded a set of equations describing three dimensional perturbations in Cartesian coordinates. In the BiGlobal approach for swirling jet flows, the equations are expressed in cylindrical coordinates and two assumptions lead to a reduction of the number of spacial dimensions:

1. The base flow is only a function of the axial coordinate, z , and the radial coordinate r . It therefore is homogeneous in azimuthal direction, θ and all derivatives of the base flow in azimuthal direction disappear: $\frac{\partial \bar{\mathbf{u}}}{\partial \theta} = 0$. This assumption is valid for most configurations.
2. The perturbations are harmonic in azimuthal direction.

The second assumption yields the BiGlobal modal approach given by

$$[\widehat{\mathbf{u}}^*(r, \theta, z), \widehat{p}^*(r, \theta, z), \widehat{\rho}^*(r, \theta, z)] = [\widehat{\mathbf{U}}^*(r, z), \widehat{P}^*(r, z), \widehat{\Psi}^*(r, z)] \exp(-i\omega t^* + im\theta). \quad (5.2.6)$$

Here, m is the azimuthal wave number, where $m = 0$ corresponds to a rotational symmetric instability (e.g. the Kelvin-Helmholtz instability in circular jet flows). An one armed PVC however is attributed to an azimuthal wave number, $m = 1$, a two armed PVC to $m = 2$ and so on.

Inserting Eqn. (5.2.6) into Eqns. (5.1.19–5.1.21) yields the equations governing the evolution of perturbations on a rotational symmetric mean flow in cylindrical coordinates. These are given by the perturbation's energy equation,

$$\begin{aligned} & \bar{\rho}^{*3} \left(\frac{\partial \widehat{U}_r^*}{\partial r^*} + \frac{\widehat{U}_r^*}{r^*} + \frac{im}{r^*} \widehat{U}_\theta^* + \frac{\partial \widehat{U}_z^*}{\partial z^*} \right) + 3\bar{\rho}^{*2} \widehat{\Psi}^* \left(\frac{\partial \bar{u}_r^*}{\partial r^*} + \frac{\bar{u}_r^*}{r^*} + \frac{\partial \bar{u}_z^*}{\partial z^*} \right) \\ & + \frac{1}{\text{Re}_{\text{eff}} \text{Pr}_{\text{eff}}} \left(\bar{\rho}^* \left(\frac{\partial^2 \widehat{\Psi}^*}{\partial r^{*2}} + \frac{1}{r^*} \frac{\partial \widehat{\Psi}^*}{\partial r^*} - \frac{m^2}{r^{*2}} \widehat{\rho}^* + \frac{\partial^2 \widehat{\Psi}^*}{\partial z^{*2}} \right) + \widehat{\Psi}^* \left(\frac{\partial^2 \bar{\rho}^*}{\partial r^{*2}} + \frac{1}{r^*} \frac{\partial \bar{\rho}^*}{\partial r^*} + \frac{\partial^2 \bar{\rho}^*}{\partial z^{*2}} \right) \right. \\ & \left. - 4 \left(\frac{\partial \widehat{\Psi}^*}{\partial r^*} \frac{\partial \bar{\rho}^*}{\partial r^*} + \frac{\partial \widehat{\Psi}^*}{\partial z^*} \frac{\partial \bar{\rho}^*}{\partial z^*} \right) \right) = 0, \end{aligned} \quad (5.2.7)$$

their continuity equation,

$$\begin{aligned} & -i\omega^* \widehat{\Psi}^* + \frac{\partial \widehat{\Psi}^*}{\partial r^*} \bar{u}_r^* + \frac{im \widehat{\Psi}^*}{r^*} \bar{u}_\theta^* + \frac{\partial \widehat{\Psi}^*}{\partial z^*} \bar{u}_z^* + \frac{\partial \bar{\rho}^*}{\partial r^*} \widehat{U}_r^* + \frac{\partial \bar{\rho}^*}{\partial z^*} \widehat{U}_z^* + \widehat{\Psi}^* \left(\frac{\partial \bar{u}_r^*}{\partial r^*} + \frac{\bar{u}_r^*}{r^*} + \frac{\partial \bar{u}_z^*}{\partial z^*} \right) \\ & + \bar{\rho}^* \left(\frac{\partial \widehat{U}_r^*}{\partial r^*} + \frac{\widehat{U}_r^*}{r^*} + \frac{im}{r^*} \widehat{U}_\theta^* + \frac{\partial \widehat{U}_z^*}{\partial z^*} \right) = 0, \end{aligned} \quad (5.2.8)$$

and the momentum conservation equation of the perturbation in radial direction

$$\begin{aligned}
 & \boxed{\overline{\rho}^*} \left(-i\omega^* \widehat{U}_r^* + \overline{u}_r^* \frac{\partial \widehat{U}_r^*}{\partial r^*} + \frac{im\overline{u}_\theta^* \widehat{U}_r^*}{r^*} + \overline{u}_z^* \frac{\partial \widehat{U}_r^*}{\partial z^*} - \frac{2\overline{u}_\theta^* \widehat{U}_\theta^*}{r^*} + \widehat{U}_r^* \frac{\partial \overline{u}_r^*}{\partial r^*} + \widehat{U}_z^* \frac{\partial \overline{u}_r^*}{\partial z^*} \right) \\
 & \quad + \boxed{\widehat{\rho}^*} \left(\overline{u}_r^* \frac{\partial \overline{u}_r^*}{\partial r^*} + \overline{u}_z^* \frac{\partial \overline{u}_r^*}{\partial z^*} - \frac{\overline{u}_\theta^{*2}}{r^*} \right) + \frac{\partial \widehat{p}^*}{\partial r^*} \\
 & \quad - \frac{1}{\text{Re}_{\text{eff}}} \left(\frac{\partial^2 \widehat{U}_r^*}{\partial r^{*2}} + \frac{1}{r^*} \frac{\partial \widehat{U}_r^*}{\partial r^*} - \frac{m^2 \widehat{U}_r^*}{r^{*2}} + \frac{\partial^2 \widehat{U}_r^*}{\partial z^{*2}} - \frac{\widehat{U}_r^*}{r^{*2}} - \frac{2im\widehat{U}_\theta^*}{r^{*2}} \right. \\
 & \quad \left. + \frac{1}{3} \left(\frac{\partial^2 \widehat{U}_r^*}{\partial r^{*2}} + \frac{1}{r^*} \frac{\partial \widehat{U}_r^*}{\partial r^*} - \frac{\widehat{U}_r^*}{r^{*2}} + \frac{im}{r^*} \frac{\partial \widehat{U}_\theta^*}{\partial r^*} - \frac{im\widehat{U}_\theta^*}{r^{*2}} + \frac{\partial^2 \widehat{u}_z^*}{\partial r^* \partial z^*} \right) \right) = 0,
 \end{aligned} \tag{5.2.9}$$

in azimuthal direction,

$$\begin{aligned}
 & \boxed{\overline{\rho}^*} \left(-i\omega^* \widehat{U}_\theta^* + \overline{u}_r^* \frac{\partial \widehat{U}_\theta^*}{\partial r^*} + \frac{im\overline{u}_\theta^* \widehat{U}_\theta^*}{r^*} + \overline{u}_z^* \frac{\partial \widehat{U}_\theta^*}{\partial z^*} + \frac{\overline{u}_\theta^* \widehat{U}_r^*}{r^*} + \widehat{U}_r^* \frac{\partial \overline{u}_\theta^*}{\partial r^*} + \widehat{U}_z^* \frac{\partial \overline{u}_\theta^*}{\partial z^*} + \frac{\widehat{U}_\theta^* \overline{u}_r^*}{r^*} \right) \\
 & \quad + \boxed{\widehat{\rho}^*} \left(\overline{u}_r^* \frac{\partial \overline{u}_\theta^*}{\partial r^*} + \overline{u}_z^* \frac{\partial \overline{u}_\theta^*}{\partial z^*} + \frac{\overline{u}_\theta^* \overline{u}_r^*}{r^*} \right) + \frac{im\widehat{p}^*}{r^*} \\
 & \quad - \frac{1}{\text{Re}_{\text{eff}}} \left(\frac{\partial^2 \widehat{U}_\theta^*}{\partial r^{*2}} + \frac{1}{r^*} \frac{\partial \widehat{U}_\theta^*}{\partial r^*} - \frac{m^2 \widehat{U}_\theta^*}{r^{*2}} + \frac{\partial^2 \widehat{U}_\theta^*}{\partial z^{*2}} - \frac{\widehat{U}_\theta^*}{r^{*2}} + \frac{2im\widehat{U}_r^*}{r^{*2}} \right. \\
 & \quad \left. + \frac{1}{3} \left(\frac{im}{r} \frac{\partial \widehat{U}_r^*}{\partial r^*} + \frac{im\widehat{U}_r^*}{r^{*2}} - \frac{m^2 \widehat{U}_\theta^*}{r^{*2}} + \frac{im}{r} \frac{\partial \widehat{U}_z^*}{\partial z^*} \right) \right) = 0,
 \end{aligned} \tag{5.2.10}$$

and in axial direction,

$$\begin{aligned}
 & + \boxed{\overline{\rho}^*} \left(-i\omega^* \widehat{U}_z^* + \overline{u}_r^* \frac{\partial \widehat{U}_z^*}{\partial r^*} + \frac{im\overline{u}_\theta^* \widehat{U}_z^*}{r^*} + \overline{u}_z^* \frac{\partial \widehat{U}_z^*}{\partial z^*} + \widehat{U}_r^* \frac{\partial \overline{u}_z^*}{\partial r^*} + \widehat{U}_z^* \frac{\partial \overline{u}_z^*}{\partial z^*} \right) \\
 & \quad + \boxed{\widehat{\Psi}^*} \left(\overline{u}_r^* \frac{\partial \overline{u}_z^*}{\partial r^*} + \overline{u}_z^* \frac{\partial \overline{u}_z^*}{\partial z^*} \right) + \frac{\partial \widehat{p}^*}{\partial z^*} \\
 & \quad - \frac{1}{\text{Re}_{\text{eff}}} \left(\frac{\partial^2 \widehat{U}_z^*}{\partial r^{*2}} + \frac{1}{r^*} \frac{\partial \widehat{U}_z^*}{\partial r^*} - \frac{m^2 \widehat{U}_z^*}{r^{*2}} + \frac{\partial^2 \widehat{U}_z^*}{\partial z^{*2}} \right. \\
 & \quad \left. + \frac{1}{3} \left(\frac{\partial^2 \widehat{U}_r^*}{\partial z^* \partial r^*} + \frac{1}{r^*} \frac{\partial \widehat{U}_r^*}{\partial z^*} + \frac{im}{r^*} \frac{\partial \widehat{U}_\theta^*}{\partial z^*} + \frac{\partial^2 \widehat{U}_z^*}{\partial z^{*2}} \right) \right) = 0.
 \end{aligned} \tag{5.2.11}$$

In the case of uniform density, the terms marked by vanish and the remaining terms in Eqns. (5.2.8–5.2.11) yield the equations describing the dynamics of the perturbation. Note that due to assuming base flow homogeneity and perturbation periodicity in azimuthal direction all dependencies on θ have vanished in this set of equations. Therefore, its integration in azimuthal direction is performed analytically by a multiplication with $2\pi r$. Consequentially, a numerical integration remains to be performed in the r - z plane only.

5.2.1.2 Solving BiGlobal Analysis with the Finite Element Method

In order to arrive at the GEVP, the linear operators A and B have to be formed by spatially integrating the set of Eqns. (5.2.7–5.2.11). In principle this can be done by countless different numerical methods. In the past, preferably high order schemes were used like the Chebychev-Collocation (e.g. Ehrenstein and Gallaire [64] and Åkverik et al. [4]). Paredes et al.[178] showed that Finite Difference Methods with uniform error (short FD-q method) are highly efficient in addressing the problem of hydrodynamic stability. A significant drawback of these methods on the other hand is the restriction to a structured grid, which obstructs the application in complex geometries, like industrial burners. In this study the integration is therefore performed by the Finite Element Method (FEM). This method is used in multiple fields of engineering and natural sciences. These reach from structural mechanics [68, 207], over investigations on earthquakes [251] to transport phenomena in fluid mechanics. In the recent years, the method has been also applied to global hydrodynamic stability analysis [227, 242, 240, 37]. A thorough description of the finite element method goes far beyond the scope of this thesis. Therefore, this section is restricted to illustrate the principles of the method. The interested reader is referred to Becker, Carey and Oden [15] for a compact introduction to the topic and Zienkiewicz and Taylor [264, 265, 266] for a comprehensive summary.

Unlike in the finite difference method, where the exact solution is approximated on discrete points only, in FEM the domain is divided in M small elements indexed by j , which often for convenience are triangle shaped in two dimensional domains. Within these elements the solution, u , is approximated by the sum of the product of the so called shape functions, which are polynomials of N th order, Φ_i , with a coefficient α_i :

$$u = \sum_{i=1}^N \alpha_i \Phi_i. \quad (5.2.12)$$

The number of polynomials per element depends on the order of the polynomials and the shape of the element. Applying Gauss-integration, a local linear operator for the coefficients α_i is determined for every element, j , based on the problem which is to be solved (e.g. in the case of a GEVP the element matrices A_j and B_j). One strength of the method is that the resulting M local linear operators can be easily combined to yield the global linear operators (A and B) for the entire domain. Finally, it is a matter of linear algebra to solve the problem, in this case the GEVP.

The software FreeFEM++ [92] was used to arrange the linear global operators, which operates based on triangular meshes in two dimensions and tetraedrons in three dimensions. For the subsequent solution of the GEVP the shift and invert method is applied with aid of software package ARPACK [123]/UMFPACK. UMFPACK solves the GEVP using the unsymmetric-pattern multifrontal method which is specialized on the lower-upper factorization of sparse matrices [50, 49]. When treating incompressible problems like structural mechanics [265] or the incompressible Navier-Stokes equations [265] with the FEM, it is well known, that the problem is ill posed if the order of shape functions for both velocity and pressure is equal. The order of shape functions for the velocity components and density is therefore chosen as 2, while the shape functions for the pressure are of first order.

Furthermore, BCs have to be applied on the boundaries. Assuming that they are sufficiently far from the instability, it is assumed that all perturbations fulfill Dirichlet conditions at all inlets and outlets. Walls are supposed to be no-slip, leading to homogeneous Dirichlet BCs for the velocity components and homogeneous Neumann conditions for pressure and density at the walls. Due to the singularity at $r = 0$, estimation of the corresponding BCs at the axis is not as trivial. Depending on the azimuthal wave number m , three different cases exist for the fluctuation of velocities and pressure [113]:

1. $m = 0$:

$$\widehat{U}_r^*(r = 0) = \widehat{U}_\theta^*(r = 0) = 0,$$

$$\widehat{U}_z^*(r = 0) \text{ and } \widehat{P}^*(r = 0) \text{ are finite.}$$

2. $m = \pm 1$:

$$\widehat{U}_z^*(r = 0) = \widehat{P}^*(r = 0) = 0,$$

$$\widehat{U}_r^*(r = 0) \pm \widehat{U}_\theta^*(r = 0) = 0,$$

$$2 \frac{\partial \widehat{U}_r^*}{\partial r}(r = 0) \pm i \frac{\partial \widehat{U}_\theta^*}{\partial r}(r = 0) = 0.$$

3. $|m| > 1$:

$$\widehat{U}_r^*(r = 0) = \widehat{U}_\theta^*(r = 0) = \widehat{U}_z^*(r = 0) = \widehat{P}^*(r = 0) = 0.$$

Finally, a BC for the density perturbation must be formulated. For reasons of symmetry, the density perturbation must be zero at the axis [143]. At inlets and outlets, the density perturbations vanish and at the walls homogeneous Neumann conditions are assumed. The resulting BCs for an azimuthal wave number of $m = 1$ is summarized in Tab. 5.1.

Inlet	Outlet	Wall	Axis
$\widehat{U}_r^* = 0$	$\widehat{U}_r^* = 0$	$\widehat{U}_r^* = 0$	$\widehat{U}_r^* + \widehat{U}_\theta^* = 0$
$\widehat{U}_\theta^* = 0$	$\widehat{U}_\theta^* = 0$	$\widehat{U}_\theta^* = 0$	$2\frac{\partial \widehat{U}_r^*}{\partial r} + i\frac{\partial \widehat{U}_\theta^*}{\partial r} = 0$
$\widehat{U}_z^* = 0$	$\widehat{U}_z^* = 0$	$\widehat{U}_z^* = 0$	$\widehat{U}_z^* = 0$
$\widehat{P}^* = 0$	$\widehat{P}^* = 0$	$\frac{\partial \widehat{P}^*}{\partial \mathbf{n}} = 0$	$\widehat{P}^* = 0$
$\widehat{\Psi}^* = 0$	$\widehat{\Psi}^* = 0$	$\frac{\partial \widehat{\Psi}^*}{\partial \mathbf{n}} = 0$	$\widehat{\Psi}^* = 0$

Table 5.1: BCs for LSA in case of $m = 1$; \mathbf{n} is the normal vector of the boundary.

5.2.1.3 Adjoint Modes and Structural Sensitivity

Adjoint analysis takes advantage of the adjoint equations in order to estimate the influence of a certain parameter in the equation on its solutions. It is considered a highly efficient method of optimization and sensitivity studies [67]. It has been and is increasingly applied in multiple fields of science [138]. Among those are meteorology [128, 243], nuclear reactor physics [181], seismic tomography [249], adaptive mesh refinement [129], shape optimization [82] and thermoacoustics [106, 140]. A pedagogical introduction to the topic is provided by Errico [67].

In recent years, the method has also been applied in the context of hydrodynamic stability analysis (e.g. Luchini et al. [137, 139], Giannetti and Luchini [83] Chandler et al. [30] and Tammissola and Juniper [241, 240]). A review of the method in this framework is provided by Luchini and Bottaro [138].

For every right GEVP like stated in Eqn. (5.2.5), a left GEVP of the form

$$\Phi^\dagger \mathbf{A} = \lambda^\dagger \Phi^\dagger \mathbf{B} \quad (5.2.13)$$

can be formulated. It can be shown that the left eigenvalues - or adjoint eigenvalues - (which are marked by the \dagger superscript) are either equal to the eigenvalues of the right GEVP or their complex conjugate [138]. The adjoint eigenvalues provide the most unstable initial condition [197] and therefore can be seen as a measure of the receptibility to external forcing [83]. In the context of sensitivity analysis to a given parameter, the change of the eigenvalue, $d\lambda$, due to the change of the LHS matrix in the GEVP due to the varying parameter, $d\mathbf{A}$, is related via the left and right eigenvalues by

$$d\lambda = \frac{\Phi^\dagger d\mathbf{A} \Phi}{\Phi^\dagger \mathbf{B} \Phi}. \quad (5.2.14)$$

Furthermore, the adjoint modes give information about the location of strongest internal feedback of a global mode. As described by Giannetti and Luchini [83], the structural

sensitivity, σ , of a global mode can be estimated as the normalized product of the velocity perturbations with the adjoint velocities:

$$\sigma = \frac{\|\hat{\mathbf{u}}^\dagger\| \|\hat{\mathbf{u}}\|}{\int \hat{\mathbf{u}}^\dagger \cdot \hat{\mathbf{u}} dS}. \quad (5.2.15)$$

Regions of high structural sensitivity and therefore high internal feedback can be seen as the origin of the global mode.

5.2.1.4 Validation of the BiGlobal stability code

The correct implementation of the BiGlobal strategy described above was tested by a reproduction of results, which were previously published in literature. Meliga et al. [154] investigated the stability of the laminar wake behind a sphere with respect to helical modes ($m = 1$). They found that for a Reynolds number of $Re = 280.7$ the wake becomes absolutely unstable to a helical mode. Their base flow for this Reynolds number was reproduced using FreeFEM++ (see Fig. 5.1) and a stability analysis was performed on the same base flow. Like Meliga et al. the respective mode is found pulsing at a frequency of $\omega = 0.669 + 0.000i$. The respective mode shapes are compared in Fig.5.2 to the mode shapes of Meliga et al. [154] showing very good agreement.

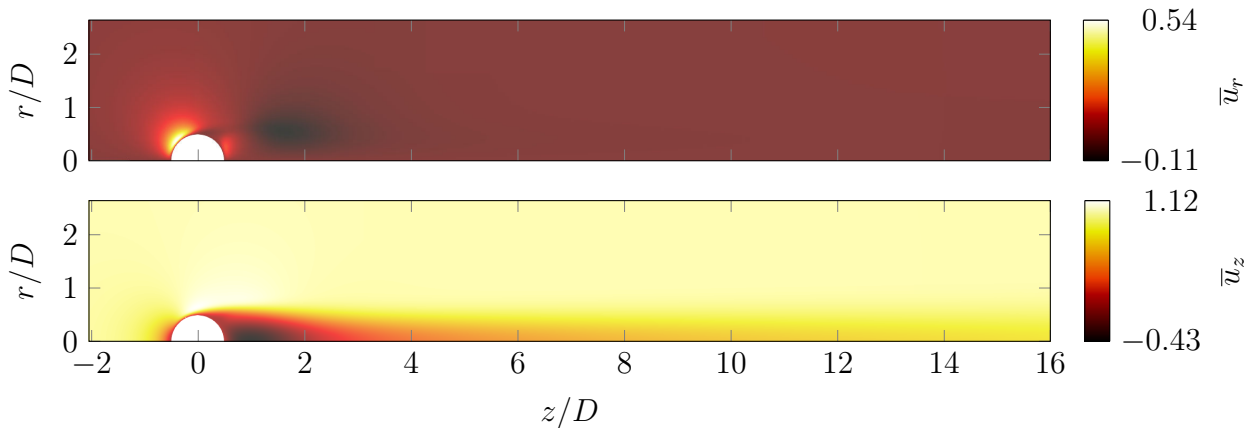
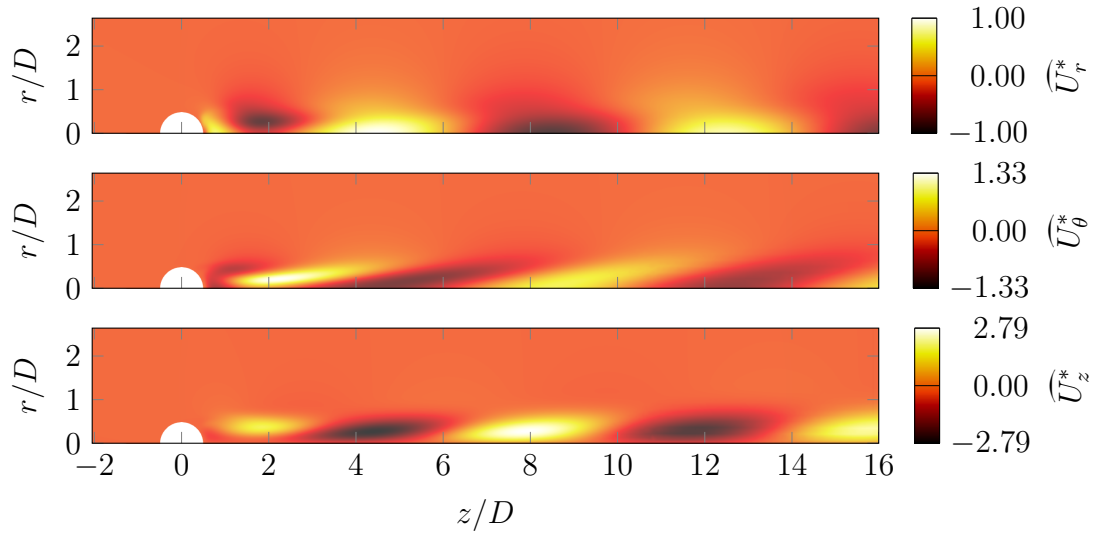
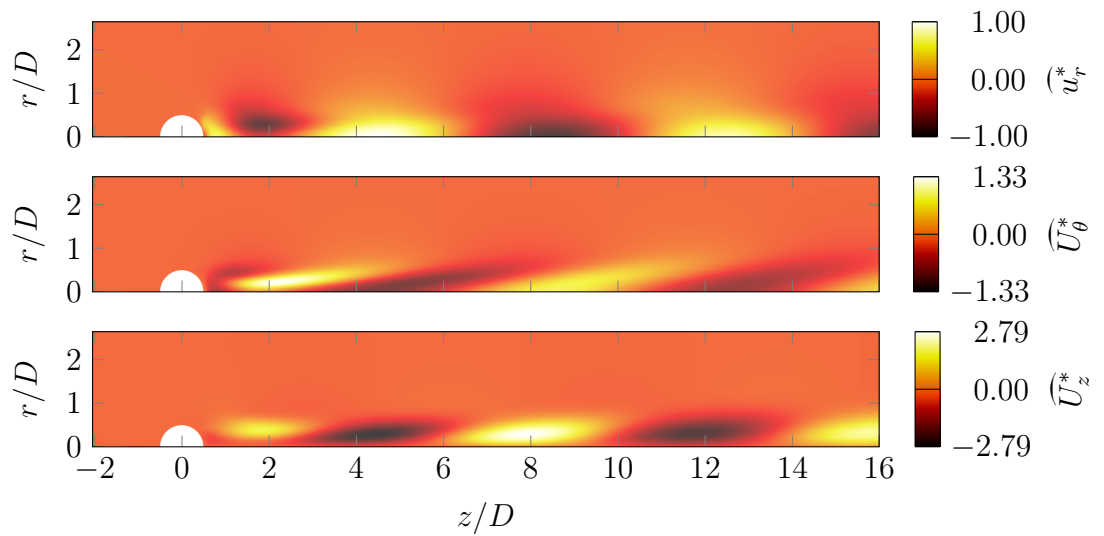


Figure 5.1: Validation of the BiGlobal code: Radial and axial velocity component of the laminar base flow around a sphere at $Re = 280.7$; Azimuthal velocity component is set to 0.



(a) Eigenfunctions based on Meliga et al. [154]



(b) Eigenfunctions based on BiGlobal stability code developed in the framework of this study

Figure 5.2: Validation of the BiGlobal code: Comparisons of eigenfunctions with results previously published in literature

5.2.2 Local Stability Analysis

5.2.2.1 Local Modal approach

So far the perturbations were assumed to be harmonic in time and in the case of BiGlobal stability analysis in azimuthal direction. In the case of local stability analysis additional assumptions are made:

1. The flow is sufficiently parallel. As a consequence both the derivative of all mean quantities with respect to the axial coordinate z and the radial velocity component are equal to zero¹:

$$\frac{\partial \widehat{\mathbf{U}}^*}{\partial x} = 0, \widehat{U}_r^* = 0. \quad (5.2.16)$$

2. The perturbations are harmonic in axial direction with the axial wave number, α^* .

The second additional assumption results in the modal approach of local stability analysis given by

$$[\widehat{\mathbf{u}}^*(r, \theta, z, t), \widehat{p}^*(r, \theta, z, t), \widehat{\rho}^*(r, \theta, z, t)] = [\widehat{\mathbf{U}}^*(r), \widehat{P}^*(r), \widehat{\Psi}^*(r)] \exp(-i\omega^*t^* + im\theta + i\alpha^*z^*) \quad (5.2.17)$$

As for the global analysis, this modal approach is inserted into Eqns. (5.1.19–5.1.21) yielding the equations for local LSA. The equations then read for the energy

$$\begin{aligned} \overline{\rho}^{*3} \left(\frac{\partial \widehat{U}_r^*}{\partial r^*} + \frac{\widehat{U}_r^*}{r^*} + \frac{im}{r^*} \widehat{U}_\theta^* + i\alpha^* \widehat{U}_z^* \right) + \frac{1}{\text{Re}_{\text{eff}} \text{Pr}_{\text{eff}}} \left(\overline{\rho}^* \left(\frac{\partial^2 \widehat{\Psi}^*}{\partial r^{*2}} + \frac{1}{r^*} \frac{\partial \widehat{\Psi}^*}{\partial r^*} - \frac{m^2}{r^{*2}} \widehat{\Psi}^* - \alpha^{*2} \widehat{\Psi}^* \right) \right. \\ \left. + \widehat{\Psi}^* \left(\frac{\partial^2 \overline{\rho}^*}{\partial r^{*2}} + \frac{1}{r^*} \frac{\partial \overline{\rho}^*}{\partial r^*} \right) - 4 \frac{\partial \widehat{\Psi}^*}{\partial r^*} \frac{\partial \overline{\rho}^*}{\partial r^*} \right) = 0, \end{aligned} \quad (5.2.18)$$

for continuity

$$-i\omega^* \widehat{\Psi}^* + \frac{im \widehat{\Psi}^*}{r^*} \overline{u}_\theta^* + i\alpha^* \widehat{\Psi}^* \overline{u}_z^* + \overline{\rho}^* \left(\frac{\partial \widehat{U}_r^*}{\partial r^*} + \frac{\widehat{U}_r^*}{r^*} + \frac{im}{r^*} \widehat{U}_\theta^* + i\alpha^* \widehat{U}_z^* \right) = 0, \quad (5.2.19)$$

¹Note that in the literature the radial velocity component often is not assumed to be zero. This results in additional remaining terms involving the radial velocity (see e.g. [8])

and for the momentum conservation in radial direction

$$\begin{aligned}
 \boxed{\bar{\rho}^*} \left(-i\omega^* \widehat{U}_r^* + \frac{im\bar{u}_\theta^* \widehat{U}_r^*}{r^*} + i\alpha^* \bar{u}_z^* \widehat{U}_r^* - \frac{2\bar{u}_\theta^* \widehat{U}_\theta^*}{r^*} \right) \boxed{-\frac{\widehat{\Psi}^* \bar{u}_\theta^{*2}}{r^*}} + \frac{\partial \widehat{P}^*}{\partial r^*} \\
 - \frac{1}{\text{Re}_{\text{eff}}} \left(\frac{\partial^2 \widehat{U}_r^*}{\partial r^{*2}} + \frac{1}{r^*} \frac{\partial \widehat{U}_r^*}{\partial r^*} - \frac{m^2 \widehat{U}_r^*}{r^{*2}} - \alpha^{*2} \widehat{U}_r^* - \frac{2im\widehat{U}_\theta^*}{r^{*2}} \right. \\
 \left. + \frac{1}{3} \left(\frac{\partial^2 \widehat{U}_r^*}{\partial r^{*2}} + \frac{1}{r^*} \frac{\partial \widehat{U}_r^*}{\partial r^*} - \frac{\widehat{U}_r^*}{r^{*2}} + \frac{im}{r^*} \frac{\partial \widehat{U}_\theta^*}{\partial r^*} - \frac{im\widehat{U}_\theta^*}{r^{*2}} + i\alpha^* \frac{\partial \widehat{U}_z^*}{\partial r^*} \right) \right) = 0, \tag{5.2.20}
 \end{aligned}$$

in azimuthal direction

$$\begin{aligned}
 \boxed{\bar{\rho}^*} \left(-i\omega^* \widehat{U}_\theta^* + \frac{im\bar{u}_\theta^* \widehat{U}_\theta^*}{r^*} + i\alpha^* \bar{u}_z^* \widehat{U}_\theta^* + \frac{\bar{u}_\theta^* \widehat{U}_r^*}{r^*} + \widehat{U}_r^* \frac{\partial \bar{u}_\theta^*}{\partial r^*} \right) + \frac{im\widehat{P}^*}{r^*} - \frac{1}{\text{Re}_{\text{eff}}} \\
 \left(\frac{\partial^2 \widehat{U}_\theta^*}{\partial r^{*2}} + \frac{1}{r^*} \frac{\partial \widehat{U}_\theta^*}{\partial r^*} - \frac{m^2 \widehat{U}_\theta^*}{r^{*2}} - \alpha^{*2} \widehat{U}_\theta^* - \frac{\widehat{U}_\theta^*}{r^{*2}} + \frac{2im\widehat{U}_r^*}{r^{*2}} \right. \\
 \left. + \frac{1}{3} \left(\frac{im}{r} \frac{\partial \widehat{U}_r^*}{\partial r^*} + \frac{im\widehat{U}_r^*}{r^{*2}} - \frac{m^2 \widehat{U}_\theta^*}{r^{*2}} - \frac{\alpha^* m \widehat{U}_z^*}{r} \right) \right) = 0, \tag{5.2.21}
 \end{aligned}$$

and in axial direction

$$\begin{aligned}
 \boxed{\bar{\rho}^*} \left(-i\omega^* \widehat{U}_z^* + \frac{im\bar{u}_\theta^* \widehat{U}_z^*}{r^*} + i\alpha^* \bar{u}_z^* \widehat{U}_z^* + \widehat{U}_r^* \frac{\partial \bar{u}_z^*}{\partial r^*} + i\alpha^* \widehat{U}_z^* \bar{u}_z^* \right) + i\alpha^* \widehat{P}^* - \frac{1}{\text{Re}_{\text{eff}}} \left(\frac{\partial^2 \widehat{U}_z^*}{\partial r^{*2}} \right. \\
 \left. + \frac{1}{r^*} \frac{\partial \widehat{U}_z^*}{\partial r^*} - \frac{m^2 \widehat{U}_z^*}{r^{*2}} - \alpha^{*2} \widehat{U}_z^* + \frac{1}{3} \left(\frac{\partial^2 \widehat{U}_r^*}{\partial z^* \partial r^*} + \frac{i\alpha^* \widehat{U}_r^*}{r^*} - \frac{\alpha^* m \widehat{U}_\theta^*}{r^*} - \alpha^{*2} \widehat{U}_z^* \right) \right) = 0. \tag{5.2.22}
 \end{aligned}$$

Note that now the set of equations depends on the radial coordinate only. This means that the number of dependencies on spatial coordinates was further reduced in comparison with the BiGlobal approach and the resulting set of equations remains to be numerically solved for a one-dimensional velocity profile. On the other hand a new unknown, the axial wave number, α^* , was introduced. The set of Eqns. (5.2.18–5.2.22) therefore are a dispersion relation for the complex axial wave number, α^* , and the complex frequency, ω^* .

5.2.2.2 Temporal Analysis, Spatial Analysis and Spatio-Temporal Analysis

The dispersion relation for the complex axial wave number and complex frequency, which was derived in the last section, describes both the spatial and temporal evolution of hydrodynamic

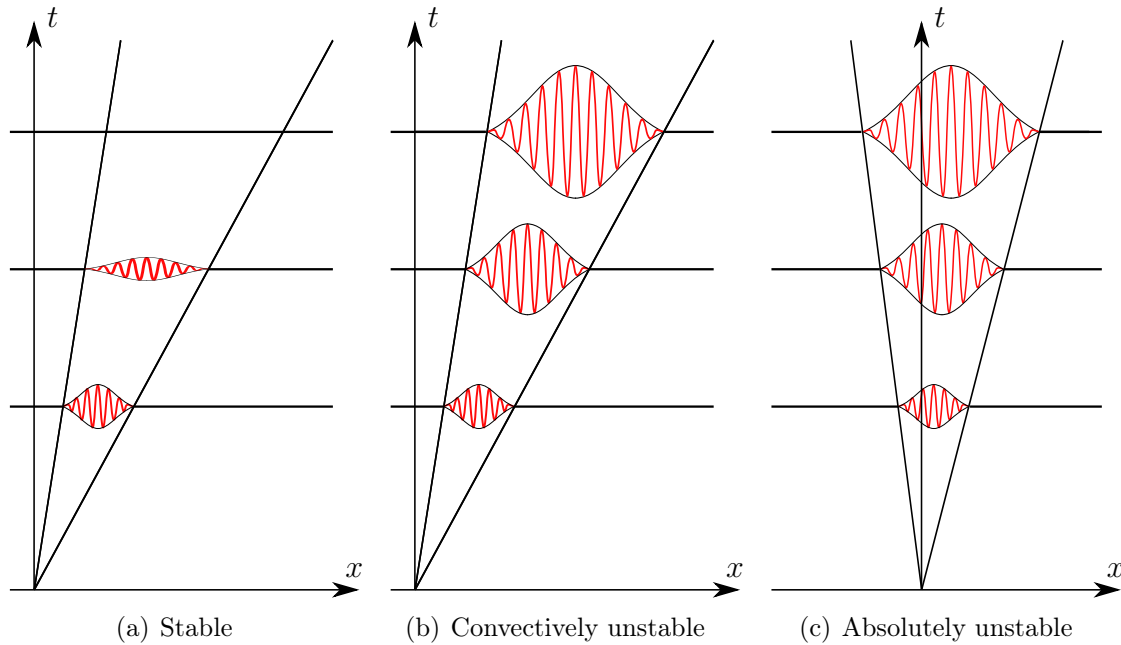


Figure 5.3: Schematic representation of a wave packet caused by a pulse introduced in the flow at $x = t = 0$ for base flows with different stability properties

waves superimposing the base flow. The x - t -diagram in Fig. 5.3 illustrates three distinctively different behaviors of perturbations superimposing a given base flow, when it is perturbed by a pulse at $x = t = 0$. In all three cases, a wave packet evolves on the base flow. If the wave packet amplitude decreases in every Galilean reference frame, i.e. independently of the position and velocity of the observer, then the base flow is called *stable* (see Fig. 5.3(a)). Furthermore, there are base flows, as depicted in Fig. 5.3(b), in which a certain wave packet grows in time, yet is swept away in the laboratory frame and therefore leaves the base flow unperturbed as $t \rightarrow \infty$. These flow are called *convectively unstable* or, since they strongly respond to harmonic forcing, *amplifier flows*. Finally, flows exist in which a wave packet is amplified in time, and at least one wave remains at the source of the pulse. Consequentially, the perturbation grows exponentially and in a parallel base flow spreads to the entire domain. These flows are called *absolutely unstable* or *oscillator flows*(see Fig. 5.3(c))[97].

In order to classify a base flow in one of these groups, a local stability analysis can be performed on the base flow. Additionally to setting the azimuthal wave number to 1 (in the case of a single helix PVC), either α^* or ω^* must be fixed to solve the GEVP for the respective other. In this context three different methods of analysis are conceivable: temporal, spatial, and spatio-temporal analysis.

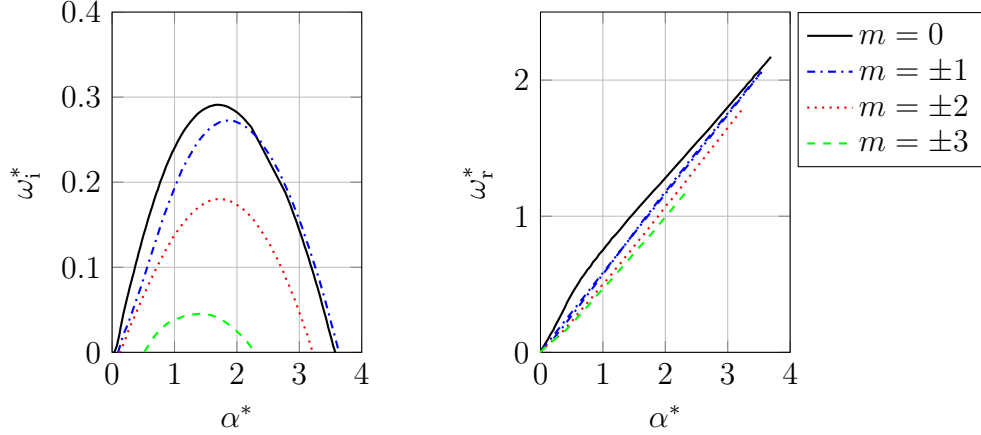


Figure 5.4: Example for temporal analysis: ω_i and ω_r as a function of the real axial wave number for various azimuthal wave numbers in a non-swirling jet; taken from Gallaire et Chomaz [74]

Temporal Analysis In the case of temporal analysis, the temporal behavior of a perturbation is under investigation. To do so, α^* is fixed to a real value and the set of Eqns. (5.2.18–5.2.22) is solved for a complex frequency, where its imaginary part ω_i^* is the corresponding temporal growth rate and its real part, ω_r^* , is the harmonic frequency in time. Temporal analyses are often used for flows, which do not show any free stream flow, like e.g. the Taylor-Couette flow [118]. Although for many other flows like free jets a temporal analysis does not suffice to fully describe hydrodynamic instabilities, it can still provide valuable information. Figure 5.4 shows a typical example of a temporal stability curve of a swirling jet flow. Is the growth rate for all perturbations and wave numbers smaller than 0, then the flow is stable, as depicted in Fig. 5.3(a). When $\omega_i^* > 0$ the flow could be prone to a global mode. If this is the case still nevertheless depends on the subsequent analyses.

Spatial Analysis In a spatial analysis the focus is on the spatial behavior of a wave with a given frequency. Here, the value of ω^* is fixed to a real value and the dispersion relation is solved for a complex α^* . The real part of α^* corresponds to the actual wave number in space. The imaginary part is the negative of the streamwise growth rate of the perturbation. This method is interesting to investigate flows which are externally or internally forced at a certain frequency (see e.g. [172]). Note, that in Eqns. (5.2.20–5.2.22) both linear and quadratic terms of α^* occur. As a consequence, a quadratic eigenvalue problem must be solved. In spatial hydrodynamic LSA the eigenvalue problem most often is linearized by adding three additional eigenfunctions, which are the product of the axial wave number, α^* , and the eigenfunctions of the velocity perturbation in all coordinate directions. The vector of eigenfunctions in the GEVP (Eqn. (5.2.5)) then becomes:

$$\Phi = [\widehat{\mathbf{U}}^*(r), \widehat{P}^*(r), \widehat{\Psi}^*(r), \alpha^* \widehat{\mathbf{U}}^*(r)]. \quad (5.2.23)$$

In temporal stability analysis, a perturbation introduced into the flow at a certain point of time, t_0 , can only impact the flow for $t > t_0$. Therefore, every eigenvalue can be related to the evolution of the mode in time. In spatial stability analysis on the other hand a perturbation at z_0 can have effects both in positive and negative z -direction. The eigenvalues determined by the spatial approach are in this context related to a growth in either positive (α^+) or negative (α^-) z -direction. With this approach alone it is *a priori* unknown if the determined eigenfunction belongs to an α^+ or an α^- -branch.

Via a spatial analysis the spatial evolution of a wave caused by a perturbation of a certain frequency is examined. Since the local approach assumes that the base flow is homogeneous in axial direction, the mode shapes do not vary in z -direction. Due to the axial growth or decay, only the amplitude of the perturbation mode varies with z . The three-dimensional mode shape can therefore be calculated by solving Eqn. (5.2.17) with the wave's corresponding complex axial wave number and complex frequency.

Spatio-temporal analysis Here, the dispersion relation is solved for a wave number and a frequency which are both complex. This method is applied on flows that show self-excited oscillations, like wakes [196, 161], mixing layers [199], jets [162] and swirling jets undergoing vortex breakdown [130, 75, 171, 211]. Using this method, the behavior of a wave governed by the dispersion relation is under investigation both in space and time. The goal here is to investigate if a flow profile is absolutely unstable (see Fig. 5.3(c)) or only temporally/convectively unstable (see Fig. 5.3(c)). With this method the group velocity of a wave packet, c , i.e. the velocity of the envelope of a wave packet, can be estimated. It is defined as

$$c = \frac{\partial \omega}{\partial \alpha}. \quad (5.2.24)$$

The principle of vanishing group velocity [23, 77] states that in case of a wave with a group velocity of zero, the envelope of the wave packet related to this wave is not moving in space (see Fig. 5.3(c)). As can be seen by Eqn. (5.2.24), a wave fulfilling this condition shows a saddle point of ω in the complex α -plane, where the corresponding complex frequency and wave number is called *absolute frequency*, ω_0 and *absolute wave number*, α_0 :

$$\frac{\partial \omega}{\partial \alpha}(\omega_0, \alpha_0) = 0. \quad (5.2.25)$$

If this wave is absolutely unstable depends on the imaginary part of ω_0 , i.e. its temporal growth rate. For $\omega_{0,i} > 0$, the flow profile is absolutely unstable and is therefore prone to a global mode.

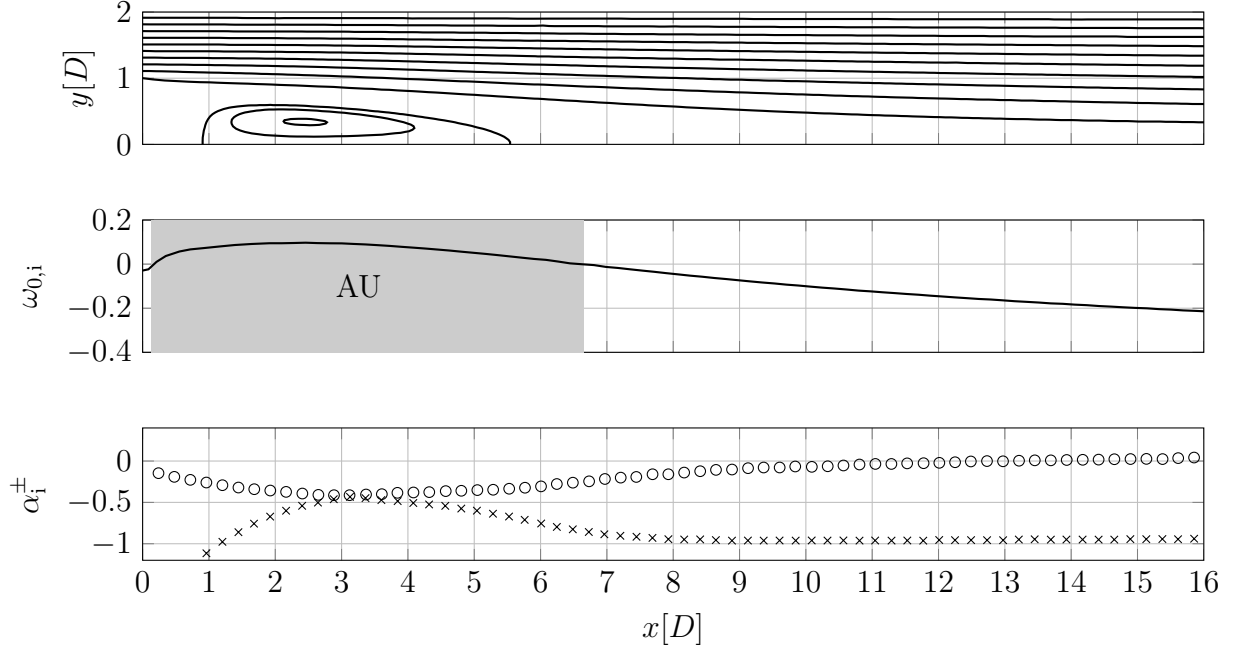


Figure 5.5: Local stability analysis of an obstacle-free wake flow at a globally constant Reynolds number $Re = 100$, taken from Juniper et al. [105]; Streamlines, and absolute frequency, $\omega_{0,i}$, α_1^+ (\circ) and α_1^- (\times) in dependence of streamwise location; The spatial analysis leading to the α^\pm branches in this case is based on the frequency of a global LSA.

5.2.3 Global Instability in Spatially Developing Flows

In the previous section, different methods of analyses and their respective purpose were laid out. So far however, the main focus was on absolutely parallel mean flows. In practice only very few fulfill this requirement. Most real flows can be split into regions of different stability properties, as shown by the example of the obstacle free wake flow in Fig. 5.5. The positive imaginary part of the absolute frequency, $\omega_{0,i}$, indicates a finite region of absolute instability around the recirculation bubble. Upstream and downstream, regions of convective instability, which are of negative absolute growth rate but positive axial growth rate, occur. The convectively unstable region downstream of the recirculation bubble spans approximately until $x = 12.5D$. Beyond this both axial and absolute growth rates are negative, and the flow is stable.

Considering the changing base flow properties in real flows demonstrated by the example of Fig. 5.5, the methods presented in the previous section are not sufficient to identify either the frequency, or reconstruct the mode shape with local LSA. Since the dispersion relation varies with the base flow in axial direction, so do both the complex frequency and axial wave number at the saddle point in the complex α -plane. Determining the frequency which

is chosen by the global mode with the aid of local LSA is therefore non-trivial. The same applies for finding the wave maker location, i.e. the location of strongest feedback and therefore the origin of the global mode, and the reconstruction of the global mode shape.

Chomaz et al. [34] examined the frequency selection of the global mode. They showed that the frequency of the global mode can be estimated by examining the global frequency, $\omega_{0,i}$, in the complex Z plane, where Z corresponds to the complex streamwise coordinate. In this plane, again saddle points are to be identified. The frequency of a global mode however is found by the saddle point of the absolute frequency ω_0 in the plane of the complex axial coordinate Z , which is closest to the real Z axis [34]:

$$\omega_s = \omega_0(Z_s) \quad (5.2.26)$$

and

$$\frac{\partial \omega_0}{\partial Z}(Z_s) = 0 \quad (5.2.27)$$

In order to obtain the ω_0 in the complex Z -plane, the curve of the absolute frequency in dependence of the streamwise location as seen in Fig. 5.5, can be expanded analytically by Padé polynomials to the complex Z -plane, as shown by Juniper et al [105].

The wave maker position, i.e. the location of greatest internal feedback, is found by the branch pinching location of the spatial branches α^+ and α^- . This is marked by the location at which both branches have the same imaginary value, as shown by Juniper et al. [107].

The reconstruction of the mode shape, as a consequence of an internal hydrodynamic feedback loop, or by external forcing is not as trivial as in absolutely parallel flows, since both eigenfunctions and the complex axial wave number, $\alpha^{*\pm}$, change in streamwise direction. In spatially slowly varying base flows however, the response of the flow to a perturbation initiated at a specific location, which is called wave maker and here is at $z = 0$, can be described by [40, 105, 170]:

$$\begin{aligned} & [\widehat{\mathbf{u}}^*(r, \theta, z, t), \widehat{p}^*(r, \theta, z, t), \widehat{\rho}^*(r, \theta, z, t)] \\ & = A_0 [\widehat{\mathbf{U}}^*(r), \widehat{P}^*(r), \widehat{\Psi}^*(r)] \exp \left(i \left(-\omega^* t^* + m\theta + \int_0^{z^*} \alpha^*(\xi) d\xi \right) \right). \end{aligned} \quad (5.2.28)$$

The factor A_0 is found by the WKBJ approach first applied to the problem of an axis-symmetric jet by Crighton and Gaster [40]. In the context of this approach, the integral corresponds to the fast variation and the complex and the slow variation is given by the complex amplitude A_0 and the eigenfunctions [98].

Oberleithner [170] argues that in the context of the investigations of a PVC, the base flow is highly non-parallel, due to jet spreading and vortex breakdown. The assumptions of the WKBJ method therefore are not fulfilled. Hence, the non-parallel correction is omitted in the framework of this thesis and the amplitude scaling is set to $A_0 = 1$.

5.2.4 A Step-by-Step Strategy to Identify the Wave Maker Position and Reconstruct the Global Mode

In the previous sections the principle of temporal, spatial and spatio-temporal stability analysis and their respective area of application was outlined. Furthermore, the frequency selection criterion for spatially developing flows based on the work of Chomaz et al. [34] was presented. In order to estimate the frequency of a global mode in the context of linear stability analysis, a spatio-temporal analysis is necessary. However, starting directly with this type of analysis can be troublesome, since several branches co-exist and intersect in the complex α^* -plane. This makes identifying the correct branch and saddle point difficult, especially in a spatially developing flows, where branches vary with the axial position. Therefore, in this section a simple step-by-step procedure will be given which simplifies the quest for the global instability.

1. The first step takes advantage of a necessary condition for a global mode. It can be shown that for the imaginary part (and therefore the growth rate) of the global frequency, the absolute frequency and the complex frequency the inequality [34]

$$0 \leq \omega_{G,i} \leq \omega_{0,i} \leq \omega_i \quad (5.2.29)$$

holds, where ω_i is based on a temporal analysis. According to this inequality, a global mode with a temporal growth rate of $\omega_{G,i} \geq 0$ can only occur, if there exists a related temporal branch with positive growth rate. It therefore is reasonable to start the analysis by a temporal analysis, identifying all branches which within a certain range of wave numbers and axial position are related to a positive imaginary part of the complex frequency, ω_i . Most often sorting out spurious eigenvalues is not necessary, since physical branches can be easily identified, in the case of this first step by plotting the temporal growth rates, ω_i , over the real axial wave number, α .

2. In the second step, a spatio-temporal analysis is conducted and the temporal stability curve from step 1 is expanded into the complex α plane, where saddle points are identified. The frequency at this saddle point corresponds to the absolute frequency of the corresponding velocity profile. The saddle point of the corresponding branch is tracked along the stream wise coordinate. This yields the complex frequency as a function of the stream wise coordinate.
3. In order to find the global frequency, $\omega_{G,i}$, the curve of the absolute frequency must be expanded to the complex stream wise coordinate. This is performed by Padé polynomials given by

$$\omega_0(Z) = \frac{\sum_{j=0}^m a_j Z^j}{1 + \sum_{k=1}^n b_k Z^k} \quad (5.2.30)$$

Consequently, the global frequency, $\omega_{G,i}$, is determined by the frequency at the saddle point, which is closest to the real axis.

4. In the last step the three dimensional mode shape is reconstructed. To do so, a spatial analysis is conducted at the frequency of the global mode which was determined in the previous step. The spatial branches of α^+ and α^- are tracked along the stream wise coordinate, and the wave maker location is found by the intersection of the imaginary parts of both branches [107]. Finally, the mode shape is reconstructed by integrating Eqn. (5.2.28) along the stream wise coordinate.

5.2.5 Numerical Approach: The Chebychev Collocation

The application of Chebychev spectral methods has been extensively used in the context of local - and later also global (e.g. [64, 3, 85, 178]) - LSA. Firstly applied by Orzsag et al. [175] on the topic of boundary layer stability, the Chebychev tau and Galerkin approaches were used later on by various other authors for similar configurations [149, 22]. Malik et al. [141] and Khorrami et al. [113] showed that the third Chebychev spectral method, the Chebychev collocation, is a highly efficient method in the framework of hydrodynamic LSA of swirling flows. In the context of local LSA of free shear layers, predominantly this method has been used thereafter (e.g. [112, 184, 210]).

Introducing the method into the topic of local hydrodynamic stability analysis, Khorrami et al. [113] state the advantages of the method: The use of coordinate transformations and several boundary conditions is simplified. The polynomials are evaluated on the Gauss-Lobatto points which cluster close to the boundaries, they distribute the error evenly in the domain and show good convergence rates as the number of terms increase.

By default the Chebychev points, ξ_i , are fixed within the interval $-1 \leq \xi \leq 1$. Therefore, a mapping from the spectral space to the physical space must be introduced. In this thesis, the mapping of Malik et al. [141] is applied:

$$\frac{r}{r_c} = \frac{1 + \xi}{1 - \xi + 2r_c/r_{\max}}. \quad (5.2.31)$$

It allows to distribute half of the Gauss-Lobatto points in the interval $0 < r < r_c$. The number of necessary Gauss-Lobatto points, Z , is estimated by a convergence study, showing that for the configuration under investigation $Z = 100$ suffices.

The spatial discretization of the GEVP (Eqn. (5.2.5)) leads to square matrices of size $4Z$ for a temporal analysis and $7Z$ for a spatial analysis (in the case of uniform density). Since the number of eigenvalues is equal to the matrix dimension, $4Z$ or respectively $7Z$ solutions of the eigenvalue problem exist. Most of these solutions however are spurious and not related to physical modes. In literature, methods to sort out these spurious eigenvalues are proposed. Firstly, in cases where the outer boundary condition is far from the shear layer, it can be assumed that eigenvectors related to a physical perturbation are close to zero as $r \rightarrow \infty$. A

criterion often used to sort out solutions of the eigenvalue problem based on this assumption can be formulated as

$$\frac{\sum_{i=1}^{Z/10} (\mathbf{F}(r_i))^2}{\sum_{i=1}^Z (\mathbf{F}(r_i))^2} < \epsilon_1, \quad (5.2.32)$$

with a provided arbitrary tolerance ϵ_1 . In confined flows however, where the shear layers of interest are close to the outer boundary layer as in this thesis, this method is not effective. A second method assumes that after mesh convergence is reached, a small variation of the number of Gauss-Lobatto points, Z , changes the eigenvalues related to a physical mode only marginally. The spectrum of spurious eigenvalues however will be effected significantly. In this context, the solutions of the GEVP for Z Gauss-Lobatto points is compared to the solution with $Z' > Z$ points. The spectrum of both GEVPs are compared and eigenvalues satisfying

$$\min|\lambda - \lambda'| < \epsilon_2 \quad (5.2.33)$$

are considered to be physical. ϵ_2 again is an arbitrary tolerance.

The correct implementation of the Chebychev collocation method was successfully validated by Oberleithner [170], who compared the results of temporal and spatial analysis of the Batchelor trailing line vortex [12] to the results of Parras and Fernandes-Feria [179] and Khorrami et al. [113]. Furthermore, results of temporal stability analysis of a PVC in a swirling jet were compared against the results of Gallaire and Chomaz [74] showing ideal agreement. In the framework of the studies on local LSA shown in this thesis, the code of Oberleithner [170] was applied without modification.

5.3 Conclusion

In this chapter an overview over different approaches of LSA of hydrodynamic instabilities is given. The numerical tools applied to solve the respective set of equations, namely the FEM and the Chebychev collocation are discussed. The local and BiGlobal approach for flows of uniform density will be applied in Chapter 6 to analyze a PVC superimposing the cold flow in an industrial, swirled fuel injection system of highly complex geometry. With respect to the goal of applying LSA on reacting flows, it must be taken into account that for these flows the density field is typically inhomogeneous if the pressure is constant. The low-Mach equations derived in this section take this into account. The governing equations of BiGlobal LSA based on the compressible Navier-Stokes equations in Low Mach flow, which are presented in this thesis, therefore are a step forward in analyzing the hydrodynamic stability of reacting flows. Results that were obtained by solving these equations on a reactive swirled base flow will be discussed in Chapter 7.

Chapter 6

The PreINTRIG Experiment and Cold Flow Simulations

Hydrodynamic instabilities play an important role in many physical processes, among others in combustion. Vortex formation in shear layers for example can lead to improved mixing and an increases in turbulence [32, 201, 203, 191]. In this chapter, the flow in an industrial, two-staged, counter-rotating, swirled injection system will be analyzed. These systems are known to be frequently prone to a PVC which evolves in the shear layer between the recirculation bubble and the surrounding jet.

Figure 6.1(a) shows a ring shaped combustion chamber of a helicopter gas turbine, which is fed by 15 swirled injectors. The swirler that is investigated in this chapter is very similar in construction to the ones welded on the ring chamber in Fig. 6.1(a). Each of the two stages of the injector is fed by eight tangential vanes. Figure 6.1 furthermore illustrates the swirler for two different configurations, which are examined in the framework of this chapter. In contrast to the first configuration (see Fig. 6.1(b)), in the second configuration a rod is attached at the jet axis within the primary injector, as can be seen in the photograph of Fig. 6.1(c). The different configurations will be referred to as no-rod case and rod case, respectively. These two cases are highly relevant for combustion cases (even if no experimental reacting results will be presented in this chapter, since only cold flow experiments were performed): Swirlers used in gas turbines are highly sensitive to the details of the flow and the rod modifies the geometry of the swirler significantly. Therefore, understanding how the rod modifies the flow is a general question for the combustion community.

Figure 6.2 shows a sketch of the swirler. The fluid in the upstream plenum enters the primary stage through its tangential vanes. In the swirler it is deflected in axial direction by the center body. After a convergent section and a section of constant cross section the primary injector opens to the secondary stage. This axial position will be referred to as exit

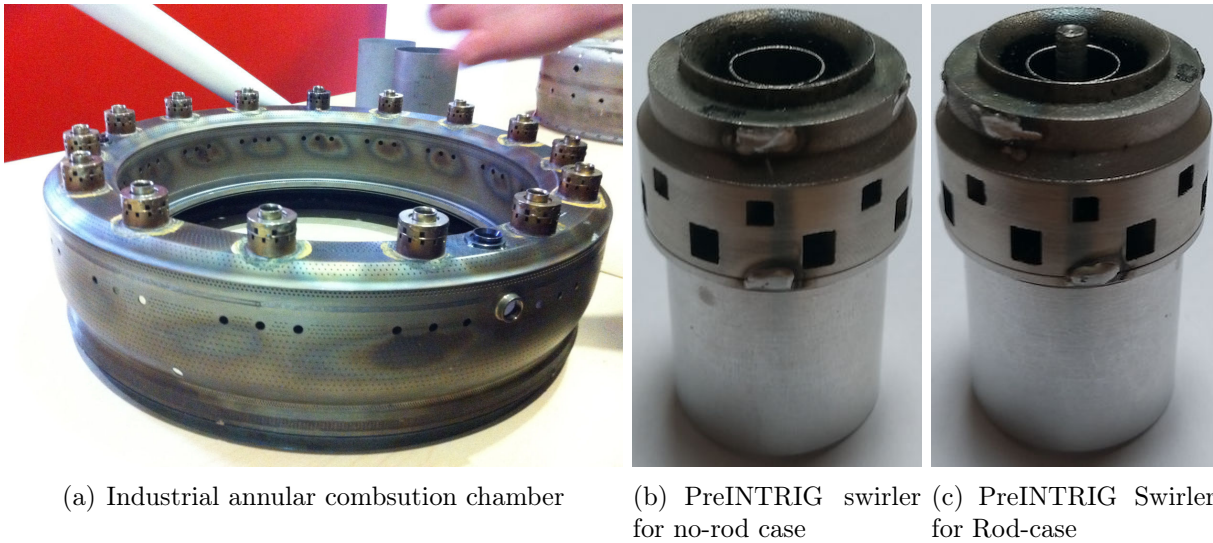


Figure 6.1: Azimuthal combustion chamber of a helicopter gas turbine; The chamber (see(a)) is fed by 15 two staged counter-rotative injectors, similar in geometry to the one under investigation in this chapter (see (b) and (c))

plane of the primary stage. At the dump plane, the fluid exits the two-staged injector. The position of the central rod is illustrated by the dashed lines.

Section 6.1 describes the experimental set up, while the numerical set-up is shown in Section 6.2.1. LES results will be validated by experiments in Section 6.2.2. The numerical results for both the rod case and the no-rod case will then be shown in Section 6.2.3 for non-reactive flows. Furthermore, a LSA will be conducted in Section 6.3. Finally, the results are concluded in Section 6.4.

6.1 The Set-Up of the PreINTRIG Experiment

A schematic illustration of the experimental set-up built for the swirled injector illustrated in Figs. 6.1(b), 6.1(c) and 6.2 is shown in Fig. 6.3. Both stages are fed by the same cylindrical plenum, which measures 88 mm in diameter and 590 mm in length. In the configuration examined in the experiments, the flow blows into the free atmosphere. For estimation of the free stream velocity profiles downstream of the injector, PIV measurements are conducted. For this purpose, the air stream is split after the mass flow meter. The first line enters the seeding vessel, where olive oil droplets are injected into the gas. Thereafter, it enters the mixing box, where it mixes with the gas from the second line, before the mixture enters the upstream plenum. Downstream of the swirler the droplets are illuminated by pulses of a

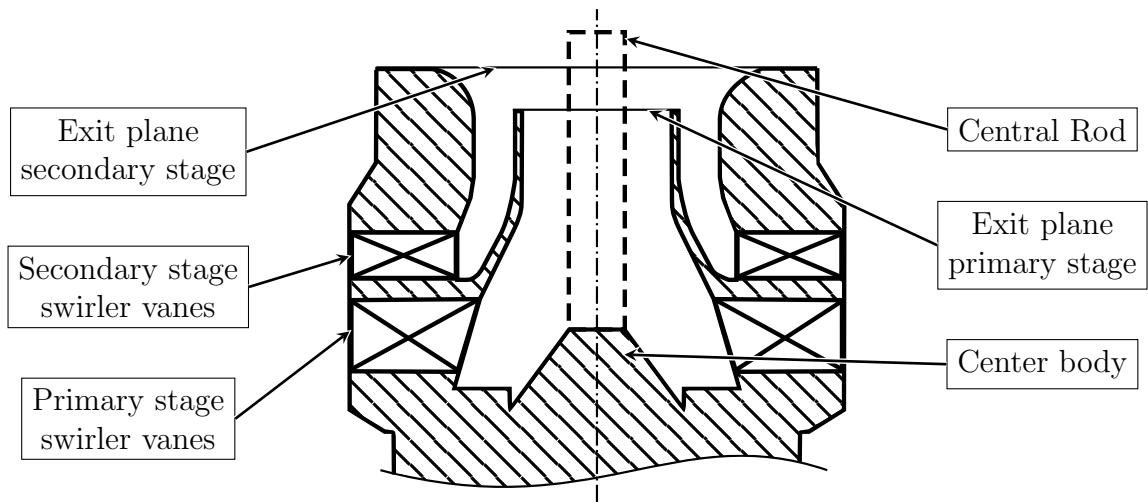


Figure 6.2: Sketch of the cross section of the swirler

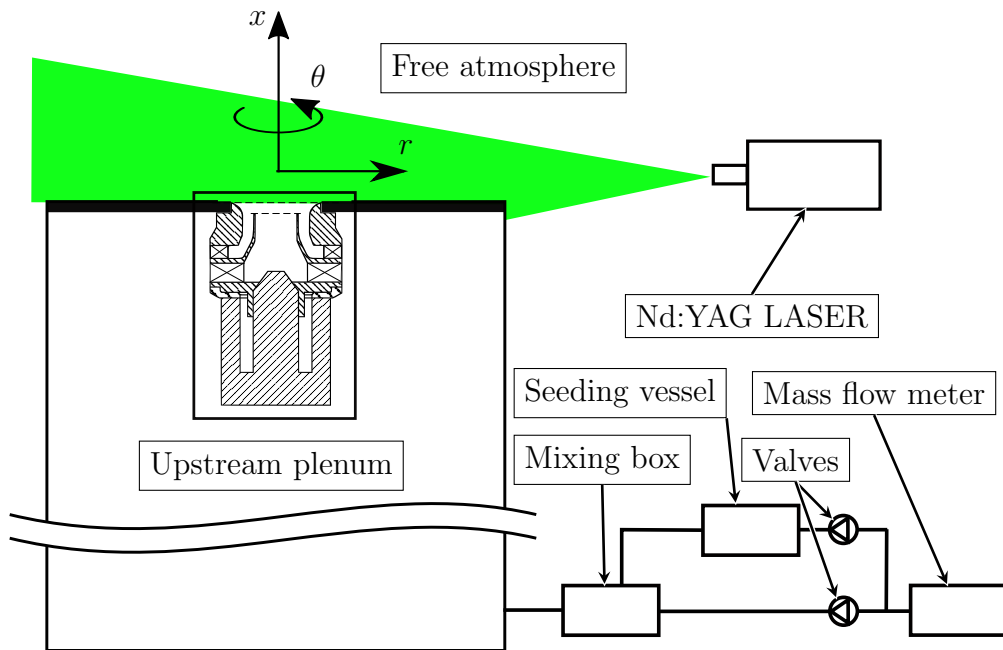


Figure 6.3: Schematic set up of the preintrig experiment

ND:YAG laser in the longitudinal plane and recorded in a window of 20 x 32 mm. Particular measures are taken to capture the velocity profiles close to the dump plane. First, in order to reduce out-of-plane displacements of seeding particles, the laser sheet is thickened to 1 mm. Second, the time delay between the pulses is chosen as $4 \mu\text{s}$ based on a parametric study. Additionally, a microphone located at $x = 0$ and $r = 300\text{mm}$ measures pressure fluctuations.

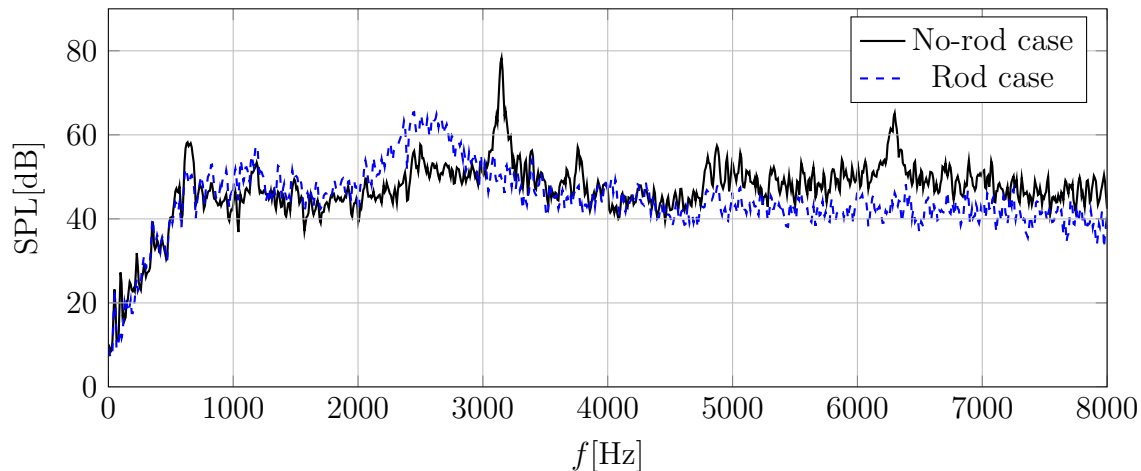


Figure 6.4: Experimental SPLs measured at $x = 0$ and $r = 300$ mm for the no-rod and rod case

The experiments show that in the no-rod case, an audible, loud whistling sound occurs. FFT of the pressure measurements show several distinct peaks, as illustrated in Fig 6.4. For a flow rate of $\dot{V} = 3.41/\text{s}$, the lowest peak is at a frequency of approximately $f \approx 700$ Hz, the most dominant one however is at $f \approx 3150$ Hz. The remaining peaks are higher harmonics of the latter. Although several distinct frequencies were measured by the microphone, a Proper Orthogonal Decomposition (POD) based on PIV snapshots did not show any coherent structures in the flow recorded in the field of sight of the camera. The experiments furthermore show, that no whistling sound is audible for the rod case for the same flow rate (see Fig. 6.4). FFT of the pressure measurements in this case show a slight elevation of the Sound Pressure Level (SPL) at $f \approx 2500\text{Hz}$. This elevation is lower in intensity than in the no-rod case and is of broad band frequency content.

Although the frequencies at which distinctive peaks occur in the FFT of the pressure recordings could be determined by experimental means, their cause could not be revealed. Nevertheless, the experimental frequency spectrum and the flow profiles in the free stream field downstream of the injector, represent a validation basis for the LES, which are presented in the following sections. Quantitative experimental measurements will be shown Section 6.2.2 in comparison with the numerical results.

6.2 Coldflow LES

The previous section has presented the set-up and qualitative results of the PreINTRIG experiment. Since in the free stream field downstream of the swirler no coherent structures are observed although microphone measurements showed peaks at distinctive frequencies, a CFD analysis is conducted in order to understand this phenomenon. The results will serve as base flows for a hydrodynamic stability analysis conducted in Section 6.3. Experimental results are the validation basis for these base flows.

6.2.1 Numerical Set-Up for Non-Reactive LES of the PreINTRIG Configuration

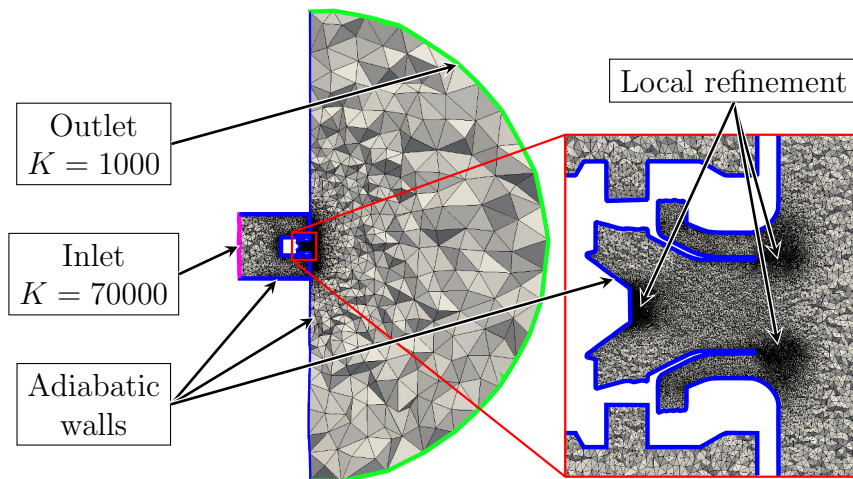


Figure 6.5: Numerical domain and grid for the non-reactive simulations

This section describes the numerical strategy and set-up used for the cold flow simulations of the PreINTRIG configuration. The LES strategy laid out in Section 4 is applied and the Favre-Averaged Navier Stokes equations are solved by the AVBP software. The σ -model [168] is applied to model the sub-grid turbulence.

Figure 6.5 illustrates the computational domain and grid used for the non-reactive configuration. The length of the upstream plenum in the simulations is 90 mm, while its diameter of $d = 88$ mm corresponds to the experiment. The free atmosphere is modeled by a half sphere as indicated in Fig. 6.5. NSCBCs [189] are used at both the inlet (reflection coefficients $K = 70000$) and at the outlet ($K = 1000$). At the inlet, air of temperature $T = 292$ K is injected with a quasi flat velocity profile ($a = 16.6$ in Eqn. (3.2.2)). All walls (i.e. upstream plenum, swirler and dump plane) are no-slip and adiabatic. The pressure in the domain is

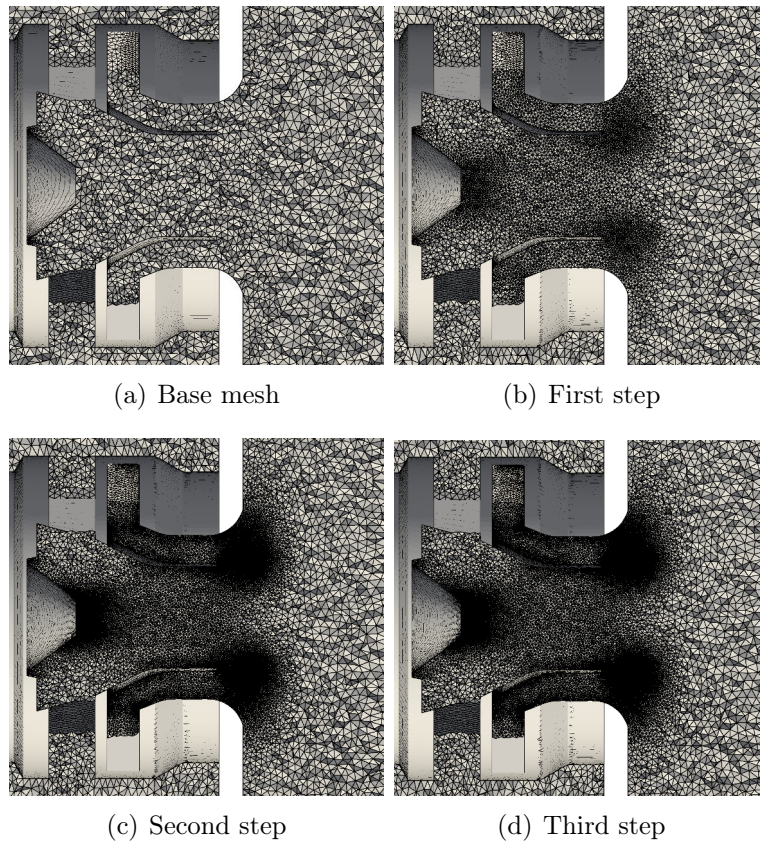


Figure 6.6: Successive mesh refinement for the no-rod case; taken from Daviller et al. [48]

regulated by setting the pressure target value of the outlet BC at the surface of the half sphere to $p = 102000$ Pa. An iterative mesh h-refinement strategy is applied in order to capture the flow field of the swirler correctly. The local mesh refinement is based on localizing the regions of highest dissipation of kinetic energy. Figure 6.6 shows the base mesh and the meshes after the three successive mesh refinement steps. This strategy was developed and conducted for the no-rod configuration by Daviller et al. [48]. They showed that while in simulations with the base mesh the pressure drop across the swirler was far off, the successive mesh refinement led to correct LES-pressure drop predictions after the third mesh refinement (see Fig. 6.7). The smallest cell size in the refined regions is $\Delta x = 45 \mu\text{m}$. The total amount of grid cells is $10.86 \cdot 10^6$. The time step is set to a fixed value of $\Delta t = 3.3 \cdot 10^{-8}$ s, which approximately corresponds to a maximal Courant-Friedrich-Lewys number of 0.9.

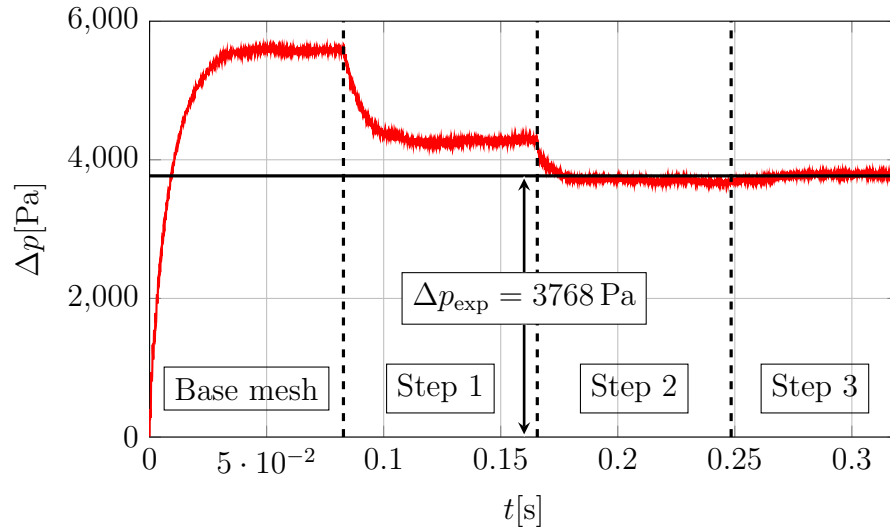


Figure 6.7: Development of LES-pressure drop across the swirler with time during the successive mesh h-refinement (red thin line) in the no-rod case; Experimental pressure drop (black thick line): $\Delta p_{\text{exp}} = 3768 \text{ Pa}$; based on Daviller et al. [48]

6.2.2 Validation of LES Results

Before further investigating the LES results in the subsequent section, here the results of LES is validated against the experimental results. First, the LES mean velocity fields in the free stream field are compared to averages of experimental PIV.

In Fig. 6.8 averages of PIV snapshots are compared to mean fields of LES for the streamwise component and the y -component, within the $z = 0$ -plane. The LES velocity fields are both temporally and azimuthally averaged. The asymmetry with respect to the jets center axis in the experimental results is due to minor deformations of the thin separation plate between the primary and secondary stage of the injector. The LES results are azimuthally averaged. The overall comparison is very satisfactory. Differences are visible for the streamwise velocity profile closest to the dump plane. It is known however, that large velocities close to the boundaries of the field of sight are underestimated by PIV. The remaining profiles are in very good agreement both for the stream wise as for the radial component.

Figures 6.9 compares the spectra LES pressure traces in the primary injector for the no-rod case and the rod case. For the no-rod case, a high peak appears at $f \approx 3100 \text{ Hz}$. Two other peaks at $f \approx 6200 \text{ Hz}$ and $f \approx 9300 \text{ Hz}$ appear to be higher harmonics of the dominant peak. The location of these peaks are in very good agreement with the location of the spikes in the experimental SPL spectrum (see Fig. 6.4). Like in the experimental SPL a minor peak at $f \approx 700 \text{ Hz}$ is discernible in Fig. 6.9. It therefore appears, that the dynamics that cause the spikes in the experimental sound pressure level spectrum are well reproduced by the LES,

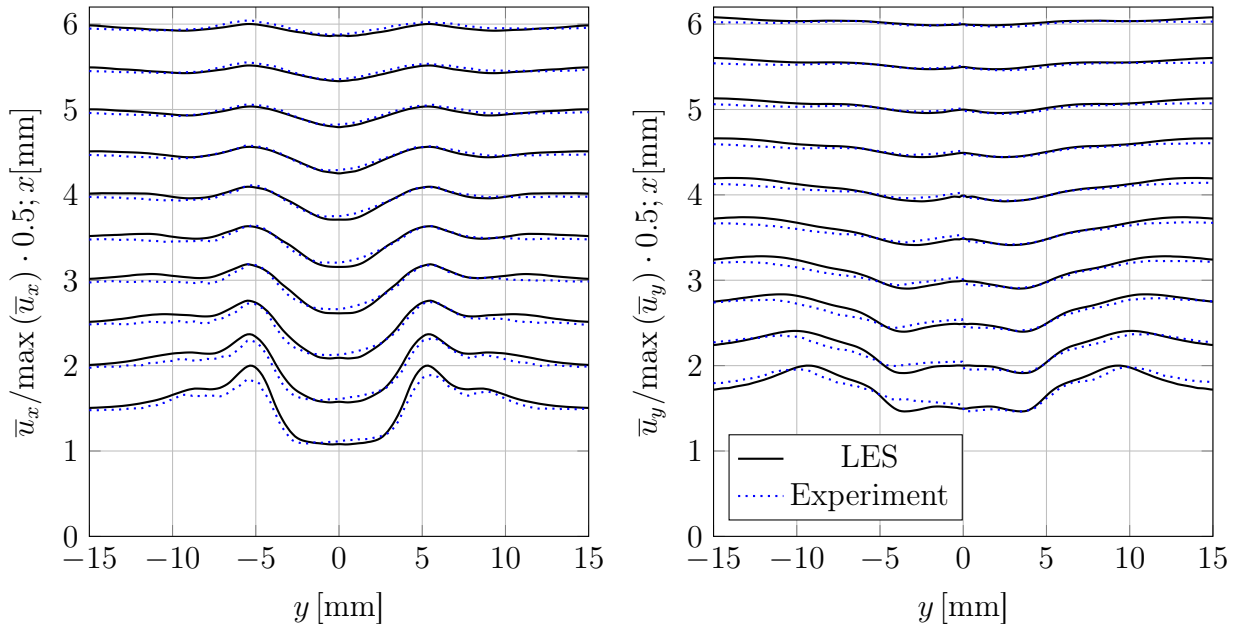


Figure 6.8: Validation of LES mean flows in the Cartesian $z = 0$ -plane in the free stream field versus the average of experimental PIV snapshots; LES fields are both temporally and azimuthally averaged.

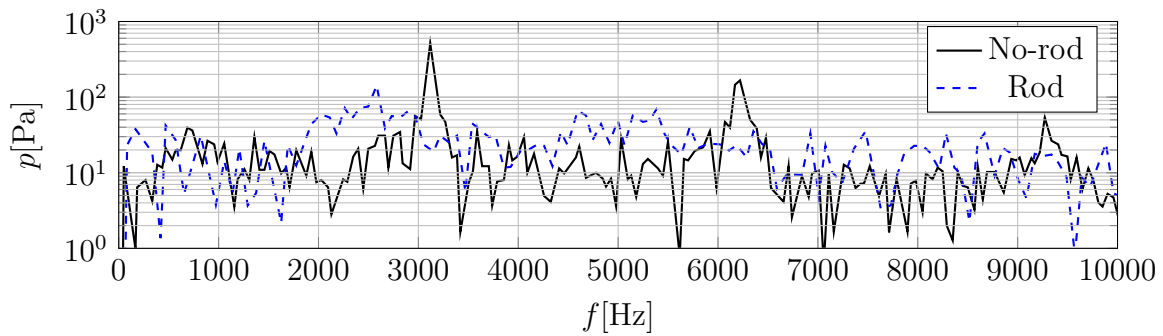


Figure 6.9: Fourier transform of numerical pressure measurements within the primary injector for the no-rod and the rod case

even if they are still unknown for the moment. Note that the location of the microphone in the experiment is exactly on the half sphere surface, which models the free atmosphere in the simulations. Since the relaxation on the outlet boundary condition modifies the pressure in the outlet, the sound pressure levels close to the outlet are not comparable to the experimental data.

As shown in Section 6.1, in the no-rod case no specific strong peaks in the experimental spectrum appear. Nevertheless, a broad band elevation of the spectrum around $f \approx 2500$ Hz is visible. Also for the LES no strong peaks appear in the spectrum, although an elevation of the spectrum at around $f \approx 2500$ Hz is discernible, which again is in good agreement with the experimental results.

All experimental data available, i.e. the velocity fields and pressure spectra, was reproduced with high accuracy by the LES. Therefore, the LES results are trusted with respect to the flow dynamics leading to the coherent pressure fluctuations as well as the mean flows. The study continues by investigating the whistling sound by purely numerical means in the subsequent section. Furthermore, the base flows obtained by the LES are used as base flows for the hydrodynamic stability analysis in Section 6.3

6.2.3 Results of Non-Reactive LES of the PreINTRIG Configuration

This section describes the results of the cold flow LES and focuses on the part of the flow, which was inaccessible by PIV measurements: the flow field within the swirler. Figure 6.10 illustrates the fields of all velocity components in cylindrical coordinates within the primary injector and a Line Integral Convolution (LIC) for the no-rod case (left) and the rod case (right).

In the no-rod case, a striking feature of the flow is that it is deflected in radial direction and attaches directly to the dump plane as it exits the swirler, which is clearly shown by the LIC illustration. This way no free stream jet evolves. This behavior is due to the very high swirl in the flow. Both the LIC and the stream wise component show a recirculation bubble downstream of the primary stage. The illustration of the stream wise component furthermore demonstrates that this component is the largest in the outer regions of the primary stage, while close to the jets center axis the flow rate remains close to 0 m/s. Additionally, downstream of the center body, a ring of high axial velocities occurs. Within the primary injector the values of the radial velocity component remain moderate, except close to the center body, where very high absolute values occur within a small area. Downstream of the primary injector however, regions of high radial velocities occur. Since the local approach of hydrodynamic stability assumes low radial velocities, it can be concluded, that this assumption is strongly violated in the region outside of the primary injector. This

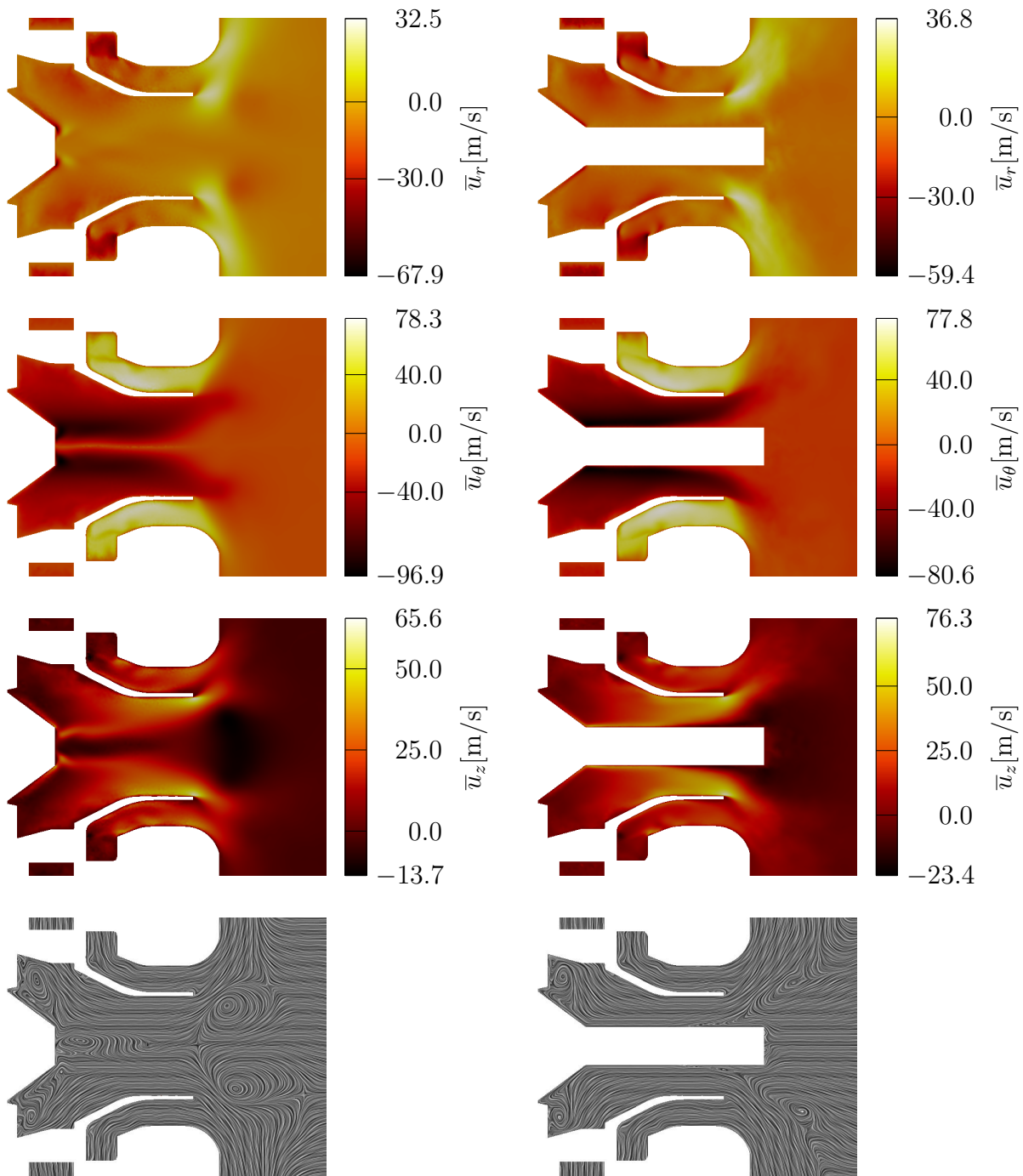


Figure 6.10: Mean fields of radial, azimuthal and axial velocity in the interior of the injector for the no-rod case (left) and the rod case (right); The LIC at the bottom are based on the mean radial and axial velocity component.

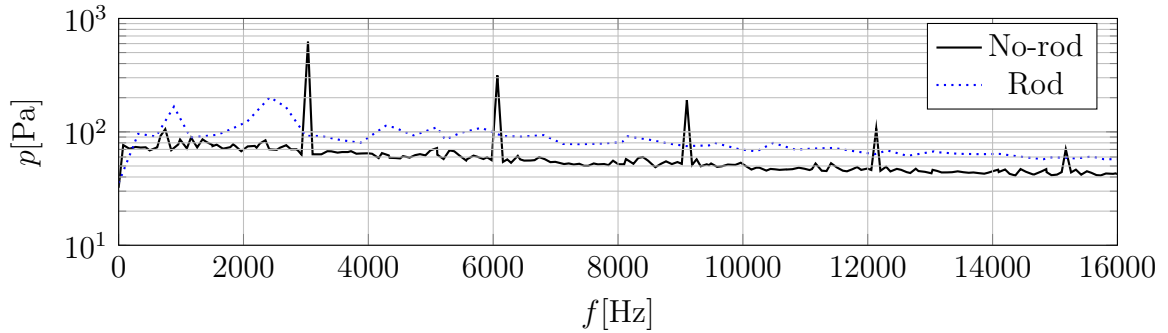


Figure 6.11: DMD spectra for the no-rod case and the rod case based on LES snapshots

problem will be addressed in detail in Section 6.3.1. The highest negative and positive values of azimuthal velocity occur in the interior of the primary and secondary stages, respectively. Downstream of the stages, the corresponding values decrease rapidly.

The influence of the rod on the flow field through the injector is surprisingly low, as the illustrations on the right of Fig. 6.10 demonstrate. The very most features described above for the no-rod case are equally valid for the rod case. The largest differences are visible in the regions close to the center body upstream in the injector, where considerably lower absolute values of velocities occur. Furthermore, the recirculation bubble is of slightly different shape.

In order to investigate the peaks occurring in both experimental and numerical pressure spectra a Dynamic Mode Decomposition (DMD) [215] of three-dimensional LES snapshots is conducted. Fig. 6.11 shows the resulting spectra for both the no-rod and the rod case. Overall, the spikes in the spectra of the no-rod case are in very good agreement with the values of both the experimental and the numerical pressure spectra. First, the minor spike at $f \approx 700$ Hz, which also occurs in the experimental sound pressure spectrum can be related by the DMD to an axisymmetric instability occurring within the injector. The focus of this study however is on the dominant instability indicated by a peak at $f \approx 3030$ Hz in the DMD spectrum. The DMD yields that this peak corresponds to a single helical instability, which occurs in the interior of the primary stage. The velocity and pressure fields of the DMD mode are shown in Figs. 6.12(a)-6.12(d) in the y - z -plane at $x = -3$ mm. The axial velocity shows a yin-yang shape. This type of pattern of axial velocity fluctuation was observed by Stöhr et al. [232] in the framework of a helical instability in a PVC by the means of POD of experimental PIV snapshots. The same pattern was also observed in light intensity measurements of a flame perturbed by a PVC by Moeck et al. [160] (see Fig. 6.13).

Like in the previous spectra illustrated in this chapter, the remaining peaks in the DMD spectrum correspond to higher harmonics of the dominant peak. The first higher harmonic is exemplary compared to the dominant mode in the Fig. 6.12. The focus of this study however is on the dominant peak, only. Figure 6.14 illustrates its mode shapes in

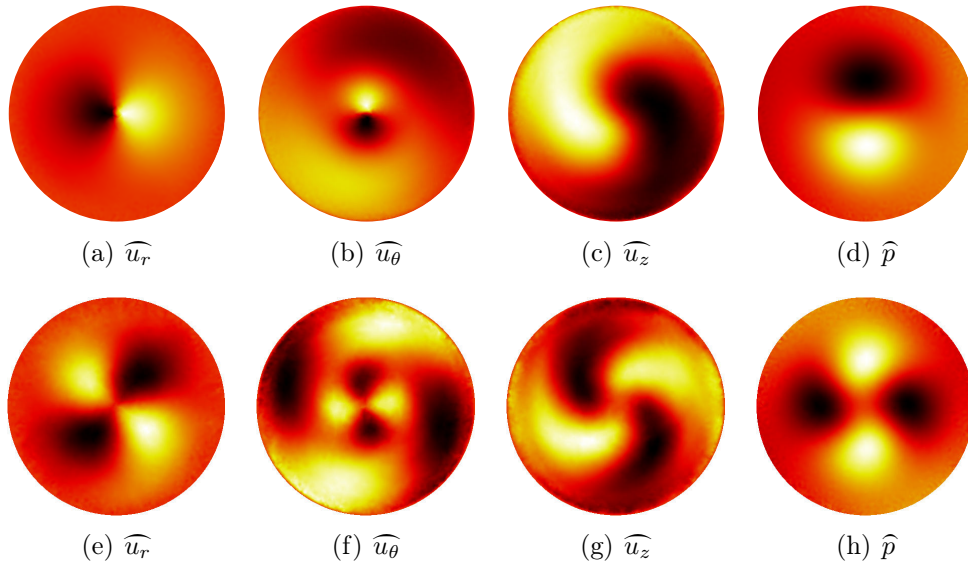


Figure 6.12: DMD-mode shapes in the y - z -plane at $x = -3$ mm (within the primary injector) based on three-dimensional LES snapshots for the no-rod PreINGTRIG case; single helix PVC in (a)-(d) corresponding to the dominant peak in Fig.6.11; double helix PVC in (e)-(h) corresponding to its first higher harmonic

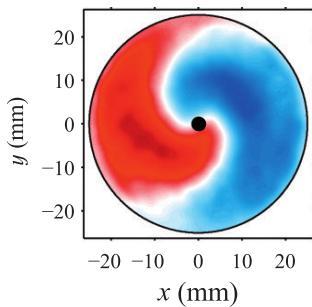


Figure 6.13: Phase averaged light intensity fluctuation of a flame perturbed by a PVC; taken from [160]

the x - y -plane. It demonstrates, why the mode could not be observed by POD based on experimental PIV measurements: The most upstream position for which the perturbations are visible is right downstream of the center body. After a region of axial growth within the primary injector, all velocity components reach their highest values close to the primary injector exit plane. Downstream of this region the modes quickly decay. This leaves the flow field downstream of the exit plane of the primary injector, which is the only region accessible to the experimental PIV measurements, mostly unperturbed by this dominant mode.

Furthermore, a DMD analysis of the rod configuration was performed. The resulting DMD spectrum is illustrated in Fig. 6.11. As in the experimental SPL spectrum and the spectrum of the pressure probe within the primary injector, no clear spike is visible in the DMD spectrum for the rod case. Instead a broad band elevation of the spectrum occurs around $f \approx 2500$ Hz. The mode shapes corresponding to the highest amplitude in the DMD spectrum are illustrated in the RHS of Fig. 6.14. The mode shapes of all components seem to correspond to the dominant mode in the no-rod configuration. In the no-rod case the mode shapes however are somewhat erratic.

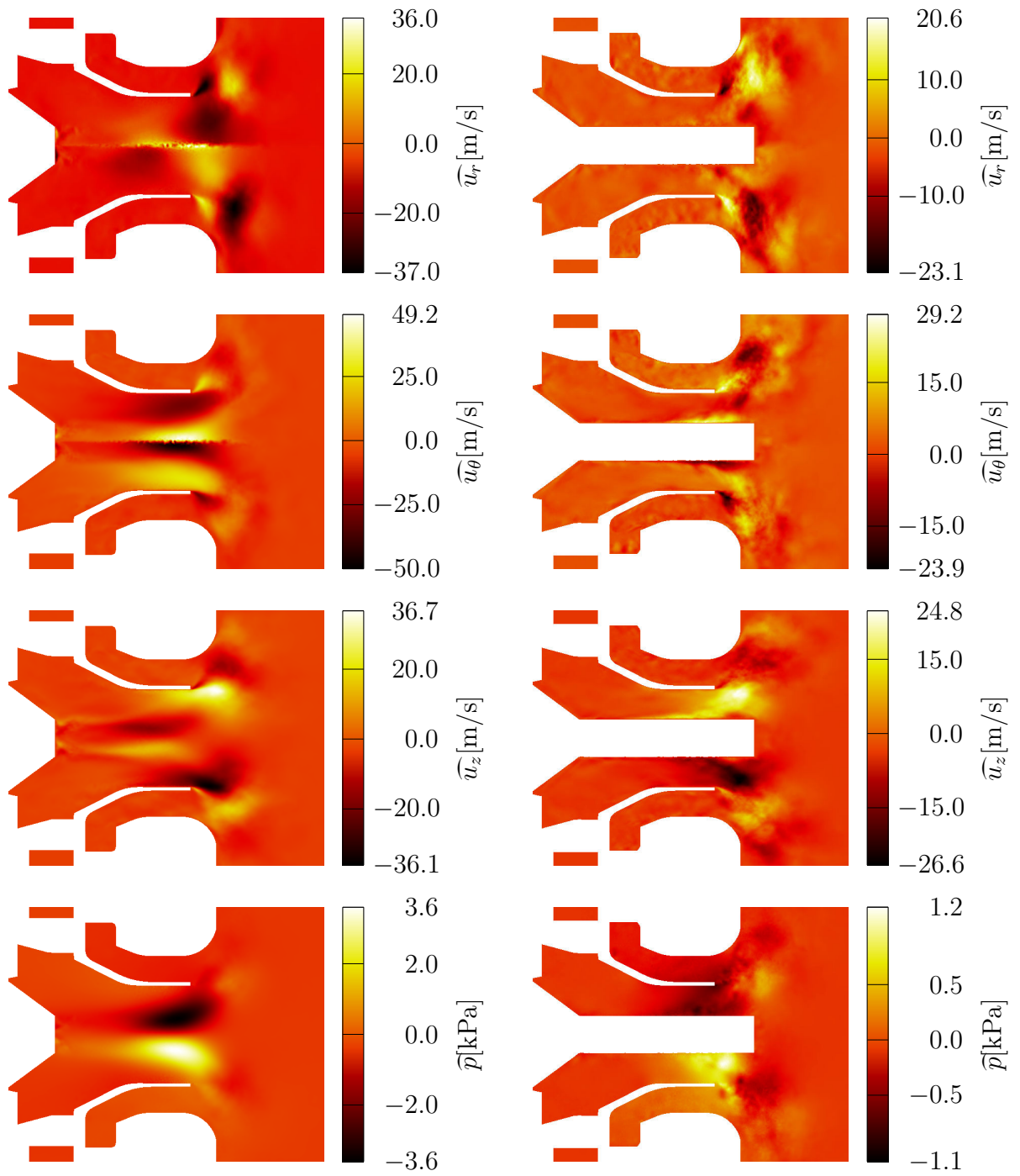


Figure 6.14: DMD mode shapes in the z -plane based on three-dimensional LES snapshots of the two PreINTRIG configurations, the no-rod case (left) and the rod case (right); for corresponding DMD spectra, see 6.11; The illustrated mode shapes correspond to the maximum amplitude in the respective spectra.

6.3 Hydrodynamic Stability Analysis of the PreINTRIG Swirler Flow

In order to investigate the coherent helical structure which was revealed and analyzed by LES means in the previous section, the PreINTRIG configuration is subject to a hydrodynamic LSA in this section. This examination is focused on addressing the following questions, regarding the different configurations:

1. Does the LSA confirm a helical hydrodynamic instability in the primary injector?
2. Which methods (local and BiGlobal) can be applied on this configuration and what are their respective limits?
3. Does LSA confirm the stabilizing influence of the central rod on flow stability seen in experiments and LES?

The base flows needed for a LSA can not be provided by experimental means, since the PVC appears within the injector only and this region is not accessible visually. Due to their excellent agreement with experiments regarding both the mean velocity fields in the free stream area and the dynamical behavior, the LES means will serve as the base flow for the subsequent LSA. For simplicity, the reference velocity, length scale and density for adimensionalization are chosen in all calculations involving the PreINTRIG configuration as $U_{\text{ref}} = 50 \text{ ms}^{-1}$, $D_{\text{ref}} = 4.2 \text{ mm}$ and $\rho_{\text{ref}} = 1.0 \text{ kgm}^{-3}$.

The interaction between the coherent structure and stochastic velocity fluctuations is determined by an eddy viscosity model as described in Section 5.1.1. The local Reynolds number depends therefore on the sum of molecular, subgrid LES viscosity and the eddy viscosity based on Eqn (5.1.16). For their respective definitions, see Section 5.1.1. The three contributions and the effective eddy viscosity are illustrated in Fig. 6.15. The minor variation of molecular viscosity is due to the inhomogeneous temperature field, but in comparison with the LES subgrid viscosity and the eddy viscosity, its contribution to the total viscosity is marginal. While within the primary injector the eddy viscosity is of the same order of magnitude as the LES subgrid viscosity, outside of the primary injector, eddy viscosity is by far the largest contribution to the total viscosity. Using the proposed model leads to a negative contribution of eddy viscosity, within an area around the recirculation zone, which is marked by a yellow line in Fig. 6.15. For the LSA calculations the eddy viscosity within this area is set to zero.

For the linear stability analysis, a mapping must be performed from the three dimensional LES mean flow to the z - r -plane. To do so the LES temporally averaged flows are averaged in azimuthal direction. The resulting fields, on which both the local and BiGlobal approach are based upon are shown in Fig. 6.16. Note that the displayed field coincides with the domain

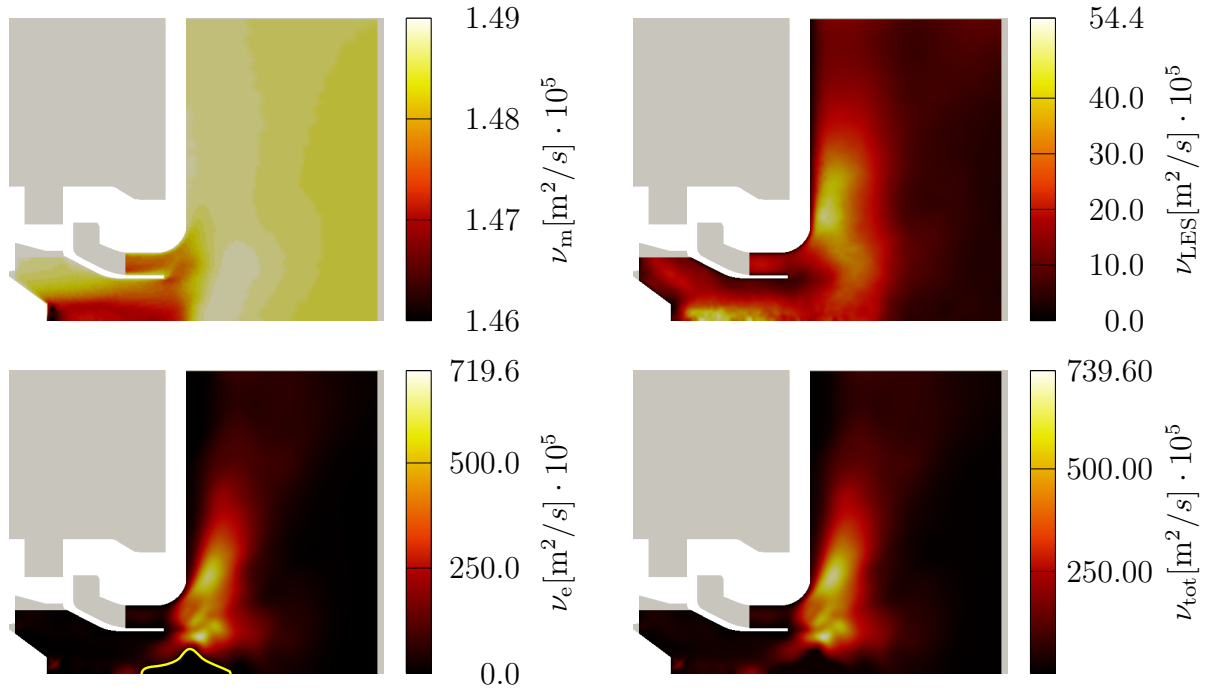


Figure 6.15: Fields of molecular, LES subgrid, eddy and total viscosity for the PreINTRIG configuration, averaged in time and azimuthal direction

for the BiGlobal approach.

In the following, first the local and then the BiGlobal approach of LSA will be applied to the fuel injector.

6.3.1 Results of Local Stability Analysis

To find the global mode, the step-by-step strategy lined out in Section 5.2.4 is applied. In the first step, a temporal stability analysis is performed on the 1-D velocity profiles for various streamwise position and all branches of positive temporal growth rate are identified. Two velocity profiles, one slightly upstream and one slightly downstream of the exit plane of the primary injector are shown in Figs. 6.17(a) and 6.17(c). The respective temporal stability maps are illustrated to their right in Figs. 6.17(b) and 6.17(d). The temporal stability analysis of both branches show various branches, most of which however are of negative temporal growth rate for all axial wave numbers. Nevertheless, it is evident that for the profile outside the primary stage by far more temporal branches related to a positive growth rate occur in comparison to the stability map of the profile within the primary stage. A possible reason for this might be the more complicated flow profile outside of the primary injector.

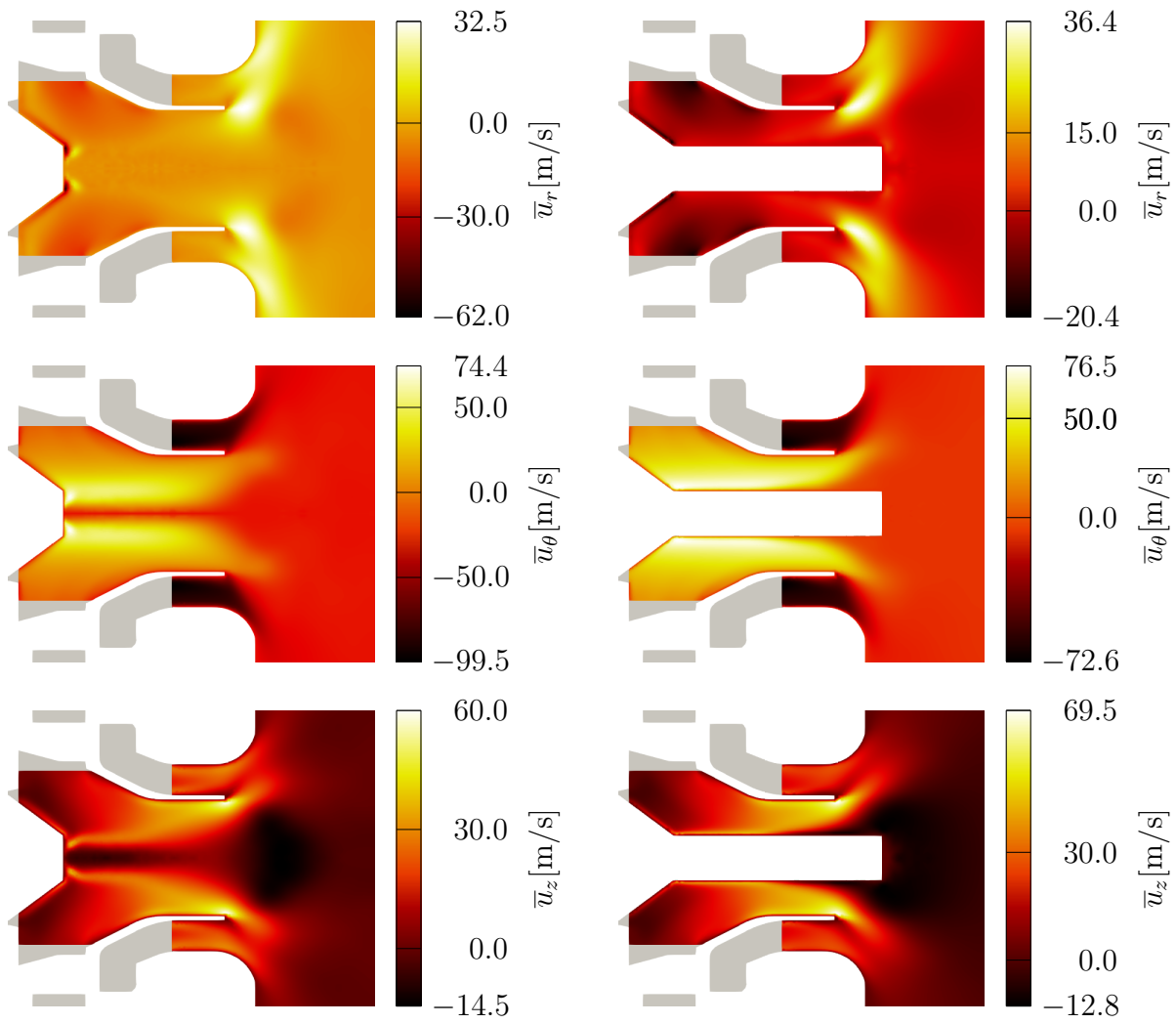


Figure 6.16: Base flow as used as input for the LSA obtained by azimuthally averaging the velocity fields illustrated in Fig. 6.10

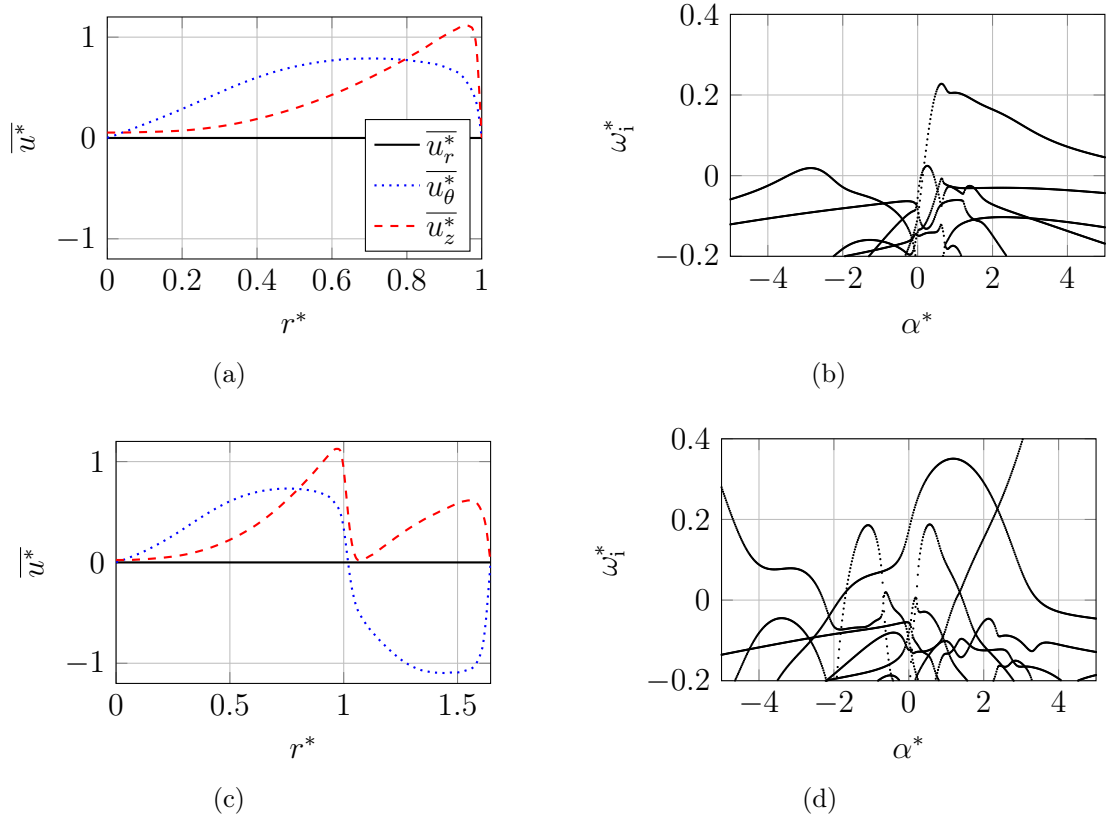


Figure 6.17: Example of local stability for two different axial positions in the swirler; Velocity profile slightly upstream (a) and slightly downstream (c) of the exit plane of the primary injector and their respective temporal stability maps (b) and (d)

While within the primary injector only one turning point in the axial velocity profile occurs (see Fig 6.17(c)), three turning points occur for the profile shown in Fig. 6.17(c). Since the mode occurs especially within the primary injector, only the branches with positive growth rate in the region upstream of its exit plane will be taken into consideration.

In the second step the temporal curves as seen in Fig. 6.17(b) are extended to the complex α -plane and saddle points, which are related to a wave with zero group velocity, are identified. It is worth mentioning, that among all branches occurring within the primary injector, only one branch with positive temporal growth rate could be identified, which showed a saddle point in the complex α -plane. This saddle point is shown in Fig. 6.18 for the velocity profile illustrated in Fig. 6.17(a). In general this is not the case for flows which are prone to a PVC, since they most often show various saddle points, which must be taken into consideration. The most outstanding difference between these flows and the PreINTRIG configuration however is that they most often involve PVCs which occur in the free stream jet, while here

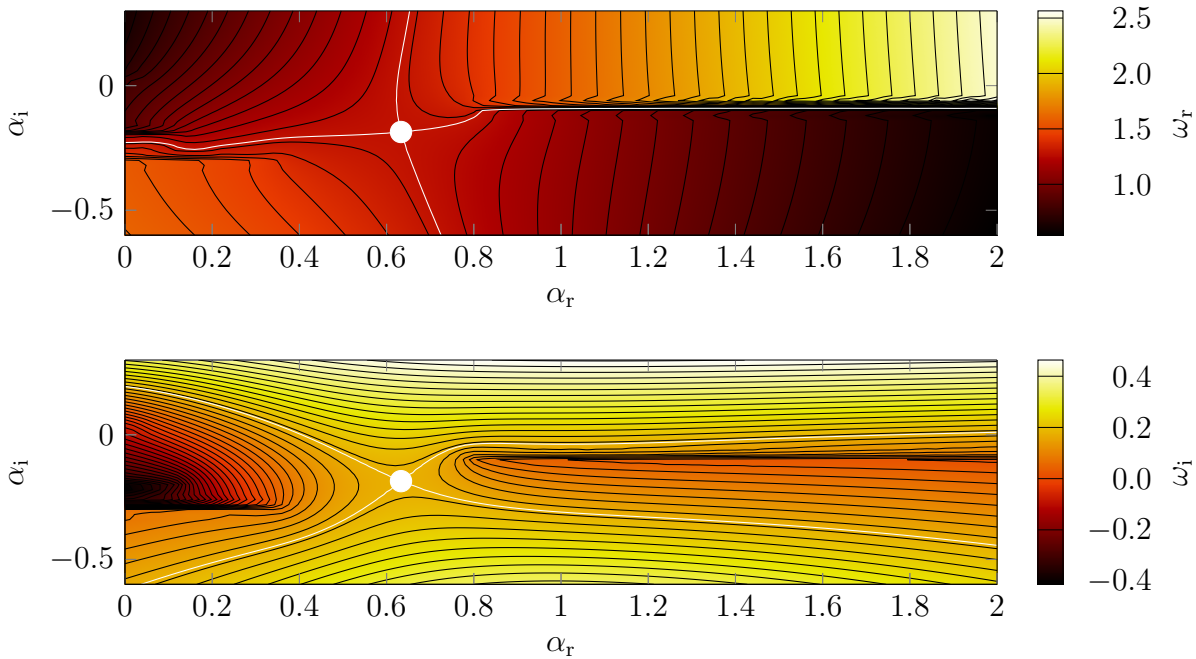


Figure 6.18: Estimation of the absolute frequency by localizing the saddle point of ω in the complex α -plane

the flow is strongly confined within the (primary) injector. While in a free stream jet an inner and an outer shear layer occurs, in the PreINTRIG case only one shear layer (and a boundary layer) is present. It is conceivable, that the free stream jets therefore pose a more complicated hydrodynamic problem and are prone to more waves of zero group velocity. This assumption was verified by analyzing velocity profiles outside the primary injector (as illustrated in Fig. 6.17(b)), where additionally to the shear layer in the primary injector a second shear layer evolves between the counter rotating flows from the primary and secondary stages. Besides the increased number of temporal branches described above, also several branches showing a saddle point in the complex α -plane could be identified. However, since the mode predominantly occurs in the primary injector, only the saddle point which is present in both the primary and the secondary stage was taken into consideration for the subsequent investigation. The frequency at the saddle point corresponds to the absolute frequency, ω_0 of the streamwise position's velocity profile which the analysis is based upon. The last part of the second step is the tracking of the saddle point in axial direction. The resulting curve, relating the real and imaginary part of the absolute frequency to the stream wise position is illustrated in Fig 6.19. Note that although the velocity profiles vary significantly in stream wise direction (see Fig.6.10) the absolute frequency tracked along the streamwise position shows a smooth curve. Even at the exit plane of the primary injector, where the computational domain increases unsteadily the absolute frequency is successfully tracked,

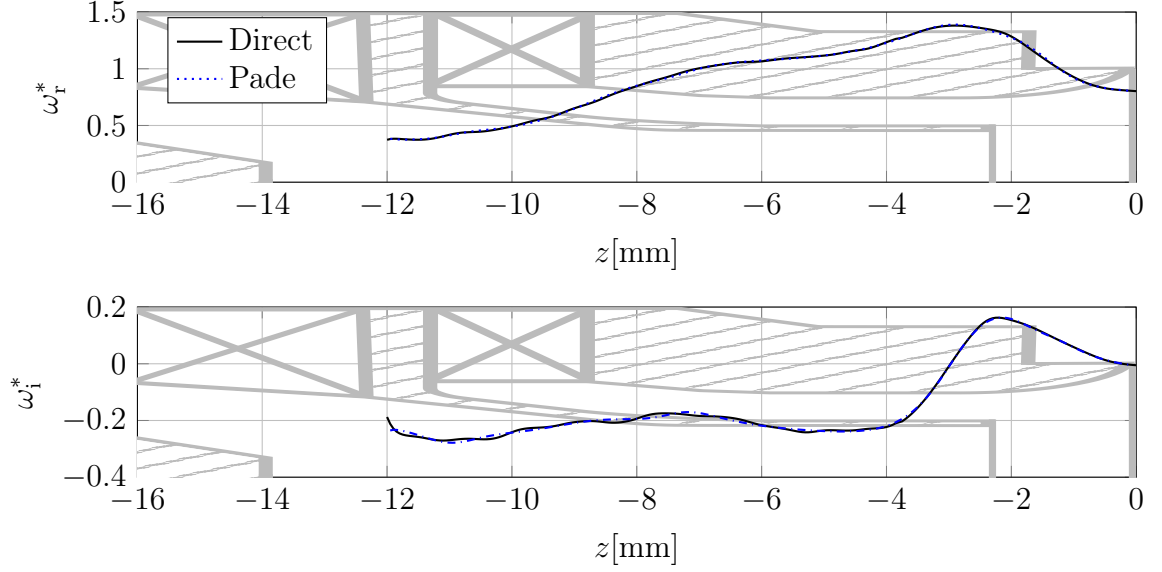


Figure 6.19: Absolute frequency as a function of the streamwise position; the streamwise coordinate is dedimensionalized by the distance between the dump plane and the center body;

showing only a small discontinuous step in its real part.

The third step is the application of the frequency selection criterion based on the work of Chomaz et al. [34]. Here, the streamwise curve absolute instability is expanded by the use of Padé polynomials to the complex Z -plane. The fit by Padé polynomials performed on the real axis of the Z -plane is illustrated in Fig. 6.19, while its expansion to the complex Z -plane is shown in Fig. 6.20. The plane of absolute frequency has a saddle point at $Z_r = -2.2$ mm and $Z_i = 0.27$ mm. The absolute frequency at this point and therefore the frequency of the global mode according to the frequency selection criterion in spatially developing flows is $\omega_g = 1.33 + 0.16i$.

In the last step, the branch switch between the α^+ - and α^- -branch is found and the global mode is reconstructed. A spatial analysis based on the global frequency determined in the preceding step yields the spatial branches shown in Fig. 6.21. The position of the wave maker is found by the streamwise position where the imaginary parts of the α^+ and α^- -branches are equal. Therefore, the wave maker is localized close to the exit plane of the primary injector. For the reconstruction of the global mode, upstream of the wave maker, the α^- -branch must be taken into consideration, while in the α^+ -branch describes the streamwise evolution in positive axial direction. The former shows a positive axial growth rate for all positions upstream of the wave maker. Downstream of the wave maker, the sign of the α^+ -branch changes at $z = -1.8$ mm, indicating a negative axial growth rate of the global mode downstream of this position. An example of the mode shape reconstructed in the cross

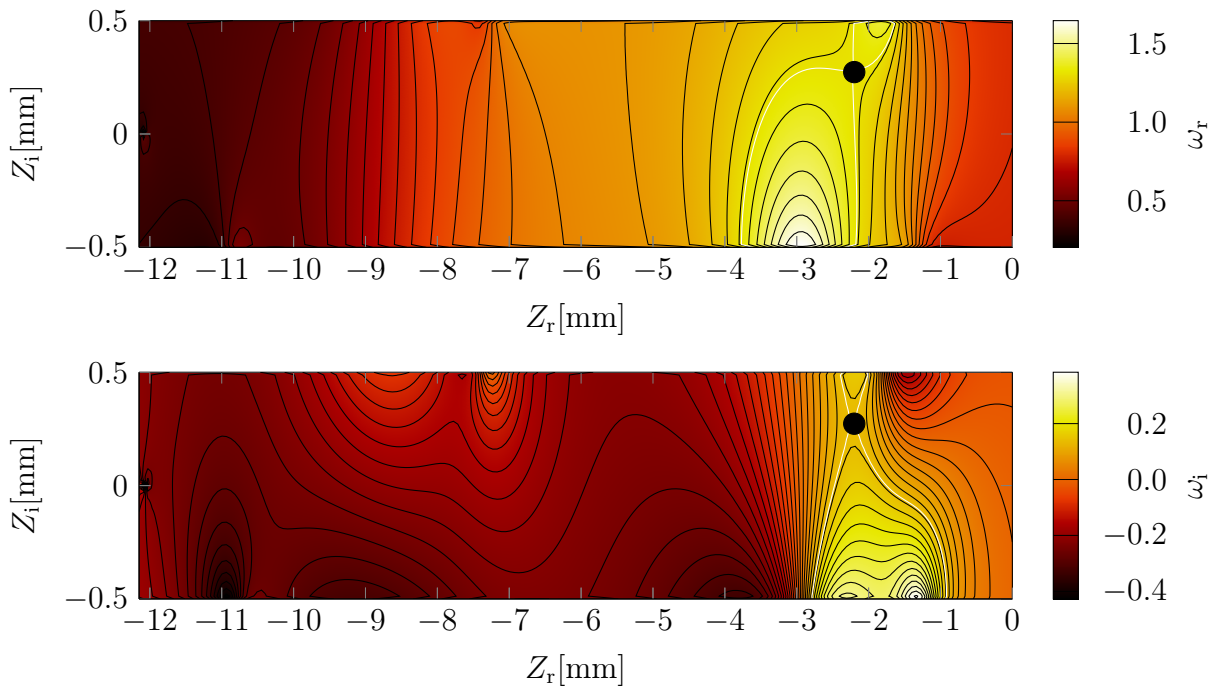


Figure 6.20: Estimation of the global frequency by localizing the saddle point of ω in the complex α -plane

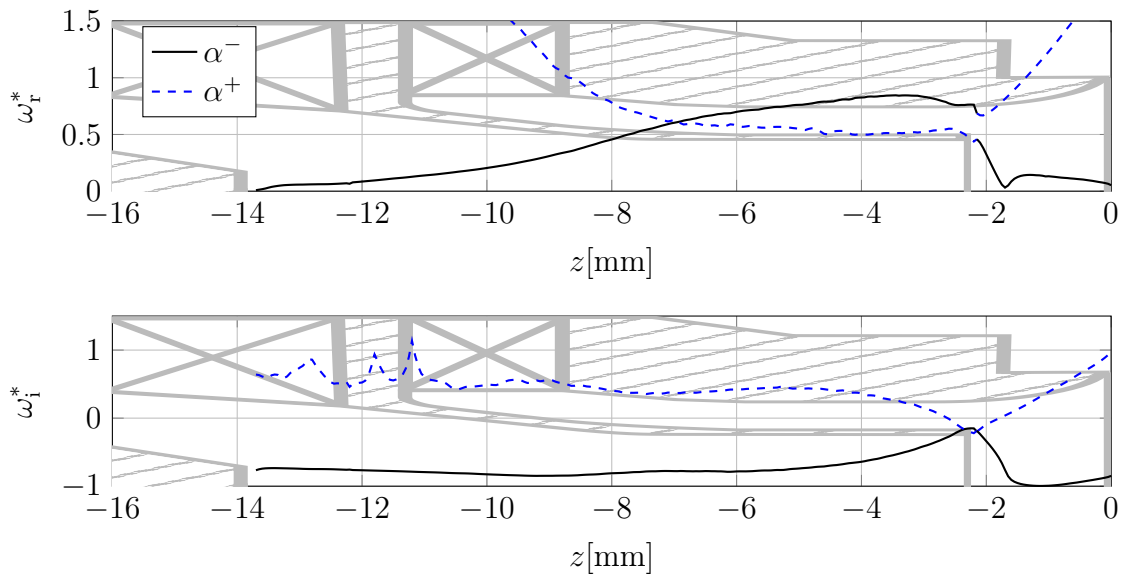


Figure 6.21: α^+ and α^- branches as a function of the axial position; the swirler drafts in the background relate the curves to the corresponding axial position in the flow.

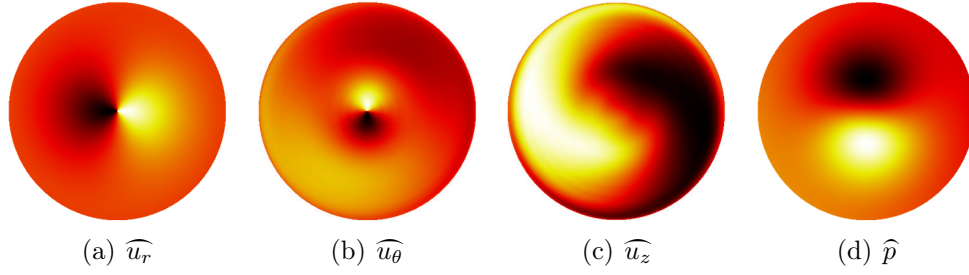


Figure 6.22: Mode shapes based on local stability analysis in a plane in the primary injector ($z = -3$ mm)

section of the primary injector is illustrated for the axial position of $z = -3$ mm in Fig. 6.22, which is equivalent to the illustration of the DMD mode in Figs. 6.12(a)-6.12(d). The local mode shapes based on local LSA analysis appear to match the DMD modes with very high accuracy within the primary injector.

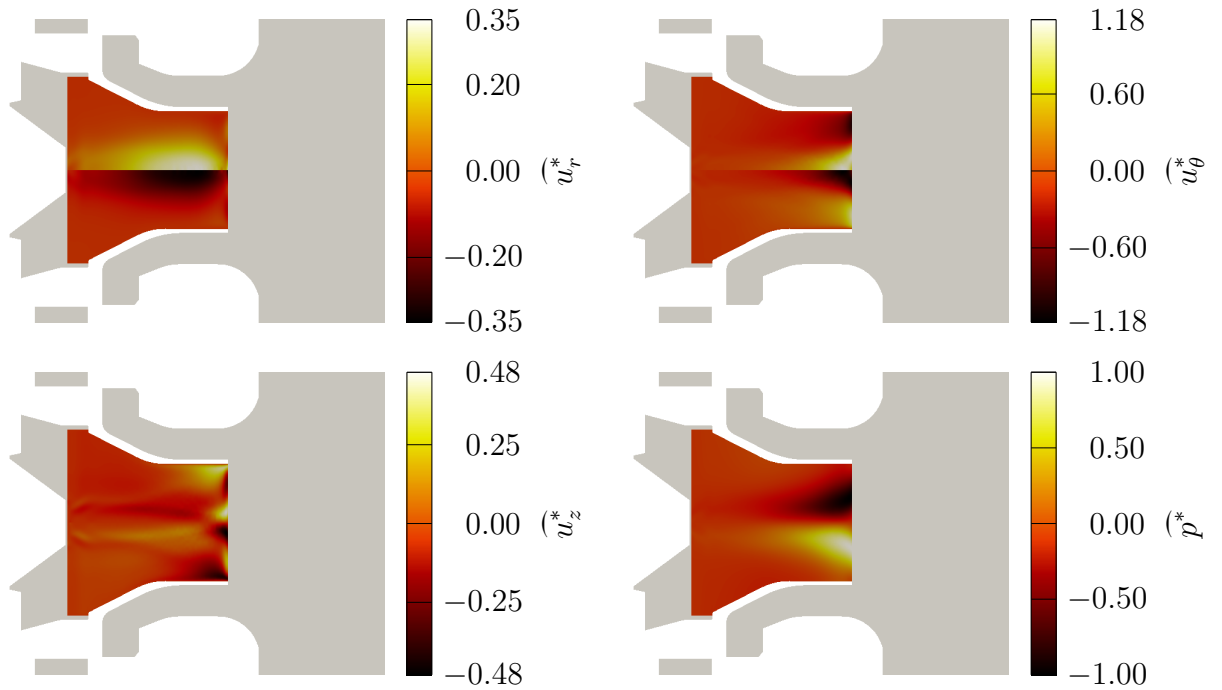


Figure 6.23: Reconstructed mode shapes based on local stability analysis in the r - z -plane

Figure 6.23 shows the reconstruction of the global mode within the primary injector according to Eqn. (5.2.28). For the reconstruction the maximum pressure of the eigenvector was taken both as reference for the azimuthal angle of the mode as well as its magnitude. Concerning the mode shapes outside of the primary injector, the reconstruction is obstructed by

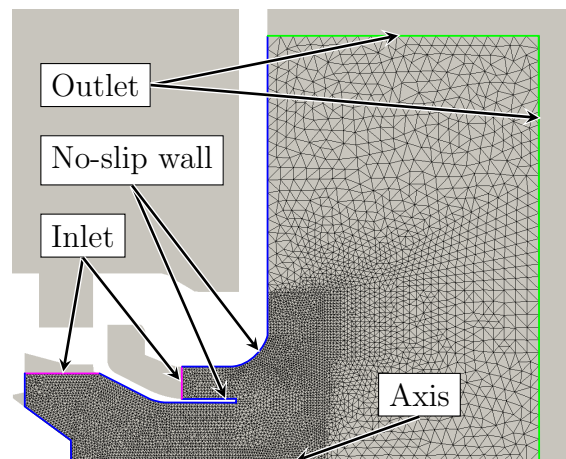


Figure 6.24: Numerical domain and grid for the BiGlobal LSA, exemplary for the no-rod configuration

two reasons. Firstly, outside the primary injector the flow is extremely non-parallel. The streamwise amplification/dampening of the mode does not at all correspond to the one seen in the DMD modes. Secondly, the ratio of the pressure modes to the corresponding velocity modes changes across the cross section increase. This leads to an abrupt increase of the magnitude of the velocity modes at the exit plane of the primary injector. In contrast, within the primary injector the mode shape is surprisingly accurate considering the non-parallel flow field. The pressure fields as well as the radial and azimuthal velocity component correspond well to the DMD of the LES snapshots. Some discrepancies are visible close to the exit plane of the primary injector for the axial component.

6.3.2 Results of BiGlobal Stability Analysis

The results in Sections 6.1 (experimentally) and 6.2.3 (numerically) demonstrate that mounting a rod in the center of the primary injector stabilizes the hydrodynamics in the injector. The aim of this section is to explain this effect with the aid of BiGlobal stability. In the process of BiGlobal stability analysis, neither a parallel flow assumption is made nor the global field has to be reconstructed from local 1D profiles as performed in the preceding section. BiGlobal stability therefore is by far more straightforward than the local stability analysis.

6.3.2.1 No-Rod Configuration

The analysis begins with the no-rod case. The computational domain for the BiGlobal LSA is illustrated in Fig. 6.24. The elements in the coarse region far from the instability is $\Delta x = 0.9$ mm, while the refined region uses elements of grid size $\Delta x = 0.2$ mm. The initial guess for the shift and invert method applied to solve the GEVP for the cold flow case of the PreINTRIG configuration is set to 1.7, which is close to the value expected based on the DMD of LES snapshots. The algorithm terminates after 100 eigenvalues are found. The resulting frequency spectrum is illustrated in Fig. 6.25. The large majority of eigenvalues is

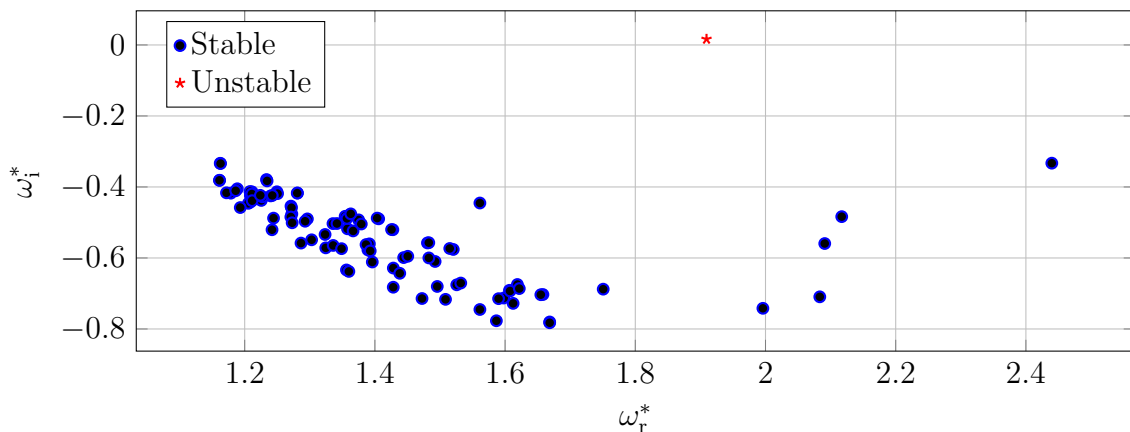


Figure 6.25: BiGlobal spectrum of the no-rod case

related to a negative temporal growth rate. In many cases, the modes in the global spectrum are arranged in a regular manner, so that they can be classified into different branches, where the mode shapes within a branch are of similar nature (see e.g. [250, 180, 37]). In the present configuration however, the eigenvalues do not organize in a regular manner but accumulate in a cloud in the spectrum. One eigenvalue ($\omega_g = 1.89 + 0.01i$) nevertheless stands out and is approximately of a zero growth rate (see star in Fig. 6.25), which is expected for modes at the limit cycle, since their amplitude does not change in time. Its frequency is approximately 18% higher than the mode occurring in the LES. The mode shapes of the corresponding BiGlobal mode are illustrated in Fig. 6.26. Pressure and axial velocity agree well with the DMD mode shown in Fig. 6.14. This is also the case for the mode shapes of azimuthal and radial velocity outside the primary injector. Upstream of the primary injector close to the axis however, the mode shapes of especially the latter velocity components differ from the mode seen in the LES. A possible reason for this is that all along the center axis until the location of vortex break down downstream of the primary injector, all mean flow velocity components are of very low magnitude. In the derivations of the governing equations it was however assumed, that the amplitude of the coherent structure is small in comparison to the mean flow. While by default the axial velocity is zero on the center axis for a single helical

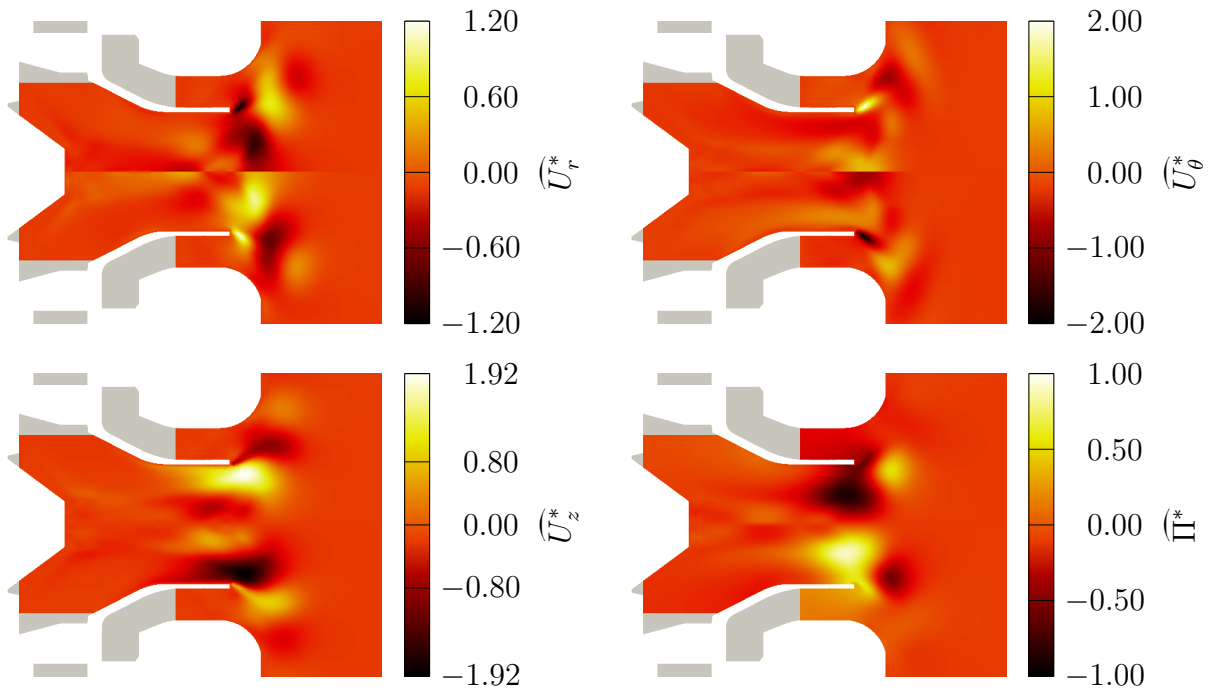


Figure 6.26: BiGlobal mode shapes of the no-rod configuration in the r - z -plane

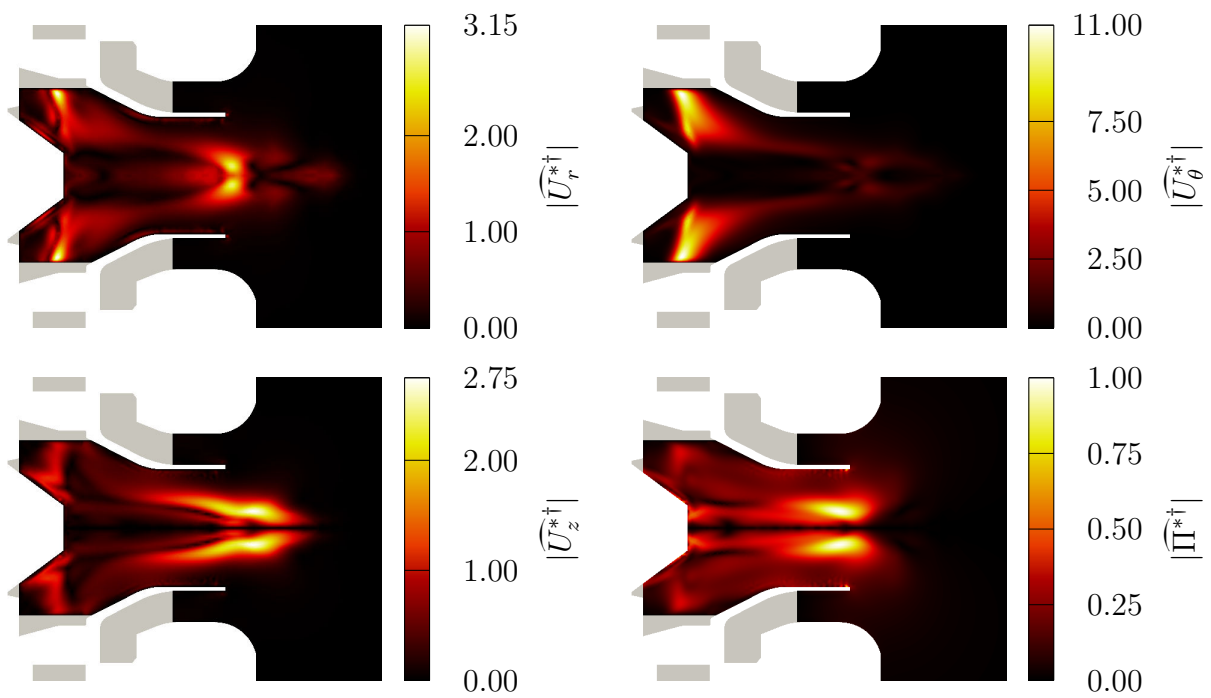


Figure 6.27: Adjoint BiGlobal mode shapes of the no-rod configuration in the r - z -plane

instability (see Section 5.2.1.2), comparing Figs. 6.12 and Fig. 6.10 shows that especially radial and azimuthal velocities exceed the mean values by far in this region. It is surprising however that the local approach yields better results within the primary injector, while relying on more simplifications than the global approach.

Fig. 6.27 illustrates the magnitude of adjoint eigenvectors of the mode illustrated in Fig. 6.26. While the maximum of both the pressure and the axial velocity component of the adjoint mode are located at the exit plane of the primary injector, the maxima of the corresponding radial and azimuthal velocities are close to the intersection between the vanes and the primary injector. Especially the azimuthal component shows very high values in this region. Since

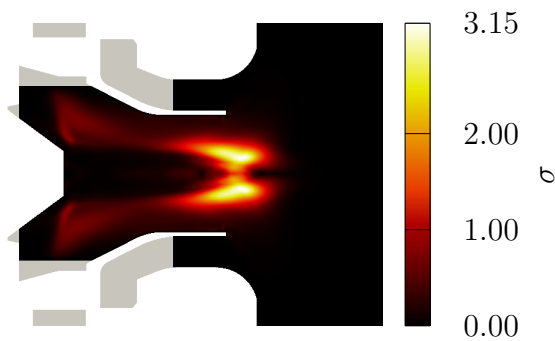


Figure 6.28: Structural sensitivity of the no-rod configuration

the adjoint modes show the sensitivity to periodic forcing, it can be concluded that it is most practical and efficient to force or control the PVC by pulsing the flow directly at the vanes. This actuates both the radial and azimuthal velocity component, where they are most receptive. The location of highest sensitivity to axial velocity forcing is far from any wall or inlet and therefore is difficult to actuate.

Furthermore, the structural sensitivity, based on Eqn. (5.2.15), is shown in Fig. 6.28. The figure demonstrates that the maximum of structural sensitivity and therefore the region of strongest feedback is located at the exit plane of the primary injector. These results are in line with the results of the local LSA, which localized the wave maker at the same position. The fact that this axial position also coincides with the region just upstream of the breakdown bubble is in line with several other studies (e.g. Quadri et al. [198], Tammisola et al. [240], Oberleithner et al. [?]). It seems that this is an universal finding. The result therefore is a very important information for gas turbine engineers: If an engineer wants to interfere with the feedback mechanism in some manner, it is most efficient to aim at the region upstream of the breakdown bubble.

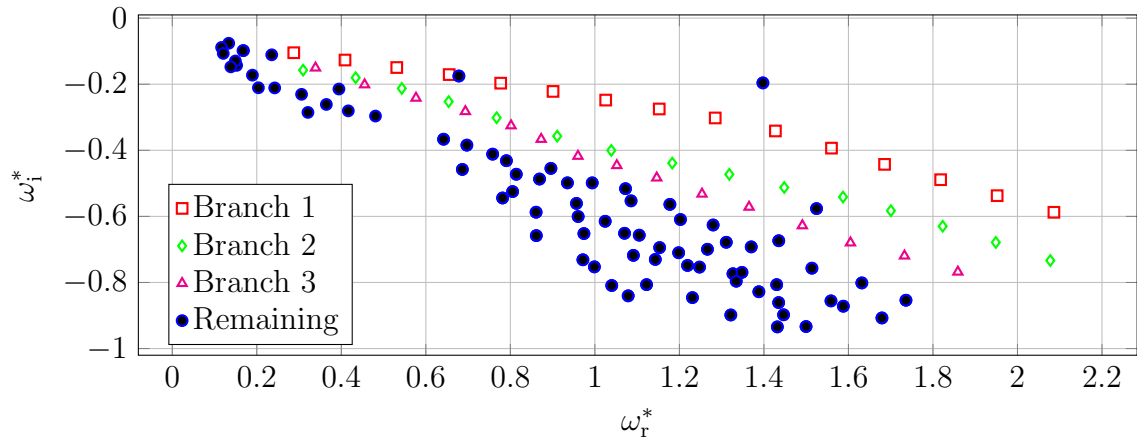


Figure 6.29: BiGlobal spectrum of the rod configuration

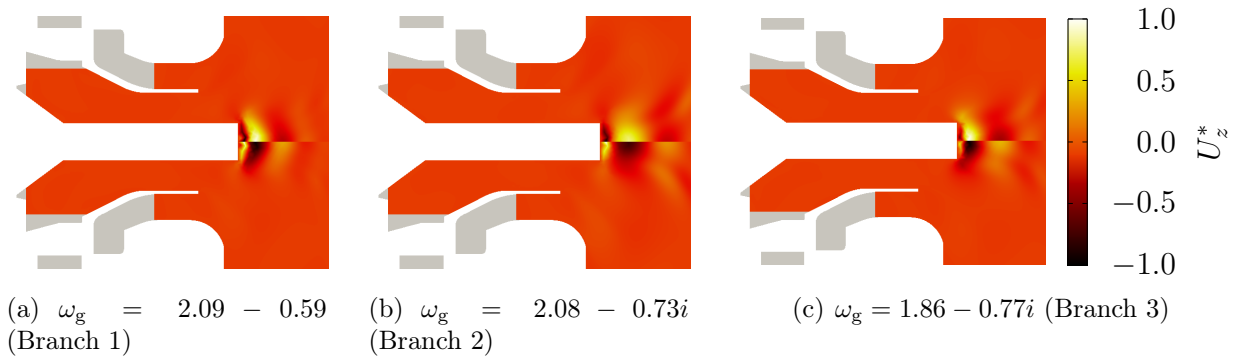


Figure 6.30: BiGlobal Mode shapes of Branches 1, 2 and 3 (see Fig.6.29) in the r - z -plane

6.3.2.2 Rod Configuration

Next, the flow field of the rod case is examined. The specifications of the mesh correspond to the mesh in the no-rod case. The resulting spectrum is illustrated in Fig. 6.29. Note that here three modes, corresponding to non-physical mode shapes with their maximum on the inlet boundary condition of the primary injector were discarded for this plot. The striking feature of the spectrum is, that all modes which are related to physical mode shapes are of negative temporal growth rate. While in the no-rod configuration, only a cloud of mode shapes with highly negative growth rates appeared, for the rod configuration in Fig. 6.29 at least three branches are present, which occur in a regular pattern in the spectrum. All of these three branches are related to modes which have highest amplitudes downstream of the rod, as shown in Fig. 6.30, which illustrates the axial velocity perturbations for the three different branches. Like in the spectrum of the no-rod configuration, also here a mode stands out which is of frequency $\omega^* \approx 1.4 - 0.2i$ and has a comparably high imaginary part, even if it is still a damped mode. This corresponds to a temporal frequency of the mode in dimensional

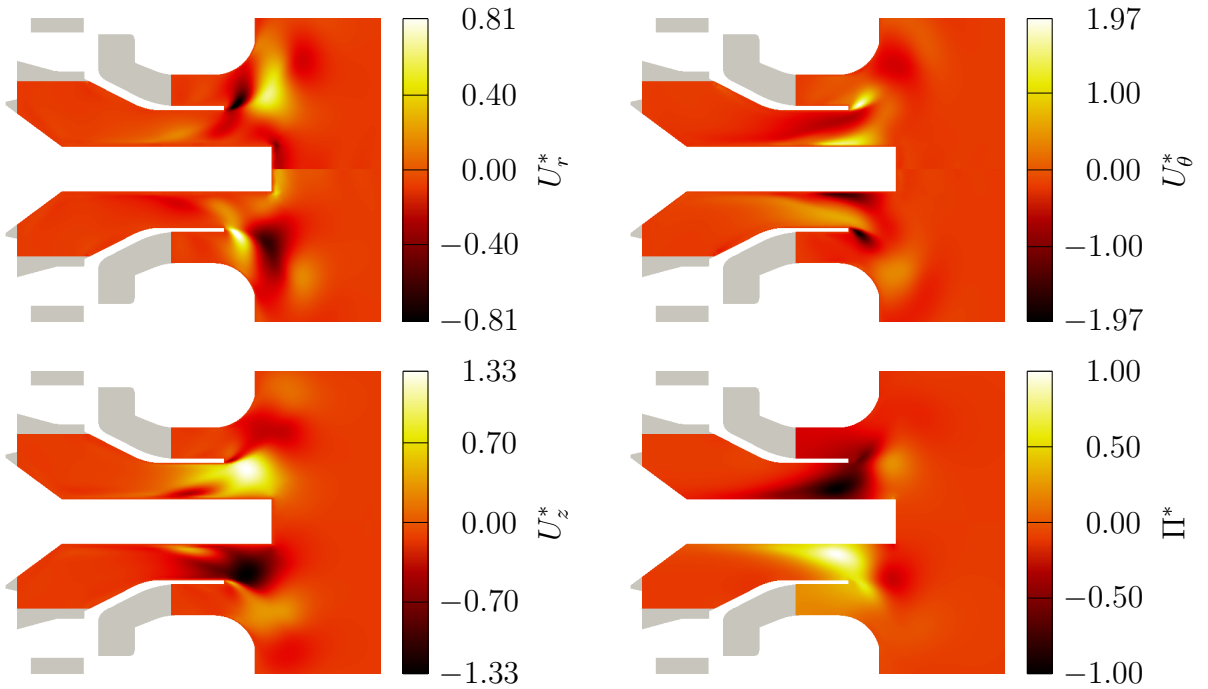


Figure 6.31: BiGlobal mode shapes of the rod configuration in the r - z -plane

space of $f \approx 2650$ Hz, which is in very good agreement with the elevation in the experimental SPL spectrum, the numerical pressure spectrum and the DMD spectrum. The corresponding mode shapes are shown in Fig. 6.31. The resemblance of the BiGlobal mode shapes with the DMD mode shapes illustrated in Fig. 6.14 is extraordinary well, too. At first glance it is

however surprising that a mode with a negative temporal linear growth rate appears in the LES. Nevertheless, it is conceivable that the mode appears as a consequence of intermittent triggering by turbulence and thereupon decays slowly. Besides the negative growth rate, the broad band elevations in the frequency spectra, in contrast to the sharp spikes in the no-rod configuration, and the erratic DMD mode shapes support this hypothesis. In order to further test this assumption, Poincaré plots, are illustrated in Fig. 6.32. These plots relate the experimental pressure fluctuation at time t to the pressure fluctuation at time $t + n\tau$, where τ corresponds to the period of the fluctuation, and $n = 1, 2, 3$. The period for the no rod configuration is based on $f = 2500$ Hz, approximately the center of the elevation in the experimental SPL spectrum. The Poincaré plots in Fig. 6.32(a) show that even after a time shift of $\Delta t = 3\tau$, the signal correlates very strongly with the initial signal. In the rod case in contrast (see Fig. 6.32(b)), the correlation even after $\Delta t = \tau$ is very erratic. Furthermore, the pressure signals p_t^* and $p_{t+3\tau}^*$ do not show any correlation anymore, as can be seen on the right in Fig. 6.32(b). The Poincaré plots therefore confirm *a posteriori* the hypothesis, that the mode is triggered intermittently in the rod case, while in the no-rod case it is triggered by a feedback loop and appears at its limit cycle.

6.4 Conclusion and Interpretation

This chapter focuses on the cold flow in a two-staged, swirled, industrial fuel injection system of highly complex geometry. Although in the experiment a loud whistling noise is audible and a strong spike in the SPL spectrum appears at approximately $f \approx 3150$ Hz, POD of PIV snapshots does not reveal any coherent structures. Nevertheless, it is shown that the whizzing noise disappears if a rod is mounted at the axis of the primary injector, leaving behind a broad-band but low amplitude elevation of the SPL spectrum at around $2250 \text{ Hz} < f < 2750 \text{ Hz}$. The phenomenon of the whistling sound is thereupon investigated by LES means, which are successfully validated against the experimental mean fields of the no-rod configuration and the corresponding frequency spectrum. A DMD analysis based on LES snapshots explains the occurrence of the whistling sound in the experiment. The flow is prone to a strong PVC of azimuthal wave number $m = 1$ in the interior of the primary injector. Its frequency matches the experimental pressure oscillations (see Tab. 6.1). The mode decays spatially before the flow reaches the downstream plenum and therefore the PVC remains invisible to experimental means, which are only applicable downstream of the dump plane.

Subsequently, both local and BiGlobal LSA analysis is performed on the LES mean flows. The local approach underestimates the frequency of the LES by approximately 17%. Both the α^+ -branch and the α^- -branch were successfully tracked along the axis, even across the cross section jump at the exit plane of the primary injector. While the approach yields very

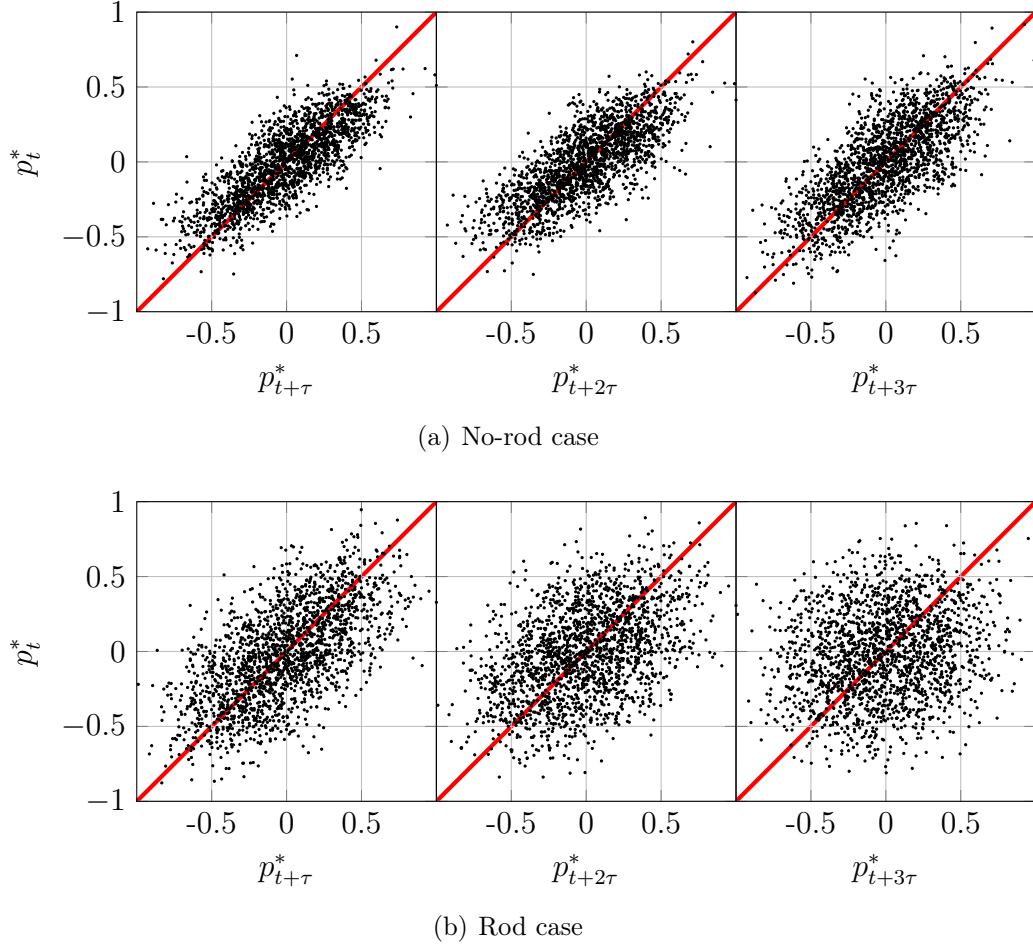


Figure 6.32: Pointcaré plots for the normalized pressure signal for both the no-rod (a) and the rod case (b) for several time shifts, $\Delta t = t + n\tau$

	Exp.	LES	Local	BiGlobal
Nondimensional frequency ω_r	1.66	1.60	1.33	1.89
Nondimensional growth rate ω_i	0	0	0.16	0.01
Error $\epsilon(\omega_r)$	—	-3.2%	-17%	+18%
Error $\epsilon(\omega_i)$	—	0	+10%	+0.6%

Table 6.1: Comparison of nondimensional PVC frequencies and growth rates in the no-rod configuration based on the experiment, the LES and BiGlobal and local stability analysis; LES errors are with respect to the experiment, while LSA errors are based on the LES frequencies. Errors of growth rates are based on the frequency of the oscillation.

good results concerning the mode shape reconstruction in the interior of the primary injector, the approach fails in reconstructing the mode shapes outside of the primary injector, due to a strong violation of the parallel flow assumption in this region.

The global approach overestimates the LES frequency by about 18%. Since it is not restricted by the parallel flow assumption, the mode shapes correspond well to the DMD modes based on the LES both in the interior and outside of the primary injector. However, upstream of the exit plane of the primary injector especially the radial and azimuthal components show some discrepancies from the DMD mode. Both BiGlobal and local LSA identify the exit plane of the primary injector as the origin of the perturbation, or the wave maker region. While the BiGlobal eigenfrequency is of approximately zero growth rate, which is assumed for a flow at a limit cycle, the local analysis overestimates the growth rate, by about 10% of the absolute frequency (see Tab. 6.1). This is in line with the observation of Juniper et al. [105] who found that in the case of confined wake flows the local approach overestimates the temporal growth rate, while the BiGlobal approach produces more precise results. The adjoint modes based on the BiGlobal analysis demonstrate that the PVC is most sensitive to azimuthal and radial forcing at the intersection of the primary injector and the vanes. These results show, that the best way to control or force the PVC is to directly perturb the flow at the primary injector vanes.

The local stability analysis produces surprisingly good results considering the highly non parallel flow field even within the primary injector. It can be concluded, that the approach can be generally applied when investigating hydrodynamic instabilities in complex geometries. Nevertheless, the limits of the approach are demonstrated by the failed attempt to reconstruct the mode shapes outside of the primary injector, where the flow is extremely non-parallel. The global approach, which is not restricted by a parallel-flow assumption can be applied to all geometries. Nevertheless, other problems emerge with this approach. While the approach of using unstructured FEM applied in this study avoids the problem of structured meshes in complex geometries, a remaining challenge of global codes is the question of applying the correct boundary conditions. While the right eigenvectors seem to be sufficiently far away from all inlets and outlets, the maximum of the adjoint modes of the radial and azimuthal velocity component are very close to the inlet of the domain. Therefore, these results should be seen with the appropriate scepticism. Experimental or numerical investigations directly examining the sensitivity to forcing in the corresponding region could presumably resolve this open question. Another way to address this question would be to solve a full three-dimensional stability analysis of the problem, where the primary injector vanes are included in the domain, since then the boundaries of the computational domain could be chosen arbitrarily.

Furthermore, LES of the rod configuration are performed. Again the numerical results are in good agreement with the experiment, with regard to the frequency content of the respective spectra. While the high amplitude peak, that caused the whistling sound in the experiment

disappears, a broad band elevation of the pressure spectrum in the interior of the primary injector emerges. A DMD of the corresponding LES snapshot reveals that this elevation is related to a PVC in the interior of the primary stage, which, judged from its mode shapes seems to correspond to the one in the no-rod configuration. Nevertheless, the mode is of significantly lower amplitude and shows somewhat erratic mode shapes. A BiGlobal stability analysis shows that the mode is of a negative temporal growth rate. A Poincaré plot of the experimental pressure traces of the no-rod and the rod configuration confirms, that the PVC in the no-rod case is at a stable limit cycle, while it is triggered intermittently by turbulence and thereupon decays in the rod case.

Chapter 7

Reactive Simulations of the PreINTRIG Configuration

In the previous chapter, the non-reactive flow in a two-staged, counter-rotative industrial fuel injection system was under investigation. Central aspect of the investigation was the PVC occurring in the interior of the primary stage. It was shown by experimental measurements, LES and hydrodynamic LSA, that the presence of a rod at the injector axis stabilizes the flow with respect to this instability.

In this chapter, the focus is on LES and hydrodynamic stability of a reactive methane-air flow in the same configuration. The goal of this chapter is twofold:

1. Investigate the effect of a flame on the stability of the flow
2. Examine the effect of the central rod on the stability of the flow and the flame

These goals are pursued by LES and LSA. The base flows for the LSA will be provided by the LES. Section 7.1.1 outlines the numerical set-up and strategy for reactive LES. The corresponding results are presented in Section 7.1.2. The LES mean flows will serve as the base flows for the BiGlobal LSA discussed in Section 7.2. The results are concluded in Section 7.3.

7.1 Reactive LES

No experimental investigations were conducted for reacting mixtures in the PreINTRIG configuration. Therefore, the LES presented in this chapter remain without experimental validation with respect to the flame shapes. Nevertheless, the validation in the cold flows performed in Section 6.2.2 shows that the non-reacting flow features are well captured.

7.1.1 Numerical Set-Up for Reactive LES of the PreINTRIG Configuration

In order to include combustion in the simulation, the numerical strategy of the non-reactive case is extended by the BFER-combustion model [71]. It accounts for two reactions and six species in methane-air combustion and predicts adiabatic flame temperatures and laminar flame speeds over a wide range of operating points. Adaptive flame thickening is applied.

Figure 7.1 shows the domain and mesh for the reactive case. The upstream plenum is a cylinder of diameter $d = 50$ mm and length $l = 69$ mm and is slightly smaller than in the non-reacting case. A second cylindrical plenum of diameter $d = 60$ mm and length $l = 99$ mm downstream of the swirler replaces the half sphere modeling the free atmosphere in the cold flow simulations and confines the hot gases. NSCBC boundary conditions model the inlet and the outlet, with reflection coefficients of $K = 1500$ and $K = 500$, respectively. The walls of the upstream plenum and the swirler, including the rod in the rod case, are set to iso-thermal walls, where the fresh gas temperature, $T = 292.0$ K, is imposed. The walls in the downstream plenum are heat-loss walls, which model the heat conduction in the material of the confinement. The values chosen correspond to a steel confinement of 10 mm thickness, with a surrounding ambient temperature of 500 K. The grid size within the flame and the swirler is set to $220 \mu\text{m}$, while it refines to $150 \mu\text{m}$ close to the interior walls of the swirler. The flame is dynamically thickened to achieve a number of eight cells in the flame front, which for a stoichiometric methane-air mixture yields a thickening factor of approximately 4 for the present mesh grid size.

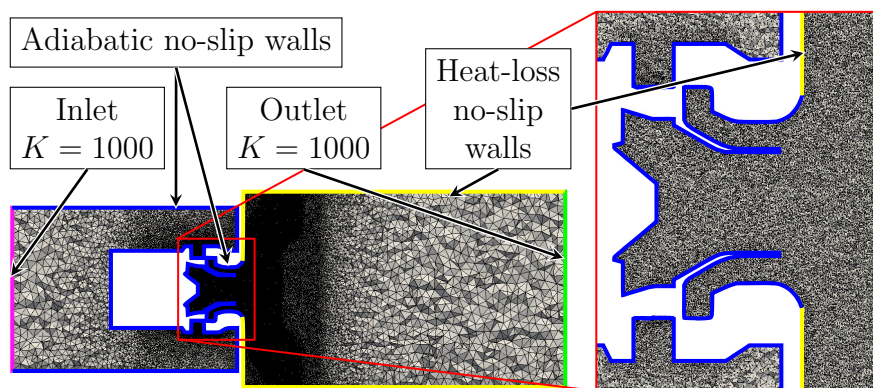


Figure 7.1: Numerical domain and grid for the reactive simulations

7.1.2 Results

7.1.2.1 Influence of the Rod on the Temporal Means

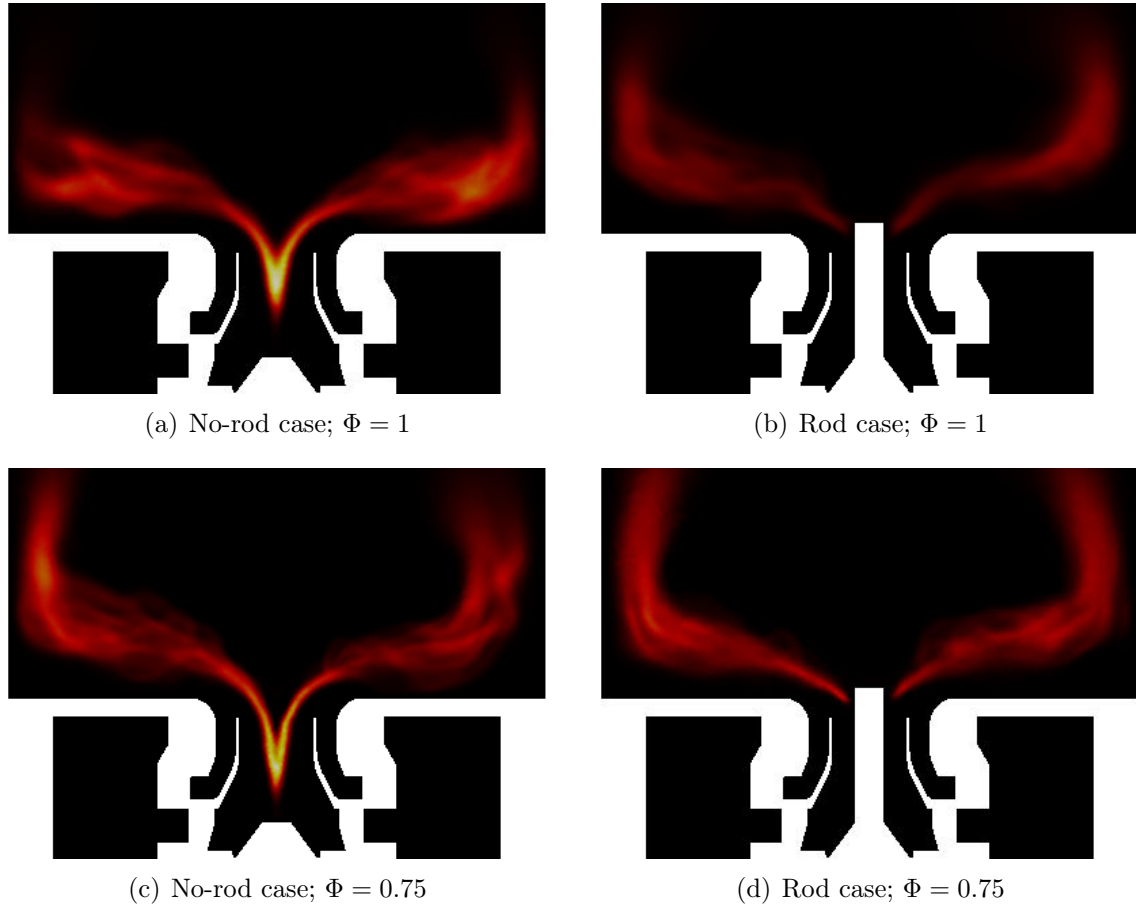


Figure 7.2: Temporal mean of heat release rates indicating the flame shapes for the rod and no-rod case for equivalence ratios of $\Phi = 0.75$ and $\Phi = 1.0$; $\dot{V} = 3.4 \text{ ls}^{-1}$

Figure 7.2 illustrates the flame shapes for the rod and the no-rod case for stoichiometric and lean conditions and a flow rate of $\dot{V} = 3.4 \text{ ls}^{-1}$. For both equivalence ratios illustrated, the flame anchors in the CRZ within the primary injector for the no-rod case. Unlike in the cold flow simulations, where the mean flow was superimposed by a strong PVC, in the reactive flow simulations no coherent structures appear in the primary injector. The anchoring point of the flame therefore remains almost unperturbed leading to the very high means in volumetric heat release rate in this region. In the downstream plenum, the flame angle is very high leading to a flat flame shape. Due to the lateral confinement, the flame bends up above the Outer Recirculation Zone (ORZ).

In Figs. 7.2(b) and 7.2(d) the flame shapes at the same operating points are illustrated for the rod configuration. Since the temperature at the rod is set to the fresh gas temperature, the anchoring of the flames close to the tip of the rod can not be related to an ignition at a hot wall, but in the CRZ. For both equivalence ratios the anchoring appears to be at the same location as in the no-rod case. Also the global flame shapes are very similar for the no-rod and the rod case. Solely, the flames in the rod configuration are slightly longer. This is due to the location of the rod, which is placed where the mean heat release is the highest in the no-rod configuration.

7.1.2.2 Blow-off in Lean Flames

In this section, the influence of the central rod in the primary injector on the flame blow-off in the lean regime is investigated. To do so the flow rate is gradually increased for both the rod and the no-rod configuration at an equivalence ratio of $\Phi = 0.725$. The respective mean heat release rates for a flow rate of $\dot{V} = 3.83 \text{ ls}^{-1}$ are illustrated for various flow rates in Fig. 7.3. Note, that especially for the rod-case and high flow rates, the flame extends beyond the region of highest spatial grid resolution (see Fig. 7.1). The region of flame anchoring however is highly resolved in all cases. Since the focus of this section is on the blow off and therefore the flame anchoring mechanism, it is assumed that the lower resolution at the flame tips has a minor impact on this analysis.

Figures 7.3(a) and 7.3(b) demonstrate, that the global flame shape of the rod and the no-rod configuration is rather similar. Nevertheless, the flame in the no-rod configuration appears to be more steady. As in the flame shapes illustrated in the previous sections, the flame in the rod configuration is longer. For the operating point illustrated in Figs. 7.3(a) and 7.3(b) this effect is more distinct than in the ones shown in the previous section.

The flow rate is gradually increased. The resulting flame shapes are illustrated in Fig. 7.3. It appears that the flame in the no-rod configuration blows off between the flow rates 3.83 ls^{-1} and 5.11 ls^{-1} . In the rod-case on the other hand the flame remains anchored in the CRZ even for very high flow rates of $\dot{V} = 6.82 \text{ ls}^{-1}$

The results demonstrate that the rod stabilizes the flame anchoring in the lean regime.

7.2 Stability Analysis of Passive Flames

In the previous section LES results of reactive methane-air flames are shown. It appears that the flame seems to have a stabilizing effect on the PVC. This observation is in line with several prior studies on this topic [171, 246, 239, 206]. It was furthermore shown that the rod in the primary injector prevents blow off for increasing flow rate in the lean regime.

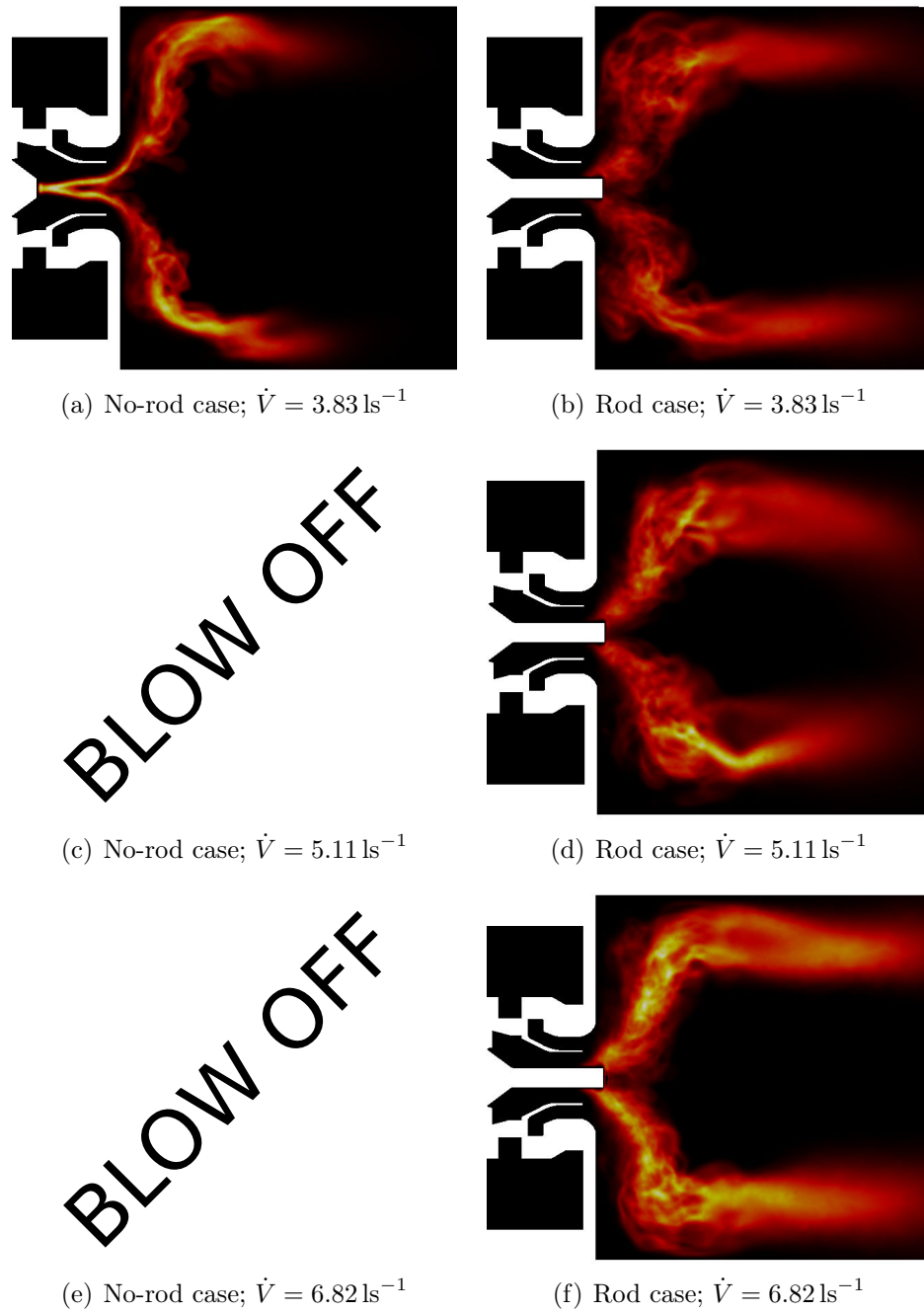


Figure 7.3: Temporal mean of heat release rates indicating the mean flame shapes for various flow rates in the rod and no-rod configuration; equivalence ratio $\Phi = 0.725$

This section addresses the following questions regarding the stability of the PVC in the underlying reacting flow:

1. What is the impact of the density gradient across the mean flame front on the PVC? (Section 7.2.1)
2. What is the influence of the rod on the stability of the PVC? (Section 7.2.2)

7.2.1 Influence of Non-uniform Density on the Stability of the PVC

For quite some time it was scientific consensus, that the increase in kinematic viscosity across the flame front leads to the dampening of coherent structures. Recent studies however suggest that this is not the major mechanism leading in many cases to the disappearance of the PVC in presence of a flame: The strong density gradient through the flame might also play a role. Indeed, Oberleithner et al. [171] and Manoharan et al. [142, 143] demonstrated by local LSA, that including the effect of the density gradient in the analysis across the flame causes a significant decrease of growth rates.

In the framework of this section this mechanism will be investigated by a BiGlobal LSA. Figure 7.4 shows the temporally and azimuthally averaged fields for the velocity components, the density and the viscosity components. The operating point corresponds to a flow rate of $\dot{V} = 1.7 \text{ l s}^{-1}$ and an equivalence ratio of $\Phi = 1.0$. As expected, the molecular viscosity, ν_m , shows an increase from $1.8 \cdot 10^{-5} \text{ ms}^{-1}$ in the fresh gases to approximately $44 \cdot 10^{-5} \text{ ms}^{-1}$ in the burnt gases. Furthermore noteworthy are the regions where the eddy viscosity based on the resolved stochastic fluctuations, ν_e , is negative. As in the cold flow case, these regions are illustrated by the yellow lines in Fig. 7.4. Although regions of negative eddy viscosity were estimated in the cold flow case as well (see Fig. 6.15), these regions are much larger here. In addition, these regions seem to appear close to the flame. It seems that the Boussinesq approximation, which is used to obtain the eddy viscosity, ν_e , fails at least close to the flame to provide reasonable values for the eddy viscosity acting on the coherent structures. The fields illustrated in Fig. 7.4 are the direct input for the hydrodynamic stability analysis.

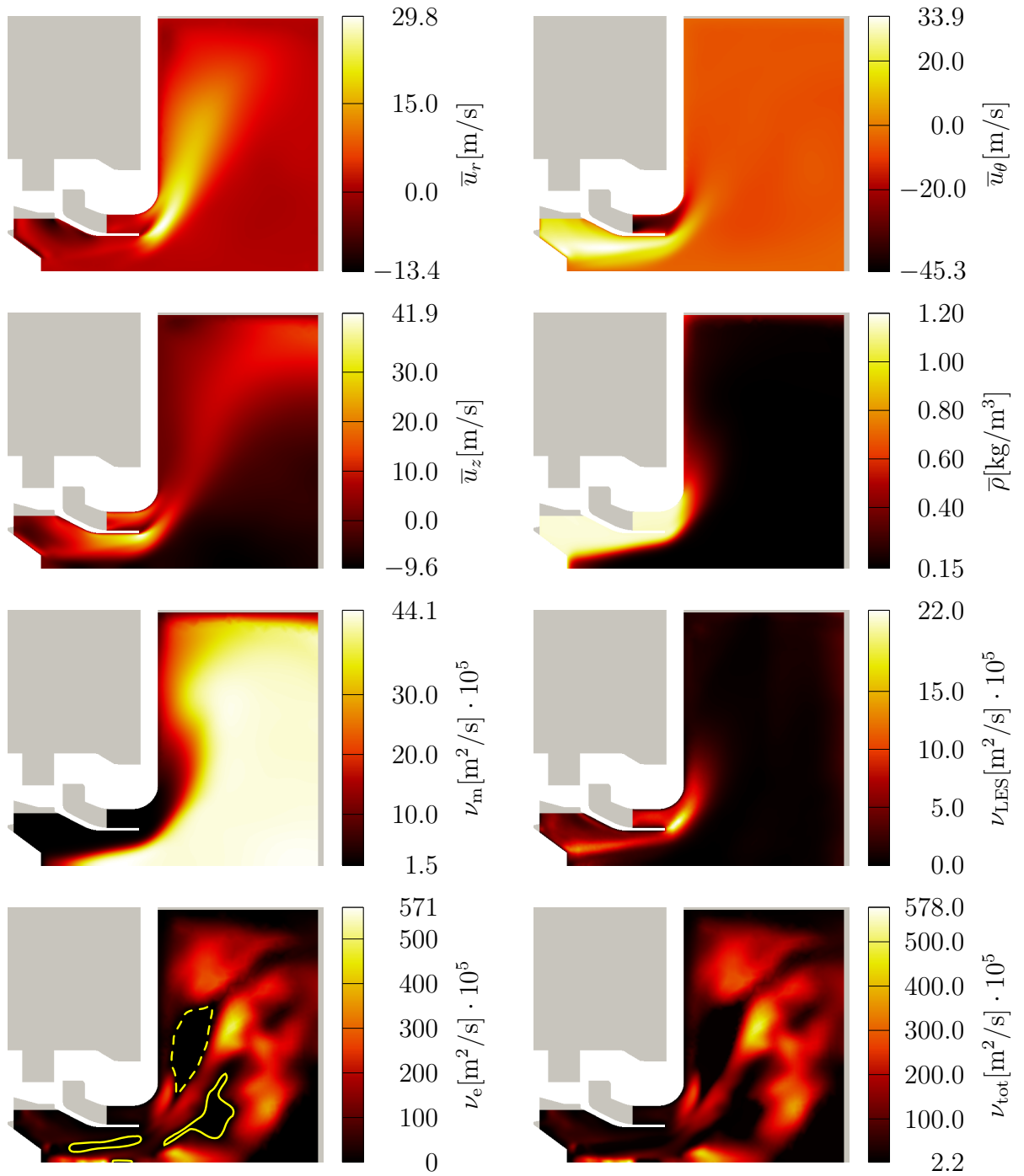


Figure 7.4: BiGlobal mean fields based on reactive LES; $\Phi = 1.0$; $\dot{V} = 1.7 \text{ ls}^{-1}$

7.2.1.1 Stability Analysis of a Reacting Flow Ignoring the Density Gradient

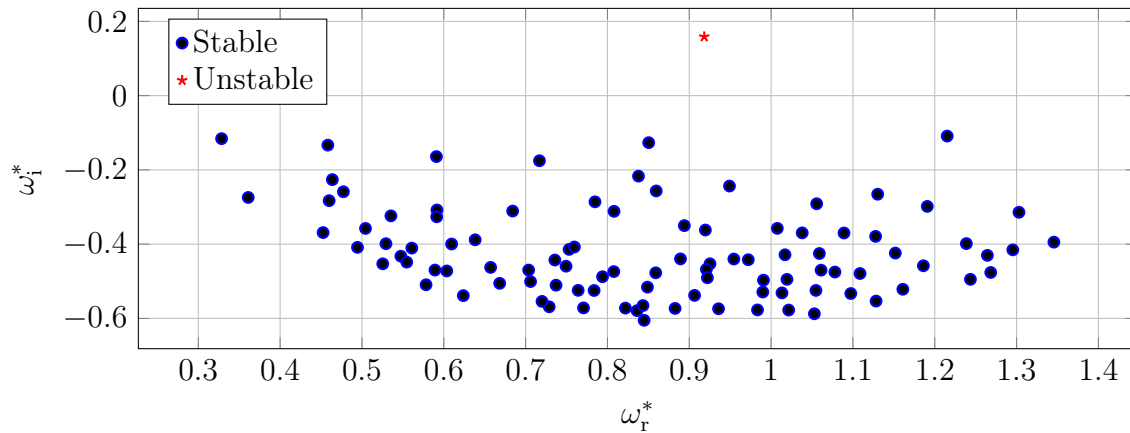


Figure 7.5: BiGlobal spectrum of the no-rod case for a reacting flow when the non-uniform mean density field is neglected; $\Phi = 1.0$; $\dot{V} = 1.7 \text{ ls}^{-1}$

The analysis begins with the LSA of the mean flow fields illustrated in Fig. 7.4, when the variation in the mean density field is ignored. Figure 7.5 shows the resulting stability spectrum. All except one eigenvalue are related to a negative temporal growth rate. The one eigenvalue standing out is of complex frequency $\omega^* = 0.92 + 0.18i$. The corresponding mode shapes and the structural sensitivity of the feedback cycle are illustrated in Fig. 7.6. The mode shapes are similar to the mode shapes appearing in the LES of the cold flow simulations (see Figs. 6.14 for comparison), nevertheless with a slightly different axial wave number. Like in the cold flow case, the structural sensitivity is the highest at the exit plane of the primary injector. The striking difference however is that while in the cold flow case the LES and experimental mean flows are perturbed by a strong PVC, no hydrodynamic structures appear in the primary injector of the reactive LES.

7.2.1.2 Stability Analysis of a Reacting Flow Taking into Account the Density Gradient

It was shown in the previous section, that the BiGlobal hydrodynamic LSA predicts a mode with positive growth rate if the non-uniform mean density field is neglected. The mode is a PVC in the interior of the primary injector. This contradicts the LES, which do not show a significant coherent structure in this region. A comparison of the density field in Fig. 7.4 and the mode shape and structural sensitivity of the mode related to positive temporal growth (see Fig. 7.6) however shows that the mode appears in regions with strong density gradients. Here, the BiGlobal LSA is repeated, however this time the non-uniform density and therefore the influence of fluctuating baroclinic torque is taken into account. The resulting spectrum

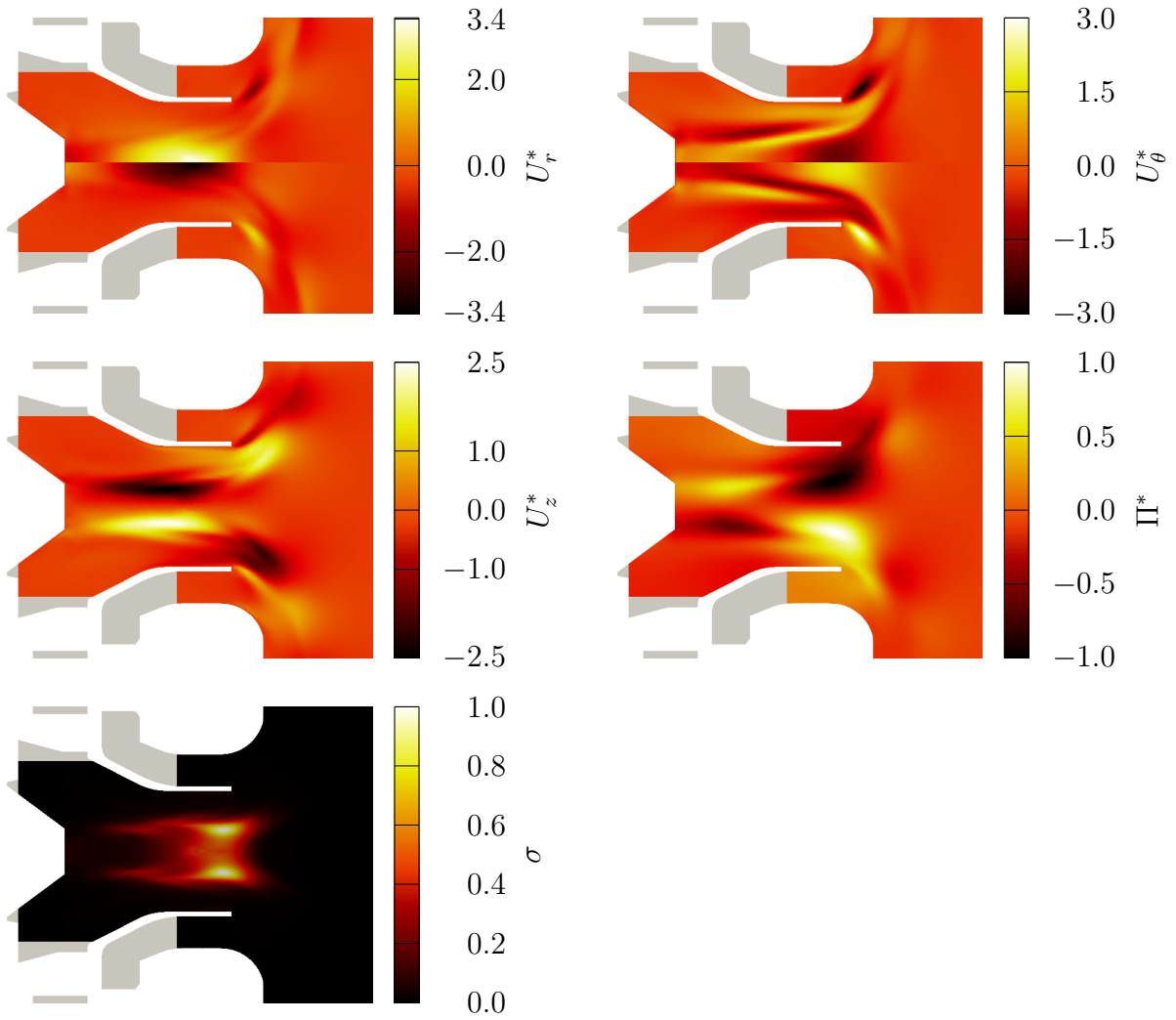


Figure 7.6: BiGlobal mode shapes of the no-rod case in the r - z -plane for a reacting flow when the non-uniform mean density field is neglected; $\Phi = 1.0$; $\dot{V} = 1.7 \text{ ls}^{-1}$

is illustrated in Fig. 7.7. The mode of interest, i.e. the mode with positive growth in the

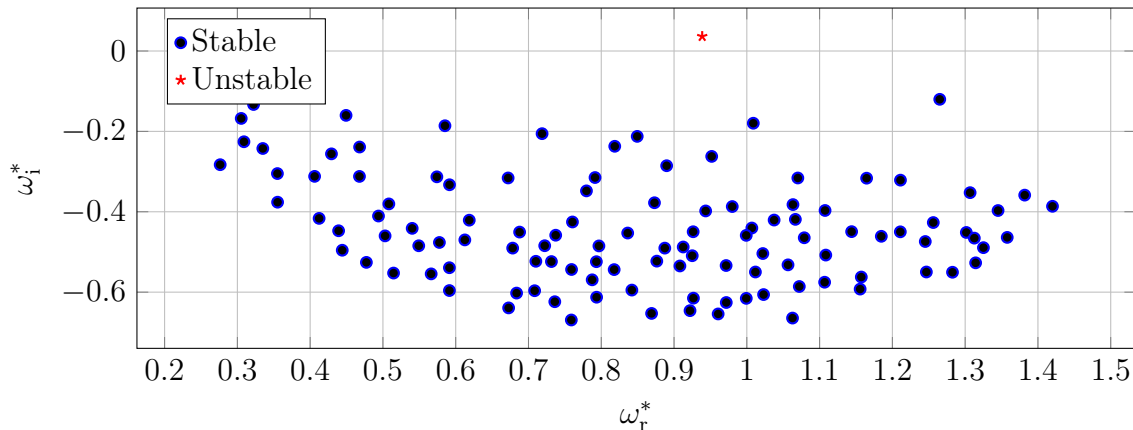


Figure 7.7: BiGlobal spectrum of the no-rod case for a reacting flow when the non-uniform mean density field is taken into account; $\Phi = 1.0$; $\dot{V} = 1.7 \text{ ls}^{-1}$

previous section is again marked by a star. The corresponding mode shapes and structural sensitivity are illustrated in Fig. 7.8. While the real part of the frequency remains only marginally affected by the density field, it is evident that taking into account the non-uniform density field significantly decreases the growth rate of the corresponding mode, which confirms the results of local LSA published by earlier studies [171, 142, 143]. Nevertheless, the growth rate remains marginally positive, which is either related to an instability at the bifurcation point or to an instability at its limit cycle. While the prior possibility is unlikely, since the same result ($\omega_i \approx 0$) was obtained for this configuration at various different flow rates, the latter contradicts the LES. Keep in mind however, that one mechanism remains not addressed by the underlying equations of hydrodynamic LSA derived in Section 5.1: The reaction chemistry. So far the analysis is purely hydrodynamic, while the influence of the flame is only modeled by its effect on the density field. The flame therefore is passive. In order to evolve to an active flame, the impact of the hydrodynamic waves on the combustion process must be modeled. In their recent work, Avdonin et al. [10] linearize the Navier-Stokes equations around the mean of a laminar flame, including the chemistry, which is based on a Westbrook and Dryer model [258] in order to reproduce the FTF of the laminar flame. It is clear however that extending the method of linearizing the chemistry to turbulent cases, where the corresponding equations are solved for a coherent structure, which appears at its limit cycle is far more challenging. Nevertheless, the effect of an active flame on hydrodynamic stability is a highly interesting, but still not well addressed question.

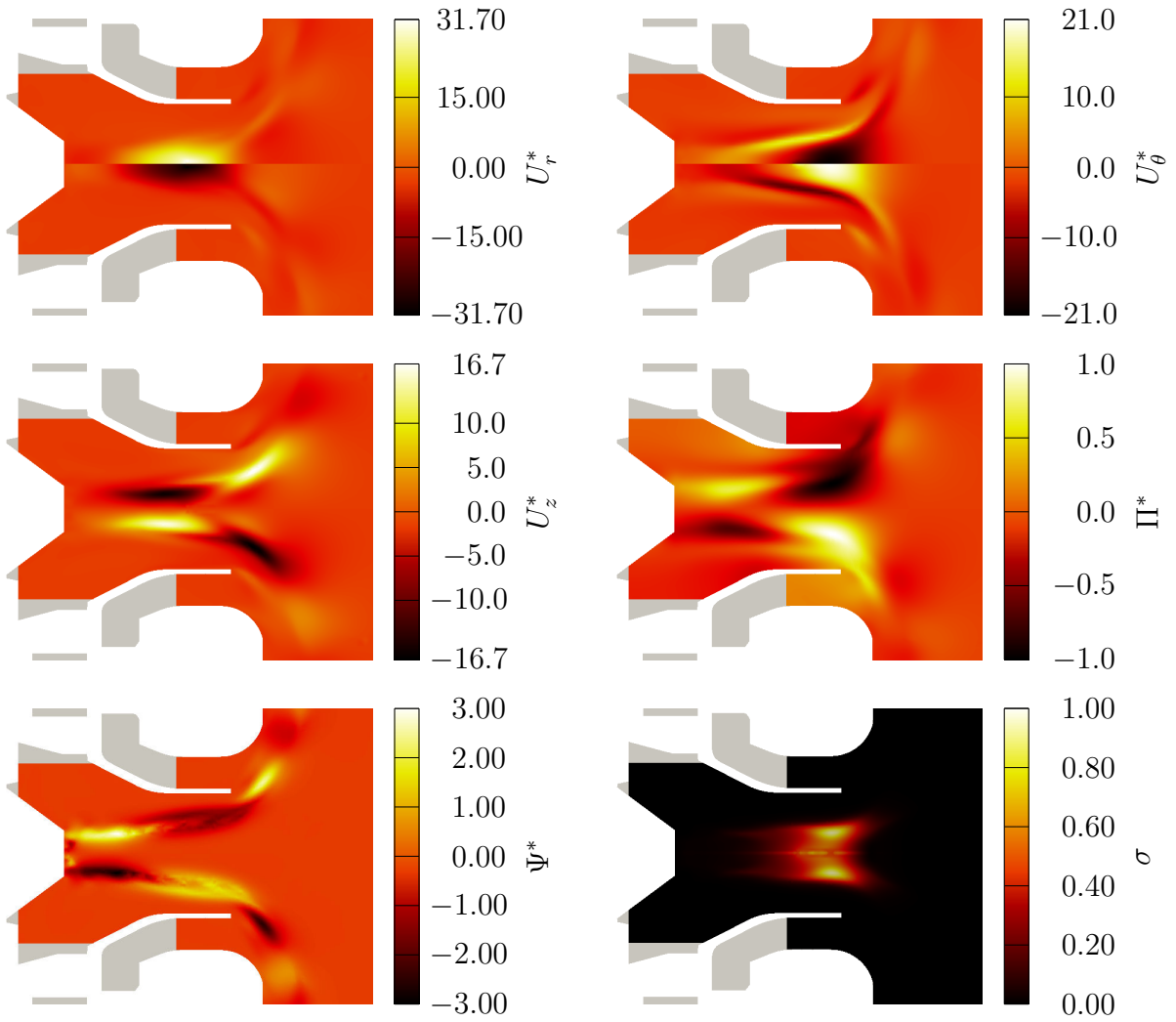


Figure 7.8: BiGlobal mode shapes of the no-rod configuration in the r - z -plane for a reacting flow when the non-uniform mean density field is taken into account; $\Phi = 1.0$; $\dot{V} = 1.7 \text{ ls}^{-1}$

7.2.2 Influence of the Central Rod on the Stability of the PVC in Reacting Flows

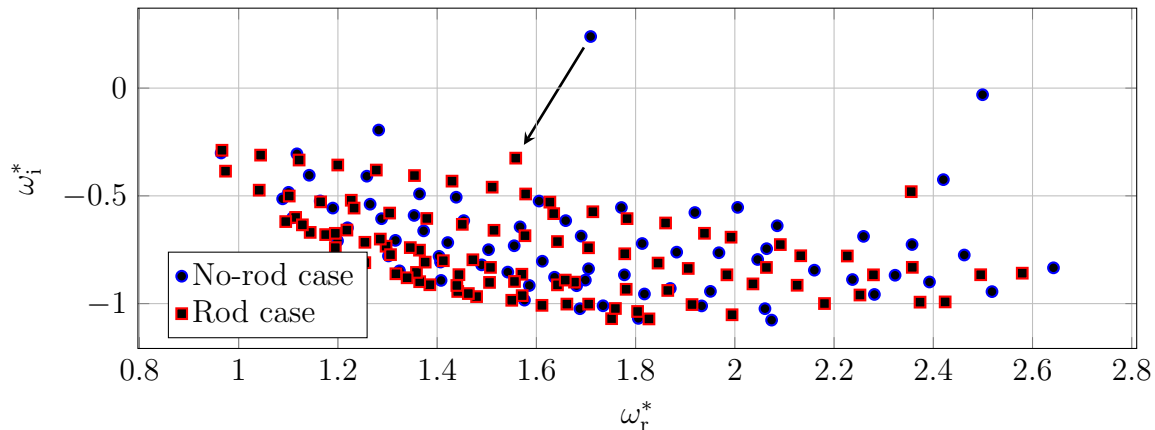


Figure 7.9: BiGlobal spectrum for the rod and the no-rod case for a reacting flow taking into account the non-uniform base flow density; $\Phi = 0.725$; $\dot{V} = 3.83 \text{ ls}^{-1}$

In the previous sections, LSA was conducted for two different configurations. In the first the base flow density gradient caused by the flame was ignored, in the second it was taken into account by the analysis. Although both analyses predicted a mode of positive growth rate, which contradicts the LES, it could be shown that the density gradient reduces its growth rate. In this section the influence of the central rod on the growth rate of the respective mode is investigated.

Figure. 7.9 illustrates the spectrum of eigenvalues for the two cases under consideration. The flow rate is $\dot{V} = 3.83 \text{ l/s}$ at an equivalence ratio of $\Phi = 0.725$. The operating point therefore corresponds to the flames which are illustrated in Figs. 7.3(a) and 7.3(b) for the no-rod and the rod case, respectively. In the spectrum of the no-rod configuration one mode stands out with a significantly positive growth rate. It is the same mode which was found for the stoichiometric operating point of lower flow rate, the spectrum of which is illustrated in Fig. 7.7. The higher frequency of the mode is due to the increase in flow rate. The spectrum of the rod case in Fig. 7.9 demonstrates that the growth rate decreases significantly due to the rod and the mode has now a negative growth rate.

7.3 Conclusion

The reactive methane-air flow through an industrial swirled fuel injection system is investigated via LES and BiGlobal hydrodynamic LSA. Two different configurations of the fuel

injector are compared with respect to various operating points. Both configurations, are the same as in Chapter 6: In contrast to the no-rod case, in the rod case a cylinder is mounted on the jet axis in the interior of the primary injector. The rod changes the flame shape only marginally. However, it is shown to have a highly beneficial influence on flame anchoring in lean conditions: While in the no-rod case, the flame blows off after the flow rate exceeds a critical level, the flame remains attached in the rod case far beyond this critical flow rate.

Furthermore, the mean flow field of the configuration was subject to a hydrodynamic LSA. First the impact of the base flow density field was analyzed for a low flow rate of a stoichiometric mixture. The corresponding LES did not show any coherent structures. It was shown, that LSA predicts a mode with strongly positive growth rate, if the base flow density gradient is not considered. Taking it into account in contrast significantly reduces the mode's growth rate, which nevertheless remains slightly positive. This contradiction with the LES results may be due to the fact, that merely a *passive flame* model is applied. This means, that while the flame's effect on the mean density field is considered, the chemistry is not linearized, and therefore fluctuations in heat release due to the hydrodynamic fluctuation are not taken into consideration.

Finally, the impact of the rod on hydrodynamic stability is investigated. To do so both configurations were compared close to the lean blow-off limit of the flame via passive-flame-LSA. While in the no-rod case the LSA analysis found a coherent structure with positive mode shape, in the rod case the corresponding mode's growth rate is shifted significantly into the negative. Like in the cold flow simulations, the rod has a strongly stabilizing effect on the coherent structure. This could also explain why the rod prevents the flame blow off in the lean conditions: In the no-rod configuration the turbulence increases with the flow rate, and leads to a quenching of the flame in the central recirculation zone. An evolution of a PVC or even its low dampening rate, is likely to contribute to the turbulence. In the rod-case however, the turbulence level is decreased due to the significantly increased dampening of the PVC and therefore flame quenching is prevented.

Concluding Remarks

Flow rotation is a topic of major importance in various fields of physics. This thesis focuses on two configurations in combustion research involving this effect.

The first addressed configuration is academical. Here a laminar flame in the wake of a cylindrical bluff body is under investigation. It is shown that rotating the cylinder around its axis causes a break of symmetry so that both flame branches have significantly different time delays. Due to destructive interference of the heat release signals, this difference in time delays causes a broad band decrease in the gain of the FTF, which is strongest at a specific frequency, where destructive interference is optimal. The difference in time delays and thereby the frequency at which the destructive interference occurs can be adjusted by the rotation speed of the cylinder. This way a flame can be built which at a chosen frequency does not react to acoustic forcing in terms of heat release fluctuation. The study therefore shows that an aimed insertion of flow rotation can be applied as a tool of open loop control in combustion devices involving a laminar flame. Regarding turbulent flames, which are more often used in industrial engines, the study ties in with a solution that was already before used in a similar way in other engines: Breaking the symmetry of a combustion chamber already helped to stabilize the F-1 rocket engine and in modern azimuthal combustion chambers studies have been conducted on breaking the symmetry by installing burners that differ e.g. in swirl direction on the same chamber. By focusing on the difference of the phase delays of the individual flames, this thesis offers another perspective on this control method: The heat release fluctuation, which is produced by one flame at a certain frequency, is annihilated by the next flame due to their opposed phase angle at the very same frequency. Keeping in mind, that the gas turbines must be operable at various different operating points, which can give rise to different unstable thermoacoustic modes, the results in this thesis underline the immense benefit of controlling the asymmetry of the flames in a running system.

In the second configuration, which is investigated in this thesis, flow rotation is used in order to anchor a turbulent flame. In gas turbine combustors, this is achieved by adding swirl to the injection mechanism, which leads to the evolution of a vortex breakdown bubble in the center axis of the jet. This provides a region of reverse flow and therefore flame anchoring. Furthermore, if the swirl is increased and reaches a critical limit a Hopf-bifurcation occurs

CONCLUDING REMARKS

Method	LES	local LSA single calculation	local LSA full 4-step strategy	BiGlobal LSA
CPU time [s]	$\sim 10^6$	$\sim 10^{-1}$	$\sim 10^3$	$\sim 10^1 - 10^2$

Table 8.1: Comparison of computational time LES vs methods of LSA

which gives rise to a helix shaped instability, the PVC. It again can be seen as a phenomenon of flow rotation, as it is a helical vortex which is rolling up the shear layer around the recirculation bubble. This phenomenon is analyzed in this thesis by various different methods in an industrial two-staged counter-rotative fuel injector of highly complicated geometry for both cold flow and reactive cases. First the phenomenon is analyzed thoroughly by cold flow LES which are rigorously validated against experimental data. In order to gain additional insight into the mechanisms leading to the PVC, LSA is applied. First local LSA, a method which previously has been predominantly applied in academical configurations is used. Although this method is developed for weakly non parallel flows, a condition which is clearly violated by the base flow of the industrial injector, it yields astonishingly well results for some flow regions. For other flow regions, i.e. the regions, where the parallel flow assumption is violated to the extremest extent, the method however fails. The second tool applied to analyze the LES data is based on a BiGlobal approach and was implemented in the framework of the studies that led to this dissertation. This method is not restricted by a parallel flow assumption and therefore can be applied without further restriction to a fuel injector. It is demonstrated that the tool not only reproduces the modal structure of the PVC, it also provides additional information: The location where the feedback takes places and the regions which are most receptive for actuation. The tool therefore provides very interesting information for gas turbine engineers who wish to control the PVC (or any other coherently fluctuating hydrodynamic flow structure). The location of highest internal feedback is found to be just upstream of the recirculation bubble, which is in line with several previous studies. This is a very precious intelligence for a gas turbine developer: If he wishes to tamper with the feedback mechanism of the instability he must adapt the region upstream of the breakdown bubble to do so. This is underlined especially by the LES and experimental results where a central rod is mounted in the interior of the primary injector, which covers most of the region of highest structural sensitivity just upstream of the recirculation bubble: The results suggest that the temporal average of the flow is barely affected by this geometry change. Nevertheless, the internal feedback of the PVC is obstructed, which leads to its suppression. Furthermore, the information on controlling the PVC comes at numerical costs, which are negligible in comparison with the LES. This is demonstrated by Tab. 8.1 which compares the methods of LES, local LSA and BiGlobal LSA in terms of CPU time.

Furthermore, the configuration was investigated with reactive LES. First, the flame anchoring is analyzed for the case without rod and with rod. Also in the reactive flow simulations the temporal-averages of the flow remain nearly unaffected by the presence of the rod. Nev-

ertheless, it was shown that the rod supports flame anchoring in the lean regime. Both the influence of the density gradient as well as the impact of the rod on the stability of the flow is analyzed. This was done by a novelty presented in this thesis: A BiGlobal hydrodynamic tool for low Mach passive flame flows. The results of the code confirm previous results based on local LSA, which showed that the inhomogeneous temporally averaged density field causes a stabilization of the PVC. Furthermore, it was shown by BiGlobal LSA that also in the reactive simulations the central rod causes a stabilization of the PVC mode.

The second part of the thesis underlines the capabilities and potential of the BiGlobal LSA approach for gas turbine engineering. The additional information, which are obtained by the approach pose highly valuable information for gas turbine engineers.

CONCLUDING REMARKS

Appendices

Appendix A

Hydrodynamic Linear Stability Analysis in Rotation Symmetric Flows of Uniform Density

Here, the constant density hydrodynamic instability equations in cylindrical coordinates for mean flows homogeneous in azimuthal direction shall be derived. We do this under the following assumptions:

- The fluid follows the perfect gas law.
- The base flow is superimposed by not more than one coherent fluctuation.
- Gas properties are constant

A.1 Derivative Operators in Cylindrical Coordinates

The following equations show some derivative operators in cylindrical coordinates:

- Scalar gradient

$$\nabla\phi = \frac{\partial\phi}{\partial r}\hat{\mathbf{r}} + \frac{1}{r}\frac{\partial\phi}{\partial\theta}\hat{\boldsymbol{\theta}} + \frac{\partial\phi}{\partial z}\hat{\mathbf{z}} \quad (\text{A.1.1})$$

- Material derivative

$$\begin{aligned}
 (\mathbf{A} \cdot \nabla) \mathbf{B} &= \left(A_r \frac{\partial B_r}{\partial r} + \frac{A_\theta}{r} \frac{\partial B_r}{\partial \theta} + A_z \frac{\partial B_r}{\partial z} - \frac{A_\theta B_\theta}{r} \right) \hat{\mathbf{r}} \\
 &+ \left(A_r \frac{\partial B_\theta}{\partial r} + \frac{A_\theta}{r} \frac{\partial B_\theta}{\partial \theta} + A_z \frac{\partial B_\theta}{\partial z} + \frac{A_\theta B_r}{r} \right) \hat{\theta} \\
 &+ \left(A_r \frac{\partial B_z}{\partial r} + \frac{A_\theta}{r} \frac{\partial B_z}{\partial \theta} + A_z \frac{\partial B_z}{\partial z} \right) \hat{\mathbf{z}}
 \end{aligned} \tag{A.1.2}$$

- Scalar Laplacian

$$\Delta \phi = \frac{1}{r} \frac{\partial}{\partial r} \left(r \frac{\partial \phi}{\partial r} \right) + \frac{1}{r^2} \frac{\partial^2 \phi}{\partial \theta^2} + \frac{\partial^2 \phi}{\partial z^2} \tag{A.1.3}$$

- Vector Laplacian

$$\begin{aligned}
 \Delta \mathbf{A} &= \left(\Delta A_r - \frac{A_r}{r^2} - \frac{2}{r^2} \frac{\partial A_\theta}{\partial \theta} \right) \hat{\mathbf{r}} \\
 &+ \left(\Delta A_\theta - \frac{A_\theta}{r^2} + \frac{2}{r^2} \frac{\partial A_r}{\partial \theta} \right) \hat{\theta} \\
 &+ \Delta A_z \hat{\mathbf{z}}
 \end{aligned} \tag{A.1.4}$$

- Vector Divergence

$$\nabla \cdot \mathbf{A} = \frac{1}{r} \frac{\partial (r A_r)}{\partial r} + \frac{1}{r} \frac{A_\theta}{\partial \theta} + \frac{\partial A_z}{\partial z} \tag{A.1.5}$$

The vectors $\hat{\mathbf{r}}$, $\hat{\theta}$ and $\hat{\mathbf{z}}$ denote the unity vectors in radial azimuthal and axial direction.

A.2 Governing Equations

We start with the set of Navier-Stokes equations and the continuity equation:

$$\rho \left(\frac{\partial \mathbf{u}}{\partial t} + (\mathbf{u} \cdot \nabla) \mathbf{u} \right) = -\nabla p + \nabla \cdot (\mu \nabla \mathbf{u}) + \frac{1}{3} \mu \nabla (\nabla \cdot \mathbf{u}) \tag{A.2.1}$$

$$\nabla \cdot \mathbf{u} = 0 \tag{A.2.2}$$

It often is convenient to express the governing equations in the non-dimensional form. The reference values are arbitrary, but in this context are defined as:

$$\mathbf{u} = U_{\text{ref}} \mathbf{u}^* \quad (\text{A.2.3a})$$

$$x = D_{\text{ref}} x^* \quad (\text{A.2.3b})$$

$$t = \frac{D_{\text{ref}}}{U_{\text{ref}}} t^* \quad (\text{A.2.3c})$$

$$p = \rho_{\text{ref}} U_{\text{ref}}^2 p^* \quad (\text{A.2.3d})$$

With the Reynolds number, which is defined as

$$\text{Re} = \frac{U_{\text{ref}} D_{\text{ref}}}{\nu_{\text{ref}}} = \frac{U_{\text{ref}} D_{\text{ref}} \rho_{\text{ref}}}{\mu} \quad (\text{A.2.4a})$$

the full set of governing equations can then be expressed as:

$$\frac{\partial \mathbf{u}^*}{\partial t^*} + (\mathbf{u}^* \cdot \nabla^*) \mathbf{u}^* = -\nabla^* p^* + \frac{1}{\text{Re}} \Delta \mathbf{u}^* \quad (\text{A.2.5})$$

$$\nabla^* \cdot \mathbf{u}^* = 0 \quad (\text{A.2.6})$$

A.3 Linearization

The primitive variables can be described as the sum of a temporal average, a coherent fluctuation, and a stochastic fluctuation:

$$\mathbf{u} = \bar{\mathbf{u}} + \epsilon \widehat{\mathbf{u}} + \mathbf{u}', \quad p = \bar{p} + \epsilon \widehat{p} + p', \quad (\text{A.3.1})$$

where $\epsilon \ll 1$. Inserting Eqns. (A.3.1) to the Navier-Stokes momentum and continuity equation yields:

$$\begin{aligned} \frac{\partial \bar{\mathbf{u}}^*}{\partial t^*} + \epsilon \frac{\partial \widehat{\mathbf{u}}^*}{\partial t^*} + \frac{\partial \mathbf{u}'^*}{\partial t^*} + (\bar{\mathbf{u}}^* \cdot \nabla^*) \bar{\mathbf{u}}^* + \epsilon (\bar{\mathbf{u}}^* \cdot \nabla^*) \widehat{\mathbf{u}}^* + (\bar{\mathbf{u}}^* \cdot \nabla^*) \mathbf{u}'^* \\ + \epsilon (\widehat{\mathbf{u}}^* \cdot \nabla^*) \bar{\mathbf{u}}^* + \epsilon^2 (\widehat{\mathbf{u}}^* \cdot \nabla^*) \widehat{\mathbf{u}}^* + \epsilon (\widehat{\mathbf{u}}^* \cdot \nabla^*) \mathbf{u}'^* \\ + (\mathbf{u}'^* \cdot \nabla^*) \bar{\mathbf{u}}^* + \epsilon (\mathbf{u}'^* \cdot \nabla^*) \widehat{\mathbf{u}}^* + (\mathbf{u}'^* \cdot \nabla^*) \mathbf{u}'^* = \\ - \nabla^* \bar{p}^* - \epsilon \nabla^* \widehat{p}^* - \nabla^* p'^* + \frac{1}{\text{Re}} (\Delta^* \bar{\mathbf{u}}^* + \epsilon \Delta^* \widehat{\mathbf{u}}^* + \Delta^* \mathbf{u}'^*) \end{aligned} \quad (\text{A.3.2})$$

and

$$\nabla^* \cdot \bar{\mathbf{u}}^* + \epsilon \nabla^* \cdot \widehat{\mathbf{u}}^* + \nabla^* \cdot \mathbf{u}'^* = 0 \quad (\text{A.3.3})$$

The derivation of mean velocity with respect to time is by definition zero. Furthermore, we neglect all terms of order ϵ^2 and higher. Temporal averaging of the equations yields for $\mathcal{O}(1)$ the non-dimensional RANS equations:

$$\frac{\partial \overline{\mathbf{u}^*}}{\partial t^*} + (\overline{\mathbf{u}^*} \cdot \nabla^*) \overline{\mathbf{u}^*} + \overline{(\mathbf{u}^{*'} \cdot \nabla^*) \mathbf{u}^{*'}} = -\nabla^* \overline{p^*} + \frac{1}{\text{Re}} \Delta^* \overline{\mathbf{u}^*}, \quad (\text{A.3.4})$$

and

$$\nabla^* \cdot \overline{\mathbf{u}^*} = 0 \quad (\text{A.3.5})$$

A phase average of Eqns.(A.3.2–A.3.3) yields:

$$\begin{aligned} \frac{\partial \overline{\mathbf{u}^*}}{\partial t^*} + \epsilon \frac{\partial \widehat{\mathbf{u}^*}}{\partial t^*} + (\overline{\mathbf{u}^*} \cdot \nabla^*) \overline{\mathbf{u}^*} + \epsilon (\overline{\mathbf{u}^*} \cdot \nabla^*) \widehat{\mathbf{u}^*} + \epsilon (\widehat{\mathbf{u}^*} \cdot \nabla^*) \overline{\mathbf{u}^*} \\ + \langle (\mathbf{u}^{*'} \cdot \nabla^*) \mathbf{u}^{*'} \rangle = -\nabla^* \overline{p^*} - \epsilon \nabla^* \widehat{p^*} + \frac{1}{\text{Re}} (\Delta^* \overline{\mathbf{u}^*} + \epsilon \Delta^* \widehat{\mathbf{u}^*}), \end{aligned} \quad (\text{A.3.6})$$

and

$$\nabla^* \cdot \overline{\mathbf{u}^*} + \epsilon \nabla^* \cdot \widehat{\mathbf{u}^*} = 0. \quad (\text{A.3.7})$$

Finally, subtracting Eqns. (A.3.4) and (A.3.5) from Eqns. (A.3.6) and (A.3.7) yields the governing equations of hydrodynamic LSA:

$$\frac{\partial \widehat{\mathbf{u}^*}}{\partial t^*} + (\widehat{\mathbf{u}^*} \cdot \nabla^*) \overline{\mathbf{u}^*} + (\overline{\mathbf{u}^*} \cdot \nabla^*) \widehat{\mathbf{u}^*} + \langle (\mathbf{u}^{*'} \cdot \nabla^*) \mathbf{u}^{*'} \rangle - \overline{(\mathbf{u}^{*'} \cdot \nabla^*) \mathbf{u}^{*'}} = -\nabla^* \widehat{p^*} + \frac{1}{\text{Re}} (\Delta^* \widehat{\mathbf{u}^*}) \quad (\text{A.3.8})$$

$$\nabla^* \cdot \widehat{\mathbf{u}^*} = 0 \quad (\text{A.3.9})$$

Note, that the non-linear terms give rise to product terms of stochastic fluctuations in the momentum equation which do not disappear after temporal and phase averaging. These terms (terms 4 and 5 in Eqn.A.3.8) can be seen as the periodic change in Reynolds stresses caused by the coherent fluctuation. In many studies these product terms are neglected, while in others their effect is modeled by an additional eddy viscosity. In the following of this derivation, it is assumed that their effect is taken into account by an appropriate decrease of the local Reynolds number due to an eddy viscosity contribution. These terms are therefore omitted in the following.

A.4 BiGlobal Stability

In the BiGlobal approach we assume that the fluctuating quantities are harmonic in time with the frequency ω and in azimuthal direction with the azimuthal wave number m , which

leads to the modal approach:

$$\begin{aligned}\widehat{\mathbf{u}} &= \widehat{\mathbf{U}} \exp(i\xi), \\ \widehat{p} &= \widehat{P} \exp(i\xi),\end{aligned}\tag{A.4.1}$$

where the phase angle ξ is described for the BiGlobal approach by:

$$\xi = m\theta - \omega t\tag{A.4.2}$$

Inserting Eqn. (A.4.2) into the continuity, Navier-Stokes and energy equation leads to:

$$\begin{aligned}\frac{\partial (\widehat{\mathbf{U}}^* \exp(i\xi))}{\partial t^*} + ((\widehat{\mathbf{U}}^* \exp(i\xi)) \cdot \nabla^*) \overline{\mathbf{u}}^* + (\overline{\mathbf{u}}^* \cdot \nabla^*) (\widehat{\mathbf{U}}^* \exp(i\xi)) \\ - \frac{1}{\text{Re}} (\Delta^* (\widehat{\mathbf{U}}^* \exp(i\xi))) = 0\end{aligned}\tag{A.4.3}$$

$$\nabla^* \cdot (\widehat{\mathbf{U}}^* \exp(i\xi)) = 0\tag{A.4.4}$$

In the BiGlobal approach the mean flow is assumed to be homogeneous in azimuthal direction. Therefore all derivatives of mean quantities with respect to the azimuthal direction are equal to zero. Furthermore, since the fluctuating quantities are harmonic in azimuthal direction, their derivatives with respect to the azimuthal direction correspond to a multiplication with im . Similarly, a derivation by time is equivalent to a multiplication by $-i\omega$.

For reasons of simplicity the derivative operators laid out in Section A.1 of mean and fluctuating quantities are given here adapted to the global approach for both mean and fluctuating quantities:

- Scalar gradient

$$\nabla \overline{\phi} = \frac{\partial \overline{\phi}}{\partial r} \mathbf{e}_r + 0 \mathbf{e}_\theta + \frac{\partial \overline{\phi}}{\partial z} \mathbf{e}_z\tag{A.4.5}$$

$$\nabla (\widehat{\phi} \exp(im\theta - i\omega t)) = \left(\frac{\partial \widehat{\phi}}{\partial r} \mathbf{e}_r + \frac{im\widehat{\phi}}{r} \mathbf{e}_\theta + \frac{\partial \widehat{\phi}}{\partial z} \mathbf{e}_z \right) \exp(im\theta - i\omega t)\tag{A.4.6}$$

- Scalar Laplacian

$$\Delta \overline{\phi} = \frac{1}{r} \frac{\partial}{\partial r} \left(r \frac{\partial \overline{\phi}}{\partial r} \right) + \frac{\partial^2 \overline{\phi}}{\partial z^2}\tag{A.4.7}$$

$$\Delta (\widehat{\phi} \exp(im\theta - i\omega t)) = \left(\frac{1}{r} \frac{\partial}{\partial r} \left(r \frac{\partial \widehat{\phi}}{\partial r} \right) - \frac{m^2}{r^2} \widehat{\phi} + \frac{\partial^2 \widehat{\phi}}{\partial z^2} \right) \exp(im\theta - i\omega t)\tag{A.4.8}$$

- Vector divergence

$$\nabla \cdot \bar{\mathbf{A}} = \frac{1}{r} \frac{\partial}{\partial r} (r \bar{A}_r) + \frac{\partial \bar{A}_z}{\partial z} \quad (\text{A.4.9})$$

$$\nabla \cdot (\widehat{\mathbf{A}} \exp(im\theta - i\omega t)) = \left(\frac{1}{r} \frac{\partial}{\partial r} (r \widehat{A}_r) + \frac{im}{r} \widehat{A}_\theta + \frac{\partial \widehat{A}_z}{\partial z} \right) \exp(im\theta - i\omega t) \quad (\text{A.4.10})$$

- Vector Laplacian

$$\begin{aligned} \Delta (\widehat{\mathbf{A}} \exp(im\theta - i\omega t)) &= \left(\Delta \widehat{A}_r - \frac{\widehat{A}_r}{r^2} - \frac{2im}{r^2} \widehat{A}_\theta \right) \mathbf{e}_r \exp(im\theta - i\omega t) \\ &+ \left(\Delta \widehat{A}_\theta - \frac{\widehat{A}_\theta}{r^2} + \frac{2im}{r^2} \widehat{A}_r \right) \mathbf{e}_\theta \exp(im\theta - i\omega t) \\ &+ \Delta \widehat{A}_z \mathbf{e}_z \exp(im\theta - i\omega t) \end{aligned} \quad (\text{A.4.11})$$

- Material derivative

$$\begin{aligned} (\mathbf{B} \cdot \nabla) \bar{\mathbf{A}} &= \left(B_r \frac{\partial \bar{A}_r}{\partial r} + B_z \frac{\partial \bar{A}_r}{\partial z} - \frac{B_\theta \bar{A}_\theta}{r} \right) \hat{\mathbf{r}} \\ &+ \left(B_r \frac{\partial \bar{A}_\theta}{\partial r} + B_z \frac{\partial \bar{A}_\theta}{\partial z} + \frac{B_\theta \bar{A}_r}{r} \right) \hat{\boldsymbol{\theta}} \\ &+ \left(B_r \frac{\partial \bar{A}_z}{\partial r} + B_z \frac{\partial \bar{A}_z}{\partial z} \right) \hat{\mathbf{z}} \end{aligned} \quad (\text{A.4.12})$$

$$\begin{aligned} (\mathbf{B} \cdot \nabla) (\widehat{\mathbf{A}} \exp(im\theta - i\omega t)) &= \\ &\left(B_r \frac{\partial \widehat{A}_r}{\partial r} + \frac{im B_\theta \widehat{A}_r}{r} + B_z \frac{\partial \widehat{A}_r}{\partial z} - \frac{B_\theta \widehat{A}_\theta}{r} \right) \hat{\mathbf{r}} \exp(im\theta - i\omega t) \\ &+ \left(B_r \frac{\partial \widehat{A}_\theta}{\partial r} + \frac{im B_\theta \widehat{A}_\theta}{r} + B_z \frac{\partial \widehat{A}_\theta}{\partial z} + \frac{B_\theta \widehat{A}_r}{r} \right) \hat{\boldsymbol{\theta}} \exp(im\theta - i\omega t) \\ &+ \left(B_r \frac{\partial \widehat{A}_z}{\partial r} + \frac{im B_\theta \widehat{A}_z}{r} + B_z \frac{\partial \widehat{A}_z}{\partial z} \right) \hat{\mathbf{z}} \exp(im\theta - i\omega t), \end{aligned} \quad (\text{A.4.13})$$

The derivative operators above can now be inserted in the set of Eqns. (A.4.3–A.4.4), which yields for the momentum equation in radial direction

$$\begin{aligned}
& -i\omega^* \widehat{U}_r^* + \overline{u}_r^* \frac{\partial \widehat{U}_r^*}{\partial r^*} + \frac{im\overline{u}_\theta^* \widehat{U}_r^*}{r^*} + \overline{u}_z^* \frac{\partial \widehat{U}_r^*}{\partial z^*} - \frac{2\overline{u}_\theta^* \widehat{U}_\theta^*}{r^*} + \widehat{U}_r^* \frac{\partial \overline{u}_r^*}{\partial r^*} + \widehat{U}_z^* \frac{\partial \overline{u}_r^*}{\partial z^*} \\
& + \frac{\partial \widehat{P}^*}{\partial r^*} - \frac{1}{\text{Re}} \left(\frac{\partial^2 \widehat{U}_r^*}{\partial r^{*2}} + \frac{1}{r^*} \frac{\partial \widehat{U}_r^*}{\partial r^*} - \frac{m^2 \widehat{U}_r^*}{r^{*2}} + \frac{\partial^2 \widehat{U}_r^*}{\partial z^{*2}} - \frac{\widehat{U}_r^*}{r^{*2}} - \frac{2im\widehat{U}_\theta^*}{r^{*2}} \right) = 0,
\end{aligned} \tag{A.4.14}$$

in azimuthal direction

$$\begin{aligned}
& -i\omega^* \widehat{U}_\theta^* + \overline{u}_r^* \frac{\partial \widehat{U}_\theta^*}{\partial r^*} + \frac{im\overline{u}_\theta^* \widehat{U}_\theta^*}{r^*} + \overline{u}_z^* \frac{\partial \widehat{U}_\theta^*}{\partial z^*} + \frac{\overline{u}_\theta^* \widehat{U}_r^*}{r^*} + \widehat{U}_r^* \frac{\partial \overline{u}_\theta^*}{\partial r^*} + \widehat{U}_z^* \frac{\partial \overline{u}_\theta^*}{\partial z^*} + \frac{\widehat{U}_\theta^* \overline{u}_r^*}{r^*} \\
& + \frac{im\widehat{P}^*}{r^*} - \frac{1}{\text{Re}} \left(\frac{\partial^2 \widehat{U}_\theta^*}{\partial r^{*2}} + \frac{1}{r^*} \frac{\partial \widehat{U}_\theta^*}{\partial r^*} - \frac{m^2 \widehat{U}_\theta^*}{r^{*2}} + \frac{\partial^2 \widehat{U}_\theta^*}{\partial z^{*2}} - \frac{\widehat{U}_\theta^*}{r^{*2}} + \frac{2im\widehat{U}_r^*}{r^{*2}} \right) = 0,
\end{aligned} \tag{A.4.15}$$

and in axial direction

$$\begin{aligned}
& -i\omega^* \widehat{U}_z^* + \overline{u}_r^* \frac{\partial \widehat{U}_z^*}{\partial r^*} + \frac{im\overline{u}_\theta^* \widehat{U}_z^*}{r^*} + \overline{u}_z^* \frac{\partial \widehat{U}_z^*}{\partial z^*} + \widehat{U}_r^* \frac{\partial \overline{u}_z^*}{\partial r^*} + \widehat{U}_z^* \frac{\partial \overline{u}_z^*}{\partial z^*} \\
& + \frac{\partial \widehat{P}^*}{\partial z^*} - \frac{1}{\text{Re}} \left(\frac{\partial^2 \widehat{U}_z^*}{\partial r^{*2}} + \frac{1}{r^*} \frac{\partial \widehat{U}_z^*}{\partial r^*} - \frac{m^2 \widehat{U}_z^*}{r^{*2}} + \frac{\partial^2 \widehat{U}_z^*}{\partial z^{*2}} \right) = 0.
\end{aligned} \tag{A.4.16}$$

Furthermore, the continuity equation becomes

$$\frac{\partial \widehat{U}_r^*}{\partial r^*} + \frac{\widehat{U}_r^*}{r^*} + \frac{im}{r^*} \widehat{U}_\theta^* + \frac{\partial \widehat{U}_z^*}{\partial z^*} = 0. \tag{A.4.17}$$

The set of Eqns. (A.4.14–A.4.17) poses a generalized eigenvalue problem with eigenvector ω :

$$A\lambda = \omega B\lambda, \tag{A.4.18}$$

where

$$\lambda = [\widehat{U}_r^*, \widehat{U}_\theta^*, \widehat{U}_z^*, \widehat{P}^*]^T \tag{A.4.19}$$

A.5 Local Stability

As in the BiGlobal approach, in the local approach we assume that the fluctuating quantities are harmonic in time with the frequency ω , in azimuthal direction with the azimuthal wave number m . Furthermore two additional assumptions are made: Firstly, it is assumed that the base flow is homogeneous in axial direction, which leads to vanishing derivatives of the

base flow in z -direction. As a result of the parallel flow assumption, the flow speed in radial direction is considered zero¹. Secondly, the coherent fluctuation is harmonic in axial direction with the complex wave number α .

The phase angle in Eqns. (A.4.1) therefore is

$$\xi = m\theta + \alpha z - \omega t \quad (\text{A.5.1})$$

Due to the adaptation of the modal approach and the assumption of base flow homogeneity in axial direction, the derivative operators of temporal means and coherent fluctuation quantities differ from those in the BiGlobal approach. All derivatives of base flow quantities with respect to z are zero. Furthermore, in a parallel flow the radial component of the base flow velocity must be zero. And finally, a derivation of a coherent fluctuation with respect to z becomes a product of $i\alpha$ with the coherent fluctuation. The derivative operators of temporal means and coherent fluctuation quantities hence become in the framework of local LSA:

- Scalar gradient

$$\nabla \bar{\phi} = \frac{\partial \bar{\phi}}{\partial r} \mathbf{e}_r + 0 \mathbf{e}_\theta + 0 \mathbf{e}_z \quad (\text{A.5.2})$$

$$\nabla \left(\widehat{\phi} \exp(im\theta - i\omega t) \right) = \left(\frac{\partial \widehat{\phi}}{\partial r} \mathbf{e}_r + \frac{im\widehat{\phi}}{r} \mathbf{e}_\theta + i\alpha \widehat{\phi} \mathbf{e}_z \right) \exp(im\theta - i\omega t) \quad (\text{A.5.3})$$

- Scalar Laplacian

$$\Delta \bar{\phi} = \frac{1}{r} \frac{\partial}{\partial r} \left(r \frac{\partial \bar{\phi}}{\partial r} \right) \quad (\text{A.5.4})$$

$$\Delta \left(\widehat{\phi} \exp(im\theta - i\omega t) \right) = \left(\frac{1}{r} \frac{\partial}{\partial r} \left(r \frac{\partial \widehat{\phi}}{\partial r} \right) - \frac{m^2}{r^2} \widehat{\phi} - \alpha^2 \widehat{\phi} \right) \exp(im\theta - i\omega t) \quad (\text{A.5.5})$$

- Vector divergence

$$\nabla \cdot \bar{\mathbf{A}} = 0 \quad (\text{A.5.6})$$

$$\nabla \cdot \left(\widehat{\mathbf{A}} \exp(im\theta - i\omega t) \right) = \left(\frac{1}{r} \frac{\partial}{\partial r} \left(r \widehat{A}_r \right) + \frac{im}{r} \widehat{A}_\theta + i\alpha \widehat{A}_z \right) \exp(im\theta - i\omega t) \quad (\text{A.5.7})$$

¹Note that literature the radial velocity component often is not assumed to be zero. This results in additional remaining terms involving the radial velocity (see e.g. [8])

- Vector Laplacian

$$\begin{aligned} \Delta (\widehat{\mathbf{A}} \exp(im\theta - i\omega t)) &= \left(\Delta \widehat{A}_r - \frac{\widehat{A}_r}{r^2} - \frac{2im}{r^2} \widehat{A}_\theta \right) \mathbf{e}_r \exp(im\theta - i\omega t) \\ &+ \left(\Delta \widehat{A}_\theta - \frac{\widehat{A}_\theta}{r^2} + \frac{2im}{r^2} \widehat{A}_r \right) \mathbf{e}_\theta \exp(im\theta - i\omega t) \\ &+ \Delta \widehat{A}_z \mathbf{e}_z \exp(im\theta - i\omega t) \end{aligned} \quad (\text{A.5.8})$$

- Material derivative

$$\begin{aligned} (\mathbf{B} \cdot \nabla) \overline{\mathbf{A}} &= \left(-\frac{B_\theta \overline{A}_\theta}{r} \right) \hat{\mathbf{r}} \\ &+ \left(B_r \frac{\partial \overline{A}_\theta}{\partial r} \right) \hat{\boldsymbol{\theta}} \\ &+ \left(B_r \frac{\partial \overline{A}_z}{\partial r} \right) \hat{\mathbf{z}} \end{aligned} \quad (\text{A.5.9})$$

$$\begin{aligned} (\mathbf{B} \cdot \nabla) (\widehat{\mathbf{A}} \exp(im\theta - i\omega t)) &= \\ &\left(B_r \frac{\partial \widehat{A}_r}{\partial r} + \frac{imB_\theta \widehat{A}_r}{r} + i\alpha B_z \widehat{A}_r - \frac{B_\theta \widehat{A}_\theta}{r} \right) \hat{\mathbf{r}} \exp(im\theta - i\omega t) \\ &+ \left(B_r \frac{\partial \widehat{A}_\theta}{\partial r} + \frac{imB_\theta \widehat{A}_\theta}{r} + i\alpha B_z \widehat{A}_\theta + \frac{B_\theta \widehat{A}_r}{r} \right) \hat{\boldsymbol{\theta}} \exp(im\theta - i\omega t) \\ &+ \left(B_r \frac{\partial \widehat{A}_z}{\partial r} + \frac{imB_\theta \widehat{A}_z}{r} + i\alpha B_z \widehat{A}_z \right) \hat{\mathbf{z}} \exp(im\theta - i\omega t), \end{aligned} \quad (\text{A.5.10})$$

The derivative operators adapted to the local approach given in Eqns. (A.5)-(A.5.10) can now be inserted in the set of Eqns. (A.4.3-A.4.4), which yields for the momentum equation in radial direction

$$\begin{aligned} &-i\omega^* \widehat{U}_r^* + \frac{im\overline{u}_\theta^* \widehat{U}_r^*}{r^*} + i\alpha^* \overline{u}_z^* \widehat{U}_r^* - \frac{2\overline{u}_\theta^* \widehat{U}_\theta^*}{r^*} \\ &+ \frac{\partial \widehat{P}^*}{\partial r^*} - \frac{1}{\text{Re}} \left(\frac{\partial^2 \widehat{U}_r^*}{\partial r^{*2}} + \frac{1}{r^*} \frac{\partial \widehat{U}_r^*}{\partial r^*} - \frac{m^2 \widehat{U}_r^*}{r^{*2}} - \alpha^{*2} \widehat{U}_r^* - \frac{\widehat{U}_r^*}{r^{*2}} - \frac{2im\widehat{U}_\theta^*}{r^{*2}} \right) = 0, \end{aligned} \quad (\text{A.5.11})$$

in azimuthal direction

$$\begin{aligned}
 & -i\omega^* \widehat{U}_\theta^* + \frac{im\overline{u}_\theta^* \widehat{U}_\theta^*}{r^*} + i\alpha^* \overline{u}_z^* \widehat{U}_\theta^* + \frac{\overline{u}_\theta^* \widehat{U}_r^*}{r^*} + \widehat{U}_r^* \frac{\partial \overline{u}_\theta^*}{\partial r^*} \\
 & + \frac{im\widehat{P}^*}{r^*} - \frac{1}{\text{Re}} \left(\frac{\partial^2 \widehat{U}_\theta^*}{\partial r^{*2}} + \frac{1}{r^*} \frac{\partial \widehat{U}_\theta^*}{\partial r^*} - \frac{m^2 \widehat{U}_\theta^*}{r^{*2}} - \alpha^{*2} \widehat{U}_\theta^* - \frac{\widehat{U}_\theta^*}{r^{*2}} + \frac{2im\widehat{U}_r^*}{r^{*2}} \right) = 0,
 \end{aligned} \tag{A.5.12}$$

and in axial direction

$$\begin{aligned}
 & -i\omega^* \widehat{U}_z^* + \frac{im\overline{u}_\theta^* \widehat{U}_z^*}{r^*} + i\alpha^* \overline{u}_z^* \widehat{U}_z^* + \widehat{U}_r^* \frac{\partial \overline{u}_z^*}{\partial r^*} + i\alpha^* \widehat{U}_z^* \overline{u}_z^* \\
 & + i\alpha^* \widehat{P}^* - \frac{1}{\text{Re}} \left(\frac{\partial^2 \widehat{U}_z^*}{\partial r^{*2}} + \frac{1}{r^*} \frac{\partial \widehat{U}_z^*}{\partial r^*} - \frac{m^2 \widehat{U}_z^*}{r^{*2}} - \alpha^{*2} \widehat{U}_z^* \right) = 0.
 \end{aligned} \tag{A.5.13}$$

Furthermore, the continuity equation becomes

$$\frac{\partial \widehat{U}_r^*}{\partial r^*} + \frac{\widehat{U}_r^*}{r^*} + \frac{im}{r^*} \widehat{U}_\theta^* + i\alpha^* \widehat{U}_z^* = 0. \tag{A.5.14}$$

The set of Eqns. (A.5.13–A.5.14) poses a dispersion relation for the complex frequency, ω^* , and the complex axial wave number, α^* . When one of them is fixed, the set of equations can be formulated as a GEVP where the respective other is the eigenvalue. When α^* is fixed, the generalized eigenvalue problem with eigenvalue ω is

$$A(\alpha)\lambda = \omega^* B(\alpha)\lambda, \tag{A.5.15}$$

where

$$\lambda = [\widehat{U}_r^*, \widehat{U}_\theta^*, \widehat{U}_z^*, \widehat{P}^*]^T. \tag{A.5.16}$$

When ω is fixed, then the eigenvalue problem of α^* is quadratic. A simple way to reduce a quadratic GEVP to a linear GEVP is introducing additional unknowns for the eigenfunctions where α^* appears quadratic. The eigenvalue problem then becomes:

$$A(\omega)\lambda = \alpha^* B(\omega)\lambda, \tag{A.5.17}$$

where

$$\lambda = [\widehat{U}_r^*, \widehat{U}_\theta^*, \widehat{U}_z^*, \widehat{P}^*, \alpha^* \widehat{U}_r^*, \alpha^* \widehat{U}_\theta^*, \alpha^* \widehat{U}_z^*]^T. \tag{A.5.18}$$

Appendix B

Hydrodynamic Linear Stability Analysis in Rotation Symmetric Flows of Non-uniform Density

Here, the compressible hydrodynamic instability equations in cylindrical coordinates for mean flows homogeneous in azimuthal direction shall be derived. We do this under the following assumptions:

- The fluid follows the perfect gas law.
- The base flow is superimposed by not more than one coherent fluctuation.
- The influence of stochastic turbulence on the coherent fluctuations is neglected.
- Gas properties, namely the specific gas constant, R_s , the heat capacities, c_v and c_p , the isotropic exponent γ , the heat conductivity, k , and the dynamic viscosity, μ , are constant.
- Base pressure is constant (Constant pressure combustion)
- Low Mach number

B.1 Derivative Operators in Cylindrical Coordinates

The following equations show some derivative operators in cylindrical coordinates:

- Scalar gradient

$$\nabla\phi = \frac{\partial\phi}{\partial r}\hat{\mathbf{r}} + \frac{1}{r}\frac{\partial\phi}{\partial\theta}\hat{\boldsymbol{\theta}} + \frac{\partial\phi}{\partial z}\hat{\mathbf{z}} \quad (\text{B.1.1})$$

- Material derivative

$$\begin{aligned}
 (\mathbf{A} \cdot \nabla) \mathbf{B} &= \left(A_r \frac{\partial B_r}{\partial r} + \frac{A_\theta}{r} \frac{\partial B_r}{\partial \theta} + A_z \frac{\partial B_r}{\partial z} - \frac{A_\theta B_\theta}{r} \right) \hat{\mathbf{r}} \\
 &+ \left(A_r \frac{\partial B_\theta}{\partial r} + \frac{A_\theta}{r} \frac{\partial B_\theta}{\partial \theta} + A_z \frac{\partial B_\theta}{\partial z} + \frac{A_\theta B_r}{r} \right) \hat{\theta} \\
 &+ \left(A_r \frac{\partial B_z}{\partial r} + \frac{A_\theta}{r} \frac{\partial B_z}{\partial \theta} + A_z \frac{\partial B_z}{\partial z} \right) \hat{\mathbf{z}}
 \end{aligned} \tag{B.1.2}$$

- Scalar Laplacian

$$\Delta \phi = \frac{1}{r} \frac{\partial}{\partial r} \left(r \frac{\partial \phi}{\partial r} \right) + \frac{1}{r^2} \frac{\partial^2 \phi}{\partial \theta^2} + \frac{\partial^2 \phi}{\partial z^2} \tag{B.1.3}$$

- Vector Laplacian

$$\begin{aligned}
 \Delta \mathbf{A} &= \left(\Delta A_r - \frac{A_r}{r^2} - \frac{2}{r^2} \frac{\partial A_\theta}{\partial \theta} \right) \hat{\mathbf{r}} \\
 &+ \left(\Delta A_\theta - \frac{A_\theta}{r^2} + \frac{2}{r^2} \frac{\partial A_r}{\partial \theta} \right) \hat{\theta} \\
 &+ \Delta A_z \hat{\mathbf{z}}
 \end{aligned} \tag{B.1.4}$$

- Vector Divergence

$$\nabla \cdot \mathbf{A} = \frac{1}{r} \frac{\partial (r A_r)}{\partial r} + \frac{1}{r} \frac{\partial A_\theta}{\partial \theta} + \frac{\partial A_z}{\partial z} \tag{B.1.5}$$

The vectors $\hat{\mathbf{r}}$, $\hat{\theta}$ and $\hat{\mathbf{z}}$ denote the unity vectors in radial, azimuthal and axial direction.

B.2 Governing Equations

We start with the set of Navier-Stokes equations, continuity equation and internal energy equation.

$$\rho \left(\frac{\partial \mathbf{u}}{\partial t} + (\mathbf{u} \cdot \nabla) \mathbf{u} \right) = -\nabla p + \nabla \cdot (\mu \nabla \mathbf{u}) + \frac{1}{3} \mu \nabla (\nabla \cdot \mathbf{u}) \tag{B.2.1}$$

$$\frac{\partial \rho}{\partial t} + \nabla \cdot (\rho \mathbf{u}) = 0 \tag{B.2.2}$$

$$\rho \frac{\partial}{\partial t} (c_v T) + \rho \mathbf{u} \nabla \cdot (c_v T) = -p \nabla \cdot \mathbf{u} + \nabla \cdot (k \nabla T) + \Phi \tag{B.2.3}$$

Furthermore, we assume that the fluid is a perfect gas:

$$p = \rho R_s T \quad (\text{B.2.4})$$

$$c_p - c_v = R_s \quad (\text{B.2.5})$$

$$\frac{c_p}{c_v} = \gamma \quad (\text{B.2.6})$$

$$\frac{R_s}{c_v} = \gamma - 1 \quad (\text{B.2.7})$$

Inserting the perfect gas law into the equation of conservation of internal energy leads to

$$\rho \frac{\partial}{\partial t} \left(\frac{c_v p}{R_s \rho} \right) + \rho \mathbf{u} \nabla \cdot \left(\frac{c_v p}{R_s \rho} \right) = -p \nabla \cdot \mathbf{u} + \nabla \cdot \left(k \nabla \frac{p}{R_s \rho} \right) + \Phi \quad (\text{B.2.8})$$

Assuming a constant isotropic exponent, heat conductivity and specific gas constant (assumption 4), Eqn. (B.2.7) allows to reformulate Eqn. (B.2.8):

$$\frac{\rho}{\gamma - 1} \left(\frac{\partial}{\partial t} \left(\frac{p}{\rho} \right) + \mathbf{u} \nabla \cdot \left(\frac{p}{\rho} \right) \right) = -p \nabla \cdot \mathbf{u} + \frac{k}{R_s} \Delta \left(\frac{p}{\rho} \right) + \Phi \quad (\text{B.2.9})$$

In low Mach number flows the compression or expansion are decoupled from pressure fluctuations so that in the energy equation the pressure is approximately equal to the thermodynamic pressure, which according to assumption 5 is constant. Eqn. B.2.9 can hence be rewritten as

$$\frac{\rho p}{\gamma - 1} \left(\frac{\partial}{\partial t} \left(\frac{1}{\rho} \right) + \mathbf{u} \nabla \cdot \left(\frac{1}{\rho} \right) \right) = -p \nabla \cdot \mathbf{u} + \frac{k p}{R_s} \Delta \left(\frac{1}{\rho} \right) + \Phi \quad (\text{B.2.10})$$

Applying the chain rule for derivation for all terms containing $\frac{1}{\rho}$ yields:

$$\frac{\rho}{\gamma - 1} \left(-\frac{p}{\rho^2} \frac{\partial \rho}{\partial t} - \frac{p}{\rho^2} \mathbf{u} \cdot \nabla \rho \right) = -p \nabla \cdot \mathbf{u} + \frac{k p}{R_s} \left(\frac{2}{\rho^3} \nabla \rho \cdot \nabla \rho - \frac{1}{\rho^2} \Delta \rho \right) + \Phi \quad (\text{B.2.11})$$

We multiply the equation by $\frac{(\gamma-1)}{p}$ and find

$$-\frac{1}{\rho} \frac{\partial \rho}{\partial t} - \frac{1}{\rho} \mathbf{u} \cdot \nabla \rho = -(\gamma - 1) \nabla \cdot \mathbf{u} + \frac{k(\gamma - 1)}{R_s} \left(\frac{2}{\rho^3} \nabla \rho \cdot \nabla \rho - \frac{1}{\rho^2} \Delta \rho \right) + \Phi \quad (\text{B.2.12})$$

Using the continuity equation (Eqn. (B.2.2)) the left hand side can be expressed as follows:

$$\nabla \cdot \mathbf{u} = -(\gamma - 1) \nabla \cdot \mathbf{u} + \frac{k(\gamma - 1)}{R_s} \left(\frac{2}{\rho^3} \nabla \rho \cdot \nabla \rho - \frac{1}{\rho^2} \Delta \rho \right) + \Phi. \quad (\text{B.2.13})$$

Inserting Eqn. (B.2.7) and multiplying the equation by ρ^3 yields an equation coupling the density to velocity:

$$\rho^3 \gamma \nabla \cdot \mathbf{u} = \frac{k}{c_v} (2 \nabla \rho \cdot \nabla \rho - \rho \Delta \rho) + \Phi, \quad (\text{B.2.14})$$

It often is convenient to express the governing equations in the non-dimensional form. The reference values are arbitrary, but in this context are defined as:

$$\mathbf{u} = U_{\text{ref}} \mathbf{u}^* \quad (\text{B.2.15a})$$

$$x = D_{\text{ref}} x^* \quad (\text{B.2.15b})$$

$$t = \frac{D_{\text{ref}}}{U_{\text{ref}}} t^* \quad (\text{B.2.15c})$$

$$\rho = \rho_{\text{ref}} \rho^* \quad (\text{B.2.15d})$$

$$p = \rho_{\text{ref}} U_{\text{ref}}^2 p^* \quad (\text{B.2.15e})$$

With the Reynolds and Prandtl number defined as

$$\text{Re} = \frac{U_{\text{ref}} D_{\text{ref}}}{\nu_{\text{ref}}} = \frac{U_{\text{ref}} D_{\text{ref}} \rho_{\text{ref}}}{\mu} \quad (\text{B.2.16a})$$

$$\text{Pr} = \frac{c_p \mu}{k}, \quad (\text{B.2.16b})$$

the full set of governing equations can then be expressed as:

$$\rho^* \left(\frac{\partial \mathbf{u}^*}{\partial t^*} + (\mathbf{u}^* \cdot \nabla^*) \mathbf{u}^* \right) = -\nabla^* p^* + \frac{1}{\text{Re}} \left(\Delta \mathbf{u}^* + \frac{1}{3} \nabla^* (\nabla^* \cdot \mathbf{u}^*) \right) \quad (\text{B.2.17})$$

$$\frac{\partial \rho^*}{\partial t^*} + \nabla^* \cdot (\rho^* \mathbf{u}^*) = 0 \quad (\text{B.2.18})$$

$$\rho^{*3} \nabla^* \cdot \mathbf{u}^* = \frac{1}{\text{Re Pr}} (2 \nabla^* \rho^* \cdot \nabla^* \rho^* - \rho^* \Delta^* \rho^*) + \Phi^*, \quad (\text{B.2.19})$$

B.3 Linearization

We assume that the energy source term is zero. When neglecting stochastic fluctuations, the primitive variables can be described as the sum of a temporal average and a coherent fluctuation:

$$\mathbf{u} = \bar{\mathbf{u}} + \epsilon \hat{\mathbf{u}}, \quad p = \bar{p} + \epsilon \hat{p}, \quad \rho = \bar{\rho} + \epsilon \hat{\rho}, \quad (\text{B.3.1})$$

where $\epsilon \ll 1$. A zero order analysis shows that the mean values fulfill the set of Eqns. (B.2.17–B.2.19). Inserting Eqn. (B.3.1) into Eqns. (B.2.17–B.2.19) furthermore yields the governing

equations of linear hydrodynamic stability. These read:

$$\begin{aligned} \bar{\rho}^* \left(\frac{\partial \widehat{\mathbf{u}}^*}{\partial t^*} + (\widehat{\mathbf{u}}^* \cdot \nabla^*) \bar{\mathbf{u}}^* + (\bar{\mathbf{u}}^* \cdot \nabla^*) \widehat{\mathbf{u}}^* \right) + \widehat{\rho}^* (\bar{\mathbf{u}}^* \cdot \nabla^*) \bar{\mathbf{u}}^* \\ = -\gamma \nabla^* \widehat{p}^* + \frac{1}{\text{Re}} \left(\Delta^* \widehat{\mathbf{u}}^* + \frac{1}{3} \nabla^* (\nabla^* \cdot \widehat{\mathbf{u}}^*) \right) \end{aligned} \quad (\text{B.3.2})$$

$$\frac{\partial \widehat{\rho}^*}{\partial t^*} + \nabla^* \widehat{\rho}^* \cdot \bar{\mathbf{u}}^* + \nabla^* \bar{\rho}^* \cdot \widehat{\mathbf{u}}^* + \bar{\rho}^* (\nabla^* \cdot \widehat{\mathbf{u}}^*) + \widehat{\rho}^* (\nabla^* \cdot \bar{\mathbf{u}}^*) = 0 \quad (\text{B.3.3})$$

$$\bar{\rho}^{*3} \nabla^* \cdot \widehat{\mathbf{u}}^* + 3\bar{\rho}^{*2} \widehat{\rho}^* \nabla^* \cdot \bar{\mathbf{u}}^* + \frac{1}{\text{Re Pr}} \left(\bar{\rho}^* \Delta^* \widehat{\rho}^* + \widehat{\rho}^* \Delta^* \bar{\rho}^* - 4 \nabla^* \widehat{\rho}^* \nabla^* \bar{\rho}^* \right) = 0 \quad (\text{B.3.4})$$

B.4 BiGlobal Stability

In the BiGlobal approach we assume that the fluctuating quantities are harmonic in time with the frequency ω and in azimuthal direction with the azimuthal wave number m , which leads to the modal approach:

$$\begin{aligned} \widehat{\mathbf{u}} &= \widehat{\mathbf{U}} \exp(i\xi), \\ \widehat{p} &= \widehat{P} \exp(i\xi), \\ \widehat{\rho} &= \widehat{\Psi} \exp(i\xi), \end{aligned} \quad (\text{B.4.1})$$

where the phase angle ξ is described for the BiGlobal approach by:

$$\xi = m\theta - \omega t \quad (\text{B.4.2})$$

Inserting Eqn. (B.4.2) into the continuity, Navier-Stokes and energy equation leads to:

$$\begin{aligned} \bar{\rho}^* \left(\frac{\partial (\widehat{\mathbf{U}}^* \exp(i\xi))}{\partial t^*} + ((\widehat{\mathbf{U}}^* \exp(i\xi)) \cdot \nabla^*) \bar{\mathbf{u}}^* + (\bar{\mathbf{u}}^* \cdot \nabla^*) (\widehat{\mathbf{U}}^* \exp(i\xi)) \right) \\ + \widehat{\rho}^* \exp(i\xi) (\bar{\mathbf{u}}^* \cdot \nabla^*) \bar{\mathbf{u}}^* + \gamma \nabla^* (\widehat{P}^* \exp(i\xi)) \\ - \frac{1}{\text{Re}} \left(\Delta^* (\widehat{\mathbf{U}}^* \exp(i\xi)) + \frac{1}{3} \nabla^* (\nabla^* \cdot (\widehat{\mathbf{U}}^* \exp(i\xi))) \right) = 0 \end{aligned} \quad (\text{B.4.3})$$

$$\begin{aligned} \frac{\partial}{\partial t^*} (\widehat{\rho}^* \exp(i\xi)) + \nabla^* (\widehat{\Psi}^* \exp(i\xi)) \cdot \bar{\mathbf{u}}^* + \nabla^* \bar{\rho}^* \cdot \widehat{\mathbf{u}}^* \exp(i\xi) \\ + \bar{\rho}^* (\nabla^* \cdot \widehat{\mathbf{U}}^* \exp(i\xi)) + \widehat{\Psi}^* \exp(i\xi) (\nabla^* \cdot \bar{\mathbf{u}}^*) = 0 \end{aligned} \quad (\text{B.4.4})$$

$$\begin{aligned} & \overline{\rho}^*{}^3 \nabla^* \cdot (\widehat{\mathbf{U}}^* \exp(i\xi)) + 3\overline{\rho}^*{}^2 \widehat{\Psi}^* \exp(i\xi) \nabla^* \cdot \overline{\mathbf{u}}^* \\ & + \frac{1}{\text{Re Pr}} \left(\overline{\rho}^* \Delta^* (\widehat{\Psi}^* \exp(i\xi)) + \widehat{\Psi}^* \exp(i\xi) \Delta^* \overline{\rho}^* - 4\nabla^* (\widehat{\Psi}^* \exp(i\xi)) \nabla^* \overline{\rho}^* \right) = 0 \end{aligned} \quad (\text{B.4.5})$$

In the BiGlobal approach the mean flow is assumed to be homogeneous in azimuthal direction. Therefore all derivatives of mean quantities with respect to the azimuthal direction are equal to zero. Furthermore, since the fluctuating quantities are harmonic in azimuthal direction, their derivatives with respect to the azimuthal direction correspond to a multiplication with im . Similarly a derivation by time is equivalent to a multiplication by $-i\omega$.

For reasons of simplicity the derivative operators laid out in Section B.1 of mean and fluctuating quantities are given here adapted to the global approach for both mean and fluctuating quantities:

- Scalar gradient

$$\nabla \overline{\phi} = \frac{\partial \overline{\phi}}{\partial r} \mathbf{e}_r + 0 \mathbf{e}_\theta + \frac{\partial \overline{\phi}}{\partial z} \mathbf{e}_z \quad (\text{B.4.6})$$

$$\nabla (\widehat{\phi} \exp(im\theta - i\omega t)) = \left(\frac{\partial \widehat{\phi}}{\partial r} \mathbf{e}_r + \frac{im\widehat{\phi}}{r} \mathbf{e}_\theta + \frac{\partial \widehat{\phi}}{\partial z} \mathbf{e}_z \right) \exp(im\theta - i\omega t) \quad (\text{B.4.7})$$

- Scalar Laplacian

$$\Delta \overline{\phi} = \frac{1}{r} \frac{\partial}{\partial r} \left(r \frac{\partial \overline{\phi}}{\partial r} \right) + \frac{\partial^2 \overline{\phi}}{\partial z^2} \quad (\text{B.4.8})$$

$$\Delta (\widehat{\phi} \exp(im\theta - i\omega t)) = \left(\frac{1}{r} \frac{\partial}{\partial r} \left(r \frac{\partial \widehat{\phi}}{\partial r} \right) - \frac{m^2}{r^2} \widehat{\phi} + \frac{\partial^2 \widehat{\phi}}{\partial z^2} \right) \exp(im\theta - i\omega t) \quad (\text{B.4.9})$$

- Vector divergence

$$\nabla \cdot \overline{\mathbf{A}} = \frac{1}{r} \frac{\partial}{\partial r} (r \overline{A}_r) + \frac{\partial \overline{A}_z}{\partial z} \quad (\text{B.4.10})$$

$$\nabla \cdot (\widehat{\mathbf{A}} \exp(im\theta - i\omega t)) = \left(\frac{1}{r} \frac{\partial}{\partial r} (r \widehat{A}_r) + \frac{im}{r} \widehat{A}_\theta + \frac{\partial \widehat{A}_z}{\partial z} \right) \exp(im\theta - i\omega t) \quad (\text{B.4.11})$$

- Vector Laplacian

$$\begin{aligned} \Delta (\widehat{\mathbf{A}} \exp(im\theta - i\omega t)) &= \left(\Delta \widehat{A}_r - \frac{\widehat{A}_r}{r^2} - \frac{2im}{r^2} \widehat{A}_\theta \right) \mathbf{e}_r \exp(im\theta - i\omega t) \\ &+ \left(\Delta \widehat{A}_\theta - \frac{\widehat{A}_\theta}{r^2} + \frac{2im}{r^2} \widehat{A}_r \right) \mathbf{e}_\theta \exp(im\theta - i\omega t) \\ &+ \Delta \widehat{A}_z \mathbf{e}_z \exp(im\theta - i\omega t) \end{aligned} \quad (\text{B.4.12})$$

- Material derivative

$$\begin{aligned}
 (\mathbf{B} \cdot \nabla) \bar{\mathbf{A}} &= \left(B_r \frac{\partial \bar{A}_r}{\partial r} + B_z \frac{\partial \bar{A}_r}{\partial z} - \frac{B_\theta \bar{A}_\theta}{r} \right) \hat{\mathbf{r}} \\
 &+ \left(B_r \frac{\partial \bar{A}_\theta}{\partial r} + B_z \frac{\partial \bar{A}_\theta}{\partial z} + \frac{B_\theta \bar{A}_r}{r} \right) \hat{\boldsymbol{\theta}} \\
 &+ \left(B_r \frac{\partial \bar{A}_z}{\partial r} + B_z \frac{\partial \bar{A}_z}{\partial z} \right) \hat{\mathbf{z}}
 \end{aligned} \tag{B.4.13}$$

$$\begin{aligned}
 (\mathbf{B} \cdot \nabla) (\widehat{\mathbf{A}} \exp(im\theta - i\omega t)) &= \\
 &\left(B_r \frac{\partial \widehat{A}_r}{\partial r} + \frac{imB_\theta \widehat{A}_r}{r} + B_z \frac{\partial \widehat{A}_r}{\partial z} - \frac{B_\theta \widehat{A}_\theta}{r} \right) \hat{\mathbf{r}} \exp(im\theta - i\omega t) \\
 &+ \left(B_r \frac{\partial \widehat{A}_\theta}{\partial r} + \frac{imB_\theta \widehat{A}_\theta}{r} + B_z \frac{\partial \widehat{A}_\theta}{\partial z} + \frac{B_\theta \widehat{A}_r}{r} \right) \hat{\boldsymbol{\theta}} \exp(im\theta - i\omega t) \\
 &+ \left(B_r \frac{\partial \widehat{A}_z}{\partial r} + \frac{imB_\theta \widehat{A}_z}{r} + B_z \frac{\partial \widehat{A}_z}{\partial z} \right) \hat{\mathbf{z}} \exp(im\theta - i\omega t),
 \end{aligned} \tag{B.4.14}$$

The derivative operators above can now be inserted in the set of Eqns. (B.4.3–B.4.5), which yields for the momentum equation in radial direction

$$\begin{aligned}
 \bar{\rho}^* \left(-i\omega^* \widehat{U}_r^* + \bar{u}_r^* \frac{\partial \widehat{U}_r^*}{\partial r^*} + \frac{im\bar{u}_\theta^* \widehat{U}_r^*}{r^*} + \bar{u}_z^* \frac{\partial \widehat{U}_r^*}{\partial z^*} - \frac{2\bar{u}_\theta^* \widehat{U}_\theta^*}{r^*} + \widehat{U}_r^* \frac{\partial \bar{u}_r^*}{\partial r^*} + \widehat{U}_z^* \frac{\partial \bar{u}_r^*}{\partial z^*} \right) \\
 + \widehat{\Psi}^* \left(\bar{u}_r^* \frac{\partial \bar{u}_r^*}{\partial r^*} + \bar{u}_z^* \frac{\partial \bar{u}_r^*}{\partial z^*} - \frac{\bar{u}_\theta^{*2}}{r^*} \right) + \frac{\partial \widehat{P}^*}{\partial r^*} \\
 - \frac{1}{\text{Re}} \left(\frac{\partial^2 \widehat{U}_r^*}{\partial r^{*2}} + \frac{1}{r^*} \frac{\partial \widehat{U}_r^*}{\partial r^*} - \frac{m^2 \widehat{U}_r^*}{r^{*2}} + \frac{\partial^2 \widehat{U}_r^*}{\partial z^{*2}} - \frac{\widehat{U}_r^*}{r^{*2}} - \frac{2im\widehat{U}_\theta^*}{r^{*2}} \right. \\
 \left. + \frac{1}{3} \left(\frac{\partial^2 \widehat{U}_r^*}{\partial r^{*2}} + \frac{1}{r^*} \frac{\partial \widehat{U}_r^*}{\partial r^*} - \frac{\widehat{U}_r^*}{r^{*2}} + \frac{im}{r^*} \frac{\partial \widehat{U}_\theta^*}{\partial r^*} - \frac{im\widehat{U}_\theta^*}{r^{*2}} + \frac{\partial^2 \widehat{u}_z^*}{\partial r^* \partial z^*} \right) \right) = 0,
 \end{aligned} \tag{B.4.15}$$

in azimuthal direction

$$\begin{aligned}
 \bar{\rho}^* \left(-i\omega^* \widehat{U}_\theta^* + \frac{\partial \widehat{U}_\theta^*}{\partial r^*} + \frac{im\bar{u}_\theta^* \widehat{U}_\theta^*}{r^*} + \frac{\partial \widehat{U}_\theta^*}{\partial z^*} + \frac{\bar{u}_\theta^* \widehat{U}_r^*}{r^*} + \widehat{U}_r^* \frac{\partial \bar{u}_\theta^*}{\partial r^*} + \widehat{U}_z^* \frac{\partial \bar{u}_\theta^*}{\partial z^*} + \frac{\widehat{U}_\theta^* \bar{u}_r^*}{r^*} \right) \\
 + \widehat{\Psi}^* \left(\frac{\bar{u}_r^* \partial \bar{u}_\theta^*}{\partial r^*} + \bar{u}_z^* \frac{\partial \bar{u}_\theta^*}{\partial z^*} + \frac{\bar{u}_\theta^* \bar{u}_r^*}{r^*} \right) + \frac{im\widehat{P}^*}{r^*} \\
 - \frac{1}{\text{Re}} \left(\frac{\partial^2 \widehat{U}_\theta^*}{\partial r^{*2}} + \frac{1}{r^*} \frac{\partial \widehat{U}_\theta^*}{\partial r^*} - \frac{m^2 \widehat{U}_\theta^*}{r^{*2}} + \frac{\partial^2 \widehat{U}_\theta^*}{\partial z^{*2}} - \frac{\widehat{U}_\theta^*}{r^{*2}} + \frac{2im\widehat{U}_r^*}{r^{*2}} \right. \\
 \left. + \frac{1}{3} \left(\frac{im}{r} \frac{\partial \widehat{U}_r^*}{\partial r^*} + \frac{im\widehat{U}_r^*}{r^{*2}} - \frac{m^2 \widehat{U}_\theta^*}{r^{*2}} + \frac{im}{r} \frac{\partial \widehat{U}_z^*}{\partial z^*} \right) \right) = 0,
 \end{aligned} \tag{B.4.16}$$

and in axial direction

$$\begin{aligned}
 \bar{\rho}^* \left(-i\omega^* \widehat{U}_z^* + \frac{\partial \widehat{U}_z^*}{\partial r^*} + \frac{im\bar{u}_\theta^* \widehat{U}_z^*}{r^*} + \frac{\partial \widehat{U}_z^*}{\partial z^*} + \widehat{U}_r^* \frac{\partial \bar{u}_z^*}{\partial r^*} + \widehat{U}_z^* \frac{\partial \bar{u}_z^*}{\partial z^*} \right) \\
 + \widehat{\Psi}^* \left(\frac{\bar{u}_r^* \partial \bar{u}_z^*}{\partial r^*} + \bar{u}_z^* \frac{\partial \bar{u}_z^*}{\partial z^*} \right) + \frac{\partial \widehat{P}^*}{\partial z^*} \\
 - \frac{1}{\text{Re}} \left(\frac{\partial^2 \widehat{U}_z^*}{\partial r^{*2}} + \frac{1}{r^*} \frac{\partial \widehat{U}_z^*}{\partial r^*} - \frac{m^2 \widehat{U}_z^*}{r^{*2}} + \frac{\partial^2 \widehat{U}_z^*}{\partial z^{*2}} \right. \\
 \left. + \frac{1}{3} \left(\frac{\partial^2 \widehat{U}_r^*}{\partial z^* \partial r^*} + \frac{1}{r^*} \frac{\partial \widehat{U}_r^*}{\partial z^*} + \frac{im}{r^*} \frac{\partial \widehat{U}_\theta^*}{\partial z^*} + \frac{\partial^2 \widehat{U}_z^*}{\partial z^{*2}} \right) \right) = 0.
 \end{aligned} \tag{B.4.17}$$

Furthermore, the continuity equation becomes

$$\begin{aligned}
 -i\omega^* \widehat{\Psi}^* + \frac{\partial \widehat{\Psi}^*}{\partial r^*} \bar{u}_r^* + \frac{im\widehat{\Psi}^*}{r^*} \bar{u}_\theta^* + \frac{\partial \widehat{\Psi}^*}{\partial z^*} \bar{u}_z^* + \frac{\partial \bar{\rho}^*}{\partial r^*} \widehat{U}_r^* + \frac{\partial \bar{\rho}^*}{\partial z^*} \widehat{U}_z^* + \widehat{\Psi}^* \left(\frac{\partial \bar{u}_r^*}{\partial r^*} + \frac{\bar{u}_r^*}{r^*} + \frac{\partial \bar{u}_z^*}{\partial z^*} \right) \\
 + \bar{\rho}^* \left(\frac{\partial \widehat{U}_r^*}{\partial r^*} + \frac{\widehat{U}_r^*}{r^*} + \frac{im}{r^*} \widehat{U}_\theta^* + \frac{\partial \widehat{U}_z^*}{\partial z^*} \right) = 0,
 \end{aligned} \tag{B.4.18}$$

and one obtains the energy equation:

$$\begin{aligned}
 & \overline{\rho}^{*3} \left(\frac{\partial \widehat{U}_r^*}{\partial r^*} + \frac{\widehat{U}_r^*}{r^*} + \frac{im}{r^*} \widehat{U}_\theta^* + \frac{\partial \widehat{U}_z^*}{\partial z^*} \right) + 3\overline{\rho}^{*2} \widehat{\Psi}^* \left(\frac{\partial \overline{u}_r^*}{\partial r^*} + \frac{\overline{u}_r^*}{r^*} + \frac{\partial \overline{u}_z^*}{\partial z^*} \right) \\
 & + \frac{1}{\text{Re Pr}} \left(\overline{\rho}^* \left(\frac{\partial^2 \widehat{\Psi}^*}{\partial r^{*2}} + \frac{1}{r^*} \frac{\partial \widehat{\Psi}^*}{\partial r^*} - \frac{m^2}{r^{*2}} \widehat{\Psi}^* + \frac{\partial^2 \widehat{\Psi}^*}{\partial z^{*2}} \right) + \widehat{\Psi}^* \left(\frac{\partial^2 \overline{\rho}^*}{\partial r^{*2}} + \frac{1}{r^*} \frac{\partial \overline{\rho}^*}{\partial r^*} + \frac{\partial^2 \overline{\rho}^*}{\partial z^{*2}} \right) \right. \\
 & \left. - 4 \left(\frac{\partial \widehat{\Psi}^*}{\partial r^*} \frac{\partial \overline{\rho}^*}{\partial r^*} + \frac{\partial \widehat{\Psi}^*}{\partial z^*} \frac{\partial \overline{\rho}^*}{\partial z^*} \right) \right) = 0.
 \end{aligned} \tag{B.4.19}$$

The set of Eqns. (B.4.17–B.4.19) poses a generalized eigenvalue problem with eigenvector ω :

$$A\lambda = \omega B\lambda, \tag{B.4.20}$$

where

$$\lambda = [\widehat{U}_r^*, \widehat{U}_\theta^*, \widehat{U}_z^*, \widehat{P}^*, \widehat{\Psi}^*]^T \tag{B.4.21}$$

B.5 Local Stability

As in the BiGlobal approach, in the local approach we assume that the fluctuating quantities are harmonic in time with the frequency ω , in azimuthal direction with the azimuthal wave number m . Furthermore two additional assumptions are made: Firstly, it is assumed that the base flow is homogeneous in axial direction, which leads to vanishing derivatives of the base flow in z -direction. Secondly, the coherent fluctuation is harmonic in axial direction with the complex wave number α .

The phase angle in Eqns. (B.4.1) therefore is

$$\xi = m\theta + \alpha z - \omega t \tag{B.5.1}$$

Due to the adaptation of the modal approach and the assumption of base flow homogeneity in axial direction, the derivative operators of temporal means and coherent fluctuation quantities differ from those in the BiGlobal approach. All derivatives of base flow quantities with respect to z are zero. Furthermore, in a parallel flow the radial component of the base flow velocity must be zero¹. And finally, a derivation of a coherent fluctuation with respect to z becomes a product of $i\alpha$ with the coherent fluctuation. The derivative operators of temporal means and coherent fluctuation quantities hence become in the framework of local LSA:

¹Note that literature the radial velocity component often is not assumed to be zero. This results in additional remaining terms involving the radial velocity (see e.g. [8])

- Scalar gradient

$$\nabla \bar{\phi} = \frac{\partial \bar{\phi}}{\partial r} \mathbf{e}_r + 0 \mathbf{e}_\theta + 0 \mathbf{e}_z \quad (\text{B.5.2})$$

$$\nabla \left(\widehat{\phi} \exp(im\theta - i\omega t) \right) = \left(\frac{\partial \widehat{\phi}}{\partial r} \mathbf{e}_r + \frac{im\widehat{\phi}}{r} \mathbf{e}_\theta + i\alpha \widehat{\phi} \mathbf{e}_z \right) \exp(im\theta - i\omega t) \quad (\text{B.5.3})$$

- Scalar Laplacian

$$\Delta \bar{\phi} = \frac{1}{r} \frac{\partial}{\partial r} \left(r \frac{\partial \bar{\phi}}{\partial r} \right) \quad (\text{B.5.4})$$

$$\Delta \left(\widehat{\phi} \exp(im\theta - i\omega t) \right) = \left(\frac{1}{r} \frac{\partial}{\partial r} \left(r \frac{\partial \widehat{\phi}}{\partial r} \right) - \frac{m^2}{r^2} \widehat{\phi} - \alpha^2 \widehat{\phi} \right) \exp(im\theta - i\omega t) \quad (\text{B.5.5})$$

- Vector divergence

$$\nabla \cdot \bar{\mathbf{A}} = 0 \quad (\text{B.5.6})$$

$$\nabla \cdot \left(\widehat{\mathbf{A}} \exp(im\theta - i\omega t) \right) = \left(\frac{1}{r} \frac{\partial}{\partial r} \left(r \widehat{A}_r \right) + \frac{im}{r} \widehat{A}_\theta + i\alpha \widehat{A}_z \right) \exp(im\theta - i\omega t) \quad (\text{B.5.7})$$

- Vector Laplacian

$$\begin{aligned} \Delta \left(\widehat{\mathbf{A}} \exp(im\theta - i\omega t) \right) &= \left(\Delta \widehat{A}_r - \frac{\widehat{A}_r}{r^2} - \frac{2im}{r^2} \widehat{A}_\theta \right) \mathbf{e}_r \exp(im\theta - i\omega t) \\ &+ \left(\Delta \widehat{A}_\theta - \frac{\widehat{A}_\theta}{r^2} + \frac{2im}{r^2} \widehat{A}_r \right) \mathbf{e}_\theta \exp(im\theta - i\omega t) \\ &+ \Delta \widehat{A}_z \mathbf{e}_z \exp(im\theta - i\omega t) \end{aligned} \quad (\text{B.5.8})$$

- Material derivative

$$\begin{aligned} (\mathbf{B} \cdot \nabla) \bar{\mathbf{A}} &= \left(-\frac{B_\theta \bar{A}_\theta}{r} \right) \hat{\mathbf{r}} \\ &+ \left(B_r \frac{\partial \bar{A}_\theta}{\partial r} \right) \hat{\boldsymbol{\theta}} \\ &+ \left(B_r \frac{\partial \bar{A}_z}{\partial r} \right) \hat{\mathbf{z}} \end{aligned} \quad (\text{B.5.9})$$

$$\begin{aligned}
 (\mathbf{B} \cdot \nabla) (\widehat{\mathbf{A}} \exp(im\theta - i\omega t)) = & \\
 \left(B_r \frac{\partial \widehat{A}_r}{\partial r} + \frac{imB_\theta \widehat{A}_r}{r} + i\alpha B_z \widehat{A}_r - \frac{B_\theta \widehat{A}_\theta}{r} \right) \hat{\mathbf{r}} \exp(im\theta - i\omega t) & \\
 + \left(B_r \frac{\partial \widehat{A}_\theta}{\partial r} + \frac{imB_\theta \widehat{A}_\theta}{r} + i\alpha B_z \widehat{A}_\theta + \frac{B_\theta \widehat{A}_r}{r} \right) \hat{\boldsymbol{\theta}} \exp(im\theta - i\omega t) & \quad (\text{B.5.10}) \\
 + \left(B_r \frac{\partial \widehat{A}_z}{\partial r} + \frac{imB_\theta \widehat{A}_z}{r} + i\alpha B_z \widehat{A}_z \right) \hat{\mathbf{z}} \exp(im\theta - i\omega t), &
 \end{aligned}$$

The derivative operators adapted to the local approach given in Eqns. (B.5.2)-(B.5.10) can now be inserted in the set of Eqns. (B.4.3-B.4.5), which yields for the momentum equation in radial direction

$$\begin{aligned}
 \bar{\rho}^* \left(-i\omega^* \widehat{U}_r^* + \frac{im\overline{u_\theta^*} \widehat{U}_r^*}{r^*} + i\alpha^* \overline{u_z^*} \widehat{U}_r^* - \frac{2\overline{u_\theta^*} \widehat{U}_\theta^*}{r^*} \right) & \\
 - \widehat{\Psi}^* \frac{\overline{u_\theta^*}^2}{r^*} + \frac{\partial \widehat{P}^*}{\partial r^*} & \\
 - \frac{1}{\text{Re}} \left(\frac{\partial^2 \widehat{U}_r^*}{\partial r^{*2}} + \frac{1}{r^*} \frac{\partial \widehat{U}_r^*}{\partial r^*} - \frac{m^2 \widehat{U}_r^*}{r^{*2}} - \alpha^{*2} \widehat{U}_r^* - \frac{\widehat{U}_r^*}{r^{*2}} - \frac{2im\widehat{U}_\theta^*}{r^{*2}} \right. & \quad (\text{B.5.11}) \\
 \left. + \frac{1}{3} \left(\frac{\partial^2 \widehat{U}_r^*}{\partial r^{*2}} + \frac{1}{r^*} \frac{\partial \widehat{U}_r^*}{\partial r^*} - \frac{\widehat{U}_r^*}{r^{*2}} + \frac{im}{r^*} \frac{\partial \widehat{U}_\theta^*}{\partial r^*} - \frac{im\widehat{U}_\theta^*}{r^{*2}} + i\alpha^* \frac{\partial \overline{u_z^*}}{\partial r^*} \right) \right) = 0, &
 \end{aligned}$$

in azimuthal direction

$$\begin{aligned}
 \bar{\rho}^* \left(-i\omega^* \widehat{U}_\theta^* + \frac{im\overline{u_\theta^*} \widehat{U}_\theta^*}{r^*} + i\alpha^* \overline{u_z^*} \widehat{U}_\theta^* + \frac{\overline{u_\theta^*} \widehat{U}_r^*}{r^*} + \widehat{U}_r^* \frac{\partial \overline{u_\theta^*}}{\partial r^*} \right) & \\
 + \frac{im\widehat{P}^*}{r^*} - \frac{1}{\text{Re}} \left(\frac{\partial^2 \widehat{U}_\theta^*}{\partial r^{*2}} + \frac{1}{r^*} \frac{\partial \widehat{U}_\theta^*}{\partial r^*} - \frac{m^2 \widehat{U}_\theta^*}{r^{*2}} - \alpha^{*2} \widehat{U}_\theta^* - \frac{\widehat{U}_\theta^*}{r^{*2}} + \frac{2im\widehat{U}_r^*}{r^{*2}} \right. & \quad (\text{B.5.12}) \\
 \left. + \frac{1}{3} \left(\frac{im}{r} \frac{\partial \widehat{U}_r^*}{\partial r^*} + \frac{im\widehat{U}_r^*}{r^{*2}} - \frac{m^2 \widehat{U}_\theta^*}{r^{*2}} - \frac{\alpha^* m}{r} \widehat{U}_z^* \right) \right) = 0, &
 \end{aligned}$$

and in axial direction

$$\begin{aligned}
 & \bar{\rho}^* \left(-i\omega^* \widehat{U}_z^* + \frac{im\widehat{u}_\theta^* \widehat{U}_z^*}{r^*} + i\alpha^* \widehat{u}_z^* \widehat{U}_z^* + \widehat{U}_r^* \frac{\partial \widehat{u}_z^*}{\partial r^*} + i\alpha^* \widehat{U}_z^* \widehat{u}_z^* \right) \\
 & + i\alpha^* \widehat{P}^* - \frac{1}{\text{Re}} \left(\frac{\partial^2 \widehat{U}_z^*}{\partial r^{*2}} + \frac{1}{r^*} \frac{\partial \widehat{U}_z^*}{\partial r^*} - \frac{m^2 \widehat{U}_z^*}{r^{*2}} - \alpha^{*2} \widehat{U}_z^* \right. \\
 & \left. + \frac{1}{3} \left(i\alpha^* \frac{\partial \widehat{U}_r^*}{\partial r^*} + \frac{i\alpha^*}{r^*} \widehat{U}_r^* - \frac{\alpha^* m}{r^*} \widehat{U}_\theta^* - \alpha^{*2} \widehat{U}_z^* \right) \right) = 0.
 \end{aligned} \tag{B.5.13}$$

Furthermore, the continuity equation becomes

$$\begin{aligned}
 & -i\omega^* \widehat{\Psi}^* + \frac{im\widehat{\Psi}^*}{r^*} \widehat{u}_\theta^* + i\alpha^* \widehat{\Psi}^* \widehat{u}_z^* + \frac{\partial \bar{\rho}^*}{\partial r^*} \widehat{U}_r^* \\
 & + \bar{\rho}^* \left(\frac{\partial \widehat{U}_r^*}{\partial r^*} + \frac{\widehat{U}_r^*}{r^*} + \frac{im}{r^*} \widehat{U}_\theta^* + i\alpha^* \widehat{U}_z^* \right) = 0,
 \end{aligned} \tag{B.5.14}$$

and one obtains the energy equation:

$$\begin{aligned}
 & \bar{\rho}^{*3} \left(\frac{\partial \widehat{U}_r^*}{\partial r^*} + \frac{\widehat{U}_r^*}{r^*} + \frac{im}{r^*} \widehat{U}_\theta^* + i\alpha^* \widehat{U}_z^* \right) \\
 & + \frac{1}{\text{Re Pr}} \left(\bar{\rho}^* \left(\frac{\partial^2 \widehat{\Psi}^*}{\partial r^{*2}} + \frac{1}{r^*} \frac{\partial \widehat{\Psi}^*}{\partial r^*} - \frac{m^2}{r^{*2}} \widehat{\Psi}^* - \alpha^{*2} \widehat{\Psi}^* \right) + \widehat{\Psi}^* \left(\frac{\partial^2 \bar{\rho}^*}{\partial r^{*2}} + \frac{1}{r^*} \frac{\partial \bar{\rho}^*}{\partial r^*} \right) \right. \\
 & \left. - 4 \frac{\partial \widehat{\Psi}^*}{\partial r^*} \frac{\partial \bar{\rho}^*}{\partial r^*} \right) = 0.
 \end{aligned} \tag{B.5.15}$$

The set of Eqns. (B.4.17–B.4.19) poses a dispersion relation for the complex frequency, ω^* , and the complex axial wave number, α^* . When one of them is fixed, the set of equations can be formulated as a GEVP where the respective other is the eigenvalue. When α^* is fixed, the generalized eigenvalue problem with eigenvalue ω is

$$A(\alpha)\lambda = \omega^* B(\alpha)\lambda, \tag{B.5.16}$$

where

$$\lambda = [\widehat{U}_r^*, \widehat{U}_\theta^*, \widehat{U}_z^*, \widehat{P}^*, \widehat{\Psi}^*]^T. \tag{B.5.17}$$

When ω is fixed, then the eigenvalue problem of α^* is quadratic. A simple way to reduce a quadratic GEVP to a linear GEVP is introducing additional unknowns for the eigenfunctions where α^* appears quadratic. The eigenvalue problem then becomes:

$$A(\omega)\lambda = \alpha^* B(\omega)\lambda, \tag{B.5.18}$$

where

$$\lambda = [\widehat{U}_r^*, \widehat{U}_\theta^*, \widehat{U}_z^*, \widehat{P}^*, \widehat{\Psi}^*, \alpha^* \widehat{U}_r^*, \alpha^* \widehat{U}_\theta^*, \alpha^* \widehat{U}_z^*, \alpha^* \widehat{\Psi}^*]^T. \tag{B.5.19}$$

B.6 Stochastic-Coherent Interaction in Non-uniform Density Flows

It was shown in Chapter A that stochastic fluctuations have an effect on the coherent structures which evolve on a base flow. The effect of the Reynolds stresses on the coherent structure is often modeled by an eddy viscosity. To do so the set of equations must be closed via the Boussinesq approximation.

It is well known, that decomposing velocities and temperature into a Reynolds average and a fluctuating part leads to additional not vanishing terms including the unknown stochastic fluctuation quantities. These make closure of the equations further difficult. The Favre averaging solves this problem for the mean flow equations.

The same problem of additional unknown terms including stochastic fluctuations appears for the governing equations of hydrodynamic instabilities in non-uniform density flows. This problem cannot be solved by applying a Favre average. In the framework of this thesis it is assumed that these additional terms are negligible in comparison with the terms which appear in the Boussinesq approximation. Therefore, the turbulence closure, which was applied on uniform-density flows will also be applied on non-uniform density flows.

Bibliography

- [1] B. Abramzon and W. Sirignano. Droplet vaporization model for spray combustion calculations. *International journal of heat and mass transfer*, 32(9):1605–1618, 1989.
- [2] Airbus. Global market forecast - growing horizons 2017-2036. Technical report, Airbus, 2017. URL https://www.airbus.com/content/dam/corporate-topics/publications/backgrounders/Airbus_Global_Market_Forecast_2017-2036_Growing_Horizons_full_book.pdf.
- [3] E. Akervik, U. Ehrenstein, F. Gallaire, and D. S. Henningson. Global two-dimensional stability measures of the flat plate boundary-layer flow. *European Journal of Mechanics - B/Fluids*, 27(5):501 – 513, 2008. ISSN 0997-7546. doi: <https://doi.org/10.1016/j.euromechflu.2007.09.004>. URL <http://www.sciencedirect.com/science/article/pii/S0997754607000908>.
- [4] E. Akverik, J. Hoepfner, U. Ehrenstein, and D. S. Henningson. Optimal growth, model reduction and control in a separated boundary-layer flow using global eigenmodes. *Journal of Fluid Mechanics*, 579:305–314, 2007. doi: 10.1017/S0022112007005496.
- [5] H. M. Altay, R. L. Speth, D. E. Hudgins, and A. F. Ghoniem. Flame–vortex interaction driven combustion dynamics in a backward-facing step combustor. *Combustion and Flame*, 156(5):1111–1125, 2009.
- [6] W. E. Anderson and V. Yang. *Liquid rocket engine combustion instability*. American Institute of aeronautics and astronautics, 1995.
- [7] S. Arrhenius. On the influence of carbonic acid in the air upon the temperature of the ground. *Philosophical Magazine and Journal of Science*, 41(5):237–276, 1896. ISSN 0036-8075. URL www.rsc.org/images/Arrhenius1896_tcm18-173546.pdf.
- [8] R. L. Ash and M. R. Khorrami. *Vortex Stability*, pages 317–372. Springer Netherlands, Dordrecht, 1995. ISBN 978-94-011-0249-0. doi: 10.1007/978-94-011-0249-0_8. URL https://doi.org/10.1007/978-94-011-0249-0_8.

- [9] K. Aung, M. Hassan, and G. Faeth. Flame stretch interactions of laminar premixed hydrogen/air flames at normal temperature and pressure. *Combustion and Flame*, 109(1): 1 – 24, 1997. ISSN 0010-2180. doi: [https://doi.org/10.1016/S0010-2180\(96\)00151-4](https://doi.org/10.1016/S0010-2180(96)00151-4). URL <http://www.sciencedirect.com/science/article/pii/S0010218096001514>.
- [10] A. Avdonin, M. Meindl, and W. Polifke. Thermoacoustic analysis of a laminar premixed flame using a linearized reactive flow solver. *Proceedings of the Combustion Institute*, 2018. ISSN 1540-7489. doi: <https://doi.org/10.1016/j.proci.2018.06.142>. URL <http://www.sciencedirect.com/science/article/pii/S1540748918303250>.
- [11] D. Barkley. Linear analysis of the cylinder wake mean flow. *EPL (Europhysics Letters)*, 75(5):750, 2006. URL <http://stacks.iop.org/0295-5075/75/i=5/a=750>.
- [12] G. K. Batchelor. Axial flow in trailing line vortices. *Journal of Fluid Mechanics*, 20(4):645–658, 1964. doi: 10.1017/S0022112064001446.
- [13] G. K. Batchelor and A. E. Gill. Analysis of the stability of axisymmetric jets. *Journal of Fluid Mechanics*, 14(4):529–551, 1962. doi: 10.1017/S0022112062001421.
- [14] M. Bauerheim, P. Salas, F. Nicoud, and T. Poinsot. Symmetry breaking of azimuthal thermo-acoustic modes in annular cavities: a theoretical study. *Journal of Fluid Mechanics*, 760:431–465, 2014.
- [15] E. B. Becker, G. F. Carey, and O. J. Tinsley. *Finite Elements - An Introduction*. Texas Institute for Computational Mechanics - The University of Texas at Austin, Austin, Texas, USA, 1981.
- [16] V. Bellucci, B. Schuermans, D. Nowak, P. Flohr, and C. O. Paschereit. Thermoacoustic modeling of a gas turbine combustor equipped with acoustic dampers. In *ASME Turbo Expo 2004: Power for Land, Sea, and Air*, pages 635–644. American Society of Mechanical Engineers, 2004.
- [17] R. G. J. Bill and K. Tarabanis. The effect of premixed combustion on the recirculation zone of circular cylinders. *Combustion Science and Technology*, 47(1-2): 39–53, 1986. doi: 10.1080/00102208608923863. URL <https://doi.org/10.1080/00102208608923863>.
- [18] R. Blumenthal, P. Subramanian, R. Sujith, and W. Polifke. Novel perspectives on the dynamics of premixed flames. *Combustion and Flame*, 160:1215–1224, 2013.
- [19] L. Boltzmann. Ableitung des Stefan’schen Gesetzes, betreffend die Abhängigkeit der Wärmestrahlung von der Temperatur aus der electromagnetischen Lichttheorie. *Annalen der Physik*, 258(6):291–294, 1884. ISSN 1521-3889. doi: 10.1002/andp.18842580616. URL <http://dx.doi.org/10.1002/andp.18842580616>.

-
- [20] BP. Bp statistical review of world energy - june 2018. Technical report, BP Global, June 2018. URL <https://www.bp.com/en/global/corporate/energy-economics/statistical-review-of-world-energy/primary-energy.html>.
- [21] M. Brebion. *Joint numerical and experimental study of thermo-acoustic instabilities*. PhD thesis, Institut de Mécanique des Fluides de Toulouse, 2016.
- [22] T. Bridges and P. Morris. Differential eigenvalue problems in which the parameter appears nonlinearly. *Journal of Computational Physics*, 55(3):437 – 460, 1984. ISSN 0021-9991. doi: [https://doi.org/10.1016/0021-9991\(84\)90032-9](https://doi.org/10.1016/0021-9991(84)90032-9). URL <http://www.sciencedirect.com/science/article/pii/0021999184900329>.
- [23] R. J. Briggs. Electron-stream interaction with plasmas. *Science*, 148(3676):1453–1454, 1964.
- [24] D. M. Brown. Combustion control for producing low no.sub.x emissions through use of flame spectroscopy. *General Electric Company*, 5480298, 1994. URL <https://patents.justia.com/inventor/dale-m-brown>.
- [25] R. BYRNE. Longitudinal pressure oscillations in ramjet combustors. In *19th Joint Propulsion Conference*, page 2018, 1983.
- [26] S. Candel, D. Durox, and T. Schuller. Flame interactions as a source of noise and combustion instabilities. In *10th AIAA/CEAS Aeroacoustics Conference*, page 2928, 2004.
- [27] S. Candel, D. Durox, S. Ducruix, A.-L. Birbaud, N. Noiray, and T. Schuller. Flame dynamics and combustion noise: progress and challenges. *International Journal of Aeroacoustics*, 8(1):1–56, 2009.
- [28] S. Candel, D. Durox, T. Schuller, N. Darabiha, L. Hakim, and T. Schmitt. Advances in combustion and propulsion applications. *European Journal of Mechanics - B/Fluids*, 40:87 – 106, 2013. ISSN 0997-7546. doi: <https://doi.org/10.1016/j.euromechflu.2013.01.002>. URL <http://www.sciencedirect.com/science/article/pii/S0997754613000034>. Fascinating Fluid Mechanics: 100-Year Anniversary of the Institute of Aerodynamics, RWTH Aachen University.
- [29] S. M. Candel. Combustion instabilities coupled by pressure waves and their active control. *Symposium (International) on Combustion*, 24(1):1277 – 1296, 1992. ISSN 0082-0784. doi: [https://doi.org/10.1016/S0082-0784\(06\)80150-5](https://doi.org/10.1016/S0082-0784(06)80150-5). URL <http://www.sciencedirect.com/science/article/pii/S0082078406801505>. Twenty-Fourth Symposium on Combustion.

- [30] G. J. Chandler, M. P. Juniper, J. W. Nichols, and P. J. Schmid. Adjoint algorithms for the navier-stokes equations in the low mach number limit. *Journal of Computational Physics*, 231(4):1900 – 1916, 2012. ISSN 0021-9991. doi: <https://doi.org/10.1016/j.jcp.2011.11.013>. URL <http://www.sciencedirect.com/science/article/pii/S0021999111006681>.
- [31] H. Chao, Y. Cao, and Y. Chen. Autopilots for small unmanned aerial vehicles: A survey. *International Journal of Control, Automation and Systems*, 8(1):36–44, Feb 2010. ISSN 2005-4092. doi: 10.1007/s12555-010-0105-z. URL <https://doi.org/10.1007/s12555-010-0105-z>.
- [32] F. Charru. *Hydrodynamic instabilities*, volume 37. Cambridge University Press, 2011.
- [33] S. Chaudhuri, S. Kostka, M. W. Renfro, and B. M. Cetegen. Blowoff dynamics of bluff body stabilized turbulent premixed flames. *Combustion and Flame*, 157(4):790 – 802, 2010. ISSN 0010-2180. doi: <https://doi.org/10.1016/j.combustflame.2009.10.020>. URL <http://www.sciencedirect.com/science/article/pii/S0010218009003125>.
- [34] J.-M. Chomaz, P. Huerre, and L. G. Redekopp. A Frequency Selection Criterion in Spatially Developing Flows. *Studies in Applied Mathematics*, 84(2):119–144, 1991. ISSN 1467-9590. doi: 10.1002/sapm1991842119. URL <http://dx.doi.org/10.1002/sapm1991842119>.
- [35] L. T. W. Chong, T. Komarek, R. Kaess, S. Foller, and W. Polifke. Identification of flame transfer functions from les of a premixed swirl burner. In *ASME turbo expo 2010: power for land, sea, and air*, pages 623–635. American Society of Mechanical Engineers, 2010.
- [36] P. Clavin. Dynamics of combustion fronts in premixed gases: From flames to detonations. *Proceedings of the Combustion Institute*, 28(1):569 – 585, 2000. ISSN 1540-7489. doi: [https://doi.org/10.1016/S0082-0784\(00\)80257-X](https://doi.org/10.1016/S0082-0784(00)80257-X). URL <http://www.sciencedirect.com/science/article/pii/S008207840080257X>.
- [37] W. Coenen, L. Lesshafft, X. Garnaud, and A. Sevilla. Global instability of low-density jets. *Journal of Fluid Mechanics*, 820:187–207, 2017. doi: 10.1017/jfm.2017.203.
- [38] O. Colin and M. Rudgyard. Development of High-Order Taylor–Galerkin Schemes for LES. *Journal of Computational Physics*, 162(2):338 – 371, 2000. ISSN 0021-9991. doi: <http://dx.doi.org/10.1006/jcph.2000.6538>. URL <http://www.sciencedirect.com/science/article/pii/S0021999100965380>.
- [39] O. Colin, F. Ducros, D. Veynante, and T. Poinso. A thickened flame model for large eddy simulations of turbulent premixed combustion. *Physics of fluids*, 12(7):1843–1863, 2000.

-
- [40] D. G. Crighton and M. Gaster. Stability of slowly diverging jet flow. *Journal of Fluid Mechanics*, 77(2):397–413, 1976. doi: 10.1017/S0022112076002176. URL <https://www.cambridge.org/core/journals/journal-of-fluid-mechanics/article/stability-of-slowly-diverging-jet-flow/323EBCEAF7C25C87974CC3C33403C679>.
- [41] L. Crocco. Aspects of combustion stability in liquid propellant rocket motors part i: fundamentals. low frequency instability with monopropellants. *Journal of the American Rocket Society*, 21(6):163–178, 1951.
- [42] L. Crocco and X. Zheng. *Theory of combustion instability in liquid propellant rocket motors*. Butterworths Scientific Publications, 1956.
- [43] P. Crumpton, J. Mackenzie, and K. Morton. Cell vertex algorithms for the compressible navier-stokes equations. *Journal of Computational Physics*, 109(1):1 – 15, 1993. ISSN 0021-9991. doi: <https://doi.org/10.1006/jcph.1993.1194>. URL <http://www.sciencedirect.com/science/article/pii/S0021999183711940>.
- [44] F. Culick. Combustion instabilities in liquid-fuelled propulsion systems, 1988. URL <http://resolver.caltech.edu/CaltechAUTHORS:20110204-151853189>.
- [45] F. E. Culick and V. Yang. Overview of combustion instabilities in liquid-propellant rocket engines. *Liquid Rocket Engine Combustion Instability*, 169:3–37, 1995.
- [46] B. Dally, D. Fletcher, and A. Masri. Flow and mixing fields of turbulent bluff-body jets and flames. *Combustion Theory and Modelling*, 2(2):193–219, 1998.
- [47] G. Damköhler. Der einfluss der turbulenz auf die flammengeschwindigkeit in gasgemischen. *Zeitschrift für Elektrochemie und angewandte physikalische Chemie*, 46(11):601–626, 1940. doi: 10.1002/bbpc.19400461102. URL <https://onlinelibrary.wiley.com/doi/abs/10.1002/bbpc.19400461102>.
- [48] G. Daviller, M. Brebion, P. Xavier, G. Staffelbach, J.-D. Müller, and T. Poinso. A mesh adaptation strategy to predict pressure losses in les of swirled flows. *Flow, Turbulence and Combustion*, 99(1):93–118, Jul 2017. doi: 10.1007/s10494-017-9808-z. URL <https://doi.org/10.1007/s10494-017-9808-z>.
- [49] T. A. Davis. A column pre-ordering strategy for the unsymmetric-pattern multifrontal method. *ACM Trans. Math. Softw.*, 30(2):165–195, June 2004. ISSN 0098-3500. doi: 10.1145/992200.992205. URL <http://doi.acm.org/10.1145/992200.992205>.
- [50] T. A. Davis and I. S. Duff. An unsymmetric-pattern multifrontal method for sparse lu factorization. *SIAM Journal on Matrix Analysis and Applications*, 18(1):140–158, 1997. doi: 10.1137/S0895479894246905. URL <https://doi.org/10.1137/S0895479894246905>.

- [51] M. DiCicco and J. Buckmaster. Role of slip in the generation of acoustic instabilities in gas turbines. *Journal of propulsion and power*, 12(1):34–40, 1996.
- [52] N. Docquier and S. Candel. Combustion control and sensors: a review. *Progress in Energy and Combustion Science*, 28(2):107 – 150, 2002. ISSN 0360-1285. doi: [https://doi.org/10.1016/S0360-1285\(01\)00009-0](https://doi.org/10.1016/S0360-1285(01)00009-0). URL <http://www.sciencedirect.com/science/article/pii/S0360128501000090>.
- [53] J. Donea. A taylor-galerkin method for convective transport problems. *International Journal for Numerical Methods in Engineering*, 20(1):101–119, 1984. doi: 10.1002/nme.1620200108. URL <https://onlinelibrary.wiley.com/doi/abs/10.1002/nme.1620200108>.
- [54] J. Donea and A. Huerta. *Finite element methods for flow problems*. John Wiley & Sons, 2003.
- [55] Q. Douasbin, C. Scalo, L. Selle, and T. Poinsot. Delayed-time domain impedance boundary conditions (d-tdibc). *Journal of Computational Physics*, 371:50 – 66, 2018. ISSN 0021-9991. doi: <https://doi.org/10.1016/j.jcp.2018.05.003>. URL <http://www.sciencedirect.com/science/article/pii/S002199911830295X>.
- [56] D. R. Dowdy, D. B. Smith, S. C. Taylor, and A. Williams. The use of expanding spherical flames to determine burning velocities and stretch effects in hydrogen/air mixtures. *Symposium (International) on Combustion*, 23(1):325 – 332, 1991. ISSN 0082-0784. doi: [https://doi.org/10.1016/S0082-0784\(06\)80275-4](https://doi.org/10.1016/S0082-0784(06)80275-4). URL <http://www.sciencedirect.com/science/article/pii/S0082078406802754>. Twenty-Third Symposium (International) on Combustion.
- [57] A. P. Dowling. A kinematic model of a ducted flame. *Journal of Fluid Mechanics*, 394: 51–72, 1999. URL doi.org/10.1017/S0022112099005686.
- [58] A. P. Dowling and Y. Mahmoudi. Combustion noise. *Proceedings of the Combustion Institute*, 35(1):65 – 100, 2015. ISSN 1540-7489. doi: <https://doi.org/10.1016/j.proci.2014.08.016>. URL <http://www.sciencedirect.com/science/article/pii/S1540748914004003>.
- [59] P. Duck and M. Foster. The inviscid stability of a trailing line vortex. *Zeitschrift für angewandte Mathematik und Physik ZAMP*, 31(4):524–532, 1980.
- [60] S. Ducruix, D. Durox, and S. Candel. Theoretical and experimental determinations of the transfer function of a laminar premixed flame. *Proceedings of the Combustion Institute*, 28(1):765 – 773, 2000. ISSN 1540-7489. doi: [https://doi.org/10.1016/S0082-0784\(00\)80279-9](https://doi.org/10.1016/S0082-0784(00)80279-9). URL <http://www.sciencedirect.com/science/article/pii/S0082078400802799>.

-
- [61] D. Durox, F. Baillot, P. Scouffaire, and R. Prud'homme. Some effects of gravity on the behaviour of premixed flames. *Combustion and Flame*, 82(1):66 – 74, 1990. ISSN 0010-2180. doi: [https://doi.org/10.1016/0010-2180\(90\)90078-6](https://doi.org/10.1016/0010-2180(90)90078-6). URL <http://www.sciencedirect.com/science/article/pii/0010218090900786>.
- [62] D. Durox, T. Schuller, N. Noiray, and S. Candel. Experimental analysis of nonlinear flame transfer functions for different flame geometries. *Proceedings of the Combustion Institute*, 32(1):1391–1398, 2009.
- [63] A. Duvvur, C. Chiang, and W. Sirignano. Oscillatory fuel droplet vaporization-driving mechanism for combustion instability. *Journal of propulsion and Power*, 12(2):358–365, 1996.
- [64] U. Ehrenstein and F. Gallaire. On two-dimensional temporal modes in spatially evolving open flows: the flat-plate boundary layer. *Journal of Fluid Mechanics*, 536:209–218, 2005. doi: 10.1017/S0022112005005112.
- [65] B. Emerson, J. O'Connor, M. P. Juniper, and T. Lieuwen. Density ratio effects on reacting bluff-body flow field characteristics. *Journal of Fluid Mechanics*, 706:219–250, 2012. ISSN 0022-1120. doi: 10.1017/jfm.2012.248. URL [http://www.journals.cambridge.org/abstract_{_}S0022112012002480](http://www.journals.cambridge.org/abstract/_S0022112012002480).
- [66] A. Ern and V. Giovangigli. *Multicomponent Transport Algorithms*, volume 2. Springer Verlag, Heidelberg, 1994.
- [67] R. M. Errico. What is an adjoint model? *Bulletin of the American Meteorological Society*, 78(11):2577–2592, 1997. doi: 10.1175/1520-0477(1997)078<2577:WIAAM>2.0.CO;2. URL [https://doi.org/10.1175/1520-0477\(1997\)078<2577:WIAAM>2.0.CO;2](https://doi.org/10.1175/1520-0477(1997)078<2577:WIAAM>2.0.CO;2).
- [68] H. A. Eschenauer and N. Olhoff. Topology optimization of continuum structures: a review. *Applied Mechanics Reviews*, 54(4):331–390, 2001.
- [69] FAA. FAA aerospace forecast - Fiscal Years 2018-2038. Technical report, Federal Aviation Administration, 2018. URL https://www.faa.gov/data_research/aviation/aerospace_forecasts/media/FY2018-38_FAA_Aerospace_Forecast.pdf.
- [70] B. Franzelli, E. Riber, M. Sanjosé, and T. Poinso. A two-step chemical scheme for kerosene-air premixed flames. *Combustion and Flame*, 157(7):1364 – 1373, 2010. ISSN 0010-2180. doi: <https://doi.org/10.1016/j.combustflame.2010.03.014>. URL <http://www.sciencedirect.com/science/article/pii/S0010218010001021>.
- [71] B. Franzelli, E. Riber, L. Y. Gicquel, and T. Poinso. Large eddy simulation of combustion instabilities in a lean partially premixed swirled flame. *Combustion*

- and Flame*, 159(2):621 – 637, 2012. ISSN 0010-2180. doi: <https://doi.org/10.1016/j.combustflame.2011.08.004>. URL <http://www.sciencedirect.com/science/article/pii/S0010218011002525>.
- [72] S. Fujii and K. Eguchi. A comparison of cold and reacting flows around a bluff-body flame stabilizer. *ASME. J. Fluids Eng.*, 103(2):328 – 334, 1981. doi: 10.1115/1.3241741.
- [73] C. Fureby and S.-I. Moeller. Large eddy simulation of reacting flows applied to bluff body stabilized flames. *AIAA Journal*, 33(12):2339–2347, dec 1995. ISSN 0001-1452. doi: 10.2514/3.12989. URL <https://doi.org/10.2514/3.12989>.
- [74] F. Gallaire and J.-M. Chomaz. Mode selection in swirling jet experiments: a linear stability analysis. *Journal of Fluid Mechanics*, 494:223–253, 2003. doi: 10.1017/S0022112003006104.
- [75] F. Gallaire, M. Ruith, E. Meiburg, J.-M. Chomaz, and P. Huerre. Spiral vortex breakdown as a global mode. *J. Fluid Mech.*, 549:71–80, 2006. doi: 10.1017/S0022112005007834.
- [76] W. C. Gardiner and W. Gardiner. *Gas-phase combustion chemistry*. Springer New York, 2000.
- [77] M. Gaster. Growth of disturbances in both space and time. *The Physics of Fluids*, 11(4):723–727, 1968. doi: 10.1063/1.1691990. URL <https://aip.scitation.org/doi/abs/10.1063/1.1691990>.
- [78] A. Gentemann, C. Hirsch, K. Kunze, F. Kiesewetter, T. Sattelmayer, and W. Polifke. Validation of Flame Transfer Function Reconstruction for Perfectly Premixed Swirl Flames, 2004. URL <http://dx.doi.org/10.1115/GT2004-53776>.
- [79] A. Ghani, T. Poinso, L. Gicquel, and G. Staffelbach. Les of longitudinal and transverse self-excited combustion instabilities in a bluff-body stabilized turbulent premixed flame. *Combustion and Flame*, 162(11):4075 – 4083, 2015. ISSN 0010-2180. doi: <https://doi.org/10.1016/j.combustflame.2015.08.024>. URL <http://www.sciencedirect.com/science/article/pii/S0010218015002989>.
- [80] A. Ghani, T. Poinso, L. Y. Gicquel, and J. Müller. LES Study of Transverse Acoustic Instabilities in a Swirled Kerosene/Air Combustion Chamber. *Flow, Turbulence and Combustion*, vol. 96(1):207–226, 2016. doi: 10.1007/s10494-015-9654-9. URL <https://hal.archives-ouvertes.fr/hal-01272073>.
- [81] E. Giacomazzi, V. Battaglia, and C. Bruno. The coupling of turbulence and chemistry in a premixed bluff-body flame as studied by les. *Combustion and Flame*, 138(4):320 – 335, 2004. ISSN 0010-2180. doi: <https://doi.org/10.1016/j.combustflame.2004.06.004>. URL <http://www.sciencedirect.com/science/article/pii/S0010218004001312>.

-
- [82] K. C. Giannakoglou and D. I. Papadimitriou. *Adjoint Methods for Shape Optimization*, pages 79–108. Springer Berlin Heidelberg, Berlin, Heidelberg, 2008. doi: 10.1007/978-3-540-72153-6_4. URL https://doi.org/10.1007/978-3-540-72153-6_4.
- [83] F. Giannetti and P. Luchini. Structural sensitivity of the first instability of the cylinder wake. *Journal of Fluid Mechanics*, 581:167–197, 2007.
- [84] J. H. Ginsberg. *Mechanical and structural vibrations: theory and applications*. Wiley New York, New York, 2001.
- [85] F. Gómez, S. L. Clainche, P. Paredes, M. Hermanns, and V. Theofilis. Four decades of studying global linear instability: Progress and challenges. *AIAA journal*, 50(12): 2731–2743, 2012.
- [86] D. G. Goodwin, H. K. Moffat, and R. L. Speth. *Cantera: An object-oriented software toolkit for chemical kinetics, thermodynamics, and transport processes*, 2017. URL <http://www.cantera.org>. Version 2.3.0.
- [87] N. Gourdain, L. Gicquel, M. Montagnac, O. Vermorel, M. Gazaix, G. Staffelbach, M. Garcia, J. Boussuge, and T. Poinot. High performance parallel computing of flows in complex geometries: I. methods. *Computational Science & Discovery*, 2(1):015003, 2009.
- [88] S. Gregory P, D. M. Golden, M. Frenklach, N. W. Moriarty, B. Eiteneer, M. Goldenberg, C. T. Bowman, R. K. Hanson, S. Song, J. William C. Gardiner, V. V. Lissianski, and Z. Q. Gri-mech, 2000. URL http://www.me.berkeley.edu/gri_mech/.
- [89] X. Gu, M. Haq, M. Lawes, and R. Woolley. Laminar burning velocity and markstein lengths of methane-air mixtures. *Combustion and Flame*, 121(1):41 – 58, 2000. ISSN 0010-2180. doi: [https://doi.org/10.1016/S0010-2180\(99\)00142-X](https://doi.org/10.1016/S0010-2180(99)00142-X). URL <http://www.sciencedirect.com/science/article/pii/S001021809900142X>.
- [90] G. H. L. Hagen. *Über den Einfluss der Temperatur auf die Bewegung des Wassers in Röhren-*. Druckerei der Königl. akademie der wissenschaften, 1854.
- [91] H.-W. Hahn. *Die Industrielle Revolution in Deutschland*. Oldenbourg Verlag, München, 2011.
- [92] F. Hecht. New development in FreeFem++. *J. Numer. Math.*, 20(3-4):251–265, 2012. ISSN 1570-2820.
- [93] J. O. Hirschfelder, C. F. Curtiss, and R. B. Bird. *Molecular theory of gases and liquids*. John Wiley and Sons, New York, 1969.

- [94] G. Hubbard, V. Denny, and A. Mills. Droplet evaporation: Effects of transients and variable properties. *International Journal of Heat and Mass Transfer*, 18(9):1003 – 1008, 1975. ISSN 0017-9310. doi: [https://doi.org/10.1016/0017-9310\(75\)90217-3](https://doi.org/10.1016/0017-9310(75)90217-3). URL <http://www.sciencedirect.com/science/article/pii/0017931075902173>.
- [95] A. Huber and W. Polifke. Dynamics of practical premixed flames, part i: Model structure and identification. *International Journal of Spray and Combustion Dynamics*, 1(2):199–228, 2009. doi: 10.1260/175682709788707431.
- [96] A. Huber and W. Polifke. Dynamics of practical premixed flames, part ii: identification and interpretation of cfd data. *International journal of spray and combustion dynamics*, 1(2):229–249, 2009.
- [97] P. Huerre and P. A. Monkewitz. Absolute and convective instabilities in free shear layers. *Journal of Fluid Mechanics*, 159:151–168, 1985. doi: 10.1017/S0022112085003147. URL <https://doi.org/10.1017/S0022112085003147>.
- [98] P. Huerre and P. A. Monkewitz. Local and global instabilities in spatially developing flows. *Annual Review of Fluid Mechanics*, 22(1):473–537, 1990. doi: 10.1146/annurev.fl.22.010190.002353. URL <https://doi.org/10.1146/annurev.fl.22.010190.002353>.
- [99] A. Hussain and W. Reynolds. The mechanics of an organized wave in turbulent shear flow. part 2. experimental results. *Journal of Fluid Mechanics*, 54(2):241–261, 1972.
- [100] A. K. M. F. Hussain and W. C. Reynolds. The mechanics of an organized wave in turbulent shear flow. *Journal of Fluid Mechanics*, 41(2):241–258, 1970.
- [101] ICAO. Icao long-term traffic forecasts - passenger and cargo. Technical report, ICAO, 2016. URL <https://www.icao.int/Meetings/aviationdataseminar/Documents/ICAO-Long-Term-Traffic-Forecasts-July-2016.pdf>.
- [102] E. M. Ivanova, B. E. Noll, and M. Aigner. A Numerical Study on the Turbulent Schmidt Numbers in a Jet in Crossflow. *Journal of Engineering for Gas Turbines and Power*, 135(1):11505–11510, nov 2012. ISSN 0742-4795. URL <http://dx.doi.org/10.1115/1.4007374>.
- [103] C. P. Jackson. A finite-element study of the onset of vortex shedding in flow past variously shaped bodies. *Journal of Fluid Mechanics*, 182:23–45, 1987. doi: 10.1017/S0022112087002234.
- [104] G. Joulin and T. Mitani. Linear stability analysis of two-reactant flames. *Combustion and Flame*, 40:235 – 246, 1981. ISSN 0010-2180. doi: [https://doi.org/10.1016/0010-2180\(81\)90127-9](https://doi.org/10.1016/0010-2180(81)90127-9). URL <http://www.sciencedirect.com/science/article/pii/0010218081901279>.

-
- [105] M. Juniper, O. Tammisola, and F. Lundell. The local and global stability of confined planar wakes at intermediate Reynolds number. *Journal of Fluid Mechanics*, 686: 218–238, 2011.
- [106] M. P. Juniper. Triggering in the horizontal rijke tube: non-normality, transient growth and bypass transition. *Journal of Fluid Mechanics*, 667:272–308, 2011. doi: 10.1017/S0022112010004453.
- [107] M. P. Juniper and B. Pier. The structural sensitivity of open shear flows calculated with a local stability analysis. *European Journal of Mechanics-B/Fluids*, 49:426–437, 2015.
- [108] T. R. Karl and K. E. Trenberth. Modern global climate change. *Science*, 302 (5651):1719–1723, 2003. ISSN 0036-8075. doi: 10.1126/science.1090228. URL <http://science.sciencemag.org/content/302/5651/1719>.
- [109] A. Kaufmann, F. Nicoud, and T. Poinsot. Flow forcing techniques for numerical simulation of combustion instabilities. *Combustion and Flame*, 131(4):371 – 385, 2002. ISSN 0010-2180. URL <http://www.sciencedirect.com/science/article/pii/S0010218002004194>.
- [110] K. Kedia, H. Altay, and A. Ghoniem. Impact of flame-wall interaction on premixed flame dynamics and transfer function characteristics. *Proceedings of the Combustion Institute*, 33(1):1113–1120, 2011.
- [111] K. S. Kedia and A. F. Ghoniem. The anchoring mechanism of a bluff-body stabilized laminar premixed flame. *Combustion and Flame*, 161(9):2327 – 2339, 2014. ISSN 0010-2180. doi: <https://doi.org/10.1016/j.combustflame.2014.02.005>. URL <http://www.sciencedirect.com/science/article/pii/S0010218014000649>.
- [112] M. R. Khorrami. A chebyshev spectral collocation method using a staggered grid for the stability of cylindrical flows. *International Journal for Numerical Methods in Fluids*, 12(9):825–833, 1991. doi: 10.1002/fld.1650120903. URL <https://onlinelibrary.wiley.com/doi/abs/10.1002/fld.1650120903>.
- [113] M. R. Khorrami, M. R. Malik, and R. L. Ash. Application of spectral collocation techniques to the stability of swirling flows. *Journal of Computational Physics*, 1989. ISSN 10902716. doi: 10.1016/0021-9991(89)90071-5.
- [114] D. Kim, J. G. Lee, B. D. Quay, D. Santavicca, K. Kim, and S. Srinivasan. Effect of flame structure on the flame transfer function in a premixed gas turbine combustor. In *ASME Turbo Expo 2008: Power for Land, Sea, and Air*, pages 757–765. American Society of Mechanical Engineers, 2008.

BIBLIOGRAPHY

- [115] C. Kraus, L. Selle, T. Poinso, C. M. Arndt, and H. Bockhorn. Influence of heat transfer and material temperature on combustion instabilities in a swirl burner. *Journal of Engineering for Gas Turbines and Power*, 139(5):051503, 2017.
- [116] B. Kumar and S. Mittal. On the origin of the secondary vortex street. *Journal of Fluid Mechanics*, 711:641–666, 2012. doi: 10.1017/jfm.2012.421.
- [117] A. C. Köne and T. Büke. Forecasting of co2 emissions from fuel combustion using trend analysis. *Renewable and Sustainable Energy Reviews*, 14(9):2906 – 2915, 2010. ISSN 1364-0321. doi: <https://doi.org/10.1016/j.rser.2010.06.006>. URL <http://www.sciencedirect.com/science/article/pii/S136403211000153X>.
- [118] R. G. Larson, E. S. G. Shaqfeh, and S. J. Muller. A purely elastic instability in taylor–couette flow. *Journal of Fluid Mechanics*, 218:573–600, 1990. doi: 10.1017/S0022112090001124. URL <https://doi.org/10.1017/S0022112090001124>.
- [119] C. Law, G. Jomaas, and J. Bechtold. Cellular instabilities of expanding hydrogen/propane spherical flames at elevated pressures: theory and experiment. *Proceedings of the Combustion Institute*, 30(1):159 – 167, 2005. ISSN 1540-7489. doi: <https://doi.org/10.1016/j.proci.2004.08.266>. URL <http://www.sciencedirect.com/science/article/pii/S0082078404003200>.
- [120] P. Lax and B. Wendroff. Systems of conservation laws. *Communications on Pure and Applied mathematics*, 13(2):217–237, 1960.
- [121] J. Lee and D. Santavicca. Experimental diagnostics for the study of combustion instabilities in lean premixed combustors. *Journal of propulsion and power*, 19(5):735–750, 2003. URL <https://arc.aiaa.org/doi/abs/10.2514/2.6191>.
- [122] J. G. Lee, K. Kim, and D. Santavicca. Measurement of equivalence ratio fluctuation and its effect on heat release during unstable combustion. *Proceedings of the Combustion Institute*, 28(1):415 – 421, 2000. ISSN 1540-7489. doi: [https://doi.org/10.1016/S0082-0784\(00\)80238-6](https://doi.org/10.1016/S0082-0784(00)80238-6). URL <http://www.sciencedirect.com/science/article/pii/S0082078400802386>.
- [123] R. Lehoucq, D. Sorensen, and C. Yang. Arpack users’ guide: Solution of large scale eigenvalue problems with implicitly restarted Arnoldi methods, 1997. URL <http://citeseerx.ist.psu.edu/viewdoc/summary?doi=10.1.1.38.616>.
- [124] A. Leonard. Energy cascade in large-eddy simulations of turbulent fluid flows. In F. Frenkiel and R. Munn, editors, *Turbulent Diffusion in Environmental Pollution*, volume 18 of *Advances in Geophysics*, pages 237 – 248. Elsevier, 1975. doi: [https://doi.org/10.1016/S0065-2687\(08\)60464-1](https://doi.org/10.1016/S0065-2687(08)60464-1). URL <http://www.sciencedirect.com/science/article/pii/S0065268708604641>.

-
- [125] M. Lessen and P. J. Singh. The stability of axisymmetric free shear layers. *Journal of Fluid Mechanics*, 60(3):433–457, 1973. URL <https://doi.org/10.1017/S0022112073000285>.
- [126] L. Lesshafft, P. Huerre, P. Sagaut, and M. Terracol. Nonlinear global modes in hot jets. *Journal of Fluid Mechanics*, 554:393–409, 2006. URL <https://www.cambridge.org/core/journals/journal-of-fluid-mechanics/article/nonlinear-global-modes-in-hot-jets/97DB993C33FF3C04A36C096E3E418469>.
- [127] B. Lewis and G. Von Elbe. *Combustion, flames and explosions of gases*. Elsevier, New York, 2012.
- [128] J. M. Lewis and J. C. Derber. The use of adjoint equations to solve a variational adjustment problem with advective constraints. *Tellus A: Dynamic Meteorology and Oceanography*, 37(4):309–322, 1985. doi: 10.3402/tellusa.v37i4.11675. URL <https://doi.org/10.3402/tellusa.v37i4.11675>.
- [129] S. Li and L. Petzold. Adjoint sensitivity analysis for time-dependent partial differential equations with adaptive mesh refinement. *Journal of Computational Physics*, 198(1): 310 – 325, 2004. ISSN 0021-9991. doi: <https://doi.org/10.1016/j.jcp.2003.01.001>. URL <http://www.sciencedirect.com/science/article/pii/S0021999104000300>.
- [130] H. Liang and T. Maxworthy. An experimental investigation of swirling jets. *Journal of Fluid Mechanics*, 525:115–159, 2005. doi: 10.1017/S0022112004002629.
- [131] T. Lieuwen. Modeling premixed combustion-acoustic wave interactions: A review. *Journal of propulsion and power*, 19(5):765–781, 2003. URL <https://arc.aiaa.org/doi/abs/10.2514/2.6193>.
- [132] T. Lieuwen and B. Zinn. The role of equivalence ratio oscillations in driving combustion instabilities in low nox gas turbines. *Proceedings of the Combustion Institute*, 27:1809–1816, 12 1998.
- [133] T. C. Lieuwen and V. Yang. *Combustion instabilities in gas turbine engines: operational experience, fundamental mechanisms, and modeling*. American Institute of Aeronautics and Astronautics, 2005.
- [134] L. Ljung, editor. *System Identification (2Nd Ed.): Theory for the User*. Prentice Hall PTR, Upper Saddle River, NJ, USA, 1999. ISBN 0-13-656695-2.
- [135] J. P. Longwell, E. E. Frost, and M. A. Weiss. Flame stability in bluff body recirculation zones. *Industrial & Engineering Chemistry*, 45(8):1629–1633, 1953.

- [136] T. Lu and C. K. Law. A criterion based on computational singular perturbation for the identification of quasi steady state species: A reduced mechanism for methane oxidation with no chemistry. *Combustion and Flame*, 154:761–774, 2008. doi: 10.1016/j.combustflame.2008.04.025.
- [137] P. Luchini and A. Bottaro. Görtler vortices: a backward-in-time approach to the receptivity problem. *Journal of Fluid Mechanics*, 363:1–23, 1998. doi: 10.1017/S0022112098008970.
- [138] P. Luchini and A. Bottaro. Adjoint equations in stability analysis. *Annual Review of Fluid Mechanics*, 46(1):493–517, 2014. doi: 10.1146/annurev-fluid-010313-141253. URL <https://doi.org/10.1146/annurev-fluid-010313-141253>.
- [139] P. Luchini, F. Giannetti, and J. Pralits. Structural sensitivity of linear and nonlinear global modes. In *5th AIAA Theoretical Fluid Mechanics Conference*, page 4227, 2008.
- [140] L. Magri and M. P. Juniper. Sensitivity analysis of a time-delayed thermo-acoustic system via an adjoint-based approach. *Journal of Fluid Mechanics*, 719:183–202, 2013. doi: 10.1017/jfm.2012.639.
- [141] M. Malik, T. Zang, and M. Hussaini. A spectral collocation method for the navier-stokes equations. *Journal of Computational Physics*, 61(1):64 – 88, 1985. ISSN 0021-9991. doi: [https://doi.org/10.1016/0021-9991\(85\)90061-0](https://doi.org/10.1016/0021-9991(85)90061-0). URL <http://www.sciencedirect.com/science/article/pii/0021999185900610>.
- [142] K. Manoharan and S. Hemchandra. Absolute/convective instability transition in a backward facing step combustor: Fundamental mechanism and influence of density gradient. *Journal of Engineering for Gas Turbines and Power*, 137(2):021501, 2015.
- [143] K. Manoharan, S. Hansford, J. O’Connor, and S. Hemchandra. Instability mechanism in a swirl flow combustor: precession of vortex core and influence of density gradient. In *ASME Turbo Expo 2015: Turbine Technical Conference and Exposition*, pages V04AT04A073–V04AT04A073. American Society of Mechanical Engineers, 2015.
- [144] F. E. Marble and S. M. Candel. An analytical study of the non-steady behavior of large combustors. *Symposium (International) on Combustion*, 17(1):761–769, 1979. URL <https://www.sciencedirect.com/science/article/pii/S0082078479800740>.
- [145] A. Maries, A. Haque, S. L. Yilmaz, M. B. Nik, and G. E. Marai. Interactive exploration of stress tensors used in computational turbulent combustion. In *New Developments in the Visualization and Processing of Tensor Fields*, pages 137–156. Springer, 2012.
- [146] G. H. Markstein. Experimental and theoretical studies of flame-front stability. *Journal of the Aeronautical Sciences*, 18(3):199–209, 1951. doi: <https://doi.org/10.2514/8.1900>.

-
- [147] C. Martin, L. Benoit, F. Nicoud, and T. Poinso. Analysis of acoustic energy and modes in a turbulent swirled combustor. In *Proceedings of the summer program*, page 1, 2004.
- [148] A. Mazza, E. Bompard, and G. Chicco. Applications of power to gas technologies in emerging electrical systems. *Renewable and Sustainable Energy Reviews*, 92:794 – 806, 2018. ISSN 1364-0321. doi: <https://doi.org/10.1016/j.rser.2018.04.072>. URL <http://www.sciencedirect.com/science/article/pii/S1364032118303083>.
- [149] G. McFadden, B. Murray, and R. Boisvert. Elimination of spurious eigenvalues in the chebyshev tau spectral method. *Journal of Computational Physics*, 91(1):228 – 239, 1990. ISSN 0021-9991. doi: [https://doi.org/10.1016/0021-9991\(90\)90012-P](https://doi.org/10.1016/0021-9991(90)90012-P). URL <http://www.sciencedirect.com/science/article/pii/002199919090012P>.
- [150] P. Mehta and M. Soteriou. *Combustion heat release effects on the dynamics of bluff body stabilized premixed reacting flows*. 2003. ISBN 9781624100994.
- [151] D. Mejia, L. Selle, R. Bazile, and T. Poinso. Wall-temperature effects on flame response to acoustic oscillations. *Proceedings of the Combustion Institute*, 35(3):3201 – 3208, 2015. ISSN 1540-7489. doi: <https://doi.org/10.1016/j.proci.2014.07.015>. URL <http://www.sciencedirect.com/science/article/pii/S1540748914003253>.
- [152] D. Mejia, M. Bauerheim, P. Xavier, B. Ferret, L. Selle, and T. Poinso. Stabilization of a premixed laminar flame on a rotating cylinder. *Proceedings of the Combustion Institute*, 36(1):1447 – 1455, 2017. ISSN 1540-7489. doi: <https://doi.org/10.1016/j.proci.2016.06.138>. URL <http://www.sciencedirect.com/science/article/pii/S1540748916301961>.
- [153] D. Mejia, M. Miguel-Brebion, A. Ghani, T. Kaiser, F. Duchaine, L. Selle, and T. Poinso. Influence of flame-holder temperature on the acoustic flame transfer functions of a laminar flame. *Combustion and Flame*, 188:5 – 12, 2018. ISSN 0010-2180. doi: <https://doi.org/10.1016/j.combustflame.2017.09.016>. URL <http://www.sciencedirect.com/science/article/pii/S0010218017303462>.
- [154] P. Meliga, J.-M. Chomaz, and D. Sipp. Unsteadiness in the wake of disks and spheres: instability, receptivity and control using direct and adjoint global stability analyses. *Journal of Fluids and Structures*, 25(4):601–616, 2009.
- [155] M. Merk, S. Jaensch, C. Silva, and W. Polifke. Simultaneous identification of transfer functions and combustion noise of a turbulent flame. *Journal of Sound and Vibration*, 422:432 – 452, 2018. ISSN 0022-460X. doi: <https://doi.org/10.1016/j.jsv.2018.02.040>. URL <http://www.sciencedirect.com/science/article/pii/S0022460X18301366>.

- [156] J. Michael. A global energy assessment. *Wiley Interdisciplinary Reviews: Energy and Environment*, 5(1):7–15, 2015. doi: 10.1002/wene.179. URL <https://onlinelibrary.wiley.com/doi/abs/10.1002/wene.179>.
- [157] D. Michaels and A. F. Ghoniem. Leading edge dynamics of lean premixed flames stabilized on a bluff body. *Combustion and Flame*, 191:39 – 52, 2018. ISSN 0010-2180. doi: <https://doi.org/10.1016/j.combustflame.2017.12.020>. URL <http://www.sciencedirect.com/science/article/pii/S001021801730487X>.
- [158] M. Miguel-Brebion, D. Mejia, P. Xavier, F. Duchaine, B. Bédard, L. Selle, and T. Poinsot. Joint experimental and numerical study of the influence of flame holder temperature on the stabilization of a laminar methane flame on a cylinder. *Combustion and Flame*, 172:153—161, 2016. doi: 10.1016/j.combustflame.2016.06.025.
- [159] A. Miura and P. Pritchett. Nonlocal stability analysis of the mhd kelvin-helmholtz instability in a compressible plasma. *Journal of Geophysical Research: Space Physics*, 87(A9):7431–7444, 1982.
- [160] J. P. Moeck, J.-F. Bourgoignie, D. Durox, T. Schuller, and S. Candel. Nonlinear interaction between a precessing vortex core and acoustic oscillations in a turbulent swirling flame. *Combustion and Flame*, 159(8):2650 – 2668, 2012. ISSN 0010-2180. doi: <https://doi.org/10.1016/j.combustflame.2012.04.002>. URL <http://www.sciencedirect.com/science/article/pii/S0010218012001216>. Special Issue on Turbulent Combustion.
- [161] P. A. Monkewitz. The absolute and convective nature of instability in two-dimensional wakes at low reynolds numbers. *The Physics of Fluids*, 31(5):999–1006, 1988. doi: 10.1063/1.866720. URL <https://aip.scitation.org/doi/abs/10.1063/1.866720>.
- [162] P. A. Monkewitz, D. W. Bechert, B. Barsikow, and B. Lehmann. Self-excited oscillations and mixing in a heated round jet. *Journal of Fluid Mechanics*, 213:611–639, 1990. doi: 10.1017/S0022112090002476.
- [163] V. Moureau, P. Domingo, and L. Vervisch. From large-eddy simulation to direct numerical simulation of a lean premixed swirl flame: Filtered laminar flame-pdf modeling. *Combustion and Flame*, 158(7):1340–1357, 2011.
- [164] C. J. Mueller, J. F. Driscoll, D. L. Reuss, M. C. Drake, and M. E. Rosalik. Vorticity generation and attenuation as vortices convect through a premixed flame. *Combustion and flame*, 112(3):342–358, 1998. doi: [https://doi.org/10.1016/S0010-2180\(97\)00122-3](https://doi.org/10.1016/S0010-2180(97)00122-3). URL [https://doi.org/10.1016/S0010-2180\(97\)00122-3](https://doi.org/10.1016/S0010-2180(97)00122-3).
- [165] G. Nathan, S. Hill, and R. Luxton. An axisymmetric ‘fluidic’ nozzle to generate jet precession. *Journal of Fluid Mechanics*, 370:347–380, 1998.

-
- [166] R.-H. NI. A multiple grid scheme for solving the Euler equations. In *5th Computational Fluid Dynamics Conference*, Fluid Dynamics and Co-located Conferences. American Institute of Aeronautics and Astronautics, jun 1981. doi: doi:10.2514/6.1981-1025. URL <https://doi.org/10.2514/6.1981-1025>.
- [167] F. Nicoud, L. Benoit, C. Sensiau, and T. Poinso. Acoustic Modes in Combustors with Complex Impedances and Multidimensional Active Flames. *AIAA Journal*, 45(2):426–441, feb 2007. ISSN 0001-1452. doi: 10.2514/1.24933. URL <https://doi.org/10.2514/1.24933>.
- [168] F. Nicoud, H. B. Toda, O. Cabrit, S. Bose, and J. Lee. Using singular values to build a subgrid-scale model for large eddy simulations. *Physics of Fluids (1994-present)*, 23(8):085106, 2011.
- [169] F. Noether. Das Turbulenzproblem. *ZAMM - Journal of Applied Mathematics and Mechanics / Zeitschrift fr Angewandte Mathematik und Mechanik*, 1(2):125–138, 1921. doi: 10.1002/zamm.19210010207. URL <https://onlinelibrary.wiley.com/doi/abs/10.1002/zamm.19210010207>.
- [170] K. Oberleithner. *On Turbulent Swirling Jets: Vortex Breakdown, Coherent Structures, and their Control*. PhD thesis, TU Berlin, 2012.
- [171] K. Oberleithner, S. Terhaar, L. Rukes, and C. O. Paschereit. Why Non-Uniform Density Suppresses the Precessing Vortex Core. *Journal of Engineering for Gas Turbines and Power*, 135(12):121506, 2013. URL <http://dx.doi.org/10.1115/GT2013-95509>.
- [172] K. Oberleithner, S. Schimek, and C. O. Paschereit. Shear flow instabilities in swirl-stabilized combustors and their impact on the amplitude dependent flame response: A linear stability analysis. *Combustion and Flame*, 162(1):86–99, 2014. ISSN 00102180. URL <http://dx.doi.org/10.1016/j.combustflame.2014.07.012>
<http://linkinghub.elsevier.com/retrieve/pii/S0010218014002077>.
- [173] J. C. Oefelein and V. Yang. Comprehensive review of liquid-propellant combustion instabilities in F-1 engines. *Journal of Propulsion and Power*, 9(5):657–677, sep 1993. ISSN 0748-4658. doi: 10.2514/3.23674. URL <https://doi.org/10.2514/3.23674>.
- [174] N. Oreskes. The scientific consensus on climate change. *Science*, 306(5702):1686–1686, 2004. ISSN 0036-8075. doi: 10.1126/science.1103618. URL <http://science.sciencemag.org/content/306/5702/1686>.
- [175] S. A. Orszag. Accurate solution of the orr–sommerfeld stability equation. *Journal of Fluid Mechanics*, 50(4):689–703, 1971. doi: 10.1017/S0022112071002842.

- [176] G. Öztarlık. *Joint numerical and experimental study of thermo-acoustic instabilities*. PhD thesis, Institut de Mécanique des Fluides de Toulouse, 2016.
- [177] P. Palies, D. Durox, T. Schuller, and S. Candel. The combined dynamics of swirler and turbulent premixed swirling flames. *Combustion and Flame*, 157(9):1698 – 1717, 2010. ISSN 0010-2180. doi: <https://doi.org/10.1016/j.combustflame.2010.02.011>. URL <http://www.sciencedirect.com/science/article/pii/S001021801000057X>.
- [178] P. Paredes, M. Hermanns, S. L. Clainche, and V. Theofilis. Order 104 speedup in global linear instability analysis using matrix formation. *Computer Methods in Applied Mechanics and Engineering*, 253:287 – 304, 2013. ISSN 0045-7825. doi: <https://doi.org/10.1016/j.cma.2012.09.014>. URL <http://www.sciencedirect.com/science/article/pii/S0045782512002964>.
- [179] L. Parras and R. Fernandez-Feria. Spatial stability and the onset of absolute instability of batchelor’s vortex for high swirl numbers. *Journal of Fluid Mechanics*, 583:27–43, 2007.
- [180] S. Pasche, F. Avellan, and F. Gallaire. Part Load Vortex Rope as a Global Unstable Mode. *Journal of Fluids Engineering*, 139(5):51102–51111, mar 2017. ISSN 0098-2202. URL <http://dx.doi.org/10.1115/1.4035640>.
- [181] E. D. Pendlebury. General perturbation theory in neutronics. *Proceedings of the Physical Society. Section A*, 68(6):474, 1955. URL <http://stacks.iop.org/0370-1298/68/i=6/a=302>.
- [182] R. E. Petersen and H. W. Emmons. Stability of Laminar Flames. *Physics of Fluids*, 1961. ISSN 00319171. doi: 10.1063/1.1706349.
- [183] C. Petz, H.-C. Hege, K. Oberleithner, M. Sieber, C. Nayeri, C. Paschereit, I. Wygnanski, and B. Noack. Global modes in a swirling jet undergoing vortex breakdown. *Physics of Fluids*, 23(9):091102, 2011.
- [184] B. Pier. On the frequency selection of finite-amplitude vortex shedding in the cylinder wake. *Journal of Fluid Mechanics*, 458:407–417, 2002. doi: 10.1017/S0022112002008054.
- [185] A. D. Pierce and R. T. Beyer. *Acoustics: An Introduction to Its Physical Principles and Applications. 1989 Edition*. ASA, 1990.
- [186] R. W. Pitz and J. W. Daily. Combustion in a turbulent mixing layer formed at a rearward-facing step. *AIAA journal*, 21(11):1565–1570, 1983.
- [187] T. Poinso. *The AVBP Handbook*. CERFACS, Toulouse, 2005.

-
- [188] T. Poinso. Prediction and control of combustion instabilities in real engines. *Proceedings of the Combustion Institute*, 36(1):1 – 28, 2017. ISSN 1540-7489. doi: <https://doi.org/10.1016/j.proci.2016.05.007>. URL <http://www.sciencedirect.com/science/article/pii/S1540748916300074>.
- [189] T. Poinso and S. Lelef. Boundary conditions for direct simulations of compressible viscous flows. *Journal of Computational Physics*, 101(1):104 – 129, 1992. ISSN 0021-9991. doi: [https://doi.org/10.1016/0021-9991\(92\)90046-2](https://doi.org/10.1016/0021-9991(92)90046-2). URL <http://www.sciencedirect.com/science/article/pii/0021999192900462>.
- [190] T. Poinso and D. Veynante. *Theoretical and Numerical Combustion*, volume 28. 01 2005.
- [191] T. J. Poinso, A. C. Trouve, D. P. Veynante, S. M. Candel, and E. J. Esposito. Vortex-driven acoustically coupled combustion instabilities. *Journal of Fluid Mechanics*, 177: 265–292, 1987. URL <http://doi.org/10.1017/S0022112087000958>.
- [192] J. L. Poiseuille. *Recherches expérimentales sur le mouvement des liquides dans les tubes de très-petits diamètres*. Imprimerie Royale, 1844.
- [193] W. Polifke, A. Poncet, C. Paschereit, and K. Döbbling. Reconstruction of acoustic transfer matrices by instationary computational fluid dynamics. *Journal of Sound and Vibration*, 245(3):483 – 510, 2001. doi: <https://doi.org/10.1006/jsvi.2001.3594>. URL <http://www.sciencedirect.com/science/article/pii/S0022460X01935941>.
- [194] S. Pope. Computations of turbulent combustion: progress and challenges. *Symposium (International) on Combustion*, 23(1):591–612, 1991.
- [195] S. B. Pope. *Turbulent Flows*. Cambridge University Press, 2000. doi: 10.1017/CBO9780511840531.
- [196] M. Provansal, C. Mathis, and L. Boyer. Bénard-von kármán instability: transient and forced regimes. *Journal of Fluid Mechanics*, 182:1–22, 1987. doi: 10.1017/S0022112087002222.
- [197] U. Qadri, D. Mistry, and M. Juniper. Sensitivity Analysis of Spiral Vortex Breakdown. In *Colloquium 525 - Instabilities and transition in three-dimensional flows with rotation*, pages hal-00600349. EU-ROMECH, 11 2011. URL <https://hal.archives-ouvertes.fr/hal-00600349/document>.
- [198] U. A. Qadri, D. Mistry, and M. P. Juniper. Structural sensitivity of spiral vortex breakdown. *Journal of Fluid Mechanics*, 720:558–581, 2013.

BIBLIOGRAPHY

- [199] S. A. Ragab and J. L. Wu. Linear instabilities in two-dimensional compressible mixing layers. *Physics of Fluids A: Fluid Dynamics*, 1(6):957–966, 1989. doi: 10.1063/1.857407. URL <https://doi.org/10.1063/1.857407>.
- [200] J. W. S. L. Rayleigh. *The Theory of Sound*. Macmillan, London, 1896.
- [201] D. Reuter, U. Hegde, and B. Zinn. Flowfield measurements in an unstable ramjet burner. *Journal of Propulsion and Power*, 6(6):680–685, 1990. URL <https://arc.aiaa.org/doi/abs/10.2514/3.23272?journalCode=jpp>.
- [202] W. Reynolds and A. Hussain. The mechanics of an organized wave in turbulent shear flow. Part 3. Theoretical models and comparisons with experiments. *Journal of Fluid Mechanics*, 54(2):263–288, 1972.
- [203] D. E. Rogers. A mechanism for high-frequency oscillation in ramjet combustors and afterburners. *Journal of Jet Propulsion*, 26(6):456–462, 1956.
- [204] S. Rönsch, J. Schneider, S. Matthischke, M. Schlüter, M. Götz, J. Lefebvre, P. Prabhakaran, and S. Bajohr. Review on methanation—from fundamentals to current projects. *Fuel*, 166:276–296, 2016.
- [205] A. Roshko. Perspectives on bluff body aerodynamics. *Journal of Wind Engineering and Industrial Aerodynamics*, 49(1):79 – 100, 1993. ISSN 0167-6105. doi: [https://doi.org/10.1016/0167-6105\(93\)90007-B](https://doi.org/10.1016/0167-6105(93)90007-B). URL <http://www.sciencedirect.com/science/article/pii/016761059390007B>.
- [206] S. Roux, G. Lartigue, T. Poinso, U. Meier, and C. B̄rat. Studies of mean and unsteady flow in a swirled combustor using experiments, acoustic analysis, and large eddy simulations. *Combustion and Flame*, 141(1):40 – 54, 2005. ISSN 0010-2180. doi: <https://doi.org/10.1016/j.combustflame.2004.12.007>. URL <http://www.sciencedirect.com/science/article/pii/S0010218005000039>.
- [207] G. Rozvany. Aims, scope, methods, history and unified terminology of computer-aided topology optimization in structural mechanics. *Structural and Multidisciplinary Optimization*, 21(2):90–108, Apr 2001. ISSN 1615-1488. doi: 10.1007/s001580050174. URL <https://doi.org/10.1007/s001580050174>.
- [208] M. A. Rudgyard. *Cell vertex methods for compressible gas flows*. PhD thesis, Oxford Univ. (England)., 1990.
- [209] M. R. Ruith, P. Chen, E. Meiburg, and T. Maxworthy. Three-dimensional vortex breakdown in swirling jets and wakes: direct numerical simulation. *Journal of Fluid Mechanics*, 486:331–378, 2003. doi: 10.1017/S0022112003004749.

- [210] L. Rukes, K. Oberleithner, and C. O. Paschereit. Local linear stability analysis of a turbulent, swirling jet undergoing vortex breakdown. In *EUROMECH Colloquium 525 - Instabilities and transition in three-dimensional flows with rotation*, Ecully, France, June 2011. URL <https://hal.archives-ouvertes.fr/hal-00600347>.
- [211] L. Rukes, M. Sieber, C. O. Paschereit, and K. Oberleithner. The impact of heating the breakdown bubble on the global mode of a swirling jet: Experiments and linear stability analysis. *Physics of Fluids*, 28(10):104102, 2016. doi: 10.1063/1.4963274. URL <https://doi.org/10.1063/1.4963274>.
- [212] N. M. C. Salvador, M. T. de Mendonca, and W. M. da Costa Dourado. Large Eddy Simulation of Bluff Body Stabilized Turbulent Premixed Flame. *Journal of Aerospace Technology and Management*, 1984. doi: <http://dx.doi.org/10.5028/jatm.v5i2.245>. URL <https://doi.org/10.2514/3.12989>.
- [213] R. F. Sawyer. Science based policy for addressing energy and environmental problems. *Proceedings of the Combustion Institute*, 32(1):45 – 56, 2009. ISSN 1540-7489. doi: <https://doi.org/10.1016/j.proci.2008.07.003>. URL <http://www.sciencedirect.com/science/article/pii/S1540748908000278>.
- [214] S. Schimek, J. P. Moeck, and C. O. Paschereit. An Experimental Investigation of the Nonlinear Response of an Atmospheric Swirl-Stabilized Premixed Flame. *Journal of Engineering for Gas Turbines and Power*, 133(10):101502–101507, apr 2011. ISSN 0742-4795. URL <http://dx.doi.org/10.1115/1.4002946>.
- [215] P. J. Schmid. Dynamic mode decomposition of numerical and experimental data. *Journal of Fluid Mechanics*, 656:5–28, 2010. doi: 10.1017/S0022112010001217.
- [216] B. Schuermans, V. Bellucci, and C. O. Paschereit. Thermoacoustic modeling and control of multi burner combustion systems. In *ASME Turbo Expo 2003, collocated with the 2003 International Joint Power Generation Conference*, pages 509–519. American Society of Mechanical Engineers, 2003.
- [217] T. Schuller, D. Durox, and S. Candel. Dynamics of and noise radiated by a perturbed impinging premixed jet flame. *Combustion and Flame*, 128(1):88 – 110, 2002. ISSN 0010-2180. doi: [https://doi.org/10.1016/S0010-2180\(01\)00334-0](https://doi.org/10.1016/S0010-2180(01)00334-0). URL <http://www.sciencedirect.com/science/article/pii/S0010218001003340>.
- [218] T. Schuller, D. Durox, and S. Candel. A unified model for the prediction of laminar flame transfer functions: comparisons between conical and v-flame dynamics. *Combustion and Flame*, 134:21–34, 2003. doi: 10.1016/S0010-2180(03)00042-7.
- [219] J. D. Schwarzkopf, M. Sommerfeld, C. T. Crowe, and Y. Tsuji. *Multiphase flows with droplets and particles*. CRC press, 2011.

BIBLIOGRAPHY

- [220] L. Selle, F. Nicoud, and T. Poinsot. Actual impedance of nonreflecting boundary conditions: Implications for computation of resonators. *AIAA journal*, 42(5):958–964, 2004.
- [221] L. Selle, T. Poinsot, and B. Ferret. Experimental and numerical study of the accuracy of flame-speed measurements for methane/air combustion in a slot burner. *Combustion and Flame*, 158(1):146–154, 2011.
- [222] S. Shafiee and E. Topal. When will fossil fuel reserves be diminished? *Energy Policy*, 37(1):181 – 189, 2009. ISSN 0301-4215. doi: <https://doi.org/10.1016/j.enpol.2008.08.016>. URL <http://www.sciencedirect.com/science/article/pii/S0301421508004126>.
- [223] S. J. Shanbhogue, S. Husain, and T. Lieuwen. Lean blowoff of bluff body stabilized flames: Scaling and dynamics. *Progress in Energy and Combustion Science*, 35(1):98 – 120, 2009. ISSN 0360-1285. doi: <https://doi.org/10.1016/j.pecs.2008.07.003>. URL <http://www.sciencedirect.com/science/article/pii/S0360128508000427>.
- [224] D.-H. Shin and T. Lieuwen. Flame wrinkle destruction processes in harmonically forced, laminar premixed flames. *Combustion and Flame*, 159(11):3312 – 3322, 2012. ISSN 0010-2180. doi: <https://doi.org/10.1016/j.combustflame.2012.06.015>. URL <http://www.sciencedirect.com/science/article/pii/S0010218012001952>.
- [225] C. F. Silva, F. Nicoud, T. Schuller, D. Durox, and S. Candel. Combining a helmholtz solver with the flame describing function to assess combustion instability in a premixed swirled combustor. *Combustion and Flame*, 160(9):1743 – 1754, 2013. ISSN 0010-2180. doi: <https://doi.org/10.1016/j.combustflame.2013.03.020>. URL <http://www.sciencedirect.com/science/article/pii/S0010218013001089>.
- [226] H.-W. Sinn. Buffering volatility: A study on the limits of germany’s energy revolution. *European Economic Review*, 99:130 – 150, 2017. ISSN 0014-2921. doi: <https://doi.org/10.1016/j.euroecorev.2017.05.007>. URL <http://www.sciencedirect.com/science/article/pii/S0014292117300995>. Combating Climate Change. Lessons from Macroeconomics, Political Economy and Public Finance.
- [227] D. Sipp and A. Lebedev. Global stability of base and mean flows: a general approach and its applications to cylinder and open cavity flows. *Journal of Fluid Mechanics*, 593:333–358, 2007. doi: 10.1017/S0022112007008907.
- [228] Sir William Thomson F.R.S. . Xlvi. hydrokinetic solutions and observations. *The London, Edinburgh, and Dublin Philosophical Magazine and Journal of Science*, 42(281):362–377, 1871. doi: 10.1080/14786447108640585. URL <https://doi.org/10.1080/14786447108640585>.

- [229] G. I. Sivashinsky. Instabilities, pattern formation, and turbulence in flames. *Annual Review of Fluid Mechanics*, 15(1):179–199, 1983. doi: 10.1146/annurev.fl.15.010183.001143. URL <https://doi.org/10.1146/annurev.fl.15.010183.001143>.
- [230] M. J. Smith. *Aircraft noise*, volume 3. Cambridge University Press, 2004.
- [231] W. Steffen, J. Rockström, K. Richardson, T. M. Lenton, C. Folke, D. Liverman, C. P. Summerhayes, A. D. Barnosky, S. E. Cornell, M. Crucifix, J. F. Donges, I. Fetzer, S. J. Lade, M. Scheffer, R. Winkelmann, and H. J. Schellnhuber. Trajectories of the earth system in the anthropocene. *Proceedings of the National Academy of Sciences*, 2018. ISSN 0027-8424. doi: 10.1073/pnas.1810141115. URL <http://www.pnas.org/content/early/2018/07/31/1810141115>.
- [232] M. Stöhr, R. Sadanandan, and W. Meier. Phase-resolved characterization of vortex–flame interaction in a turbulent swirl flame. *Experiments in Fluids*, 51(4):1153–1167, Oct 2011. ISSN 1432-1114. doi: 10.1007/s00348-011-1134-y. URL <https://doi.org/10.1007/s00348-011-1134-y>.
- [233] M. Stöhr, I. Boxx, C. D. Carter, and W. Meier. Experimental study of vortex-flame interaction in a gas turbine model combustor. *Combustion and flame*, 159(8):2636–2649, 2012.
- [234] M. Stöhr, K. Oberleithner, M. Sieber, Z. Yin, and W. Meier. Experimental Study of Transient Mechanisms of Bistable Flame Shape Transitions in a Swirl Combustor. *Journal of Engineering for Gas Turbines and Power*, 140(1):11503–11508, sep 2017. ISSN 0742-4795. URL <http://dx.doi.org/10.1115/1.4037724>.
- [235] W. Strahle. Some results in combustion generated noise. *Journal of Sound and Vibration*, 23(1):113 – 125, 1972. ISSN 0022-460X. doi: [https://doi.org/10.1016/0022-460X\(72\)90792-4](https://doi.org/10.1016/0022-460X(72)90792-4). URL <http://www.sciencedirect.com/science/article/pii/0022460X72907924>.
- [236] D. L. Straub and G. A. Richards. Effect of fuel nozzle configuration on premix combustion dynamics. In *ASME 1998 International Gas Turbine and Aeroengine Congress and Exhibition*, pages V003T06A044–V003T06A044. American Society of Mechanical Engineers, 1998.
- [237] R. Struijs. *Multi-dimensional upwind discretization method for the Euler equations on unstructured grids*. PhD thesis, Technische Univ., Delft (Netherlands)., 1994.
- [238] C. J. Sung and J.-Y. Law, C. K. andChen. Augmented reduced mechanisms for no emission in methane oxidation. *Combustion and Flame*, 125:906–919, 2001. doi: 10.1016/S0010-2180(00)00248-0.

- [239] N. Syred. A review of oscillation mechanisms and the role of the precessing vortex core (pvc) in swirl combustion systems. *Progress in Energy and Combustion Science*, 32(2):93 – 161, 2006. ISSN 0360-1285. doi: <https://doi.org/10.1016/j.pecs.2005.10.002>. URL <http://www.sciencedirect.com/science/article/pii/S0360128505000353>.
- [240] O. Tammisola and M. Juniper. Coherent structures in a swirl injector at $Re=4800$ by nonlinear simulations and linear global modes. *Journal of Fluid Mechanics*, 792:620–657, 2016.
- [241] O. Tammisola and M. P. Juniper. Adjoint sensitivity analysis of hydrodynamic stability in a gas turbine fuel injector. In *ASME Turbo Expo 2015: Turbine Technical Conference and Exposition*, pages V04AT04A057–V04AT04A057. American Society of Mechanical Engineers, 2015.
- [242] O. Tammisola, F. Giannetti, V. Citro, and M. P. Juniper. Second-order perturbation of global modes and implications for spanwise wavy actuation. *Journal of Fluid Mechanics*, 755:314–335, 2014. doi: 10.1017/jfm.2014.415.
- [243] A. Tarantola. Book reviews - inverseproblem theory. methods for ata fitting and model parameter estimation. *Geophysical Journal*, 94(1):167–168, 1987. doi: 10.1111/j.1365-246X.1988.tb03436.x. URL <https://onlinelibrary.wiley.com/doi/abs/10.1111/j.1365-246X.1988.tb03436.x>.
- [244] Tennet. Tatsächliche und prognostizierte solarergieeespeisung. Technical report, 2018. URL http://www.tennettso.de/site/Transparenz/veroeffentlichungen/netzkennzahlen/tatsaechliche-und-prognostizierte-solarenergieeespeisung_land?lang=de_DE.
- [245] Tennet. Tatsächliche und prognostizierte windenergieeespeisung. Technical report, 2018. URL <http://www.tennettso.de/site/Transparenz/veroeffentlichungen/netzkennzahlen/tatsaechliche-und-prognostizierte-windenergieeespeisung>.
- [246] S. Terhaar and C. Paschereit. High-Speed PIV Investigation of Coherent Structures in a Swirl-Stabilized Combustor Operating at Dry and Steam-Diluted Conditions. In *Proceedings of the 16th Symposium on Applications of Laser Techniques to Fluid Mechanics*, pages 1–12. Instituto Superior Tecnico, 2012. URL <https://www.researchgate.net/publication/268257636>.
- [247] M. Thompson, K. Hourigan, and J. Sheridan. Three-dimensional instabilities in the wake of a circular cylinder. *Experimental Thermal and Fluid Science*, 12(2):190 – 196, 1996. ISSN 0894-1777. doi: [https://doi.org/10.1016/0894-1777\(95\)00098-4](https://doi.org/10.1016/0894-1777(95)00098-4). URL <http://www.sciencedirect.com/science/article/pii/0894177795000984>.

-
- [248] H. B. Toda, O. Cabrit, G. Balarac, S. Bose, J. Lee, H. Choi, and F. Nicoud. A subgrid-scale model based on singular values for les in complex geometries. In *Proc. of the Summer Program*, pages 193–202, 2010.
- [249] J. Tromp, C. Tape, and Q. Liu. Seismic tomography, adjoint methods, time reversal and banana-doughnut kernels. *Geophysical Journal International*, 160(1):195–216, 2005.
- [250] K. Tsiglifilis and A. D. Lucey. Global stability of three-dimensional disturbances in blasius boundary-layer flow over a compliant panel. *Proc. 19th Australasian Fluid Mechanics Conference*, 335, 12 2014.
- [251] A. K. Vaish and A. K. Chopra. Earthquake finite element analysis of structure-foundation systems. *Journal of the Construction Division*, 100(ASCE 10990), 1974.
- [252] K. K. Venkataraman, L. H. Preston, D. W. Simons, B. J. Lee, J. G. Lee, and D. A. Santavicca. Mechanism of Combustion Instability in a Lean Premixed Dump Combustor. *Journal of Propulsion and Power*, 15(6):909–918, nov 1999. ISSN 0748-4658. doi: 10.2514/2.5515. URL <https://doi.org/10.2514/2.5515>.
- [253] O. Vermorel, S. Richard, O. Colin, C. Angelberger, A. Benkenida, and D. Veynante. Towards the understanding of cyclic variability in a spark ignited engine using multi-cycle les. *Combustion and Flame*, 156(8):1525–1541, 2009.
- [254] D. Veynante and L. Vervisch. Turbulent combustion modeling. *Progress in Energy and Combustion Science*, 28(3):193 – 266, 2002. ISSN 0360-1285. doi: [https://doi.org/10.1016/S0360-1285\(01\)00017-X](https://doi.org/10.1016/S0360-1285(01)00017-X). URL <http://www.sciencedirect.com/science/article/pii/S036012850100017X>.
- [255] H. L. F. von Helmholtz. Xliii. on discontinuous movements of fluids. *The London, Edinburgh, and Dublin Philosophical Magazine and Journal of Science*, 36(244): 337–346, 1868. doi: 10.1080/14786446808640073. URL <https://doi.org/10.1080/14786446808640073>.
- [256] H. von Karman. über laminare und turbulente reibung. *Zeitschrift für angewandte Mathematik und Mechanik*, 1(4):233–2522, 1921. doi: 10.1002/zamm.19210010401. URL <http://onlinelibrary.wiley.com/doi/10.1002/zamm.19210010401/full>.
- [257] H. Wang, C. Law, and T. Liewen. Linear response of stretch-affected premixed flames to flow oscillations. *Combustion and Flame*, 156(4):889 – 895, 2009. ISSN 0010-2180. doi: <https://doi.org/10.1016/j.combustflame.2009.01.012>. URL <http://www.sciencedirect.com/science/article/pii/S0010218009000194>.
- [258] C. K. Westbrook and F. L. Dryer. Simplified reaction mechanisms for the oxidation of hydrocarbon fuels in flames. *Combustion Science and Technology*, 27(1-2):

BIBLIOGRAPHY

- 31–43, 1981. doi: 10.1080/00102208108946970. URL <https://doi.org/10.1080/00102208108946970>.
- [259] F. A. Williams. *Combustion Theory*, volume 2. Benjamin/Cummings Publishing Company, Menlo Park, California, 1985.
- [260] G. Williams. *Combustion theory*. Addison-Wesley, 1985.
- [261] C. H. Williamson. Vortex dynamics in the cylinder wake. *Annual review of fluid mechanics*, 28(1):477–539, 1996.
- [262] P. Xavier, A. Ghani, D. Mejia, M. Miguel-Brebion, M. Bauerheim, L. Selle, and T. Poinso. Experimental and numerical investigation of flames stabilised behind rotating cylinders: interaction of flames with a moving wall. *Journal of Fluid Mechanics*, 813:127—151, 2017. doi: 10.1017/jfm.2016.864.
- [263] X. Zhang, C. Bauer, C. L. Mutel, and K. Volkart. Life cycle assessment of power-to-gas: Approaches, system variations and their environmental implications. *Applied Energy*, 190:326 – 338, 2017. ISSN 0306-2619. doi: <https://doi.org/10.1016/j.apenergy.2016.12.098>. URL <http://www.sciencedirect.com/science/article/pii/S0306261916318682>.
- [264] O. C. Zienkiewicz and R. L. Taylor. *The Finite Element Method – Volume 1: The Basis*. Butterworth Heinemann, Linacre House, Jordan Hill, Oxford OX2 8DP, Great Britain, 2000.
- [265] O. C. Zienkiewicz and R. L. Taylor. *The Finite Element Method – Volume 2: Solid Mechanics*. Butterworth Heinemann, Linacre House, Jordan Hill, Oxford OX2 8DP, Great Britain, 2000.
- [266] O. C. Zienkiewicz and R. L. Taylor. *The Finite Element Method – Volume 3: Fluid Dynamics*. Butterworth Heinemann, Linacre House, Jordan Hill, Oxford OX2 8DP, Great Britain, 2000.
- [267] H.-J. Ziesing. Energieverbrauch in deutschland im jahr 2017. Technical report, AG Energiebilanzen e.V., February 2018. URL <https://ag-energiebilanzen.de>.
- [268] H.-J. Ziesing. Bruttostromerzeugung in deutschland ab 1990 nach energieträgern. Technical report, AG Energiebilanzen e.V., February 2018. URL <https://ag-energiebilanzen.de>.
- [269] E. ZUKOSKI. Combustion instability sustained by unsteady vortex combustion. In *21st Joint Propulsion Conference*, page 1248, 1985.